

Intraplate Earthquakes in Nordland, Northern Norway

Insight from Seismic Tomography and Earthquake Analysis

Hasbi Ash Shiddiqi

Thesis for the degree of Philosophiae Doctor (PhD)
University of Bergen, Norway
2023

UNIVERSITY OF BERGEN



Intraplate Earthquakes in Nordland, Northern Norway

Insight from Seismic Tomography and Earthquake
Analysis

Hasbi Ash Shiddiqi



Thesis for the degree of Philosophiae Doctor (PhD)
at the University of Bergen

Date of defense: 19.01.2023

© Copyright Hasbi Ash Shiddiqi

The material in this publication is covered by the provisions of the Copyright Act.

Year: 2023

Title: Intraplate Earthquakes in Nordland, Northern Norway

Name: Hasbi Ash Shiddiqi

Print: Skipnes Kommunikasjon / University of Bergen

Scientific environment

The research presented in this dissertation has been performed mainly at the Department of Earth Science, University of Bergen (UiB), Norway, between February 2019 and September 2022. Parts of the thesis were performed during research visits at the CSIR – National Geophysical Research Institute (NGRI), Hyderabad, India and Instituto Dom Luiz, Faculty of Science, University of Lisbon, Portugal.

Main Supervisor: Prof. Lars Ottemöller (UiB)

Co-supervisors: Prof. Stéphane Rondenay (UiB) and Dr. M. Ravi Kumar (CSIR-NGRI).

The PhD position was funded by the Research Council of Norway through the project “IPSIN - Intraplate Seismicity in India and Norway: Distribution, properties and causes”. The candidate received additional support from the Norwegian National Seismic Network Project, which is funded by the Norwegian Oil and Gas Association. As a member of the Norwegian Research School for Dynamics and Evolution of Earth and Planets (DEEP), the candidate received funding to attend an external course held at the University of Oslo.

Acknowledgements

Looking back at my PhD journey, this achievement would not be possible without the support and motivation from many people.

I would like to express my gratitude to my supervisor Lars Ottemöller, for the opportunities to work on exciting projects, and for all his guidance and help in academia and life. I first arrived at UiB in the autumn of 2016. Since then I have been working with Lars on several projects and I have learned a lot from his vast knowledge and research experience in observational seismology. I am very grateful to my co-supervisor Stéphane Rondenay, for being motivational and positive, for all his guidance and support, and for all exciting scientific discussions. I also thank my co-supervisor M. Ravi Kumar-sir, for all his support during my visits to India.

I would like to thank present and former members of the seismology group for all discussions and helps during my time at the University of Bergen. I thank Felix Halpaap, who is my office mate for the past six years, for his great help on many aspects of my work and for creating a great working environment, Henk Keers for his advice especially on seismic ray tracing and tomography, Mathilde Böttger Sørensen and Kuvvet Atakan especially for discussions on tectonic and seismicity in Nordland, Jens Havskov for advice on earthquake data processing, Øyvind Natvik for the IT support and to Jan Michálek, Berit Marie Storheim, Marte Louise Strømme, Zeinab Jeddi, Sara Rezaei, Andrea Demuth, Maren Kjos Karlsen and Katharina Newrkla for sharing their knowledge on various aspects of seismology and data processing. I thank Berit Marie for the help in translating the abstract to Norwegian, and Mathilde, Maren, and Felix for improving the translation.

The findings presented in this thesis would not be possible without collaboration and support from many people. I would like to thank Susana Custódio, for hosting my visit to the University of Lisbon and for her interest in intraplate earthquakes and SSA analysis. I thank colleagues at the Geological Survey of Norway: Sofie Gradmann, Claudia Pavez-Orrego, and Odleiv Olesen, who provided insight on the geology and geophysical background of Nordland. I thank colleagues at NORSAR and Norwegian

Geotechnical Institute: Tormod Kværna, Annie E. Jerkins, and Steven J. Gibbons, for all collaborations and discussions on earthquakes in Norway. I also express my gratitude to colleagues at CSIR-National Geophysical Research Institute, Hyderabad, India: Vineet K. Gahalaut-sir, Kalpna Gahalaut-mam, M. Ravi Kumar-sir, Rajeev K. Yadav, N. Purnachandra Rao-sir, and D. Srinagesh-sir, for hosting my visits and for fruitful discussions.

I thank my previous mentors: Pak Sri Widiyantoro, Pak Andri Dian Nugraha, Pak Irwan Meilano, Pak M. Rachmat Sule and Pak Afnimar for inspiring me to take the path of earthquake seismology and to continue my education. I thank many early career Indonesian geoscientists for exciting discussions and research collaboration on tectonics and seismology in the past few years: David Sahara, Fernando Hutapea, Haikal Sedayo, Ryan Pranantyo, Rino Salman, Kadek Palgunadi, and Pepen Supendi.

I would also like to thank my fellow PhD candidates and colleagues at GEO for discussions and the time shared together. Among them I would like to mention Thomas Theunissen (especially for discussion on tectonics and seismic tomography), Jhon Meyer Munoz Barrera (especially for discussion on geology of Nordland), Sebastian Georg Wolf (especially for discussion on tectonics and geodynamics), Xingguo Huang, Kui Xiang (especially for proof-reading my thesis), Enry Horas Sihombing, Durra H. Saputera, and Ujjwal Shekhar. I am also grateful for the administrative support from Andrea Grimnes, Anders Bjørnsen Kulseng and Mareile Andersson.

Being away from home for a long time, especially during the pandemic, is difficult. I am grateful to the Indonesian community in Bergen and Oslo for all their support and help and all those tasty foods. Among them I would like to mention Mas Boya, Ara, Tante Emmy, Sandi, Uni Lusi, Mas Baim, Mbak Aini, Eko, Feni, Royan, Pipit, Ulin, Ila, Gesa, Mas Pras, Enry, and Durra.

I would like to thank my parents and my mother-in-law for all their support throughout my education. Similarly, I also thank my sister, sisters-in-law and brothers-in-law for your support. Last, I thank the two most important persons in my life: my wife, Asnin, and son, Nauli. To my son, thank you for being a nice and smart boy. To my wife, thank you for your love, for being there and for all your support through many ups and downs.

Abstract

Intraplate seismicity occurs in regions that are not affected by recent plate boundary processes. The total seismic moment release from these earthquakes is much smaller than that from plate boundary earthquakes. However, intraplate seismicity, particularly in continental settings, can also cause considerable damage. The majority of intraplate events occur along rifted margins, where pre-existing structures are reactivated due to present-day stress. The understanding and detailed observations of intraplate seismicity are mostly limited to well instrumented regions, e.g., New Madrid seismic zone in the eastern U.S. and West Bohemia in Czech Republic. In other regions, including Nordland (northern Norway), a lack of dense seismic station networks hindered such studies in the past.

Nordland, situated along the rifted mid-Norwegian margin, has one of the highest seismicity rates in continental Northern Europe. The 1819 M 5.9 event, which occurred in Lurøy, Nordland, is the largest documented earthquake in Norway. Recent earthquakes have small to moderate magnitudes, with frequent seismic swarm activity in several areas. Seismological observations in Nordland have been ongoing for more than four decades. However, detailed spatio-temporal behaviour and mechanism of the Nordland seismicity have not yet been resolved due to the sparse seismic station coverage in the past. The increasing number of seismic stations in the past ten years allows us to study the seismicity in more detail.

This thesis provides insight into intraplate seismicity, particularly in Nordland. The research is divided into three parts: 1) a seismic tomography study, which highlight heterogeneity in the crust and its relation to seismicity, 2) an analysis of the seismic swarm sequence in Jektvik, Nordland, which focuses on constraining the seismicity spatio-temporal evolution and its modulation and 3) a comparison between earthquake clusters along the most seismically active areas in coastal Nordland.

Part 1 investigates the crustal structure in Nordland and its relation to intraplate seismicity. This study develops 3-D seismic velocity models using travel-time seismic tomography. The tomography images reveal complexity in the crust, including a sharp

Moho transition between the southern part of Lofoten islands and mainland Nordland, which we refer to as Moho step. The NE-SW extent of this Moho step is located near the corridor of seismic activity in Nordland. Furthermore, areas of frequent seismic swarm occurrence, namely Jektvik and Steigen, are characterized by low P-wave velocity and varying P-to-S wave velocity ratio anomalies, which are interpreted as fractured crust and presence of fluids. Focal mechanisms computed in this study have normal and oblique-normal solutions that reflect an extensional stress regime in the shallow crust. This extension deviates from the expected regional compressive regime associated with mid-Atlantic ridge push. The deviation is ascribed to a contribution from glacial isostatic adjustment and sediment redistribution.

Part 2 characterizes the spatio-temporal evolution of a nearly decade-long swarm sequence in Jektvik, Nordland. Using an improved earthquake catalog, we resolve four major groups of events, which show activity progression outward from the center. The computed focal mechanisms with predominantly normal solutions confirm the local extensional regime. The swarm sequence seems to occur within fluid-saturated fracture zones that are reactivated due to this extension. An examination of the time distribution of earthquakes reveals a recurrent increase in activity between February and May of each year, which coincides with the late winter and spring time in Norway. This further coincides with hydrological loading that is observed as elastic deformation on Global Navigation Satellite Systems (GNSS) stations. The preferential timing of the seismicity leads to the hypothesis that the Jektvik earthquakes are hydrologically modulated. This study shows that the loading can promote failure in a critically stressed normal faulting system. Furthermore, the possibility of co-seismic triggering within swarm sequence is explored in this study.

Part 3 compares the seismicity characteristics of two adjacent areas in Nordland: Jektvik and Rana. Both areas have swarm-like behaviour, but exhibit distinct spatio-temporal patterns. Jektvik seismicity shows outward seismicity migration, whereas earthquakes in Rana occur within isolated spots with no indication of activity migration. Singular spectrum analysis reveals that Jektvik has a dominant near-annual periodicity, indicating hydrological load modulation. Seismicity in Rana does not show similar periodicity, even though the area is also affected by the load changes, which is evidenced by GNSS data. We hypothesize that Jektvik seismicity occurs within fluid saturated fractures and is modulated by hydrological loading, whereas Rana seismicity occurs within fault irregularities that accumulate stress and rupture repeatedly over time.

Taken together, this thesis provides important new insight into the crustal structure and complex seismogenic processes associated with intraplate seismicity, particularly in the Nordland region of northern Norway. This study highlights the close interaction between

lithosphere and hydrosphere contributing to the occurrence of intraplate earthquake swarm activity. Furthermore, this thesis presents a case study that shows that adjacent areas in an intraplate setting can have distinct seismogenic behaviour.

Abstrakt

Intraplate-seismisitet refererer til jordskjelv i områder som ikke er påvirket av prosessene langs aktive plategrenser. Det totale seismiske momentet utløst fra intraplatejordskjelv er mye mindre enn fra jordskjelv i forbindelse med aktive plategrenser. Likevel kan intraplate seismisitet gi betydelige ødeleggelser, særlig i kontinentale områder. De fleste intraplate jordskjelv skjer langs riftmarginer hvor eksisterende strukturer blir reaktivert av nyere oppbygget spenning. Detaljerte observasjoner og god forståelse av intraplate-spenninger er i hovedsak begrenset til områder med høy instrumenttetthet, eksempler på slike områder er New Madrid Seismic Zone i det østlige USA og vestre Bøhmen i Den Tsjekiske republikk. I andre områder, inkludert Nordland, har lav instrumenttetthet hindret detaljerte studier av intraplate-seismisiteten.

I Nordland finnes et av de mest aktive seismiske områdene i Fastlands-Nordeuropa. Jordskjelvet i 1819 (M 5.9) lokalisert til Lurøy, Nordland, er det største dokumenterte jordskjelvet i Norge. Nyere jordskjelv har lave til moderate magnituder, med hyppige seismiske svermer i flere områder. På 1980 tallet ble det installert flere seismiske stasjoner i Nordland, men stasjonstettheten var fortsatt lav frem til ca 2010 da flere midlertidige og permanente seismiske stasjoner ble installert. Økt stasjonstetthet har gjort det mulig å gjennomføre detaljerte studier av seismisiteten i området.

Denne doktorgradsavhandling øker forståelsen av intraplate-seismisitet, særlig i Nordland området. Forskningsprosjektet består av tre deler: 1) seismisk tomografi med fokus på heterogeniteter i jordskorpen og korrelasjon med lokal seismisitet, 2) analyse av seismisk svermaktivitet i Jektvik, Nordland, og 3) en sammenligning mellom klynger av jordskjelv i de mest seismisk aktive områdene langs kysten av Nordland.

Del 1 undersøker jordskorpestrukturen i Nordland og potensiell korrelasjon med intraplate-seismisiteten i området. Dette studiet bruker seismisk tomografi for å utvikle en 3D seismisk hastighetsmodell. Tomografien avdekker en kompleks skorpestruktur med bl.a. en skarp Mohogrense (senere referert til som Mohotrinnet) mellom de sørlige øyene i Lofoten og fastlandet mot øst. Den nordøst-sørvestlige forlengelsen av Mohotrinnet er lokalisert nær korridoren med seismisk aktivitet i Nordland. I tillegg er områdene

med mange seismiske svermer, Jektvik og Steigen, karakterisert som anomalier ved lav P-bølgehastighet og forskjellige P-S bølgehastighetsforhold, som blir tolket som områder med oppsprekket skorpe og væskeinnhold. Fokalmekanismene funnet i dette studiet viser normal og skrå-normale bevegelser som reflekterer et ekstensjonsregime i den øvre skorpen. Denne ekstensjonen avviker fra den forventede kompresjonsbevegelsen assosiert med bevegelsene langs den midtatlantiske sprederyggen. Ekstensjonen kan forklares med bidrag fra glasial isostatisk justering og sedimentfordeling.

Del 2 karakteriserer utviklingen i tid og rom av en tiårig svermsekvens i Jektvik, Nordland. Ved å bruke en forbedret jordskjelvkatalog identifiseres fire hovedgrupper av jordskjelv som viser aktivitet som utvikler seg ut fra senter. Fokalmekanismene viser i hovedsak normal bevegelse som bekrefter ekstensjon. Svermsekvensene ser ut til å oppstå i våte forkastningssoner som er reaktivert av ekstensjonen. Tidsfordelingen av jordskjelvene viser årlig tilbakevendende økt aktivitet mellom Februar og Mai, hvilket sammenfaller med sen vinter/vår i Norge. Videre sammenfaller dette med hydrologisk vektning som er observert som elastisk deformasjon på *Global Navigation Satellite Systems* (GNSS) stasjoner. Tidsfordelingen av jordskjelvene leder mot en hypotese om at Jektvik jordskjelvene har en hydrologisk opprinnelse.

Del 3 sammenligner den seismiske karakteristikken for to nærliggende områder i Nordland, Jektvik og Rana. I begge områdene observeres sverm-lignende sekvenser, med tydelig fordeling i rom og tid. Den seismiske aktiviteten i Jektvik migrerer utover mens aktiviteten i Rana er lokalisert i isolerte punkt uten tegn til migrering over tid. Enkelt-spektrum analyse (*singular spectrum analysis*) avdekker at det i Jektvik er en periodisk gjentakelse på nesten ett år. Seismisiteten i Rana viser ikke lignende periodisitet selv om området, som vist av GNSS målinger, også blir påvirket av varierende hydrologisk vekt. Hypotesen som fremsettes er at seismisiteten i Jektvik oppstår i våte sprekker og blir styrt av hydrologisk vekt, mens seismisiteten i Rana oppstår innenfor forkastningssområder som akkumulerer spenninger som blir utløst over tid.

Denne doktorgradsavhandlingen gir viktig ny informasjon om skorpestrukturen og de kompliserte prosessene forbundet med intraplate seismisitet, spesielt i Nordland regionen i Norge. Studiet setter fokus på hvordan det nære forholdet mellom litosfære og hydrosfære bidrar til dannelsen av intraplate seismisk sverm aktivitet. Videre presenterer dette studiet hvordan seismisitet i nærliggende områder kan ha ulike egenskaper.

List of publications

The following publications are included in this PhD dissertation:

- Paper 1 Shiddiqi, Hasbi Ash**, Ottemöller, L., Rondenay, S., Halpaap, F., Gradmann, S., and Michálek, J. (2022). Crustal structure and intraplate seismicity in Nordland, Northern Norway: insight from seismic tomography, *Geophysical Journal International*, Volume 230, Issue 2, August 2022, pp. 813–830. doi: <https://doi.org/10.1093/gji/ggac086>.
- Paper 2 Shiddiqi, Hasbi Ash**, Ottemöller, L., Rondenay, S., Custódio, S., Gahalaut, V.K., Yadav, R.K., Halpaap, F. and Gahalaut, K. (2022). Seismicity modulation due to hydrological loading in stable continental region: a case study from Jektvik swarm sequence in Northern Norway. (submitted to *Geophysical Journal International*).
- Paper 3 Shiddiqi, Hasbi Ash**, Ottemöller, L., Rondenay, S., Custódio, S., Halpaap, F. and Gahalaut, V.K. (2022). Comparison of earthquake clusters in a stable continental region: a case study from Nordland, Northern Norway. (submitted to *Seismological Research Letters*).

The following additional publications are also appended in the dissertation to provide methodological background:

- Appendix 1 Shiddiqi, Hasbi Ash**, Tun, P.P., and Ottemöller, L. (2019). Minimum 1D Velocity Model and Local Magnitude Scale for Myanmar. *Seismological Research Letters*, Volume 90, Issue 5. pp. 1923–1936. doi: <https://doi.org/10.1785/0220190065>.
- Appendix 2 Newrkla, Katharina, Shiddiqi, H.A.**, Jerkins, A.E., Keers, H., and Ottemöller, L. (2019). Implications of 3D Seismic Raytracing on Focal Mechanism Determination. *Bulletin of the Seismological Society of America*, Volume 109, Issue 6. pp. 2746–2754. doi: <https://doi.org/10.1785/0120190184>.

Contributions at scientific meetings during PhD study, but not included in the dissertation:

1. Newrkla, K., **Shiddiqi, H.A.**, Jerkins, A.E., Keers, H., and Ottemöller, Implications of 3D teleseismic ray-tracing on focal mechanism determination. (Oral) *American Geophysical Union Fall Meeting*; 9-13 December 2019, San Francisco, United States of America.
2. **Shiddiqi, Hasbi Ash**, Tun, P.P., and Ottemöller, L., The development of 1D seismic velocity model and the intermediate depth seismicity analysis in the Indo-Burma Subduction zone, Myanmar. (Poster) *American Geophysical Union Fall Meeting*; 9-13 December 2019, San Francisco, United States of America.
3. **Shiddiqi, Hasbi Ash**, Ottemöller, L., Rondenay, S., Halpaap, F., and Michálek, J. Intraplate seismicity in Nordland, Northern Norway: Insight from Seismic Tomography. (Oral) *American Geophysical Union Fall Meeting*; 1-17 December 2020, virtual meeting.
4. **Shiddiqi, Hasbi Ash**, Ottemöller, L., Rondenay, S., Halpaap, F., Gradmann, S. and Michálek, J. Intraplate seismicity in Nordland, northern Norway: insight from seismic tomography and hypocenter relocation. (Oral) *The International Association of Geomagnetism and Aeronomy-International Association of Seismology and Physics of the Earth's Interior Joint Scientific Assembly 2021*; 21-27 August 2021, virtual meeting.
5. **Shiddiqi, Hasbi Ash**, Ottemöller, L., Rondenay, S., Halpaap, F. Earthquake swarms and clusters in stable continental regions: a case study from Northern Norway , (Oral) *European Geosciences Union General Assembly 2022*; 23-27 May 2022, Vienna, Austria.

Paper I is published under an open-access license which permits the use and distribution, provided the original work is properly cited. Appendices I and II are published under a green open access option from the Seismological Society of America, which permits redistribution of the accepted version of the manuscripts.

Contents

Scientific environment	i
Acknowledgements	iii
Abstract	v
Abstrakt	ix
List of publications	xi
1 Introduction	1
1.1 Intraplate earthquakes in continental settings	1
1.2 Research Questions and Objectives	3
1.3 Study area: Tectonics, crustal structure and seismicity in Nordland, Northern Norway	4
1.3.1 Tectonic and geological setting	4
1.3.2 Geophysical investigations in Nordland	6
1.3.3 Seismicity	8
1.4 Data and Methods	10
1.4.1 Data	10
1.4.2 Methods	13

2	Synthesis	27
2.1	Main findings	27
2.2	Outlook	29
3	Scientific results	49
3.1	Paper 1	49
3.2	Paper 2	80
3.3	Paper 3	119
	Appendices	155
	Appendix 1	157
	Appendix 2	188

Chapter 1

Introduction

The generating mechanisms of intraplate earthquakes, which occur within tectonic plates, are not as well understood as earthquakes occurring along the plate boundaries [e.g., Calais et al., 2016; Talwani, 2014]. This thesis aims to improve the understanding of continental intraplate seismicity, with focus on the Nordland region of Northern Norway, from detailed tomographic images in connection with enhanced seismicity catalogs and modelling of causative processes.

1.1 Intraplate earthquakes in continental settings

Continental intraplate earthquakes occur within stable continental regions (SCR), which are largely not affected by the active plate boundary processes [Johnston, 1989; Schulte and Mooney, 2005]. Common characteristics of intraplate earthquakes are higher stress drop [Allmann and Shearer, 2009] and long return periods for large earthquakes [Talwani, 2017]. While most of the global seismic moment is released by earthquakes along the plate boundaries, intraplate events are responsible for a considerable part of damage. Among the largest and best known intraplate earthquakes are 1811-1812 New Madrid, 1976 Tangshan, and 2001 Bhuj. In Norway, the largest intraplate earthquakes in historic times are the M 5.9 Rana in 1819 [Bungum and Olesen, 2005; Mäntyniemi et al., 2020; Muir-Wood, 1989] and the Ms 5.4 Oslo in 1904 [Bungum et al., 2009]. More recently, a M_w 6.1 Storfjorden earthquake occurred in the southern part of the Svalbard archipelago [Ottemöller et al., 2021a; Pirli et al., 2010].

There are several causative mechanisms of intraplate earthquakes: strain localization [Zoback et al., 1985] and local stress concentration, which reactivate pre-existing weak zones [Talwani, 2014]. Glacial isostatic adjustment (GIA) also contributes to local stress

at higher latitudes, e.g. Scandinavia [Gradmann et al., 2018; Keiding et al., 2015] and Eastern Canada [Steffen, 2013]. Weak structures within rift zones are preferentially re-activated by a regional stress field within the continent [Talwani, 2014]. As a result, the stress accumulates on discrete structures, which are identified as local stress concentrators. Liu and Zoback [1997] and Cloetingh et al. [2005] suggested that seismic zones in intraplate settings can be associated with areas of weak lithosphere due to inherited structures and thermal perturbation in New Madrid, and West and Central Europe. On the contrary, McKenna et al. [2007] found that New Madrid is not significantly weaker and hotter than the surrounding regions.

Seismic swarms are defined as earthquake sequences without clear mainshocks, and are commonly observed in volcanic and plate boundary settings, where they are associated with fluid migration and aseismic slip [Fischer et al., 2014; Passarelli et al., 2018]. Detailed studies of swarms in SCR settings are limited to a number of areas, including West Bohemia [Fischer et al., 2014], Western India [Gahalaut et al., 2022], and New Madrid [Bisrat et al., 2012]. These swarms are mostly suggested to be related to presence of fluids, for example swarms in West Bohemia are associated with CO₂ that originates from the mantle [Fischer et al., 2014; Mousavi et al., 2015] and swarms in western India and New Madrid are associated with rainfall [Bisrat et al., 2012; Gahalaut et al., 2022]. Swarms have been reported as well in other intraplate regions such as Western Iberia [Matos et al., 2018], Brazil [Lopes et al., 2010], Greenland [Larsen et al., 2014], and Northern Norway [Atakan et al., 1994; Bungum et al., 1979; Michálek et al., 2018]. However, detailed characterization of those swarms is still lacking.

Modulation of seismicity due to hydrological processes has been suggested in various settings: interplate seismicity, e.g., California [Christiansen et al., 2007] and Taiwan [Hsu et al., 2021] and intraplate setting, e.g., New Madrid seismic zone [Craig et al., 2017] and Western India [Gahalaut et al., 2022]. Observations in several intraplate continental settings show that brittle crust is critically stressed [Townend and Zoback, 2000], and small changes in Coulomb stress (ΔCFF) and pore-pressure can trigger seismic events [Wilson et al., 2022].

Stress interactions, deformation localization as well as the effect of lithospheric heterogeneity in continental intraplate settings remain an open question. The causes of seismic swarms in such settings are also unclear. Recent upgrades of seismic networks and temporary deployments in many regions, including Northern Norway, provide an opportunity to study the seismicity in detail and to produce high resolution local seismic tomography images. Deployments of Global Navigation Satellite System (GNSS) stations can further help to understand deformation in intraplate settings.

1.2 Research Questions and Objectives

The overarching objective in this thesis is to improve our understanding of the physics of intraplate earthquakes and the earth structure in the areas where they occur. In this work, I investigate the seismicity in Nordland, Northern Norway. This is one of the most seismically active regions in mainland Norway where seismicity has been monitored for more than four decades. Recent improvements of the seismic monitoring allow us to perform detailed seismicity analysis. The questions that I address are:

1. How does the crustal structure affect intraplate seismicity in Nordland?

This question is addressed in Paper 1, where I focus on improving the crustal structure model using seismic tomography and investigating its link to earthquakes in Nordland. The objectives in this part are:

- a) To obtain 3-D models of P-wave velocity (V_P) and P-to-S wave velocity ratio (V_P/V_S) of the crust.
- b) To improve earthquake locations and focal mechanisms using the 3-D velocity models.
- c) To analyze the 3-D models and infer Moho depth, rock composition, and existence of fluids.
- d) To investigate links between the crustal structure, crustal stress, and earthquakes.

2. What are the causes of seismic swarms and what are the physical processes within and between swarms in Nordland?

In Paper 2, I investigate an earthquake swarm sequence that occurred in Jektvik, Nordland. The objectives in this part are:

- a) To develop a comprehensive earthquake catalog, identify earthquake clusters and obtain focal mechanisms.
- b) To investigate the spatio-temporal pattern of the swarm sequence and possible triggering between earthquake clusters.
- c) To link the seismicity to tectonic and geological processes.
- d) To investigate seasonal trends in seismicity, and if identified link these to physical processes.

3. Do nearby areas in an intraplate setting have different seismicity characteristics, and if so why?

In Paper 3, I investigate seismicity in a wider region by comparing the characteristics of two adjacent seismically active areas in Nordland, namely Jektvik and Rana. The objectives are:

- a) To develop a comprehensive earthquake catalog, identify clusters and multiplets of highly similar events.
- b) To compare the characteristics and spatio-temporal patterns of earthquake clusters in Rana and Jektvik.
- c) To investigate the periodicity in the earthquake catalog and its relation to different processes.
- d) To interpret the active faults kinematics in the study area using earthquake hypocenters and focal mechanisms.

1.3 Study area: Tectonics, crustal structure and seismicity in Nordland, Northern Norway

This section closely follows the background information related to tectonic setting, crustal structure and seismicity of the study area presented in Paper 1 (Section 2: Background) [Shiddiqi et al., 2022].

1.3.1 Tectonic and geological setting

The Nordland region is bounded by the Northern Scandes mountain range to the east and the Lofoten-Vesterålen margin to the west. The region is a rifted margin, which contains abundant faults and weak zones formed by episodes of tectonic processes. The region mostly consists of the Caledonian domain (Fig. 1.1), shaped by the collision of Baltica and Laurentia, then followed by the collapse of the orogen in the Devonian and the long phases of extension and rifting culminated in the continental breakup and opening of the Atlantic in the Early Eocene [Corfu et al., 2014; Faleide et al., 2008; Tsikalas et al., 2001]. The breakup was followed by the formation of the North Atlantic Igneous Province and the Norwegian margin [see e.g., Eldholm and Grue, 1994; Horni et al., 2017].

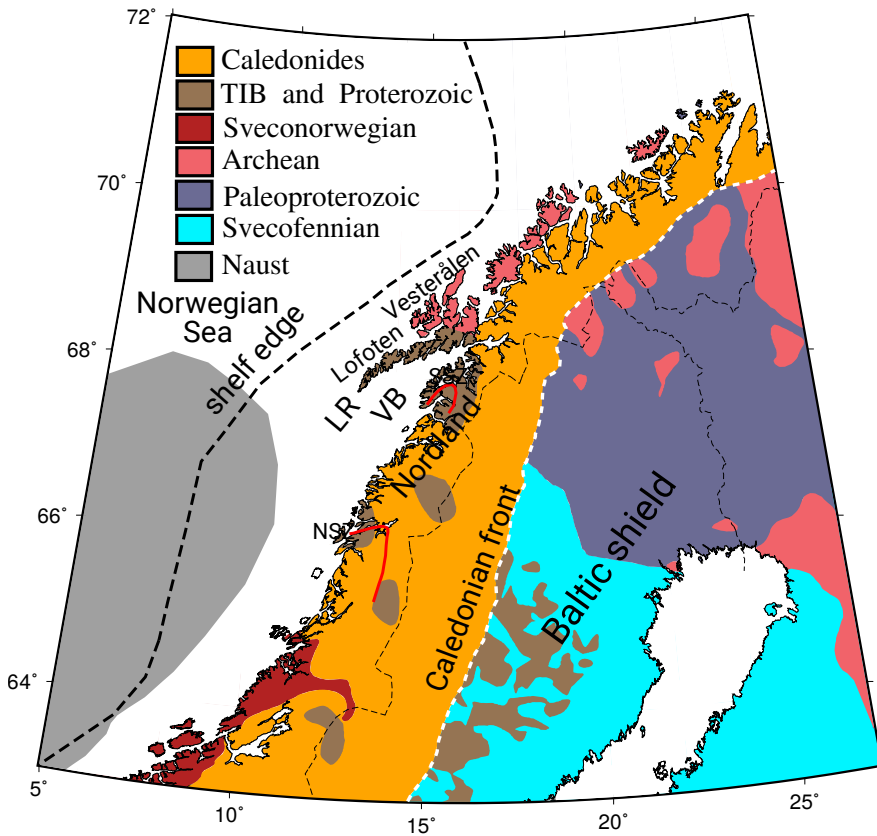


Figure 1.1: Simplified geological map of northwestern Fennoscandia including Nordland (based on Grund and Ritter [2020] and Högdahl et al. [2004]). TIB is Transscandinavian igneous belt. LR is the Lofoten Ridge and VB is the Vestfjorden Basin. White dashed line represents the Caledonian front. Shelf edge is depicted by a thick dashed black line. Gray area shows the approximate location of the Naust formation. Red lines are the shear zones mentioned in the text. NSZ: Nesna Shear Zone, SSZ: Sagfjord Shear zone.

The narrow Lofoten-Vesterålen margin is situated between the Senja Fracture zone in the north and the Vøring margin in the south. The margin is marked by the exposed Lofoten-Vesterålen islands, which comprise the Archean and Proterozoic basement (National bedrock database, Geological Survey of Norway [2011]). Between the islands and the mainland lies the Vestfjorden basin with sediment thickness up to 8 km [Brønner et al., 2013; Maystrenko et al., 2017].

The mainland area is dominated by a stack of nappe complexes formed during the collision [Corfu et al., 2014]. During the continental break up, extensional shear zones formed along the Caledonian domain with WSW-ENE directions in central and northern Norway [Fossen, 2010]. These shear zones appear to extend down to the basement, in some cases are suggested to reach the deeper part of the crust [Fossen, 2010]. Major features in Nordland include the Sagfjord shear zone in the north and the Nesna shear zone in the south (Fig. 1.1).

During the Late Pliocene and Pleistocene, Fennoscandia underwent several sequences of deglaciation and erosion, which deposited large volumes of sediments offshore [Rise et al., 2005]. Along the mid-Norwegian margin, large parts of these sediments were deposited as Naust formation (between 62° N to 68° N) (Fig. 1.1). The deeper part of the formation was formed ca. 2.8 - 1.5 Ma, and the uppermost part was deposited less than 200,000 years ago [Rise et al., 2005]. The effect of deglaciation is still observed today as GIA, which causes significant uplift in Fennoscandia [e.g., Vestøl et al., 2019].

1.3.2 Geophysical investigations in Nordland

In the past few decades, the focus of crustal structure studies in Nordland has been on the offshore area, which was investigated extensively using deep seismic surveys [e.g., Avedik et al., 1984; Breivik et al., 2017, 2020; Mjelde et al., 1993; Sellevoll, 1983]. In contrast, the crustal structure in the mainland area is less constrained. But over the past decade, crustal and lithospheric scale models derived from seismic imaging techniques have been developed using temporary seismic networks [Ben-Mansour et al., 2018; Bulut et al., 2022; Mauerberger et al., 2022; Michálek et al., 2018]. This section summarizes the geophysical investigations of crustal structure in Nordland, which serve as background for developing a 3-D seismic velocity model performed in this thesis.

Crustal thickness in the southern Lofoten has been subject of investigation in the past few decades. Earlier seismic studies [Avedik et al., 1984; Mjelde and Sellevoll, 1993; Mjelde et al., 1993] suggested that the crust in southern Lofoten is thin (less than 30 km). Mjelde et al. [1993] suggested that the crust becomes thinner toward the Lofoten ridge, where

the Moho is as shallow as 20 km – as indicated by a strong seismic interface in a seismic refraction profile. More recently, Mjelde et al. [2013] suggested that this seismic interface is the top of a lower crust eclogitic body, and revised the Moho interface to 25 km depth. Receiver functions also show that the Moho depth in southern Lofoten-Vesterålen is between 20-25 km and in the northern Lofoten-Vesterålen greater than 30 km [Michálek et al., 2018]. Thicker crust of about 36 km in the northern part of the islands was also found by Breivik et al. [2017]. Using more recent seismic surveys, Breivik et al. [2020] suggested that the Moho for the whole Lofoten-Vesterålen is actually deeper than what had been interpreted previously. This illustrates that despite years of investigations, the depth of the Moho below southern Lofoten is still a subject of debate.

Recent broadband seismological studies provided more information on the onshore crustal and lithospheric structure. These studies mainly focus on investigating the origin of the high topography Scandes mountains. Ben-Mansour et al. [2018] derived a crustal thickness model in Northern Norway and Northern Sweden, which showed a gradual change of Moho depth from 38 km along the Caledonides to 43 km in the Baltic shield. However, the topography variation at the surface does not reflect this gradual Moho change. Therefore, Ben-Mansour et al. [2018] concluded that the classical Airy isostatic model cannot explain the surface topography. Recently, Mauerberger et al. [2022] suggested that the lithosphere of the northern Scandes experiences isostasy. Furthermore, an edge-driven convection due to a sharp lithospheric step is suggested to provide dynamic support [Mauerberger et al., 2022].

In addition to seismological experiments, gravity and magnetic methods have been used extensively to probe the crustal structure in Nordland [e.g., Maystrenko et al., 2017; Olesen et al., 2002; Tsikalas et al., 2005]. These methods bridge the gap between offshore and the mainland area, where seismic data is lacking [Olesen et al., 2002]. The gravity data point to two distinct anomalies: a large part of the mainland has a low gravity anomaly and Lofoten has a high gravity anomaly [Olesen et al., 2010]. Gradmann et al. [2017] suggested that a combination of shallow Moho and crustal root (e.g., eclogitic layer) can explain the high gravity anomaly in Lofoten. Furthermore, the mainland low gravity anomaly is possibly associated with low density rocks within the crust or the upper mantle [Gradmann and Ebbing, 2015; Maystrenko et al., 2017]. Areas with low gravity anomaly coincide with the northwest extension of the Transscandinavian igneous belt. However, other igneous belt locations in Scandinavia are only associated with minor gravity lows [Gradmann and Ebbing, 2015].

1.3.3 Seismicity

Nordland is a region with one of the highest seismicity rates in continental Northern Europe, with earthquakes occurring mostly onshore along the coastal area and offshore along the shelf edge (Fig. 1.2). The 31 August 1819, M 5.9 Lurøy earthquake, the largest documented earthquake in mainland Norway, was widely felt throughout Fennoscandia and triggered major landslides and rockfalls in the epicentral area [Mäntyniemi et al., 2020]. Historical accounts also reported a number of earthquakes that were felt in the area few years before and after the event [Heltzen, 1982; Olesen and Lindholm, 2019]. In recent times, earthquakes are mostly small to moderate magnitude, with a number of swarm activities observed along the coast, e.g., 1978-1979 Meløy [Bungum et al., 1979, 1982], 1994 Steigen [Atakan et al., 1994] and Jektvik (2013-) [Janutyte et al., 2017; Michálek et al., 2018]. These swarms had normal and oblique-normal mechanisms reflecting shallow NW-SE extension [Bungum et al., 1979; Janutyte et al., 2017; Michálek et al., 2018]. The Meløy and Jektvik swarms are not associated with any major faults or structures. Further to the north, the 1994 Steigen swarm is possibly associated with the Sagfjord shear zone [Atakan et al., 1994].

Shallow earthquakes along the coast of Nordland are associated with normal and oblique-normal faulting, reflecting an extensional stress regime. In contrast, offshore - especially along the shelf edge, earthquakes are generally thought to be associated with thrust faulting, reflecting a compressional stress regime [Bungum et al., 1991; Gregersen et al., 2021; Hicks et al., 2000]. However, the solutions are poorly constrained and mostly derived using observations from mainland stations, since the earthquakes are generally smaller than magnitude 4.

Present day stress in Nordland is a result of interference between several regional and local sources [Bungum et al., 2010; Gradmann et al., 2018] (Fig. 1.3). Regionally, Nordland experiences compressive ridge push stress from the mid-Atlantic ridge. Fennoscandia undergoes GIA, where Nordland is uplifted at a rate of 2 - 6 mm/year [Keiding et al., 2015; Steffen and Kaufmann, 2005; Vestøl et al., 2019]. The coast of Nordland, especially around Rana, has the highest uplift gradient indicating a high deformation rate [Keiding et al., 2015]. GIA can create shallow extension around the edge of the former ice sheet, including Nordland [Fjeldskaar et al., 2000; Wu and Hasegawa, 1996]. Furthermore, the offshore area with compressive regime is situated beyond the former ice edge [Fjeldskaar et al., 2000; Steffen et al., 2021]. In addition to GIA, other local stress sources, e.g. sediment redistribution and topography effects can also influence the stress regime. The combination of these regional and local sources and lateral heterogeneity in the lithosphere is responsible for the present day stress in the region [e.g. Bungum et al.,

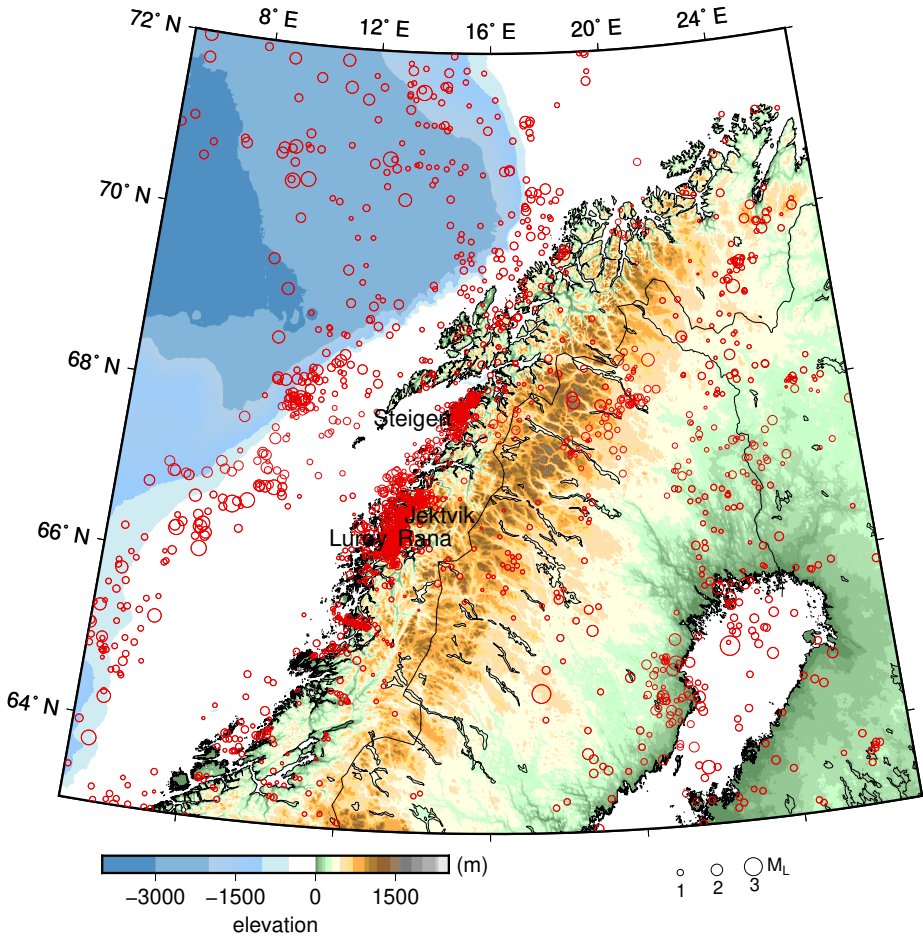


Figure 1.2: Earthquake distribution in northern Fennoscandia including Nordland for the period of 1990-2022 with $M_L \geq 1.5$. The epicenters, shown as red open circles, are obtained from the Norwegian National Seismic Network catalog [Ottemöller et al., 2018]. Seismically active areas mentioned in the text are shown in the figure.

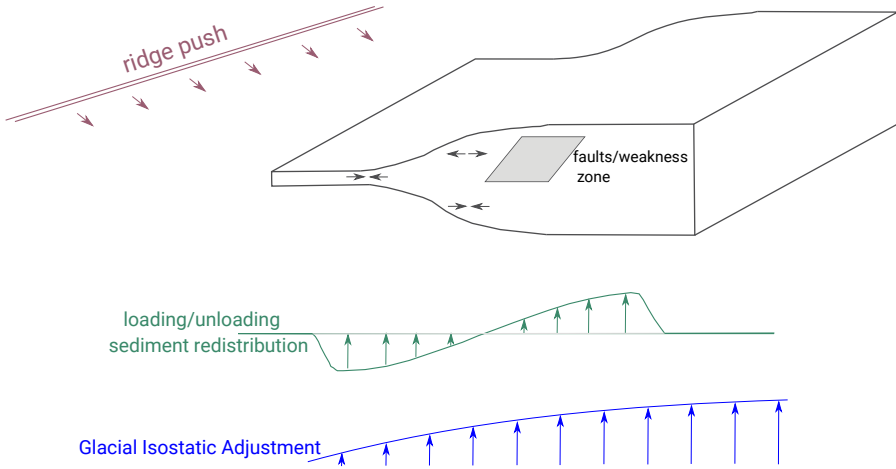


Figure 1.3: Schematics stress sources in Nordland, which is a combination of ridge push, sediment redistribution and glacial isostatic adjustment. The figure is modified from Gradmann et al. [2018].

2010; Fejerskov and Lindholm, 2000; Gradmann and Steffen, 2021; Gradmann et al., 2018; Keiding et al., 2015] (Fig. 1.3).

1.4 Data and Methods

This research is largely based on seismological data and a number of methods from data processing, inversion and analysis. This section summarizes the datasets and methods that I used to achieve the research objectives.

1.4.1 Data

Earthquake activity in Nordland has been monitored for more than 40 years. In addition to permanent seismic stations run by the Norwegian National Seismic Network (NNSN) [Ottemöller et al., 2021b; University of Bergen, 1982], a number of temporary seismic networks were deployed in the region. Temporary deployments help to improve the earthquake detection levels and also seismic ray path coverage, which increases the resolution of 3-D seismic tomography results. This research used the earthquake catalog reported by the NNSN [Ottemöller et al., 2018] as a base. The catalog contains phase picks, earthquake locations and magnitudes M_L . In Paper 1, I extended the catalog by

adding phase picks from temporary seismic networks to improve the ray path coverage. In Papers 2 and 3, I processed earthquakes that were not reported in the NNSN catalog using all available continuous waveforms from stations in the region.

Most permanent NNSN stations were initially deployed in the southern part of the study area (mainly around Rana) and near Steigen with a total number of up to nine stations. Since 2018, NNSN installed more stations under the framework of the European Plate Observing System-Norway project (EPOS-N) [Atakan et al., 2018], resulting in fifteen stations that cover the region. The continuous waveforms are available from the European Integrated Data Archive (EIDA) [Strollo et al., 2021] node at the University of Bergen (UiB-NORSAR) [Ottemöller et al., 2021b]. Temporary seismic networks deployed during 2008-2009 and 2013-2016 covered large parts of northwestern Fennoscandia including Nordland. The main temporary network that covered large parts of Nordland is the Neotectonics in Nordland - Implications for petroleum exploration project (NEONOR2) between August 2013 and May 2016 (available through UiB-NORSAR EIDA node). I also used data from Scanlips2 (2007 - 2009) and Scanlips3D (2013-2014) [England et al., 2016], available through the Incorporated Research Institutions for Seismology Data Management Center and Scanarray (2013-2016) [Thybo et al., 2021] available through EIDA [Strollo et al., 2021]. In addition, nearby permanent seismic stations are used mainly to improve the ray coverage for seismic tomography: NORSAR [Schweitzer et al., 2021], the Swedish National Seismic Network (SNSN) (2013-2016) [Lund et al., 2021] and Finnish National Seismic Network (FNSN) [Veikkolainen et al., 2021]. The distribution of seismic stations used in this research is shown in Fig. 1.4.

To support the seismological studies conducted in this thesis, I used Global Navigation Satellite System (GNSS) and hydrological data, which are as follows:

- GNSS data

The GNSS stations in Nordland are installed and operated by Norwegian Mapping Authority since 2019 under the EPOS-N project. In total, I used four GNSS stations surrounding Jektvik and Rana. The GNSS data were processed by Nevada Geodetical Laboratory (<http://geodesy.unr.edu>).

- Hydrological loading model

Hydrological loading model (HYDL) is a surface deformation model derived using global hydrological constraints [Dill and Dobsław, 2013]. HYDL is used to complement the GNSS data, which have limited observation time. The HYDL loading model is available at the Earth System Modelling Group of GeoForschungsZentrum portal (<ftp://esmdata.gfz-potsdam.de/LOADING>).

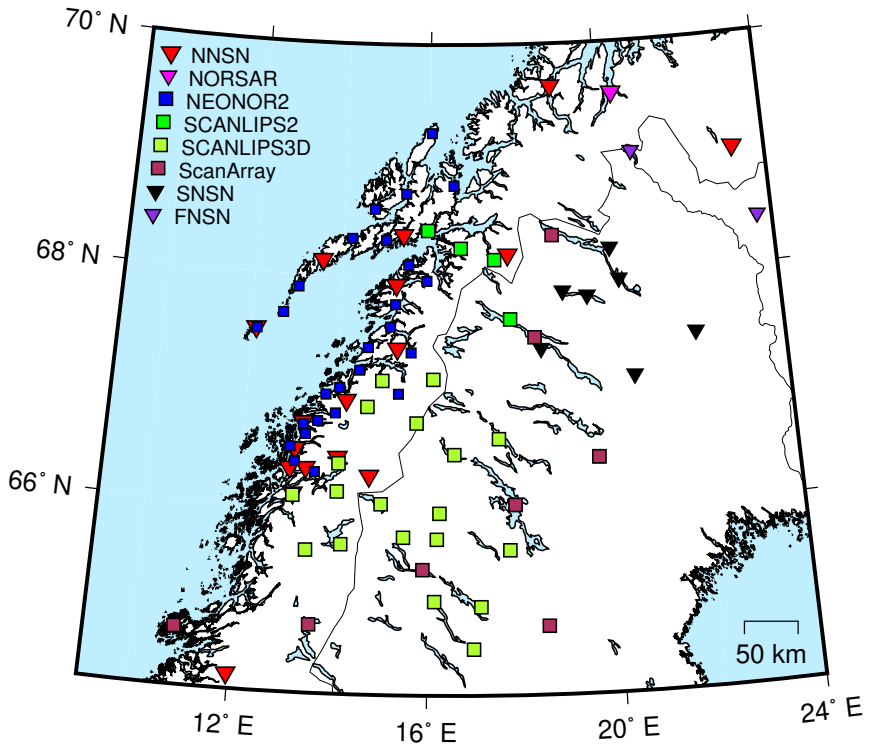


Figure 1.4: Seismic stations used in this research, which covered northwestern Fennoscandia for the time span 2005 to 2021. Permanent and temporary stations are shown as inverted triangles and squares, respectively.

- Snow and precipitation records

The snow and precipitation records are provided by Norwegian Meteorological Institute, Norwegian Public Roads Administration (Statens vegvesen) and Norwegian Water Resources and Energy Directorate. The records are obtained from Varsom Xgeo (<https://www.xgeo.no/>) and SeNorge (<https://www.senorge.no/>) portals.

1.4.2 Methods

Earthquake Data Processing

Earthquake data processing includes event detection, phase arrival determination and phase association. Determination of seismic phase arrival times, often referred as phase picking, is an important task in earthquake seismology. Errors in phase picking contribute to errors in hypocenter locations and seismic tomography models [Husen and Hardebeck, 2010; Rawlinson et al., 2014]. Manual phase picking can produce good datasets if it is conducted by trained seismologists. However, this process is time-consuming, and it is still affected by human subjectivity. Automatic picking, on the other hand, can speed up the data processing, especially when dealing with a huge dataset, and produce a more consistent dataset [Diehl et al., 2009]. For Paper 1, I manually picked additional arrival times for earthquakes reported in the NNSN catalog using the SEISAN package [Havskov and Ottemöller, 1999; Havskov et al., 2020]. Then in Papers 2 and 3, I used a deep-learning based algorithm to detect and process earthquakes that were not reported in the NNSN catalog.

To improve the earthquake catalog, I employed a deep-learning based algorithm, Eq-transformer, to perform automatic earthquake detection and phase picking [Mousavi et al., 2020]. The algorithm consists of recurrent and convolutional layers that include attention mechanisms, which highlight data elements based on their importance. The networks estimate the probabilities associated with earthquakes, P- and S-phase signals. The algorithm is pre-trained using STanford EArthquake Dataset (STEAD) [Mousavi et al., 2019], which contains global earthquakes recorded at local distances and noise datasets. The seismic event identification and phase picking are performed individually for each station. Then the picks at individual stations are associated and combined together if they overlap in a sliding time window.

In order to improve the earthquake locations, I performed earthquake relative location method, which uses waveform correlation coefficient (CC) and traveltimes as inputs. The CC value represents similarity between two discrete waveforms $y_1(t)$ and $y_2(t)$

as a function of time delay τ [e.g., Bachura and Fischer, 2019; Schaff and Waldhauser, 2005]:

$$CC(\tau) = \frac{\sum_t^{t+\tau} y_1(t)y_2(t-\tau)}{\sqrt{\sigma(y_1(t))\sigma(y_2(t))}} \quad (1.1)$$

in which $\sigma(y_1(t))$ and $\sigma(y_2(t))$ are the signal variances. The waveform correlation is performed using EQcorrscan package [Chamberlain et al., 2017] and I used Obspy Python package [Beyreuther et al., 2010; Krischer et al., 2015; The ObsPy Development Team, 2020] to manage the waveforms and remove instrument responses before performing waveform correlation.

Earthquake location

Earthquake location, which consists of hypocenter coordinates and origin time, is an important information in studying seismicity. A common approach to obtain the location is using earthquake travel time inversion. The inversion is performed iteratively to minimize a misfit function and obtain the preferred solution. Although the earthquake location algorithm minimizes travel time residual functions (expressed in seconds), location errors (expressed in kilometers or meters) provide a more direct way to evaluate the earthquake location quality. Therefore, assessing earthquake location quality using travel time residuals and location errors is an essential step before the location is used in further analysis. The location quality is affected by number of observations, network geometry, initial location and velocity model used to compute travel times [Husen and Hardebeck, 2010]. In this research, earthquakes are selected based on these criteria where the parameters are adjusted based on specific cases. In Paper 1, I used strict criteria for earthquake selection since it largely affects seismic tomography results. Then in Papers 2 and 3 which analyzed detailed evolution of small earthquakes, I used relaxed criteria to ensure the location quality without discarding a large number of earthquakes. I used two types of earthquake location algorithms: 1. HYPOCENTER to locate each earthquake individually [Lienert and Havskov, 1995], 2. relative earthquake location using GrowClust to locate earthquakes jointly and combine them into clusters [Trugman and Shearer, 2017].

The HYPOCENTER program is integrated in the SEISAN package and mainly used for routine earthquake location. The algorithm uses a linearized inversion approach to minimize the root-mean-square (RMS) of the misfit function between observed and calculated travel times (L2 norm). The calculated travel times are computed using a

1-D velocity model, derived for the Nordland region in Paper 1 [Shiddiqi et al., 2022]. In the program, earthquake location errors are estimated from the covariance matrix. In Papers 2 and 3, the location errors are estimated using bootstrap statistical resampling in order to provide a more robust and comparable estimate to the GrowClust algorithm. The bootstrap analysis is based on the procedure used in Appendix 1 [Shiddiqi et al., 2019].

To improve the earthquake locations, the neighboring earthquakes are located jointly using GrowClust program, which is a hybrid of earthquake relative location and hierarchical clustering algorithm [Trugman and Shearer, 2017]. The program uses a grid-search approach to minimize the L1 norm of relative travel time residuals (R), which are expressed as:

$$R = \sum_k |dtt_{ij,k} - \hat{dtt}_{ij,k}| \quad (1.2)$$

The relative observed and calculated travel time residuals for an event pair (i,j) at station k are denoted as $dtt_{ij,k}$ and $\hat{dtt}_{ij,k}$. GrowClust uses a 1-D velocity model to compute the synthetic travel times for direct arrivals (i.e., Pg and Sg), and does not take into account Moho refracted arrivals (i.e., Pn and Sn). A pair of two events is determined based on CC, event separation and maximum RMS of travel time residuals threshold. For each event pairs, the similarity is computed via CC parameters. Then the algorithm starts locating event pairs with the highest similarities followed by pairs with lower similarities. These pairs can be merged into a cluster if they fulfil the selected criteria. The location errors are estimated using bootstrap statistical resampling.

Earthquake magnitude and magnitude of completeness

Earthquake magnitude is used to express the size of an earthquake. I used the local magnitude (M_L), which was introduced by Richter [1935] as:

$$M_L = \log A - \log A_0 + S \quad (1.3)$$

where A is the maximum amplitude on a Wood-Anderson (WA) seismogram, $\log A_0$ is the epicentral-distance-dependent term and S is the station correction. Since WA seismographs are no longer used today, the A is measured on digital seismograms that have been convolved with the WA seismograph response. The $\log A_0$ is formulated as [Bakun and Joyner, 1984]:

$$-\log A_0 = a \log\left(\frac{R}{100\text{km}}\right) + b(R - 100\text{km}) + C \quad (1.4)$$

in which R is the hypocentral distance. The a and b parameters depend on geometrical spreading and attenuation, respectively. C is the base level. Parameters a , b and C need to be adjusted to local conditions. The WA amplitude measurements and M_L computation in this study were performed using the SEISAN software [Havskov et al., 2020] using the M_L scale for Norway [Alsaker et al., 1991] with a short-distance correction term for Nordland [Luckett et al., 2018].

Physical size of earthquakes can be expressed by the seismic moment (M_0), which is proportional to total displacement on a fault surface [Aki, 1972]. Using M_0 , we can infer the size of an earthquake or clusters of earthquakes and use a scaling relation to estimate the fault size. Since earthquakes in this study are generally smaller than M_L 4, it is assumed that the M_L is equal to M_w . Then we can obtain M_0 using the following relation [e.g., Bormann et al., 2013; Havskov and Ottemöller, 2010]:

$$\log M_0 = 1.5M_w + 9.105 \quad (1.5)$$

where M_0 is in Nm.

The magnitude of completeness M_c , which is defined as the minimum magnitude at which earthquakes are completely detected by a seismic network [Wiemer and Wyss, 2000], is an important parameter in analyzing earthquake catalogs. It allows us to compare the catalogs from different time periods where the detection levels vary due to configuration changes in a seismic network. The M_c is often estimated in relation to the Gutenberg-Richter relationship [Gutenberg and Richter, 1944]:

$$\log_{10} N = a - bM \quad (1.6)$$

where N is the cumulative number of earthquakes, M is earthquake magnitude, a is the earthquake productivity and b depends on the relative distribution of large and small earthquakes. The M_c is often estimated as the lower end of the frequency-magnitude where the distribution deviates from the Gutenberg-Richter relationship [Mignan and Woessner, 2012; Wiemer and Wyss, 2000]. In most active tectonic regions, the b -value is close to 1. Deviations from this value can provide information on the stress condition and type of seismic sequences.

Travel-time tomography

A good seismic velocity model is essential in obtaining reliable earthquake locations. This relation is often described as coupled velocity-hypocenter problem, where both parameters are solved simultaneously [Thurber, 1992]. The coupled velocity-hypocenter problem can be expressed as:

$$r = \Delta t_o + \sum_{k=1}^3 \left[\frac{\partial t_{ij}}{\partial x_{kj}} \Delta x_{kj} \right] + \sum_{n=1}^N \left[\frac{\partial t_{ij}}{\partial v_l} \Delta v_n \right] \quad (1.7)$$

I used arrival time datasets to develop velocity models for Nordland. These are used to interpret the crustal structure and to improve earthquake locations. I used two approaches to improve the seismic velocity model: 1) 1-D velocity inversion using the VELEST code [Ellsworth, 1978; Kissling et al., 1994], 2) 3-D travel time tomography using the SIMULR16 code [Bleibinhaus, 2003; Bleibinhaus and Gebrande, 2006; Bleibinhaus and Hilberg, 2012].

The 1-D velocity model derived using the VELEST program [Kissling et al., 1994] serves as the initial model for the 3-D velocity inversion. The code inverts the earthquake travel times to simultaneously obtain 1-D velocity model, hypocenters and station delays. The station delays reflect the lateral variations of seismic velocity that are not captured by the 1-D model. To develop an appropriate 1-D model for the study area, often referred to as a minimum 1-D velocity model, I considered a number of initial models with different Moho depth. Then I tested the range of possible input models following the procedures from Appendix 1 [Shiddiqi et al., 2019] by randomly perturbing the initial models before running the inversion. To perform this test, I wrote a number of Python and bash scripts to create inputs and control the VELEST program. The preferred model is selected based on RMS travel time residuals and distribution of solutions.

In Paper 1, the 1-D velocity inversion gave large negative delays for stations above the Lofoten islands up to -1 second, which I interpreted as high velocities that could be due to the shallow crust beneath Lofoten [Shiddiqi et al., 2022]. I performed an additional test (not presented in Paper 1) to verify the interpretation by calculating travel time differences between 1-D V_P , 2-D V_P with thinner crust on one side and a 1-D V_P model perturbed with a high velocity anomaly body in the lower crust. I computed the travel times using a ray tracing algorithm from Appendix 2 [Newrkla et al., 2019] and Galtung et al. [2021] implemented in Matlab (Fig. 1.5). The test confirms that the large delays can be explained by the Moho step rather than by the high velocity body.

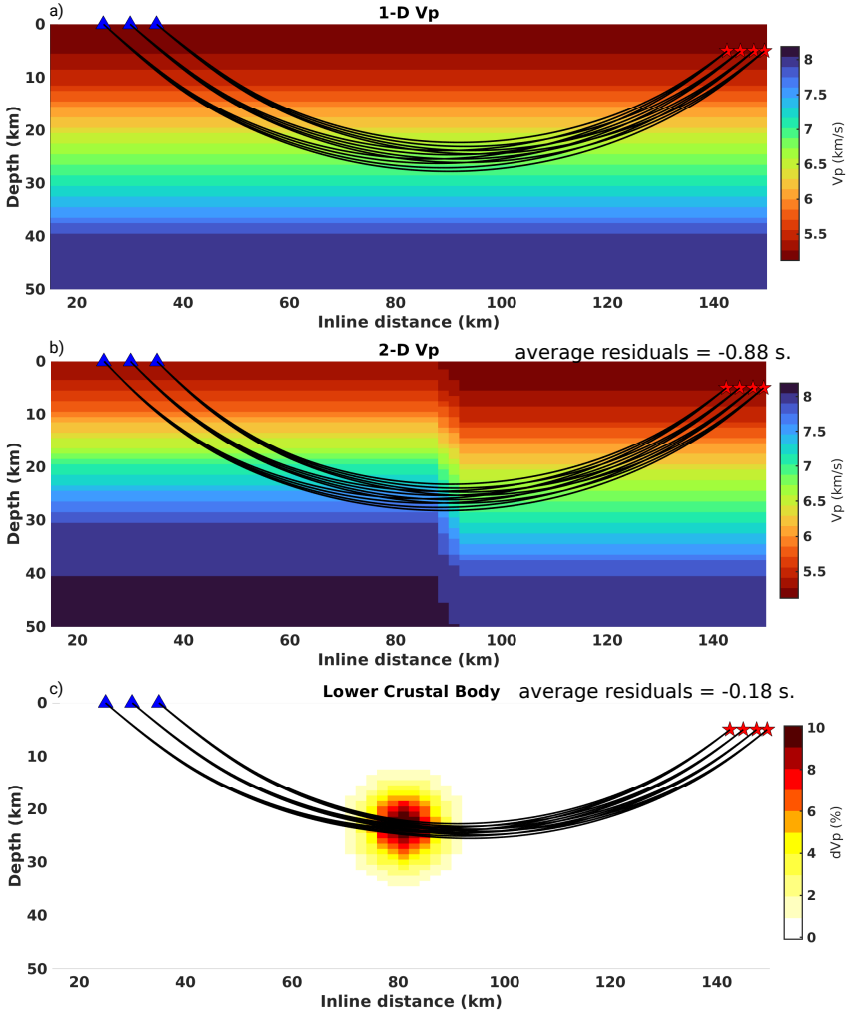


Figure 1.5: Ray tracing tests to evaluate the effect of Moho step and high velocity body anomaly on travel time delays. The ray tracing performed in 3 velocity models: a) 1-D V_P , b) 2-D V_P with Moho step, and c) 1-D V_P perturbed with positive V_P anomaly blob, the model is shown in perturbation relative to the 1-D V_P model. In b) and c) the average travel time residuals relative to the 1-D model are shown as well. The earthquake locations and seismic stations are represented by red stars and blue triangles, respectively. Seismic ray paths are shown as black lines.

Similar to the 1-D velocity inversion, the 3-D tomography uses earthquake travel times to obtain the hypocenters and seismic velocity simultaneously. I used the SIMULR16 code [Bleibinhaus, 2003; Bleibinhaus and Gebrande, 2006; Bleibinhaus and Hilberg, 2012], which is a modified version of the SIMUL family of codes [Evans et al., 1994; Rietbrock, 1996; Thurber, 1983; Thurber and Eberhart-Phillips, 1999], to perform the 3-D tomography. The code performs a damped iterative least-square inversion to obtain 3-D V_P , V_P/V_S ratio and station delays. In each iteration, the model parameters are updated by a perturbation Δm , which is expressed as:

$$\Delta m = (G^T G + \Theta^2 E)^{-1} G^T \Delta d \quad (1.8)$$

in which G is the Jacobian matrix, Θ is the damping parameter, E is the error matrix and Δd is residuals between observed and synthetic travel times. The damping parameter Θ is usually obtained using trade-off analysis between data and model variances (Fig. 1.6). The synthetic travel time is computed using a modified approximate ray tracing (ART) and pseudo-bending method (PB). To improve the accuracy of ray tracing at regional distances, Bleibinhaus [2003] modified the ART and incorporated an iterative segmentation for PB. In this work, the 3-D tomography was performed in a series of inversions with an increasing number of grid nodes in each step. The inversion is started with a coarse grid setup ($6 \times 8 \times 12$ grid nodes) then subsequently followed by more detailed setups with a medium grid setup ($9 \times 13 \times 12$ grid nodes) and a fine grid setup ($18 \times 23 \times 12$ grid nodes).

To test the reliability of the seismic tomography result, I used ray density, diagonal resolution element and synthetic tests. The synthetic tests are performed by computing travel times from synthetic velocity models, then these are inverted to obtain velocity models. I performed two types of synthetic tests: 1) checkerboard test by creating alternating positive and negative velocity anomalies on a 3-D velocity model and 2) synthetic tests with specific anomalies, e.g., Moho step and local high or low velocity anomalies. A range of tools is used to evaluate the reliability and limitation of the 3-D velocity model before analyzing and interpreting it.

Focal Mechanism

Focal mechanisms represent earthquake faulting in terms of strike, dip and rake. The mechanisms are used to reveal the stress regime of a seismically active region. In this thesis, the mechanisms were determined using the FOCMEC program [Snoke, 2003] implemented in SEISAN package, which uses first motion polarities and SH/P amplitude

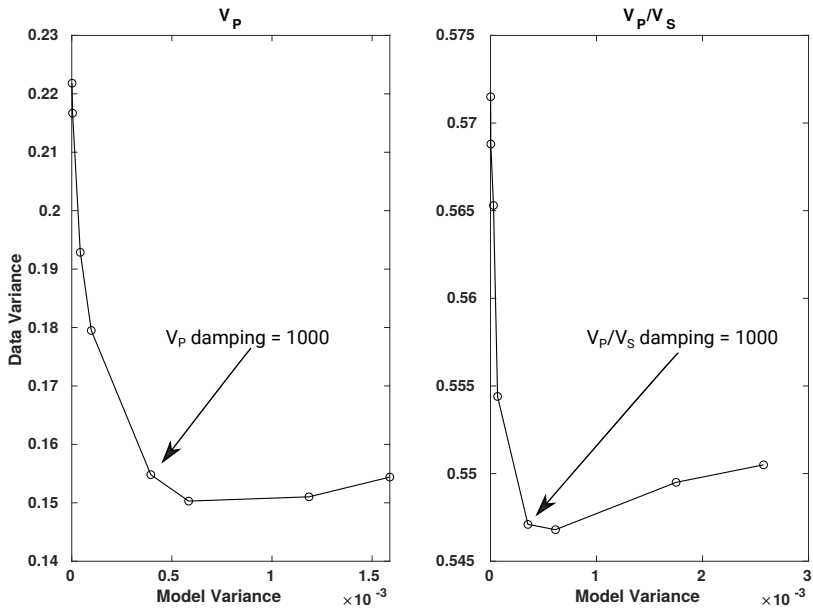


Figure 1.6: Example of trade-off between data and model variances (L-curve) to determine the optimum damping for V_P and V_P/V_S ratio for a coarse grid setup in Paper 1 [Shiddiqi et al., 2022].

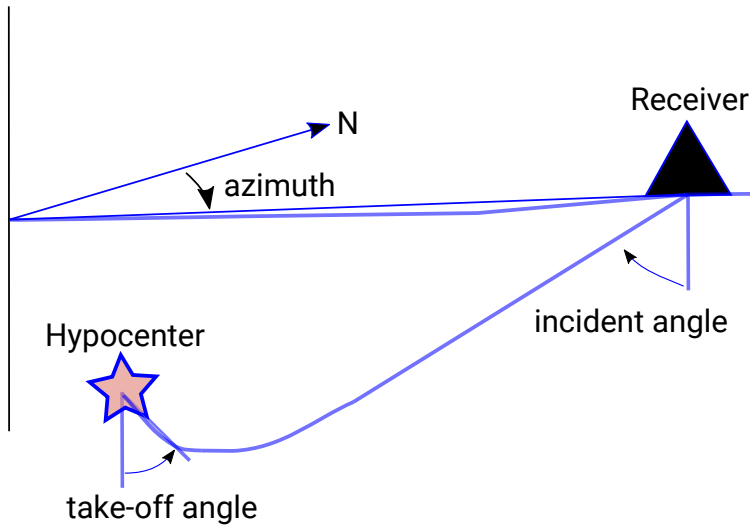


Figure 1.7: Sketch showing parameters used in focal mechanism determination: take-off angle, azimuth and incident angle.

ratios. I did not use waveform based inversion to obtain the mechanisms due to the small earthquake size, where it becomes difficult to model seismograms at high frequencies.

The radiation pattern of earthquakes generates variation in first motion polarities and seismic wave amplitudes. The focal mechanisms can be obtained using a set of polarities and seismic wave amplitudes. Alternatively, one can use the SH/P amplitude ratios, since it is more straightforward to model the ratio than the absolute amplitude of seismic waves. The FOCMEC algorithm searches for solutions using a grid-search approach to find suitable mechanisms that initially fit the polarity observations. Then possible solutions are further constrained by using the SH/P amplitude ratios.

Take-off angle and azimuth determine the position of the observation points on the focal sphere. The take-off angle is defined as the angle between the vertical axis and the outgoing seismic ray leaving the hypocenter, and the azimuth is the angle between outgoing ray and the north direction (Fig. 1.7). These parameters are often computed using ray parameters computed in a 1-D velocity model. In Appendix 2 [Newrkla et al., 2019], we showed that use of a 3-D velocity model can potentially improve the focal mechanism estimation. In Paper 1, I applied a similar approach on the local scale to determine the focal mechanisms. This shows that the use of 3-D velocity model improves the focal mechanism estimation.

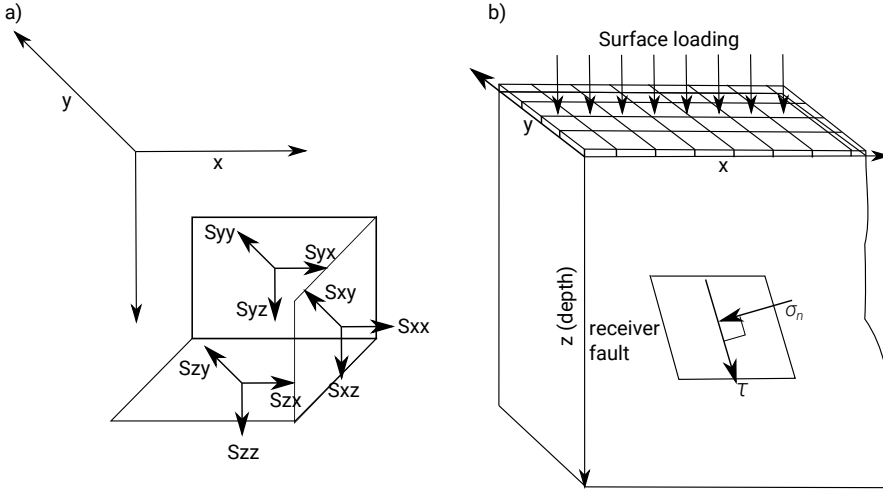


Figure 1.8: a) All elements of 3-D stress tensors within the Cartesian coordinate system. b) Sketch showing surface load and the direction of shear (τ) and normal (σ_n) stress on a normal fault.

Coulomb stress modeling

I performed Coulomb stress change (ΔCFF) modeling to evaluate: 1) the effect of surface loading due to snow load and 2) the possibility of co-seismic triggering and interaction between earthquake clusters.

ΔCFF theory is widely used to evaluate earthquakes triggering process. The ΔCFF is defined as:

$$\Delta CFF = \Delta\tau + \mu(\Delta\sigma_n - \Delta P) \quad (1.9)$$

where $\Delta\tau$ and $\Delta\sigma_n$ are defined as changes in shear and normal stress. $\Delta\tau$ is positive in the fault slip direction and $\Delta\sigma_n$ is positive if the fault is unclamped. μ is the effective friction coefficient. ΔP represents the pore-pressure change, which is assumed to be negligible in this study. The calculation of stress changes due to loading was performed using Boussinesq-Cerruti solutions [Deng et al., 2010], which I implemented in Matlab. And the calculation of co-seismic ΔCFF was performed using the Coulomb 3.3 software [Lin and Stein, 2004; Toda et al., 2005].

To compute the stress changes due to surface loading, a 3-D stress tensor $S(x,y,z)$ is computed (Fig. 1.8). The tensor $S(x,y,z)$ contains six unique elements, i.e., S_{xx} , S_{yy} ,

S_{zz} , S_{xy} , S_{yz} and S_{xz} , due to surface loading $F(x,y)$ on a half-space elastic medium is expressed as:

$$S(x, y, z) = \iint_A G(x, y, z) F(x, y) dx dy \quad (1.10)$$

where A is the surface loading area and $G(x,y,z)$ is the Green's function tensor. Then the changes in shear ($\Delta\tau$) and normal ($\Delta\sigma_n$) stresses on a fault are computed as:

$$\Delta\sigma_n = -[(S_{yy}\sin^2\delta + S_{zz}\cos^2\delta) - S_{yz}\sin 2\delta] \quad (1.11)$$

$$\Delta\tau = [S_{xy}\sin\delta + S_{xz}\cos\delta]\cos\lambda - [0.5\sin 2\delta(S_{yy} - S_{zz}) + S_{yz}(\sin^2\delta - \cos^2\delta)]\sin\lambda \quad (1.12)$$

where δ and λ are the fault's dip and rake angles.

In the next stage, I performed ΔCFF modeling to evaluate the potential triggering between earthquake clusters. To evaluate the interaction between clusters, we used cumulative seismic moment to define the magnitude, dimension and slip of the source fault. A rectangular source fault plane, constrained by a scaling relation for SCR earthquakes [Leonard, 2010] is used as input for the modeling. The 3-D static deformation vectors ($U_m(x, y, z)$) due to fault slip are computed based on Okada [1992]. The $U_m(x, y, z)$ vectors are converted into strain and then into stress using Hooke's analytic expression for static displacement [King and Daves, 2007; Okada, 1992].

Singular Spectrum Analysis

Singular spectrum analysis (SSA) is a non-parametric technique, which decomposes and reconstructs time-series. The SSA method allows us to extract the periodic and non periodic components of a time-series. Fig. 1.9 shows an example of a time series, which is constructed using a combination of a parabolic signal representing the time series trend, two periodic signals and noise. Using the SSA method, we can identify these components and rank them based on amplitudes, hence contributions to the time series. Previously, SSA has been applied to analyze the periodicity of seismicity [Yadav et al., 2014] and volcanic activity [Dumont et al., 2021] and their relation to different processes.

The decomposition of the time-series with length N begins with the construction of a

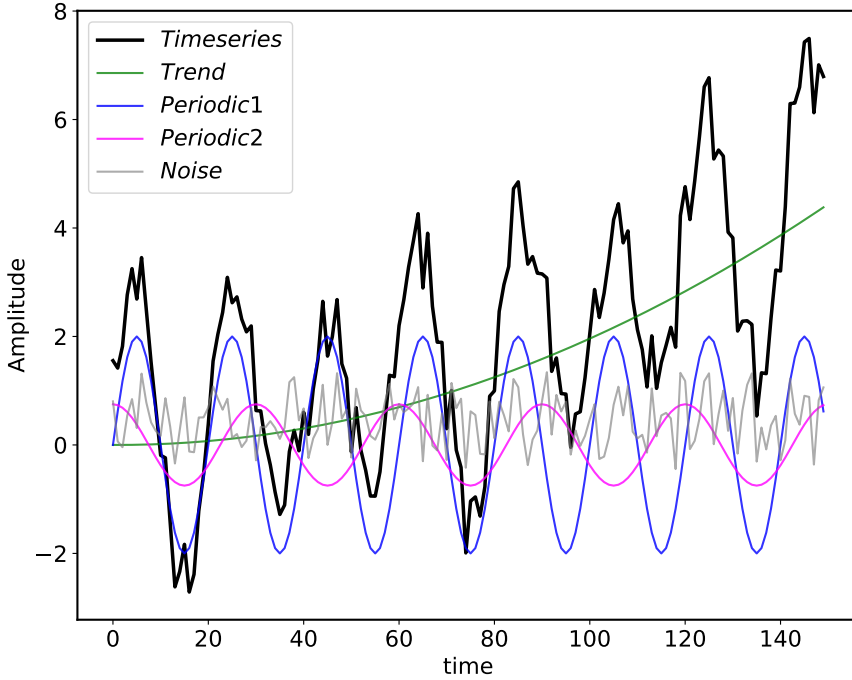


Figure 1.9: An example of a time series, which is composed by combining a parabolic signal representing the time series trend, periodic signals and noise. The SSA analysis allows us to extract these periodic and non-periodic components from a time series.

$L \times K$ Hankel matrix H , which contains lagged copies of time series segments with the length of L . K is defined as $N-L+1$. The Hankel matrix is then decomposed using singular value decomposition using the following relation [e.g., Dumont et al., 2021; Tiwari and Rekapalli, 2020]:

$$H = \sum_{i=1} \sqrt{\lambda_i} U_i V_i^T \quad (1.13)$$

in which U_i and V_i are eigenvectors and λ_i are the eigenvalues.

The SSA analysis is used in Paper 3 to analyze the earthquake catalog, GNSS and hydrological time series. To perform SSA, I used a Python code written by Susana Custódio (a co-author in Papers 2 and 3) based on Dumont et al. [2021].

Summary of methods and tools

In this section, I present a summary of methods, tools and in which paper they are implemented (Table 1.1).

Table 1.1: Summary of methods, tools and in which papers they are used.

Methods	Tools	Used in Paper
Manual phase picking	SEISAN	1, 2 and 3
Automatic detection and picking	Eqtransformer	2 and 3
Waveform cross-correlation	Eqcorrscan	2 and 3
Hypocenter location	HYPOCENTER	1, 2 and 3
Hypocenter relocation	GrowClust	2 and 3
Earthquake magnitude	SEISAN	2 and 3
1-D velocity inversion	VELEST	1
3-D velocity inversion	SIMULR16	3
Focal mechanism determination	FOCMEC	1, 2 and 3
ΔCFF surface load	Implemented in Matlab	2
Co-seismic ΔCFF	Coulomb 3.3	2
SSA	Python code	3

Chapter 2

Synthesis

In this chapter, I provide a summary of the main findings from the research Papers 1-3. Paper 1 focuses on investigating the crustal structure of Nordland and its possible relation to seismicity. The findings in Paper 1 on seismic velocity variations within areas with high seismicity provide motivation for Papers 2 and 3. The focus of Paper 2 is on a smaller scale processes, in which we present a detailed characterization of a seismic swarm sequence in Jektvik, Northern Norway. Then Paper 3 provides a comparison of earthquake activity in adjacent areas in Nordland, in terms of spatio-temporal evolution, focal mechanisms and periodicity. Papers 2 and 3 provide detailed insight on the conclusion from Paper 1 on seismic swarm activity within fluid saturated fractures/faults. The summary is followed by a research outlook, which provides perspective for future research.

2.1 Main findings

The main outcomes of the research papers can be summarized as follows:

1. **Paper 1:** Crustal structure and intraplate seismicity in Nordland, Northern Norway: insight from seismic tomography

The tomography images developed in this study show that the crustal structure varies considerably across the study area. Below the Lofoten-Vesterålen islands, crustal thickness ranges from ~ 35 km in the north to ~ 27 km in the south. Between southern Lofoten and the mainland, we identified a coast-parallel Moho step, located near the region that shows a high seismicity rate. We detected low V_P and variable V_P/V_S ratio anomalies within the Jektvik and Steigen swarm re-

gions, which we interpreted as an indication of fractures and fluids in the upper crust. Furthermore, we found that the computed focal mechanisms are predominately normal and oblique-normal, indicating local extension. This extensional regime deviates from the regional compression imposed by the mid-Atlantic ridge push. The deviation seems to arise at shallow depth due to interference with local flexural stress caused by rapid sediment redistribution and glacial isostatic adjustment. From the distribution of earthquakes, it appears that deformation is localized within pre-existing faults or zones of weakness, which are possibly fluid-saturated. These conditions lead to the occurrence of shallow intraplate earthquakes and are favorable to the development of swarm activity, which became the focus of Papers 2 and 3.

Paper 1 was published in *Geophysical Journal International* in February 2022.

2. **Paper 2:** Seismicity modulation due to hydrological loading in a stable continental region: a case study from Jektvik swarm sequence in Northern Norway

We developed an enhanced earthquake catalog for the Jektvik area that spans almost a decade. From the data analysis, we identified four major groups of events, consisting of several clusters each, that have distinct spatio-temporal patterns. The seismic activity shows an outward progression from its center, first toward southwest and later toward east and northeast. Focal mechanism solutions for this swarms are mostly normal with NNE-SSW strike reflecting the near vertical maximum principal stress and NW-SE near horizontal minimum principal stress. The mechanisms are in agreement with solutions obtained in Paper 1 and show that the upper crustal stress is controlled by local NW-SE extension. We hypothesize that the swarm sequence occurs in fluid-saturated fracture zones that are reactivated due to this local extension. Furthermore, the activity tends to increase during the late winter and spring time (February-May). This seasonality trend is linked to hydrological loading, mainly due to snow load, which is observable in regional GNSS data. The stress modeling shows that the snow load increases the ΔCFF on the normal fault system and is possibly responsible for triggering and modulating the seismicity. Once a cluster is activated, it can also trigger the neighboring events via co-seismic stress transfer. These new results show the close interactions between lithosphere and hydrosphere in promoting seismic swarm activity in Jektvik, Northern Norway.

Paper 2 was submitted to *Geophysical Journal International*.

3. **Paper 3:** Comparison of earthquake clusters in a stable continental region: a case study from Nordland, Northern Norway.

This paper provides a comparison of earthquake activity in adjacent areas in Nord-

land. After we presented a detailed analysis of swarm activity in Jekvtik (Paper 2), we expanded the study into a larger geographical area to include Rana in the south of Jekvtik. Rana is an area where seismic swarms have been observed for more than two decades. Observations made in this study show that these two areas have different behavior. The most significant difference is the spatio-temporal behavior, where Jekvtik seismicity shows progression from one cluster to another and Rana clusters seem to be isolated and occur independently. Singular spectrum analysis indicated dominant near annual periodicity for Jekvtik seismicity, but not for Rana. The hydrological load changes are observed by GNSS stations both in Jekvtik and Rana indicating that these areas undergo similar changes. The hypothesis is that hydrological load changes seem to trigger seismicity in Jekvtik, but has an insignificant effect on Rana seismicity. Detailed inspection of earthquake catalogs showed that seismicity in both areas is controlled by local extensional regimes, where the centers of activity tend to have larger maximum magnitude and lower b-value. Combining all observations, this study suggests that Jekvtik seismicity occurs within a fracture system that is modulated by hydrological loading, while Rana seismicity takes place within fault irregularities, including fault intersections, which accumulate stress and rupture repeatedly. This study presents a case where adjacent areas within an intraplate setting can have significantly different seismogenic behaviors despite being controlled by the same stress regime.

Paper 3 was submitted to Seismological Research Letters.

2.2 Outlook

In this section, I provide an outlook for future research, which can be grouped into three parts: 1) improving the tomography images, 2) improving our understanding of the stress interaction in Nordland, and 3) further investigation of hydrological modulation of seismicity.

This study benefited from the seismic network improvement in Nordland in the past ten years. Dense temporary networks deployed between 2013-2016 significantly improve earthquake detection threshold and raypath coverage. Since the permanent stations are less dense, we could not resolve the seismicity in longer time period with the same resolution as during 2013-2016. Therefore, increasing number of stations along the active spots in Nordland will result in a more complete long-term earthquake catalog. Specifically around Jekvtik, more stations would help to further reduce the magnitude threshold, resulting in a better catalog to investigate modulation. Furthermore, coverage in offshore areas is still lacking, which makes the earthquake locations have higher uncertainties and

some parts of the crustal structure are still unresolved from the 3-D tomography, including the structure near the shelf edge and the extension of shallow Moho beneath Lofoten. Deployment of ocean bottom seismometer along the Norwegian margin will improve the location accuracy of offshore earthquakes and the 3-D velocity model.

A comprehensive model of crustal seismic velocities and hypocenters has been developed in this research. Applying a number of techniques can enhance the seismic images in the area, including introducing discontinuities in the model to improve the Moho estimate, using Moho reflected phases, PmP and SmS, and other secondary arrivals to improve the mid-crustal velocity model [e.g., Wang et al., 2018; Wu et al., 2022]. At the same time, several lithospheric scale velocity models for Scandinavia have been developed using dense seismic experiments [Bulut et al., 2022; Mauerberger et al., 2022] with the focus on geodynamic processes and their relation to the Scandinavian mountain range. Integrating the crustal model developed in this study with these lithospheric scale models can potentially provide a broader context in relation to the intraplate seismicity.

The interaction between stresses in Nordland is still not well understood. In Paper 1, we summarized recent findings on the causative mechanisms of earthquakes in Nordland, and discuss how stresses interfere and create the present-day stress regime. Previous efforts to model the stress in Nordland have been performed using a relatively simple lithosphere model [e.g., Gradmann and Steffen, 2021; Gradmann et al., 2018], the use of improved crustal structure can enhance the modeling result. Furthermore, information on crustal deformation can be better constrained by combining data from recently deployed GNSS stations in Nordland with previous geodetic observations.

The link between seismicity and hydrological processes has been made in this research. Further investigations that consider different factors are required to reveal the detailed physical processes behind the seismicity modulation. Temporal seismic velocity model changes can provide evidence for pore-pressure changes at depth due to hydrological processes [e.g., Andajani et al., 2020; Guillemot et al., 2021; Meier et al., 2010]. The velocity changes obtained using ambient-noise coda wave interferometry can identify temporal variation within the crust due to different processes, including pore-pressure variation and fluid migration. Modeling changes in stress and pore-pressure over time can help us to understand the complete effect of hydrological modulation on seismicity [Büyükkapınar et al., 2021; Deng et al., 2010]. Furthermore, water reservoirs have been linked to seismicity in intraplate settings [e.g., El Hariri et al., 2010; Gahalaut et al., 2004; Yadav et al., 2017]. However, in the case of Nordland it is still not clear whether water level changes in water reservoirs in the vicinity of the Svartisen glacier have an effect on seismicity. This question can be addressed with 3-D fluid flow numerical modelling to analyze the pore-pressure diffusion and its effect on seismicity [e.g., Yadav et al., 2017].

The continued earthquake monitoring with denser stations distribution will provide important datasets to confirm and to improve previous findings. Meanwhile, the methods suggested above serve as recommendation for future research direction to further improve our knowledge on intraplate seismicity in Nordland.

References cited in Introduction and Synthesis

- K. Aki. Earthquake mechanism. *Tectonophysics*, 13(1):423–446, 1972. ISSN 0040-1951. doi: [https://doi.org/10.1016/0040-1951\(72\)90032-7](https://doi.org/10.1016/0040-1951(72)90032-7).
- B. P. Allmann and P. M. Shearer. Global variations of stress drop for moderate to large earthquakes. *Journal of Geophysical Research: Solid Earth*, 114(B1), 2009. doi: <https://doi.org/10.1029/2008JB005821>.
- A. Alsaker, L. B. Kvamme, R. A. Hansen, A. Dahle, and H. Bungum. The ML scale in Norway. *Bulletin of the Seismological Society of America*, 81(2):379–398, 1991. ISSN 0037-1106. doi: 10.1785/BSSA0810020379.
- R. D. Andajani, T. Tsuji, R. Snieder, and T. Ikeda. Spatial and temporal influence of rainfall on crustal pore pressure based on seismic velocity monitoring. *Earth, Planets and Space*, 72(1):177, Nov 2020. ISSN 1880-5981. doi: 10.1186/s40623-020-01311-1.
- K. Atakan, C. D. Lindholm, and J. Havskov. Earthquake swarm in Steigen, northern Norway: an unusual example of intraplate seismicity. *Terra Nova*, 6(2):180–194, 1994. doi: 10.1111/j.1365-3121.1994.tb00652.x.
- K. Atakan, K. Tellefsen, and the EPOS-Norway Consortium. European Plate Observing System – Norway (EPOS-N): A National Consortium for the Norwegian Implementation of EPOS. In *EGU General Assembly Conference Abstracts*, pages EGU2018–8119, 2018.
- F. Avedik, D. Berendsen, H. Fucke, S. Goldflam, H. B. Hirschleber, R. O. Meissner, M. A. Sellevoll, and W. Weinrebe. Seismic investigations along the scandinavian blue norma profile. *Annales Geophysicae*, 2(5):571–577, 1984.
- M. Bachura and T. Fischer. Waveform Cross-Correlation for Differential Time Measurement: Bias and Limitations. *Seismological Research Letters*, 90(5):2005–2014, 2019. ISSN 0895-0695. doi: 10.1785/0220190096.

- W. H. Bakun and W. B. Joyner. The ML scale in central California. *Bulletin of the Seismological Society of America*, 74(5):1827–1843, 1984. ISSN 0037-1106. doi: 10.1785/BSSA0740051827.
- W. Ben-Mansour, R. W. England, S. Fishwick, and M. Moorkamp. Crustal properties of the northern Scandinavian mountains and Fennoscandian shield from analysis of teleseismic receiver functions. *Geophysical Journal International*, 214(1):386–401, 2018. ISSN 0956-540X. doi: 10.1093/gji/ggy140.
- M. Beyreuther, R. Barsch, L. Krischer, T. Megies, Y. Behr, and J. Wassermann. ObsPy: A Python Toolbox for Seismology. *Seismological Research Letters*, 81(3):530–533, 05 2010. ISSN 0895-0695. doi: 10.1785/gssrl.81.3.530.
- S. Bisrat, H. R. DeShon, and C. Rowe. Microseismic Swarm Activity in the New Madrid Seismic Zone. *Bulletin of the Seismological Society of America*, 102(3):1167–1178, 2012. ISSN 0037-1106. doi: 10.1785/0120100315.
- F. Bleibinhaus. *3D Simultaneous Refraction and Reflection Seismic Travel Time Tomography and Application to Deep Seismic TRANSALP Wide-Angle Data*. PhD dissertation, Ludwig-Maximilians-Universität, München, Germany, 2003. URL <https://edoc.ub.uni-muenchen.de/1263/>.
- F. Bleibinhaus and H. Gebrande. Crustal structure of the Eastern Alps along the TRANSALP profile from wide-angle seismic tomography. *Tectonophysics*, 414(1): 51 – 69, 2006. ISSN 0040-1951. doi: <https://doi.org/10.1016/j.tecto.2005.10.028>. TRANSALP.
- F. Bleibinhaus and S. Hilberg. Shape and structure of the Salzach Valley, Austria, from seismic travelttime tomography and full waveform inversion. *Geophysical Journal International*, 189(3):1701–1716, 2012. ISSN 0956-540X. doi: 10.1111/j.1365-246X.2012.05447.x.
- P. Bormann, S. Wendt, and D. DiGiacomo. *Seismic Sources and Source Parameters*, pages 1–259. Deutsches GeoForschungsZentrum GFZ, 2013. doi: https://doi.org/10.2312/GFZ.NMSOP-2_ch3.
- A. J. Breivik, J. I. Faleide, R. Mjelde, E. R. Flueh, and Y. Murai. A new tectonomagmatic model for the Lofoten/Vesterålen Margin at the outer limit of the Iceland Plume influence. *Tectonophysics*, 718:25–44, 2017. ISSN 0040-1951. doi: <https://doi.org/10.1016/j.tecto.2017.07.002>.
- A. J. Breivik, J. I. Faleide, R. Mjelde, E. R. Flueh, and Y. Murai. Crustal structure and erosion of the Lofoten/Vesterålen shelf, northern Norwegian margin. *Tectonophysics*, 776:228318, 2020. ISSN 0040-1951. doi: <https://doi.org/10.1016/j.tecto.2020.228318>.

- M. Brönnner, L. Gernigon, and A. Nasuti. *Lofoten-Vestfjorden Aeromagnetic Survey 2011 – LOVAS-11 Acquisition, processing and interpretation report*. Geological Survey of Norway, Trondheim, 3rd ed. edition, 2013.
- N. Bulut, H. Thybo, and V. Maupin. Highly heterogeneous upper-mantle structure in Fennoscandia from finite-frequency P-body-wave tomography. *Geophysical Journal International*, 230(2):1197–1214, 2022. ISSN 0956-540X. doi: 10.1093/gji/ggac107.
- H. Bungum and O. Olesen. The 31st of August 1819 Lurøy earthquake revisited. *Norwegian Journal of Geology*, (85):245–252, 2005.
- H. Bungum, B. K. Hokland, E. S. Husebye, and F. Ringdal. An exceptional intraplate earthquake sequence in Meløy, Northern Norway. *Nature*, (280):32–35, 1979. doi: 10.1038/280032a0.
- H. Bungum, S. Vaage, and E. S. Husebye. The Meløy earthquake sequence, northern Norway: source parameters and their scaling relations. *Bulletin of the Seismological Society of America*, 72(1):197–206, 1982. ISSN 0037-1106.
- H. Bungum, A. Alsaker, L. B. Kvamme, and R. A. Hansen. Seismicity and seismotectonics of Norway and nearby continental shelf areas. *Journal of Geophysical Research: Solid Earth*, 96(B2):2249–2265, 1991. doi: 10.1029/90JB02010.
- H. Bungum, F. Pettenati, J. Schweitzer, L. Sirovich, and J. I. Faleide. The 23 October 1904 MS 5.4 Oslofjord Earthquake: Reanalysis Based on Macroseismic and Instrumental Data. *Bulletin of the Seismological Society of America*, 99(5):2836–2854, 2009. ISSN 0037-1106. doi: 10.1785/0120080357.
- H. Bungum, O. Olesen, C. Pascal, S. Gibbons, C. Lindholm, and O. Vestøl. To what extent is the present seismicity of Norway driven by post-glacial rebound? *Journal of the Geological Society*, 167(2):373–384, 2010. ISSN 0016-7649. doi: 10.1144/0016-76492009-009.
- P. Büyükakpınar, S. Cesca, S. Hainzl, M. Jamalreyhani, S. Heimann, and T. Dahm. Reservoir-Triggered Earthquakes Around the Atatürk Dam (Southeastern Turkey). *Frontiers in Earth Science*, 9, 2021. ISSN 2296-6463. doi: 10.3389/feart.2021.663385.
- E. Calais, T. Camelbeeck, S. Stein, M. Liu, and T. J. Craig. A new paradigm for large earthquakes in stable continental plate interiors. *Geophysical Research Letters*, 43(20): 10,621–10,637, 2016. doi: <https://doi.org/10.1002/2016GL070815>.
- C. J. Chamberlain, C. J. Hopp, C. M. Boese, E. Warren-Smith, D. Chambers, S. X. Chu, K. Michailos, and J. Townend. EQcorrscan: Repeating and Near-Repeating

- Earthquake Detection and Analysis in Python. *Seismological Research Letters*, 89(1): 173–181, 2017. ISSN 0895-0695. doi: 10.1785/0220170151.
- L. B. Christiansen, S. Hurwitz, and S. E. Ingebritsen. Annual modulation of seismicity along the San Andreas Fault near Parkfield, CA. *Geophysical Research Letters*, 34(4), 2007. doi: <https://doi.org/10.1029/2006GL028634>.
- S. Cloetingh, P. A. Ziegler, F. Beekman, P. A. M. Andriessen, N. Hardebol, and P. Dèzes. Intraplate deformation and 3d rheological structure of the rhine rift system and adjacent areas of the northern alpine foreland. *International Journal of Earth Sciences*, 94(4):758–778, Sep 2005. ISSN 1437-3262. doi: 10.1007/s00531-005-0502-3.
- F. Corfu, T. B. Andersen, and D. Gasser. The Scandinavian Caledonides: main features, conceptual advances and critical questions. *Geological Society, London, Special Publications*, 390(1):9–43, 2014. ISSN 0305-8719. doi: 10.1144/SP390.25.
- T. J. Craig, K. Chanard, and E. Calais. Hydrologically-driven crustal stresses and seismicity in the New Madrid Seismic Zone. *Nature Communications*, 8(1):2143, Dec 2017. ISSN 2041-1723. doi: 10.1038/s41467-017-01696-w.
- K. Deng, S. Zhou, R. Wang, R. Robinson, C. Zhao, and W. Cheng. Evidence that the 2008 Mw 7.9 Wenchuan Earthquake Could Not Have Been Induced by the Zippingpu Reservoir. *Bulletin of the Seismological Society of America*, 100(5B):2805–2814, 2010. ISSN 0037-1106. doi: 10.1785/0120090222.
- T. Diehl, E. Kissling, S. Husen, and F. Aldersons. Consistent phase picking for regional tomography models: application to the greater Alpine region. *Geophysical Journal International*, 176(2):542–554, 2009. ISSN 0956-540X. doi: 10.1111/j.1365-246X.2008.03985.x.
- R. Dill and H. Dobslaw. Numerical simulations of global-scale high-resolution hydrological crustal deformations. *Journal of Geophysical Research: Solid Earth*, 118(9): 5008–5017, 2013. doi: <https://doi.org/10.1002/jgrb.50353>.
- S. Dumont, G. Silveira, S. Custódio, F. Lopes, J.-L. Le Mouël, M. Gouhier, and Y. Guéhenneux. Response of Fogo volcano (Cape Verde) to lunisolar gravitational forces during the 2014–2015 eruption. *Physics of the Earth and Planetary Interiors*, 312:106659, 2021. ISSN 0031-9201. doi: <https://doi.org/10.1016/j.pepi.2021.106659>.
- M. El Hariri, R. E. Abercrombie, C. A. Rowe, and A. F. do Nascimento. The role of fluids in triggering earthquakes: observations from reservoir induced seismicity in Brazil. *Geophysical Journal International*, 181(3):1566–1574, 2010. doi: 10.1111/j.1365-246X.2010.04554.x.

- O. Eldholm and K. Grue. North Atlantic volcanic margins: dimensions and production rates. *Journal of Geophysical Research: Solid Earth*, 99(B2):2955–2968, 1994. doi: 10.1029/93JB02879.
- W. L. Ellsworth. *Three-dimensional structure of the crust and mantle beneath the island of Hawaii*. PhD dissertation, Massachusetts Institute of Technology, 1978. URL <http://hdl.handle.net/1721.1/52834>.
- R. W. England, J. Ebbing, and W. Ben-Mansour. SCANDinavian Lithosphere P and S wave experiment 3 D, 2016. URL <https://gef.nerc.ac.uk/documents/report/959.pdf>.
- J. Evans, D. Eberhart-Phillips, and C. Thurber. User’s manual for SIMULPS12 for imaging Vp and Vp/Vs: A derivative of the Thurber tomographic inversion SIMUL3 for local earthquakes and explosions. *U.S. Geological Survey Open File Report*, 94–431, 1994.
- J. I. Faleide, F. Tsikalas, A. J. Breivik, R. Mjelde, O. Ritzmann, øyvind Engen, J. Wilson, and O. Eldholm. Structure and evolution of the continental margin off Norway and the Barents Sea. *Episodes*, 31(1):82–91, 2008. doi: 10.18814/epiiugs/2008/v31i1/012.
- M. Fejerskov and C. Lindholm. Crustal stress in and around Norway: an evaluation of stress-generating mechanisms. *Geological Society, London, Special Publications*, 167 (1):451–467, 2000. ISSN 0305-8719. doi: 10.1144/GSL.SP.2000.167.01.19.
- T. Fischer, J. Horálek, P. Hrubcová, V. V. č uk, K. B. uer, and H. K. mpf. Intra-continental earthquake swarms in west-bohemia and vogtland: A review. *Tectonophysics*, 611:1–27, 2014. ISSN 0040-1951. doi: <https://doi.org/10.1016/j.tecto.2013.11.001>.
- W. Fjeldskaar, C. Lindholm, J. F. Dehls, and I. Fjeldskaar. Postglacial uplift, neotectonics and seismicity in Fennoscandia. *Quaternary Science Reviews*, 19(14):1413 – 1422, 2000. ISSN 0277-3791. doi: [https://doi.org/10.1016/S0277-3791\(00\)00070-6](https://doi.org/10.1016/S0277-3791(00)00070-6).
- H. Fossen. Extensional tectonics in the North Atlantic caledonides: a regional view. In *Continental tectonics and mountain building: the legacy of Peach and Horne*. Geological Society of London, 2010. ISBN 9781862393004. doi: 10.1144/SP335.31.
- K. Gahalaut, V. Gahalaut, N. Bandari, M. Shekar, T. Sunilkumar, and D. Srinagesh. 04 2022.
- V. K. Gahalaut, Kalpna, and S. K. Singh. Fault interaction and earthquake triggering in the Koyna-Warna region, India. *Geophysical Research Letters*, 31(11), 2004. doi: <https://doi.org/10.1029/2004GL019818>.

- K. T. Galtung, H. Keers, M. Sarajärvi, and G. Hope. Efficient modeling for ocean acoustics. *Proceedings of Meetings on Acoustics*, 44(1):022002, 2021. doi: 10.1121/2.0001463.
- Geological Survey of Norway. Nasjonal berggrunnsdatabase, 2011. URL <http://geo.ngu.no/kart/berggrunn/?lang=English>.
- S. Gradmann and J. Ebbing. Large-scale gravity anomaly in northern Norway: tectonic implications of shallow or deep source depth and a possible conjugate in northeast Greenland. *Geophysical Journal International*, 203(3):2070–2088, 2015. ISSN 0956-540X. doi: 10.1093/gji/ggv426.
- S. Gradmann and R. Steffen. *Crustal-Scale Stress Modelling to Investigate Glacially Triggered Faulting*, page 402–416. Cambridge University Press, 2021. doi: 10.1017/9781108779906.030.
- S. Gradmann, C. Haase, and J. Ebbing. Isostasy as a tool to validate interpretations of regional geophysical datasets – application to the mid-Norwegian continental margin. *Geological Society, London, Special Publications*, 447(1):279–297, 2017. ISSN 0305-8719. doi: 10.1144/SP447.13.
- S. Gradmann, O. Olesen, M. Keiding, and Y. Maystrenko. *The Regional 3d Stress Field of Nordland, Northern Norway - Insights from Numerical Modelling*, chapter Neotectonics in Nordland - Implications for petroleum exploration (NEONOR2). Geological Survey of Norway, Trondheim, 2018.
- S. Gregersen, C. Lindholm, A. Korja, B. Lund, M. Uski, K. Oinonen, P. H. Voss, and M. Keiding. *Seismicity and Sources of Stress in Fennoscandia*, page 177–197. Cambridge University Press, 2021. doi: 10.1017/9781108779906.014.
- M. Grund and J. R. R. Ritter. Shear-wave splitting beneath Fennoscandia — evidence for dipping structures and laterally varying multilayer anisotropy. *Geophysical Journal International*, 223(3):1525–1547, 2020. ISSN 0956-540X. doi: 10.1093/gji/ggaa388.
- A. Guillemot, A. van Herwijnen, E. Larose, S. Mayer, and L. Baillet. Effect of snowfall on changes in relative seismic velocity measured by ambient noise correlation. *The Cryosphere*, 15(12):5805–5817, 2021. doi: 10.5194/tc-15-5805-2021.
- B. Gutenberg and C. F. Richter. Frequency of earthquakes in California. *Bulletin of the Seismological Society of America*, 34(4):185–188, 10 1944. ISSN 0037-1106. doi: 10.1785/BSSA0340040185.
- J. Havskov and L. Ottemöller. SeisAn Earthquake Analysis Software. *Seismological Research Letters*, 70(5):532–534, 1999. ISSN 0895-0695. doi: 10.1785/gssrl.70.5.532.

- J. Havskov and L. Ottemöller. *Routine Data Processing in Earthquake Seismology: With Sample Data, Exercises and Software*. Springer, 2010. ISBN 978-90-481-8696-9. doi: <https://doi.org/10.1007/978-90-481-8697-6>.
- J. Havskov, P. H. Voss, and L. Ottemöller. Seismological Observatory Software: 30 Yr of SEISAN. *Seismological Research Letters*, 91(3):1846–1852, 2020. ISSN 0895-0695. doi: 10.1785/0220190313.
- I. Heltzen. *Ranens beskrivelse, 1834*. Rana Museums- og historielag, 1982. ISBN 9788299079150.
- E. C. Hicks, H. Bungum, and C. D. Lindholm. Stress inversion of earthquake focal mechanism solutions from onshore and offshore Norway. *Norsk Geologisk Tidsskrift*, 80(4):235–250, 2000. doi: 10.1080/00291960051030545.
- K. Högdahl, U. B. Andersson, and O. Eklund. *The Transscandinavian Igneous Belt (TIB) in Sweden: a review of its character and evolution*. Geological Survey of Finland, 2004. URL https://tupa.gtk.fi/julkaisu/specialpaper/sp_037.pdf.
- J. Á. Horni, J. R. Hopper, A. Blischke, W. H. Geisler, M. Stewart, K. McDermott, M. Judge, Ö. Erlendsson, and U. Ártung. Regional distribution of volcanism within the North Atlantic Igneous Province. *Geological Society, London, Special Publications*, 447(1):105–125, 2017. ISSN 0305-8719. doi: 10.1144/SP447.18.
- Y.-J. Hsu, H. Kao, R. Bürgmann, Y.-T. Lee, H.-H. Huang, Y.-F. Hsu, Y.-M. Wu, and J. Zhuang. Synchronized and asynchronous modulation of seismicity by hydrological loading: A case study in taiwan. *Science Advances*, 7(16):eabf7282, 2021. doi: 10.1126/sciadv.abf7282.
- S. Husen and J. Hardebeck. *Earthquake location accuracy*. Community Online Resource for Statistical Seismicity Analysis, 2010. doi: <http://dx.doi.org/10.5078/corssa-55815573>.
- I. JanuYTE, C. Lindholm, and O. Olesen. Relation between seismicity and tectonic structures offshore and onshore Nordland, northern Norway. *Norwegian Journal of Geology*, 97(3):211–225, 2017. doi: <https://dx.doi.org/10.17850/njg97-3-02>.
- A. C. Johnston. *The Seismicity of ‘Stable Continental Interiors’*, pages 299–327. Springer Netherlands, Dordrecht, 1989. ISBN 978-94-009-2311-9. doi: 10.1007/978-94-009-2311-9_18.
- M. Keiding, C. Kreemer, C. Lindholm, S. Gradmann, O. Olesen, and H. Kierulf. A comparison of strain rates and seismicity for Fennoscandia: depth dependency of de-

- formation from glacial isostatic adjustment. *Geophysical Journal International*, 202 (2):1021–1028, 2015. doi: 10.1093/gji/ggv207.
- G. King and M. H. Daves. Fault interaction, earthquake stress changes, and the evolution of seismicity. In G. Schubert, editor, *Treatise on Geophysics*, pages 225–255. Elsevier, Amsterdam, 2007. ISBN 978-0-444-52748-6. doi: <https://doi.org/10.1016/B978-044452748-6.00069-9>.
- E. Kissling, W. L. Ellsworth, D. Eberhart-Phillips, and U. Kradolfer. Initial reference models in local earthquake tomography. *Journal of Geophysical Research: Solid Earth*, 99(B10):19635–19646, 1994. doi: 10.1029/93JB03138.
- L. Krischer, T. Megies, R. Barsch, M. Beyreuther, T. Lecocq, C. Caudron, and J. Wassermann. Obspy: A bridge for seismology into the scientific python ecosystem. *Computational Science Discovery*, 8:014003, 05 2015. doi: 10.1088/1749-4699/8/1/014003.
- T. B. Larsen, P. H. Voss, T. Dahl-Jensen, and H. P. Rasmussen. Earthquake swarms in greenland. *GEUS Bulletin*, 31:75–78, 2014. doi: 10.34194/geusb.v31.4665. URL <https://geusbulletin.org/index.php/geusb/article/view/4665>.
- M. Leonard. Earthquake fault scaling: self-consistent relating of rupture length, width, average displacement, and moment release. *Bulletin of the Seismological Society of America*, 100(5A):1971–1988, 2010. ISSN 0037-1106. doi: 10.1785/0120090189.
- B. R. Lienert and J. Havskov. A computer program for locating earthquakes both locally and globally. *Seismological Research Letters*, 66(5):26–36, 1995. ISSN 0895-0695. doi: 10.1785/gssrl.66.5.26.
- J. Lin and R. S. Stein. Stress triggering in thrust and subduction earthquakes and stress interaction between the southern San Andreas and nearby thrust and strike-slip faults. *Journal of Geophysical Research: Solid Earth*, 109(B2), 2004. doi: <https://doi.org/10.1029/2003JB002607>.
- L. Liu and M. D. Zoback. Lithospheric strength and intraplate seismicity in the new madrid seismic zone. *Tectonics*, 16(4):585–595, 1997. doi: <https://doi.org/10.1029/97TC01467>.
- A. E. V. Lopes, M. Assumpção, A. F. Do Nascimento, J. M. Ferreira, E. A. S. Menezes, and J. R. Barbosa. Intraplate earthquake swarm in Belo Jardim, NE Brazil: reactivation of a major Neoproterozoic shear zone (Pernambuco Lineament). *Geophysical Journal International*, 180(3):1303–1312, 2010. ISSN 0956-540X. doi: 10.1111/j.1365-246X.2009.04485.x.

- R. Luckett, L. Ottemöller, A. Butcher, and B. Baptie. Extending local magnitude ML to short distances. *Geophysical Journal International*, 216(2):1145–1156, 2018. ISSN 0956-540X. doi: 10.1093/gji/ggy484.
- B. Lund, P. Schmidt, Z. Hossein Shomali, and M. Roth. The Modern Swedish National Seismic Network: Two Decades of Intraplate Microseismic Observation. *Seismological Research Letters*, 92(3):1747–1758, 2021. ISSN 0895-0695. doi: 10.1785/0220200435.
- P. B. Mäntyniemi, M. B. Sørensen, T. N. Tatevossian, R. E. Tatevossian, and B. Lund. A reappraisal of the Lurøy, Norway, earthquake of 31 August 1819. *Seismological Research Letters*, 2020. ISSN 0895-0695. doi: 10.1785/0220190363.
- C. Matos, S. Custódio, J. Batló, J. Zahradník, P. Arroucau, G. Silveira, and S. Heimann. An active seismic zone in intraplate West Iberia inferred from high-resolution geophysical data. *Journal of Geophysical Research: Solid Earth*, 123(4):2885–2907, 2018. doi: <https://doi.org/10.1002/2017JB015114>.
- A. Mauerberger, S. H., V. Maupin, Gudmundsson, and F. Tilmann. A shear-wave velocity model for the Scandinavian lithosphere from Rayleigh waves and ambient noise - Implications for the origin of the topography of the Scandes mountain range. *Tectonophysics*, 838:229507, 2022. ISSN 0040-1951. doi: <https://doi.org/10.1016/j.tecto.2022.229507>.
- Y. Maystrenko, O. Olesen, L. Gernigon, and S. Gradmann. Deep structure of the Lofoten-Vesterålen segment of the Mid-Norwegian continental margin and adjacent areas derived from 3-D density modeling. *Journal of Geophysical Research: Solid Earth*, 122(2):1402–1433, 2017. doi: 10.1002/2016JB013443.
- J. McKenna, S. Stein, and C. A. Stein. Is the New Madrid seismic zone hotter and weaker than its surroundings? In *Continental Intraplate Earthquakes: Science, Hazard, and Policy Issues*. Geological Society of America, 2007. ISBN 9780813724256. doi: 10.1130/2007.2425(12).
- U. Meier, N. M. Shapiro, and F. Brenguier. Detecting seasonal variations in seismic velocities within Los Angeles basin from correlations of ambient seismic noise. *Geophysical Journal International*, 181(2):985–996, 2010. ISSN 0956-540X. doi: 10.1111/j.1365-246X.2010.04550.x.
- J. Michálek, N. Tjåland, A. Drottning, M. L. Strømme, B. M. Storheim, S. Rondenay, and L. Ottemöller. *Report on seismic observations within the NEONOR2 project in the Nordland region, Norway (Aug. 2013 - May 2016)*, chapter Neotectonics in Nordland - Implications for petroleum exploration (NEONOR2). Geological Survey of Norway, Trondheim, 2018.

- A. Mignan and J. Woessner. *Estimating the magnitude of completeness for earthquake catalogs*. Community Online Resource for Statistical Seismicity Analysis, 2012. doi: <http://dx.doi.org/10.5078/corssa-00180805>.
- R. Mjelde and M. A. Sellevoll. Possible shallow crustal shear wave anisotropy off Lofoten, Norway, inferred from three-component ocean-bottom seismographs. *Geophysical Journal International*, 115(1):159–167, 1993. ISSN 0956-540X. doi: 10.1111/j.1365-246X.1993.tb05596.x.
- R. Mjelde, M. A. Sellevoll, H. Shimamura, T. Iwasaki, and T. Kanazawa. Crustal structure beneath Lofoten, N. Norway, from vertical incidence and wide-angle seismic data. *Geophysical Journal International*, 114(1):116–126, 1993. ISSN 0956-540X. doi: 10.1111/j.1365-246X.1993.tb01471.x.
- R. Mjelde, A. Goncharov, and R. D. Müller. The Moho: Boundary above upper mantle peridotites or lower crustal eclogites? A global review and new interpretations for passive margins. *Tectonophysics*, 609:636 – 650, 2013. ISSN 0040-1951. doi: <https://doi.org/10.1016/j.tecto.2012.03.001>. Moho: 100 years after Andrija Mohorovicic.
- S. Mousavi, K. Bauer, M. Korn, and B. Hejrani. Seismic tomography reveals a mid-crustal intrusive body, fluid pathways and their relation to the earthquake swarms in West Bohemia/Vogtland. *Geophysical Journal International*, 203(2):1113–1127, 2015. ISSN 0956-540X. doi: 10.1093/gji/ggv338.
- S. M. Mousavi, Y. Sheng, W. Zhu, and G. C. Beroza. STanford EArthquake Dataset (STEAD): A Global Data Set of Seismic Signals for AI. *IEEE Access*, 7:179464–179476, 2019. doi: 10.1109/ACCESS.2019.2947848.
- S. M. Mousavi, W. Ellsworth, Z. Weiqiang, L. Chuang, and G. Beroza. Earthquake transformer—an attentive deep-learning model for simultaneous earthquake detection and phase picking. *Nature Communications*, 11:3952, 08 2020. doi: 10.1038/s41467-020-17591-w.
- R. Muir-Wood. The Scandinavian earthquakes of 22 December 1759 and 31 August 1819. *Disasters*, (412):223–236, 1989.
- K. Newrkla, H. A. Shiddiqi, A. E. Jerkins, H. Keers, and L. Ottemöller. Implications of 3D Seismic Raytracing on Focal Mechanism Determination. *Bulletin of the Seismological Society of America*, 109(6):2746–2754, 2019. ISSN 0037-1106. doi: 10.1785/0120190184.
- Y. Okada. Internal deformation due to shear and tensile faults in a half-space. *Bulletin of the Seismological Society of America*, 82(2):1018–1040, 1992. ISSN 0037-1106. doi: 10.1785/BSSA0820021018.

- O. Olesen and C. Lindholm. 200 år siden lurøyskjelvet, August 2019. URL <https://geoforskning.no/200-ar-siden-luroyskjelvet/>.
- O. Olesen, E. Lundin, O. Nordgulen, P. Osmundsen, J. Skilbrei, M. Smethurst, A. Solli, and C. Bugge, T. and Fichler. Bridging the gap between onshore and offshore geology in Nordland, northern Norway. *Norwegian Journal of Geology*, 82(4):243–262, 2002.
- O. Olesen, J. Ebbing, J. Gellein, O. Kihle, R. Myklebust, M. Sand, J. Skilbrei, D. Solheim, and S. Usov. Gravity anomaly map, Norway and adjacent areas; Scale 1:3 mill., 2010. URL <https://www.ngu.no/en/publikasjon/gravity-anomaly-map-norway-and-adjacent-areas-scale-13-mill>.
- L. Ottemöller, M. L. Strømme, and B. M. Storheim. *Seismic monitoring and data processing at the Norwegian National Seismic Network*, volume 52, chapter Summary of the Bulletin of the International Seismological Centre 2015 January-June, pages 27–40. International Seismological Centre, Thatcham, United Kingdom, 2018. doi: <https://doi.org/10.31905/1M97CSYL>.
- L. Ottemöller, W. Kim, F. Waldhauser, N. Tjåland, and W. Dallmann. The Storfjorden, Svalbard, Earthquake Sequence 2008–2020: Transtensional Tectonics in an Arctic Intraplate Region. *Seismological Research Letters*, 92(5):2838–2849, 2021a. ISSN 0895-0695. doi: 10.1785/0220210022.
- L. Ottemöller, J. Michalek, J.-M. Christensen, U. Baadshaug, F. Halpaap, ø. Natvik, T. Kværna, and V. Oye. UiB-NORSAR EIDA Node: Integration of Seismological Data in Norway. *Seismological Research Letters*, 2021b. ISSN 0895-0695. doi: 10.1785/0220200369.
- L. Passarelli, E. Rivalta, S. Jónsson, M. Hensch, S. Metzger, S. S. Jakobsdóttir, F. Maccaferri, F. Corbi, and T. Dahm. Scaling and spatial complementarity of tectonic earthquake swarms. *Earth and Planetary Science Letters*, 482:62–70, 2018. ISSN 0012-821X. doi: <https://doi.org/10.1016/j.epsl.2017.10.052>.
- M. Pirl, J. Schweitzer, L. Ottemöller, M. Raeesi, R. Mjelde, K. Atakan, A. Guterch, S. J. Gibbons, B. Paulsen, W. Debski, P. Wiejacz, and T. Kværna. Preliminary Analysis of the 21 February 2008 Svalbard (Norway) Seismic Sequence. *Seismological Research Letters*, 81(1):63–75, 01 2010. ISSN 0895-0695. doi: 10.1785/gssrl.81.1.63.
- N. Rawlinson, A. Fichtner, M. Sambridge, and M. K. Young. Chapter One - Seismic Tomography and the Assessment of Uncertainty. volume 55 of *Advances in Geophysics*, pages 1–76. Elsevier, 2014. doi: <https://doi.org/10.1016/bs.agph.2014.08.001>.
- C. F. Richter. An instrumental earthquake magnitude scale. *Bulletin of the Seismological Society of America*, 25(1):1–32, 1935. ISSN 0037-1106. doi: 10.1785/BSSA0250010001.

- A. Rietbrock. *Entwicklung eines Programmsystems zur konsistenten Auswertung großer seismologischer Datensätze mit Anwendung auf die Untersuchung der Absorptionsstruktur der Loma-Prieta-Region, Kalifornien*. PhD dissertation, Ludwig-Maximilians-Universität, München, Germany, München, 1996.
- L. Rise, D. Ottesen, K. Berg, and E. Lundin. Large-scale development of the mid-Norwegian margin during the last 3 million years. *Marine and Petroleum Geology*, 22(1):33–44, 2005. ISSN 0264-8172. doi: <https://doi.org/10.1016/j.marpetgeo.2004.10.010>.
- D. P. Schaff and F. Waldhauser. Waveform Cross-Correlation-Based Differential Travel-Time Measurements at the Northern California Seismic Network. *Bulletin of the Seismological Society of America*, 95(6):2446–2461, 2005. ISSN 0037-1106. doi: 10.1785/0120040221.
- S. M. Schulte and W. D. Mooney. An updated global earthquake catalogue for stable continental regions: reassessing the correlation with ancient rifts. *Geophysical Journal International*, 161(3):707–721, 2005. ISSN 0956-540X. doi: 10.1111/j.1365-246X.2005.02554.x.
- J. Schweitzer, A. Köhler, and J. M. Christensen. Development of the NORSAR Network over the Last 50 Yr. *Seismological Research Letters*, 92(3):1501–1511, 2021. ISSN 0895-0695. doi: 10.1785/0220200375.
- M. Sellevoll. A study of the earth’s crust in the island area of Lofoten-Vesterålen, Northern Norway. *Norsk Geologisk Tidsskrift*, (380):235–243, 1983.
- H. A. Shiddiqi, P. P. Tun, and L. Ottemöller. Minimum 1D Velocity Model and Local Magnitude Scale for Myanmar. *Seismological Research Letters*, 90(5):1923–1936, 2019. ISSN 0895-0695. doi: 10.1785/0220190065.
- H. A. Shiddiqi, L. Ottemöller, S. Rondenay, F. Halpaap, S. Gradmann, and J. Michálek. Crustal structure and intraplate seismicity in Nordland, Northern Norway: Insight from Seismic Tomography. *Geophysical Journal International*, 2022. ISSN 0956-540X. doi: 10.1093/gji/ggac086.
- J. A. Snoke. FOCMEC: Focal mechanism determinations. *International Handbook of Earthquake and Engineering Seismology*, 85:1629–1630, 2003.
- H. Steffen and G. Kaufmann. Glacial isostatic adjustment of Scandinavia and northwestern Europe and the radial viscosity structure of the Earth’s mantle. *Geophysical Journal International*, 163(2):801–812, 2005. ISSN 0956-540X. doi: 10.1111/j.1365-246X.2005.02740.x.

- R. Steffen. *The influence of glacial isostatic adjustment on intraplate seismicity in north-eastern Canada*. PhD dissertation, University of Calgary, Canada, Calgary, 2013.
- R. Steffen, P. Wu, and B. Lund. *Geomechanics of Glacially Triggered Faulting*, page 20–40. Cambridge University Press, 2021. doi: 10.1017/9781108779906.004.
- A. Stollo, D. Cambaz, J. Clinton, P. Danecek, C. P. Evangelidis, A. Marmureanu, L. Ottemöller, H. Pedersen, R. Sleeman, K. Stammer, D. Armbruster, J. Bienkowski, K. Boukouras, P. L. Evans, M. Fares, C. Neague, S. Heimers, A. Heinloo, M. Hoffmann, P. Kaestli, V. Lauciani, J. Michalek, E. Odon Muhire, M. Ozer, L. Palangeanu, C. Pardo, J. Quinteros, M. Quintiliani, J. Antonio Jara-Salvador, J. Schaeffer, A. Schloemer, and N. Triantafyllis. EIDA: The European Integrated Data Archive and Service Infrastructure within ORFEUS. *Seismological Research Letters*, 92(3): 1788–1795, 2021. ISSN 0895-0695. doi: 10.1785/0220200413.
- P. Talwani. *Unified model for intraplate earthquakes*, page 275–302. Cambridge University Press, Cambridge, 2014. ISBN 9781139628921. doi: <https://doi.org/10.1017/CBO9781139628921>.
- P. Talwani. On the nature of intraplate earthquakes. *Journal of Seismology*, 21(1):47–68, Jan 2017. ISSN 1573-157X. doi: 10.1007/s10950-016-9582-8.
- The ObsPy Development Team. Obspy 1.2.2. 2020. doi: 10.5281/zenodo.3921997.
- C. H. Thurber. Earthquake locations and three-dimensional crustal structure in the Coyote Lake Area, central California. *Journal of Geophysical Research: Solid Earth*, 88(B10):8226–8236, 1983. doi: 10.1029/JB088iB10p08226.
- C. H. Thurber. Hypocenter-velocity structure coupling in local earthquake tomography. *Physics of the Earth and Planetary Interiors*, 75(1):55–62, 1992. ISSN 0031-9201. doi: [https://doi.org/10.1016/0031-9201\(92\)90117-E](https://doi.org/10.1016/0031-9201(92)90117-E).
- C. H. Thurber and D. Eberhart-Phillips. Local earthquake tomography with flexible gridding. *Computers Geosciences*, 25(7):809 – 818, 1999. ISSN 0098-3004. doi: [https://doi.org/10.1016/S0098-3004\(99\)00007-2](https://doi.org/10.1016/S0098-3004(99)00007-2).
- H. Thybo, N. Bulut, M. Grund, A. Mauerberger, A. Makushkina, I. M. Artemieva, N. Balling, O. Gudmundsson, V. Maupin, L. Ottemøller, J. Ritter, and F. Tilmann. ScanArray—A Broadband Seismological Experiment in the Baltic Shield. *Seismological Research Letters*, 2021. ISSN 0895-0695. doi: 10.1785/0220210015.
- R. K. Tiwari and R. Rekapalli. *Singular Spectrum Analysis-Based Time Domain Frequency Filtering*, pages 23–31. Springer International Publishing, Cham, 2020. ISBN 978-3-030-19304-1. doi: 10.1007/978-3-030-19304-1_3.

- S. Toda, R. S. Stein, K. Richards-Dinger, and S. B. Bozkurt. Forecasting the evolution of seismicity in southern California: Animations built on earthquake stress transfer. *Journal of Geophysical Research: Solid Earth*, 110(B5), 2005. doi: <https://doi.org/10.1029/2004JB003415>.
- J. Townend and M. D. Zoback. How faulting keeps the crust strong. *Geology*, 28(5):399–402, 2000. ISSN 0091-7613. doi: [10.1130/0091-7613\(2000\)28<399:HFKTCS>2.0.CO;2](https://doi.org/10.1130/0091-7613(2000)28<399:HFKTCS>2.0.CO;2).
- D. T. Trugman and P. M. Shearer. Growclust: A hierarchical clustering algorithm for relative earthquake relocation, with application to the Spanish Springs and Sheldon, Nevada, earthquake sequences. *Seismological Research Letters*, 88(2A):379–391, 2017.
- F. Tsikalas, J. I. Faleide, and O. Eldholm. Lateral variations in tectono-magmatic style along the Lofoten–Vesterålen volcanic margin off Norway. *Marine and Petroleum Geology*, 18(7):807 – 832, 2001. ISSN 0264-8172. doi: [https://doi.org/10.1016/S0264-8172\(01\)00030-7](https://doi.org/10.1016/S0264-8172(01)00030-7).
- F. Tsikalas, O. Eldholm, and J. I. Faleide. Crustal structure of the Lofoten–Vesterålen continental margin, off Norway. *Tectonophysics*, 404(3):151 – 174, 2005. ISSN 0040-1951. doi: <https://doi.org/10.1016/j.tecto.2005.04.002>.
- University of Bergen. University of Bergen Seismic Network [Data set], 1982.
- T. Veikkolainen, J. Kortström, T. Vuorinen, I. Salmenperä, T. Luhta, P. Mäntyniemi, G. Hillers, and T. Tiira. The Finnish National Seismic Network: Toward Fully Automated Analysis of Low-Magnitude Seismic Events. *Seismological Research Letters*, 92(3):1581–1591, 2021. ISSN 0895-0695. doi: [10.1785/0220200352](https://doi.org/10.1785/0220200352).
- O. Vestøl, J. Ågren, H. Steffen, H. Kierulf, and L. Tarasov. NKG2016LU: a new land uplift model for Fennoscandia and the Baltic Region. *Journal of Geodesy*, 93:1759–1779, 2019. doi: [10.1007/s00190-019-01280-8](https://doi.org/10.1007/s00190-019-01280-8).
- H. Wang, D. Zhao, Z. Huang, M. Xu, L. Wang, Y. Nishizono, and H. Inakura. Crustal tomography of the 2016 Kumamoto earthquake area in West Japan using P and PmP data. *Geophysical Journal International*, 214(2):1151–1163, 2018. ISSN 0956-540X. doi: [10.1093/gji/ggy177](https://doi.org/10.1093/gji/ggy177).
- S. Wiemer and M. Wyss. Minimum Magnitude of Completeness in Earthquake Catalogs: Examples from Alaska, the Western United States, and Japan. *Bulletin of the Seismological Society of America*, 90(4):859–869, 2000. ISSN 0037-1106. doi: [10.1785/0119990114](https://doi.org/10.1785/0119990114).
- M. P. Wilson, G. R. Foulger, C. Saville, S. P. Graham, and B. R. Julian. Earthquake weather and climate change: Should we stress about the forecast? In *In the Footsteps*

- of Warren B. Hamilton: New Ideas in Earth Science*. Geological Society of America, 2022. ISBN 9780813725536. doi: 10.1130/2021.2553(15).
- P. Wu and H. S. Hasegawa. Induced stresses and fault potential in eastern Canada due to a disc load: a preliminary analysis. *Geophysical Journal International*, 125(2): 415–430, 1996. ISSN 0956-540X. doi: 10.1111/j.1365-246X.1996.tb00008.x.
- S. Wu, T. Li, D. Wang, and P. Tong. Lower crust structures and dynamics of southern California revealed by first P and PmP travelttime data. *Tectonophysics*, 830:229328, 2022. ISSN 0040-1951. doi: <https://doi.org/10.1016/j.tecto.2022.229328>.
- A. Yadav, K. Gahalaut, K. Mallika, and N. Purnachandra Rao. Annual Periodicity in the Seismicity and Water Levels of the Koyna and Warna Reservoirs, Western India: A Singular Spectrum Analysis. *Bulletin of the Seismological Society of America*, 105(1):464–472, 2014. ISSN 0037-1106. doi: 10.1785/0120140234.
- A. Yadav, K. Gahalaut, and N. Rao. 3-D modeling of pore pressure diffusion beneath Koyna and Warna reservoirs, western India. *Pure and Applied Geophysics*, 174(5): 2121–2132, May 2017. ISSN 1420-9136. doi: 10.1007/s00024-017-1519-9.
- M. D. Zoback, W. H. Prescott, and S. W. Krueger. Evidence for lower crustal ductile strain localization in southern New York. *Nature*, 317(6039):705–707, Oct 1985. ISSN 1476-4687. doi: 10.1038/317705a0.

Chapter 3

Scientific results

3.1 Paper 1

Crustal structure and intraplate seismicity in Nordland, Northern Norway: insight from seismic tomography

H.A. Shiddiqi, L. Ottemöller, S. Rondenay, F. Halpaap, S. Gradmann and J. Michálek

Geophysical Journal International, **Volume 230**, Issue 2, pp. 813–830 (2022). DOI: <https://doi.org/10.1093/gji/ggac086>



Crustal structure and intraplate seismicity in Nordland, Northern Norway: insight from seismic tomography

H.A. Shiddiqi¹,¹ L. Ottemöller,¹ S. Rondenay,¹ F. Halpaap,¹ S. Gradmann² and J. Michálek¹

¹Department of Earth Science, University of Bergen, 5007 Bergen, Norway. E-mail: hasbi.shiddiqi@uib.no

²Geological Survey of Norway, Trondheim N-7491, Norway

Accepted 2022 February 24. Received 2022 February 23; in original form 2021 December 1

SUMMARY

The Nordland region, Northern Norway, situated in an intraplate continental setting, has the highest seismicity rate in mainland Norway. However, the exact cause of seismicity in this region is still debated. Better understanding of factors that influence the seismicity in Nordland can help increase knowledge of intraplate seismicity in general. Here, we address this problem with the aid of a new high-resolution 3-D V_P and V_P/V_S ratio images of the crust in Nordland using seismic traveltime tomography. These images show the existence of a localized, 10–15 km Moho step that runs parallel to the coast. The north–south extent of this step coincides with the region that exhibits the highest rates of seismicity. Focal mechanisms of selected earthquakes computed in this study are dominated by normal and oblique-normal, indicating a coast-perpendicular extension. The coast-perpendicular extensional stress regime deviates from the regional compression imposed by the ridge push from the North Atlantic. This deviation is thought to stem from the additional interference with local flexural stress caused by sediment redistribution and glacial isostatic adjustment, and possibly exacerbated by gravitational potential energy stress associated with the Moho step. The deformation due to the extensional regime is localized on pre-existing faults and fractures along the coastline. The tomography result shows that two distinct seismic swarms occurred in the coastal area with low V_P and variable V_P/V_S ratio anomalies, pointing towards fractured crust and possibly the presence of fluids. The existence of fluids here can change the differential stress and promote seismic rupture.

Key words: Europe; Body waves; Crustal imaging; Seismic tomography; Intraplate processes.

1 INTRODUCTION

Intraplate earthquakes occur within stable continental regions away from the plate boundaries. Many of these events occur within reactivated ancient rift systems or continental passive margins (Schulte & Mooney 2005). This general framework applies to Norway, which has a low-to-moderate rate of intraplate seismicity. Here, seismicity is highest along the shelf edge, in the North sea, and along the coast. The largest known earthquake to have affected the region is the 1819, M 5.9 earthquake, which occurred in Lurøy, Nordland, Northern Norway (Muir-Wood 1989; Bungum & Olesen 2005; Mäntyniemi *et al.* 2020).

The Nordland region, which extends between 66°N and 69°N and includes the Lofoten-Vesterålen islands (Fig. 1), is an example of a seismically active intraplate setting where various sources of intraplate stress interact in a relatively small region. The offshore area of Nordland is a rifted passive margin, whereas the mainland

area comprises the remainders of the Scandinavian Caledonides, which includes the high topography region of the northern Scandes mountains.

Investigating the crustal structure of passive margins can improve our understanding of the causes of seismicity in these tectonic settings. However, since many regions are still monitored by sparse seismic networks, providing a better 3-D crustal structure remains a challenge. This is also the case for the Nordland region as a whole—to date, only the offshore region, for example the Lofoten-Vesterålen margin, has been mapped in detail by deep seismic surveys (e.g. Mjelde *et al.* 1993, 1998; Breivik *et al.* 2017).

In this study, we investigate the generating mechanism of intraplate seismicity in the Nordland region. We made use of permanent and recent temporary seismic networks to develop a 3-D seismic velocity model using seismic traveltime tomography. In addition, we determined the focal mechanisms using the 3-D velocity model. The resulting velocity model gives insight into the complex

814 H.A. Shiddiqi et al.

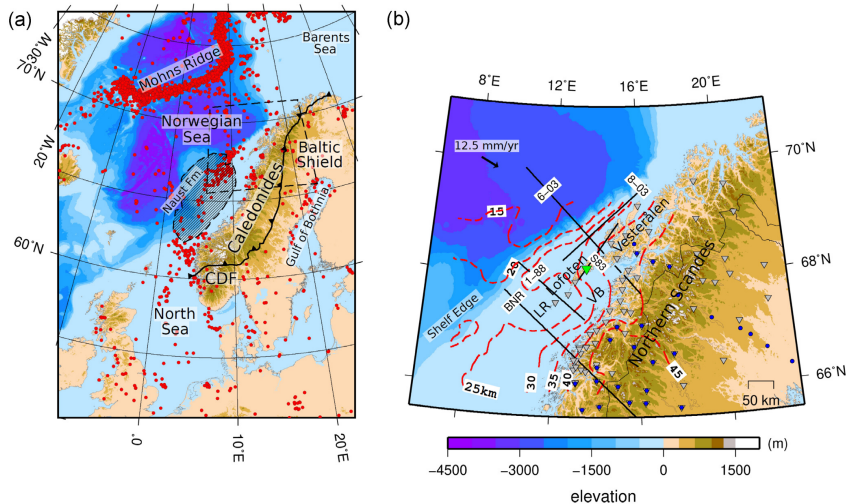


Figure 1. (a) The map of major tectonic features in the region encompassing Fennoscandia and the North Atlantic regions along with the distribution of earthquakes ($M \geq 3$) (red circles) for the period of 1990–2020 obtained from the National Norwegian Seismic Network catalogue. The dashed rectangle is the study region shown in Fig. 1(b). The Naust formation (Naust Fm.) is shown as black stripes area. LR, Lofoten Ridge; VB, Vestfjorden Basin; JMFZ, Jan Mayen Fracture Zone; SFZ, Senja Fracture Zone; CDF, Caledonian Deformation Front. The study area is shown as the dashed box. (b) Map of Nordland and the surrounding region. Contours of Moho depth (in km) from Maystrenko *et al.* (2017) are shown as red dashed lines. Plate velocity relative to the North American Plate (shown as black arrow) obtained from ITRF 2014 model (Altamimi *et al.* 2016). Bathymetry and topography data are obtained from SRTM15+ (Tozer *et al.* 2019). Seismic stations used in this study are shown as grey reverse triangles. Station LOF is depicted as blue reverse triangle. Stations used by Ben-Mansour *et al.* (2018) to obtain Moho depth using receiver function method are depicted by blue circles. Deep seismic profiles mentioned in the text are shown as black solid lines.

crustal structure and composition of the region. Finally, we considered together the 3-D velocity models and the focal mechanism solutions to explore the relation between the crustal structure and the intraplate seismicity in Nordland. Knowledge obtained in this study will not only improve our ability to assess the hazards posed by Nordland earthquakes but it may also help better understand the cause of seismicity in other similar passive margin environments.

2 BACKGROUND

Here, we summarize the tectonic setting and provide a simplified geological overview of the study area. Then, we describe the state of the art for geophysical constraints on the crustal structure of Nordland. In the last part of this section, we highlight the main tectonic forces that influence the present day stress field, and reiterate the hypotheses regarding the causative mechanism of intraplate seismicity in Nordland from previous studies.

2.1 Tectonic setting of Nordland

The Nordland region comprises the high topography of the Northern Scandes to the east and the Lofoten–Vesterålen margin, which is part of the Mid-Norwegian margin, to the west (Fig. 1). The region is part of the Caledonian domain, affected by the late stages of collision of Baltica and Laurentia (Corfu *et al.* 2014). Following the collapse of the Caledonian orogen in the Devonian, the Mid-Norwegian margin was formed through several tectono-magmatic stages (Tsikalas *et al.* 2001; Falcide *et al.* 2008). The long phases of extension and

rifting culminated in the continental breakup and opening of the Atlantic in the Early Eocene. The continental breakup was followed by the formation of the North Atlantic Igneous Province and the Norwegian margin (see e.g. Eldholm & Grue 1994; Horni *et al.* 2017).

The narrow Lofoten–Vesterålen margin is located between the Senja Fracture zone to the north and the Vøring margin to the south, and marked by the exposed Lofoten–Vesterålen islands. The islands comprises the exposed Archean and Proterozoic basement [National bedrock database, Geological Survey of Norway (2011)]. Between the Lofoten islands and the Norwegian mainland lies the Vestfjorden basin with a basement depth ranging from 6 to 10 km (Brønner *et al.* 2013; Maystrenko *et al.* 2017).

The Nordland area is dominated by a stack of nappe complexes formed as a result of the collision. Nordland is mostly covered by the upper and the uppermost Allochthon (Corfu *et al.* 2014). During the late Caledonian era, several extensional shear zones formed along the Caledonian domain with WSW–ENE directions in central and northern Norway (Fossen 2010). These shear zones appear to extend down into the basement, in some cases reaching the deeper part of the crust (Fossen 2010). Major shear zones in Nordland include the Sagfjord shear zone in the north, and the Nesna shear zone in the south, which extends further offshore and is connected to the Bivrost lineament (Fig. 2).

During the Late Pliocene and Pleistocene, Scandinavia underwent several sequences of deglaciation and erosion, which deposited large volumes of sediments offshore (Rise *et al.* 2005). The Naust formation located along the Mid-Norwegian margin (between 62°N

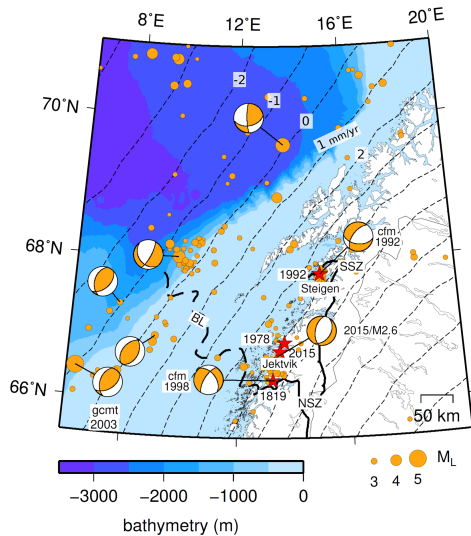


Figure 2. Seismicity in the study region from NNSN catalogue for the period of 1980–2019 ($M \geq 2.5$) shown as orange circles. Red stars depict the notable seismic events in the coastal area of Nordland: 1819 Luroy earthquake, and three series of seismic swarms mentioned in the text. Focal mechanism of offshore events are obtained from Bungum *et al.* (1991), except for the 2003 M_w 5.1 event obtained from global CMT catalogue (labelled as ‘gcmf 2003’, Ekström *et al.* 2012). Composite focal mechanisms labelled with ‘cfm’ labels are obtained from Hicks *et al.* (2000a) for the 1998 solution, and from Atakan *et al.* (1994) for the 1992 solution. The 2015 solution is obtained from Michálek *et al.* (2018). The uplift contours (every 1 mm yr^{-1}) for Fennoscandia (NKG2016LU model, Vestøl *et al.* 2019) are shown as thin dashed lines. The location of shear zones and other structures are obtained from Olesen *et al.* (2002). BL, Bivrost Lineament; NSZ, Nesna Shear zone; SSZ, Sagfjord shear zone.

and 68°N) (Fig. 1) was deposited as a result of this process. The older part of the Naust formation was deposited *ca.* 2.8–1.5 Ma, and the youngest part was formed less than 200 000 yr ago (Rise *et al.* 2005). The total volume of the Naust formation is estimated to be 80 000 km³, with a maximum thickness of over 1500 m (Evans *et al.* 2000).

2.2 Crustal structure of Nordland

In most parts of offshore Nordland, the crustal structure has been studied extensively using deep seismic surveys (e.g. Sellevoll 1983; Avedik *et al.* 1984; Mjelde *et al.* 1993; Breivik *et al.* 2017, 2020). In contrast, the crustal structure in the mainland area remains poorly constrained. But over the past decade, crustal models derived from receiver function and surface wave studies have been developed using temporary seismic networks (Ben-Mansour *et al.* 2018; Michálek *et al.* 2018; Mauerberger *et al.* 2020).

Earlier seismic studies (Avedik *et al.* 1984; Mjelde *et al.* 1993; Mjelde & Sellevoll 1993) suggested that the crust in southern Lofoten is thin (<30 km), based on the seismic profiles BNR and 1–88 crossing the Lofoten ridge (see Fig. 1 for locations of seismic profiles and station described here). Mjelde *et al.* (1993) interpreted that the crust becomes thinner towards the Lofoten ridge, where

Crustal structure and seismicity in Nordland 815

the Moho is as shallow as 20 km—as indicated by a strong seismic interface in profile 1–88. More recently, Mjelde *et al.* (2013) suggested that this seismic interface is not the Moho, but rather the top of an eclogitic body located in the lower crust. This led these authors to revise the Moho depth for the region, placing it below the eclogite layer at 25 km depth. Based on receiver functions, the crustal thickness beneath station LOF (see Fig. 1) was estimated at approximately 30 km (Ottemöller & Midzi 2003). Michálek *et al.* (2018) estimated that the crustal thickness beneath the southern Lofoten-Vesterålen is between 20 and 25 km. Based on profile S83, Sellevoll (1983) suggested a thin crust for Lofoten-Vesterålen (between 20 and 26 km) with the southern part being the thinnest. Further to the north, the crust in the northern Lofoten-Vesterålen is thicker—around 36 km—based on profile 8-03 (Breivik *et al.* 2017). Using a combination of seismic lines 8-03 and 6-03, Breivik *et al.* (2020) suggested that the crustal thickness for the whole Lofoten-Vesterålen is actually greater than what has been interpreted previously. This shows that despite years of investigations, the depth of the Moho below southern Lofoten is still debated.

Recent broad-band seismological studies provide more information on the onshore crustal structure. Crustal thickness derived using receiver functions from stations deployed in northern Norway and Sweden (Fig. 1) showed a gradual change of crustal thickness from 38 km along the Caledonides to 43 km in the Baltic shield (Ben-Mansour *et al.* 2018). This gradual change does not reflect the topography variation at the surface. Therefore, Ben-Mansour *et al.* (2018) suggested that the surface topography cannot be explained by the classical isostatic model.

In addition to seismological experiments, potential field including gravity and magnetic methods have been used extensively to study the crustal structure in Nordland (e.g. Olesen *et al.* 2002; Tsikalas *et al.* 2005; Maystrenko *et al.* 2017). These methods provide constraints where seismic data is absent, especially in the mainland area. Maystrenko *et al.* (2017) performed 3-D density modelling to investigate the lithospheric structure along the Lofoten-Vesterålen margin. They constrained their model with various sources of crustal thickness observations: Ben-Mansour *et al.* (2018) for the mainland, Breivik *et al.* (2017) for the northern Lofoten-Vesterålen where the Moho is as deep as 36 km, and Mjelde *et al.* (1993) for the southern Lofoten-Vesterålen where it was suggested that the Moho depth is 22 km. The crustal thickness compiled by Maystrenko *et al.* (2017) is shown in Fig. 1. However, recently Breivik *et al.* (2020) pointed out that the crustal thickness used by Maystrenko *et al.* (2017) for the southern Lofoten-Vesterålen islands should be greater and questioned the existence of a lower density mantle. We will shed some additional light onto this question with the results from our topography.

The gravity data point to two distinct anomalous features: Lofoten has a high gravity anomaly, whereas a large part of the mainland has a low gravity anomaly (Olesen *et al.* 2010). Gradmann *et al.* (2017) argues that the elevated Lofoten ridge is not isostatically supported if the Moho is shallow, but that a crustal root (e.g. eclogitic layer) is needed. In addition, low-density mantle rocks can play a role (Maystrenko *et al.* 2017). The mainland low gravity anomaly is possibly associated with low density rocks within the crust or the upper mantle (Gradmann & Ebbing 2015; Maystrenko *et al.* 2017). The location of the low gravity anomaly coincides with the northwest extension of the Transscandinavian igneous belt. However, other igneous belt locations in Scandinavia are only associated with minor gravity lows (Gradmann & Ebbing 2015).

2.3 Intraplate seismicity and present-day stress

Nordland has the highest seismicity rate in mainland Norway, with earthquakes occurring mostly along the coastal area and offshore along the shelf edge (Fig. 2). The 31 August 1819, M 5.9 Lurøy earthquake, the largest known earthquake in mainland Norway, was widely felt in Scandinavia and triggered major rockfalls and landslides in the epicentral area (Mäntyniemi *et al.* 2020). In recent times, a number of earthquake swarms have occurred mainly along the coast, for example 1978–1979 Meløy (Bungum *et al.* 1979, 1982), 1992 Steigen (Atakan *et al.* 1994) and Jektvik (April 2015–March 2016, Janutyte *et al.* 2017a; Michálek *et al.* 2018). Previous studies suggested that the Meløy and Jektvik swarms had normal and oblique-normal focal mechanisms with approximately coast-perpendicular extensional direction (Bungum *et al.* 1979; Janutyte *et al.* 2017a; Michálek *et al.* 2018). Further to the north, the 1994 Steigen swarm occurred near the Sagfjord shear zone. The composite focal mechanism for the Steigen swarm is oblique-normal (Atakan *et al.* 1994).

In the offshore area, the earthquakes are generally thought to be associated with thrust faulting (Bungum *et al.* 1991; Hicks *et al.* 2000b). However, the focal mechanisms are mostly derived from mainland stations and are poorly constrained. As a result, it is not unexpected that the focal mechanisms vary quite significantly (Fig. 2). Since the earthquakes are generally smaller than magnitude 5, only one event (M_w 5.1 on 4 August 2003) with thrust mechanism has been reported in the global CMT catalogue (Ekström *et al.* 2012, Fig. 2).

Present day stress in Nordland is influenced by several regional and local sources (Bungum *et al.* 2010). At the regional scale, Nordland experiences compressive ridge push stress from the Mohs ridge (Fig. 1). Scandinavia is also influenced by glacial isotatic adjustment (GIA) with the Gulf of Bothnia being the area with the highest uplift (9–10 mm yr⁻¹, Steffen & Kaufmann 2005; Keiding *et al.* 2015; Vestøl *et al.* 2019, Fig. 1). Keiding *et al.* (2015) showed that the coast of Nordland has the highest uplift gradient even though this region has a comparatively low uplift rate (3–4 mm yr⁻¹). To give a clear picture of the uplift in Nordland and in Fennoscandia, we plotted the NKG2016LU land uplift model, developed using geodetic observations and GIA model (Vestøl *et al.* 2019) in Fig. 2.

The effect of GIA can create extension around the edge of the ice load which in Nordland lies approximately around the coastal area (Wu & Hasegawa 1996; Fjeldskaar *et al.* 2000). The models of Fjeldskaar *et al.* (2000) suggest compression beyond the ice edge, consistent with the present-day stress regime offshore Nordland. Rapid sedimentary loading offshore and topography effects can also influence the stress regime in the area to some extent. The combination of these local effects, tectonic stress and lateral variations in the lithosphere seems to control the stress state in the region (e.g. Fejerskov & Lindholm 2000; Bungum *et al.* 2010; Keiding *et al.* 2015; Gradmann *et al.* 2018).

3 DATA AND PREPROCESSING

To develop a high resolution seismic velocity model, we conducted 3-D seismic traveltome tomography. We used P - and S -wave arrival times from earthquakes and mining blasts recorded in Nordland and the surrounding region. Furthermore, to obtain information on earthquake mechanisms, we used first motion polarities and amplitude ratios of selected earthquakes. We recomputed the focal mechanism catalogue published by Michálek *et al.* (2018), who used a 1-D velocity model to derive the solutions. Here we tested the use

of a 3-D velocity model to improve focal mechanism estimation and get better information on the crustal stress.

Most arrival time data used in this study were obtained from the Norwegian National Seismic Network (NNSN) catalogue for the period of 2007–2019 (Ottemöller *et al.* 2018), which contains data from permanent NNSN (Ottemöller *et al.* 2021) and Norsar (Schweitzer *et al.* 2021) stations and from the temporary Neonor2 deployment (2013–2016, Michálek *et al.* 2018). We manually picked arrival times from additional temporary and permanent networks deployed in the region, that is the Swedish National Seismic Network (SNSN, 2013–2016, Lund *et al.* 2021), Finnish National Seismic Network (FNSN, Veikkolainen *et al.* 2021), Scanlips2 (2007–2009), Scanlips3D (2013–2014, England *et al.* 2016) and Scanarray (2013–2016, Thybo *et al.* 2021). In total, these manual picks contribute approximately 20 per cent of the phase picks in the new combined data set used in this study. The ray paths from the NNSN catalogue are dominated by coast-parallel azimuths (Fig. S1), but the additional phase picks have increased the ray coverage mostly in coast-perpendicular azimuths (Fig. S1). The data set contains the 2015–2016 Jektvik swarm and a small cluster of events in Steigen that occurred in 2008–2009 (Fig. 2). The cluster in Steigen is located in the vicinity of the 1994 Steigen swarm. In addition to earthquake data, we also included a few mining related events to improve the coverage. The events occurred in the Kvannevan mine in the southern part of Nordland and are labelled as mining events in the NNSN catalogue.

All phase picking was done using the Seisan software package (Havskov & Ottemöller 1999; Havskov *et al.* 2020). We assigned three levels of phase pick quality: (1) clear impulsive, (2) clear emergent and (3) unclear emergent, and assigned a corresponding weight in the hypocentre determination, that is 100, 75 and 50 per cent, respectively. Other phase picks with lower quality were discarded, and observations at stations with timing issues were removed. A systematic estimate of the picking errors is not available as we used picks from different sources. We made some visual estimation of the errors, and decided to use a slightly conservative error estimate of 0.1 s.

We tuned the data set by first locating all events with a 1-D velocity model, and then systematically selecting only high quality events and reliable stations for further use in the tomography. We removed stations that had fewer than 15 observations which may indicate low data quality at the stations and to avoid the artefacts in the velocity model near the stations. The events were located using the Hypocentre program (Lienert & Havskov 1995) and the traveltimes computed with the 1-D NNSN velocity model (Havskov & Bungum 1987). Then we selected earthquakes based on the following criteria: (1) local magnitude $M_L \geq 0.5$, (2) recorded by a minimum of eight stations and (3) azimuthal gap $\leq 200^\circ$. To avoid the ray paths being dominated by events from the same area, we used a larger magnitude criterion ($M_L \geq 1.0$) for the area of the Jektvik swarm, which resulted in 150 events. Out-of-network offshore earthquakes have a larger azimuthal gap and larger location uncertainties. However, these events can improve ray coverage at depth and near the edge of the model (Koulakov 2009). In our case, the out-of-network events improve ray coverage in the offshore region. For these events, we required a depth of less than 25 km and a minimum number of 15 recording stations.

The final data set consists of 527 earthquakes with a total of 7868 P -wave and 6470 S -wave arrival times recorded by a total of 79 seismic stations for the period of 2007–2019. Approximately 85 per cent of our events have an azimuthal gap $\leq 180^\circ$ and the peak of the azimuthal gap distribution is $\sim 100^\circ$. In addition, we

used 16 mining events, which yield an additional 161 P -wave and 153 S -phase observations. Since the mine is relatively small, approximately 3 km², we did not locate these events but we fixed the hypocentres to the centre of the mine.

The data set needed for the focal mechanism calculation are the first motion polarities and the SH/P amplitude ratios. We re-computed solutions from (Michálek *et al.* 2018), which had been computed using the permanent NNSN and temporary Neonor2 networks. Here we added measurements from additional temporary stations, for example Scanlips3D and Scanarray. We computed the focal mechanisms for 41 events that have at least six clear first motion polarities. The SH/P amplitude ratios were computed using an automatic procedure integrated in Seisan (Michálek *et al.* 2018). We only used amplitudes of the direct phases, that is Pg and Sg phases and limited the epicentral distance to 100 km. The P and SH displacement amplitudes were measured in the frequency domain on the vertical and transverse components, respectively.

4 METHODS

In order to produce 3-D seismic V_P and V_P/V_S ratio models for the Nordland region, we applied a procedure comprising the following two steps: (1) 1-D V_P and V_S inversion used to find 1-D initial model for tomography and (2) 3-D V_P and V_P/V_S ratio inversion. The 3-D take-off angles computed in step (2) were later used to improve the focal mechanisms. In this section, we describe details of the methods that were applied.

4.1 Seismic velocity inversion

The seismic tomography results strongly depend on the starting model (Kissling *et al.* 1994). Consequently, as a first step, we inverted for a 1-D velocity model that will be used as starting model in the 3-D inversion. We used the Velost code (Ellsworth 1978; Kissling 1995), which performs velocity inversion simultaneously with hypocentres and station delays. The station delay terms are introduced to accommodate for near-surface and large scale velocity heterogeneity (Husen *et al.* 2011). Here we tested two input 1-D velocity models: (1) the 1-D NNSN velocity model from Havskov & Bungum (1987) and (2) the average Crust1.0 model for the entire study area (Laske *et al.* 2013). We found that the average crustal thickness in the area is ≈ 40 km from Crust1.0 and the Moho depth compiled by Maystrenko *et al.* (2017). We tested different crustal thicknesses of 35, 40 and 45 km for both input 1-D models. The layer thicknesses were not inverted, but were adjusted during the preparation. We divided the 1-D model into 5 km layers and used the velocities interpolated from the respective input model. A layer adjustment test was performed by inverting for velocities for the models, and then we combined the layers with similar velocities.

To test the range of feasible input models, we followed the procedure of Shiddiqi *et al.* (2019) by creating 500 model variations for each initial model. This was done by randomly perturbing the V_P and V_S for each layer within a range of ± 10 per cent, but keeping the V_P/V_S ratio within the range of 1.6–1.9. We only accepted the results within the lowest 10 per cent root mean square (RMS) residuals, which were then averaged. The next step was to refine the averaged velocity models to obtain the final models and the respective station delays by performing an additional inversion on it. In this stage, we assigned a higher damping weight to the velocity model, so that the velocity model is not changed significantly during the inversion. The preferred minimum 1-D velocity model,

which was selected based on its traveltimes residuals, is presented and described in Section 5.1.

The next step was to perform the 3-D traveltimes tomography using the SIMULR16 code (Bleibinhaus 2003; Bleibinhaus & Grande 2006; Bleibinhaus & Hilberg 2012), which is a modified version of the well-established SIMUL family codes (Thurber 1983; Evans *et al.* 1994; Thurber & Eberhart-Phillips 1999; Rietbrock 1996). The SIMULR16 code uses a damped iterative least-square inversion scheme to obtain 3-D V_P , V_P/V_S ratio, and station delays. To compute the traveltimes, the code employs a combination of approximate ray tracing (ART) and pseudo-bending method (PB) to calculate the traveltimes. Bleibinhaus (2003) modified the ART and included an iterative segmentation for PB to compute more accurate ray paths at regional distance within a heterogeneous medium. These modifications improve the accuracy of the ART-PB ray tracer by more than 1 order of magnitude for distances above 140 km (Bleibinhaus 2003).

To produce a robust 3-D model, we performed a series of inversions where the complexity increases as the number of inversion grid nodes increases and the horizontal grid spacing decreases. First, we ran the inversion on a coarse grid model ($6 \times 8 \times 12$ grid nodes; smallest horizontal grid spacing: 100 km) using the preferred 1-D velocity model as the starting model (See Fig. S7 and Section 5.1). Then, we performed two additional inversions with refined grid spacing, a medium grid ($9 \times 13 \times 12$ grid nodes; smallest horizontal grid spacing: 50 km), and a fine grid ($18 \times 23 \times 12$ grid nodes; smallest horizontal grid spacing: 25 km; see Fig. S2). The final model in each inversion stage is used as the starting model for the next stage. We used ray density and the checkerboard test results to evaluate the model resolution throughout the process. The final 3-D model, which we present and describe in Section 5.2, is the result of the inversion using the fine grid nodes. The distributions of ray paths and fine grid nodes are shown in Fig. S2.

The observations were weighted based on the phase picking quality (we applied the same weighting scheme as for the hypocentre determination in Data section), and traveltimes residuals. The earthquake hypocentres and origin times were updated iteratively before the velocity inversion in each iteration. The hypocentres were fixed for the mining events, but the origin times were recomputed. We evaluated the reliability of earthquake depth at each inversion stage, especially for ‘out-of-network’ events. The inversions were repeated after we removed events that have unreliable locations. The damping parameters, which control the model perturbation in each iteration, are determined using a trade-off curve between model variance and data misfit.

4.2 Focal mechanism

Focal mechanisms provide important information about the stress regime of an active tectonic region. In order to obtain accurate focal mechanisms for selected earthquakes in Nordland, we used a combination of first motion polarities and SH/P amplitude ratios. Initially, we computed focal mechanisms by using the Focmec program (Snoko 2003) based on a 1-D model, but then transitioned to our resulting 3-D model to allow for improved take-off angles. Previous studies have demonstrated that the use of 3-D velocity models can improve the focal mechanism solutions (e.g. Takemura 2016; Newrkla 2019). We used the final hypocentres, determined using the 3-D seismic velocity model, for both analyses. Focmec performs a grid search over strike, dip and rake and finds solutions that are within given error criteria. We computed the take-off angles,

emergence angles and azimuths using ray paths obtained from the SIMULR16 code.

Amplitude ratios are useful to constrain the solutions that were initially obtained using polarities only. The amplitude ratios between P and S waves were corrected for attenuation and free surface and then depend only on the radiation pattern (e.g. Havskov & Ottemöller 2010). The free surface correction requires V_P/V_S ratio (here a constant value of 1.74 is used) and the emergence angles. The attenuation correction is based on the quality factors Q for P and S waves. Since we only have information for Q_{Lg} for mainland Norway, we assume that Q_P and Q_S have the same value as Q_{Lg} and we adopted $Q_{Lg} = 529^{\theta/42}$ (Demuth *et al.* 2019). To assess the quality of amplitude ratios, we used the amplitude ratio misfit, which is the difference between the observed and synthetic SH/ P amplitude ratios. To ensure the solution's quality, the amplitude ratios that have logarithmic misfits larger than 0.2 were rejected (see the Focmec manual (Snøke 2003)).

We computed the focal mechanisms following a two-step approach described in Halpaap *et al.* (2019). First, the solutions were determined using polarities alone. We proceeded to the second step if the solutions were similar (i.e. P - and T -axes fall into small area on the lower hemisphere projection). Then we refined the solutions by combining polarities and SH/ P amplitude ratios computed in the frequency domain. We did not allow for any polarity error, and the maximum number of rejected amplitude ratios had to be less than 50 per cent of the observations. The poorly constrained events were removed—that is those with more than 50 solutions for a grid spacing of 2° . We used the solution uncertainties to evaluate the solution qualities similar to Hardebeck & Shearer (2002), but here we adopted more relaxed criteria. We considered the absolute maximum difference in strike, dip and rake as an indicator of solution uncertainties and assigned three solution qualities: (1) events that have all solution uncertainties less than 25° were given quality A, (2) events that have solution uncertainties (in either strike, dip or rake) larger than 25° and less than 45° were given quality B and (3) events that have larger uncertainties or events that have more than 50 solutions were given quality C. We only considered events with quality A and B as stable solutions that can be used for further analysis.

5 RESOLUTION

5.1 Hypocentre error estimation

In each stage of the velocity inversion, the hypocentres are relocated and their quality strongly affects the velocity model. In the SIMULR16 code, the location error is estimated using the variance and the outer product of an SVD-derived general inverse operator (see Klein 2002; Halpaap *et al.* 2018). The variance itself is a combination of the picking error, and weighted traveltimes residuals. We assigned a conservative value of 0.1 s for the picking error (see Section 3). Fig. 3(a) shows that the RMS of traveltimes residuals are reduced by about 20 per cent and the average location errors are reduced by about 30 per cent during the three stages of tomography inversion. The station delays are reset to zero at the beginning of each stage. Therefore, the starting RMS in medium and fine grids are higher than the previous iteration of the larger grids. Furthermore, we also evaluated the solutions convergence by showing the velocity and hypocentre changes for each iteration in Figs 3(b) and (c). In each stage, largest solution changes happened in the first few iterations, and then the solutions did not change significantly

afterwards. This pattern is expected and indicates that the solutions converge.

5.2 Tomography resolution tests

To evaluate the resolution and robustness of our tomography results, we conducted a series of synthetic tests. We performed the tests to investigate how well synthetic anomalies can be recovered, in terms of their size, location and strength, by our inversion setup. First, we created two types of synthetic velocity models: (1) checkerboard velocity models and (2) synthetic models based on velocity anomalies in the tomography results. Then we calculated synthetic traveltimes using the final hypocentres and the synthetic velocity models. We added random Gaussian noise to the traveltimes with a standard deviation of 0.1 second based on our picking error estimate. We did not directly shift the hypocentres, but the starting locations are shifted during the initial adjustment before the velocity inversion due to the noise and the use of an initial velocity model. We then inverted the synthetic data to obtain V_P , V_P/V_S ratio along with the hypocentres.

In a first series of resolution experiments, we performed checkerboard tests by alternately perturbing the final 3-D velocity model by ± 5 per cent. The checkerboard test results for three depth slices (8, 24, 32 km) and coast parallel cross-sections are shown in Fig. 4. The tests show that V_P and V_P/V_S ratio can be recovered (Fig. 4) and we are able to recover the central part of the model (Lofoten–Vestfjorden basin–coastal area—and some part of the mainland area) down to the Moho depth. In this central part, at shallow depth, both shape and anomaly strength are quite well resolved and in the deeper part, we can still recover the anomalies but they are weaker and start to smear. In the northeastern corner of the model, we can recover the checkerboard anomalies but smearing affects the results. The anomalies are getting weaker in the mid-crust (17–24 km) due to limited number of direct ray paths crossing this part of the model. This area is dominated by refracted ray paths (P_n and S_n phases), and has a limited number of direct ray paths (P_g and S_g). This ray path distribution can resolve the Moho well, but not the shallower structure in the corners of the model.

In a second series of resolution tests, we performed synthetic anomaly recovery to evaluate whether prominent velocity anomalies expected in our tomographic models are more likely to be real features or artefacts of the inversion. We performed two such synthetic anomaly recovery tests as described in the following:

(i) Moho step

Earlier results (e.g. Maystrenko *et al.* 2017; Michálek *et al.* 2018) showed that there is a transition between the shallow Moho in the southern Lofoten and deeper Moho in the mainland. Our early tomography tests indicated the existence of a sharp transition, which we refer to as Moho step. Here we tested the robustness of this Moho step. We created a synthetic 3-D V_P model with a simplified Moho step. This was achieved by using the initial 1-D model with Moho depth of 40 km onshore, and by adapting a shallow Moho model of 27 km for southern Lofoten. Then we inverted the synthetic data by following our inversion grid scheme: starting from coarse grid, then medium and fine grid size model. The synthetic model and inversion results are shown in Fig. S3. We were able to recover the shallow Moho and the Moho step beneath southern Lofoten in profiles B–B' until E–E' (see Fig. 4 for the location of the profiles). The Moho transition in profile F–F' appears to be smoother due to limited ray path coverage.

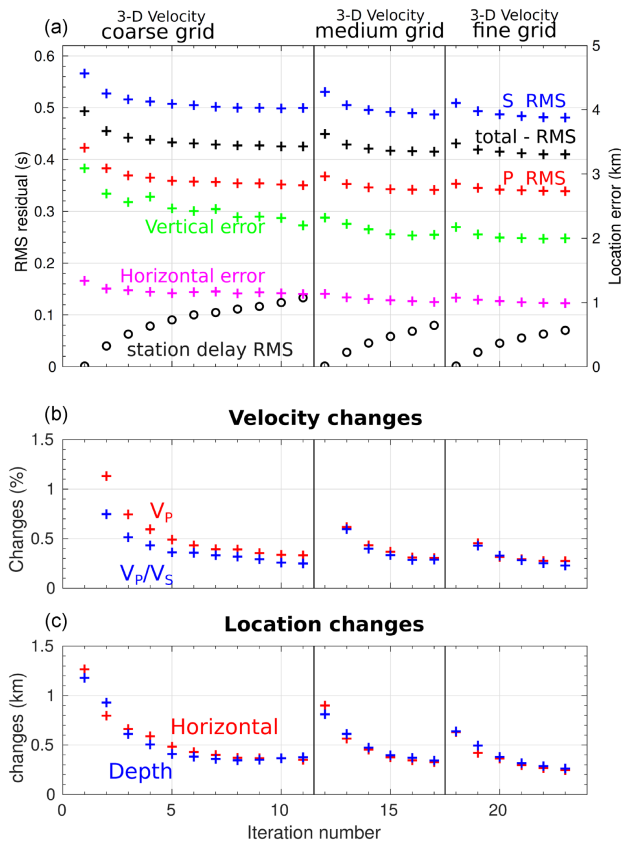


Figure 3. (a) Plot of traveltime RMS residuals, station delays RMS, and the average location error changes for each iteration. At the beginning of each inversion stage, the station delays are set to zero. Therefore, the starting RMS in medium and fine grids is higher than the last iteration of the larger grids. (b) Plot showing the average velocity changes. The change is the difference between the current iteration (n) and the previous iteration ($n-1$) for each grid. (c) The average location changes for each iteration.

Next we verified whether the Moho step can be artificially created by our inversion set-up. Previous models showed that the Moho transition from southern Lofoten towards the mainland is smooth (e.g. Maystrenko *et al.* 2017). Therefore, we created an additional synthetic test by modifying the simplified Moho step model. As opposed to an abrupt change in the Moho depth, we modified the model to make the velocity smoother. Then we inverted the synthetic data using the same inversion scheme. The initial model and inversion result are shown in Fig. S4. The inversion results show that the Moho transition is relatively smooth. These tests showed that we can resolve the shallow Moho beneath southern Lofoten and the Moho step feature, and that the Moho step is unlikely to be an artefact.

(ii) Robustness of the anomalies near the Moho step

Uneven ray path distribution is usually expected in earthquake travel-time tomography. Velocity anomalies can influence the ray path distribution as well, by focusing or defocusing the ray path. In our

case, seismic events are concentrated along the coast near the Moho step. Therefore, the ray paths become concentrated in this area (see cross-section plots of the ray paths in Fig. S5) and it is important to verify that a high V_p/V_s ratio anomaly is not an artefact due to uneven ray path distribution.

To achieve this aim, we performed a set of synthetic tests by creating three synthetic models: (1) model with constant V_p/V_s ratio but added higher random Gaussian noise with a standard deviation of 0.2 s, (2) model with low V_p/V_s ratio anomaly in the offshore region and (3) model with high V_p/V_s ratio anomaly in the onshore region. In all of these models, we do not introduce any anomalies near the step. The synthetic models and the results are shown in Fig. S6.

From these tests, no strong velocity anomaly is introduced near the Moho step. Although there are small patches of high V_p/V_s ratio perturbation near the step, the anomaly strength is less than 1 per cent. This could be caused by the random noise added to the

820 H.A. Shiddiqi et al.

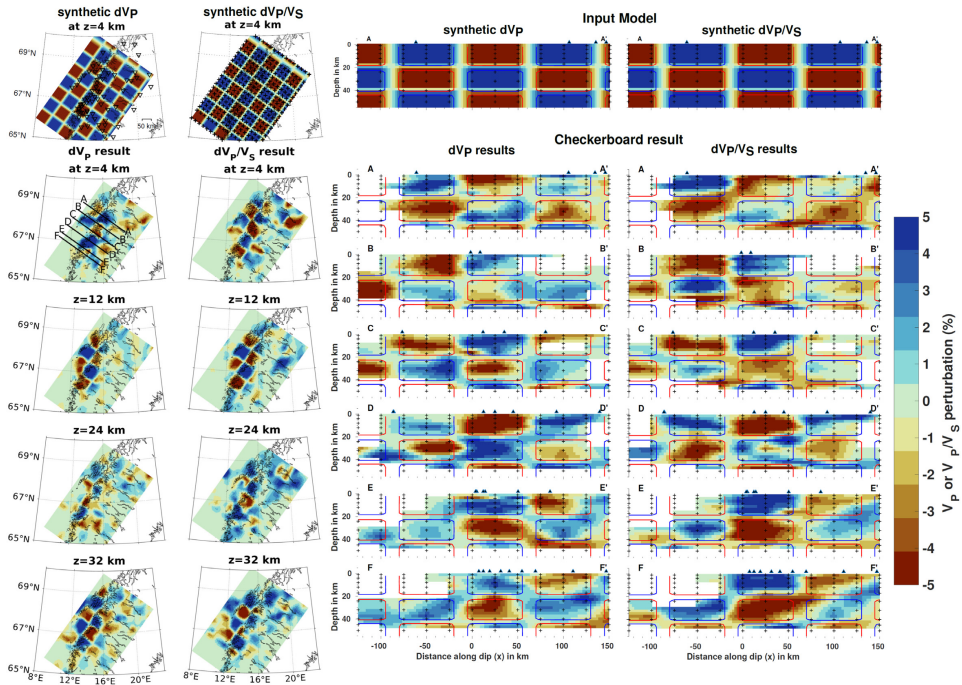


Figure 4. Checkerboard test for V_p and V_p/V_s ratio in the map view slices and cross-sections. The input synthetic model, created by alternately perturbing the final 3-D velocity model, is shown in the top row. All velocity plots are shown as the perturbation to the final 3-D velocity model. Stations (open inverted triangles) and inversion grid positions (crosses) are shown on the map view of synthetic V_p and V_p/V_s ratio models, respectively. The cross-section lines are shown on the map view V_p inversion result at 4 km depth. In the cross-section plots, grid node positions are also shown as cross symbols. The red and blue boxes highlight the area with low and high perturbation inputs, respectively.

synthetic data. Therefore, we conclude that the Moho step feature does not create an artificial anomaly.

6 RESULTS

6.1 1-D velocity inversion

We tested six input models which consider several Moho depths, that is 35, 40 and 45 km and the output models are shown in Fig. S7. The NNSN-based models contain four crustal layers and the Crust1.0-based models consist of six layers. All 1-D velocity models have quite similar velocities for depth down to 20 km, and the largest variation occurs in the lower crustal and the mantle velocities. We found that the inversion using the averaged Crust1.0 velocities with the Moho at 40 km as starting model gives the lowest overall RMS residual. The preferred 1-D V_p , V_s and V_p/V_s ratio are shown in Fig. 5. All accepted inversion results tend to converge to a small range of parameter values except for V_p in the lower crust, between 20 and 40 km depth, where the results are quite spread out, especially for V_p . This pattern likely indicates strong lateral variation of V_p due to strong differences in crustal thickness, which cannot be captured by a 1-D velocity model. V_s is not as spread out as V_p because of

the S -ray paths sampled a smaller area of the lower crust due to a smaller number of S -picks for stations further inland.

The P - and S -wave station delays for the preferred velocity model are shown in Figs 5(b) and (c). We chose permanent station MOR8 as the reference station, because it is located near the centre of the model, and was in operation throughout the period of our event catalogue. The positive and negative station delays represent late and early arrival times, respectively (e.g. Wright 2008; Midzi et al. 2010). Comparison of the P -wave delays for all velocity models are shown in Fig. S8. The contrast between delays on southern Lofoten and the mainland can be attributed to the deviation of the layer geometry, for example due to the crustal thickness variation. The stations on Lofoten have large negative P - and S -wave delays indicating large positive velocity perturbation along the ray paths beneath the southern Lofoten indicating a thinner crust. Stations on the mainland have positive P -wave delays, which correspond to negative velocity perturbation pointing towards a thicker crust.

6.2 Final hypocentre locations and 3-D velocity model

The hypocentre locations of 527 earthquakes used in the 3-D seismic tomography are shown in Fig. 6. There are only eight offshore events near the shelf edge that have reliable hypocentre locations. The

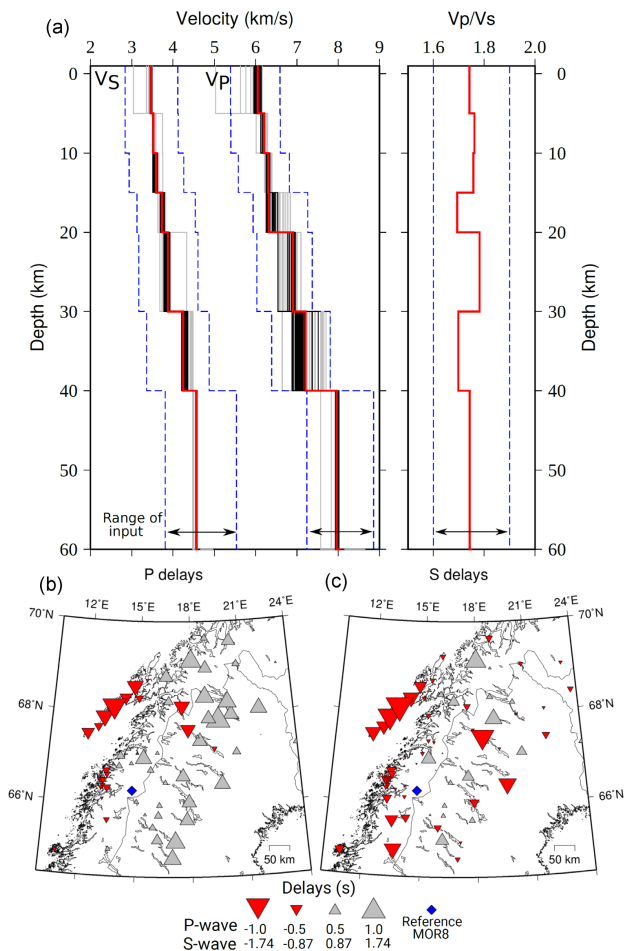


Figure 5. (a) Preferred 1-D velocity model. The final V_P , V_S and V_P/V_S ratio models are depicted by red lines. The range of input are shown as blue dashed lines. The inversion results are shown as grey lines and the accepted models are shown as black lines. Station delays for P and S waves are shown in (b) and (c), respectively. Symbols for S -wave delays are scaled down to the average V_P/V_S ratio, 1.74.

coastal seismicity is distributed from less than 5 km down to 18 km. The location of the Jektvik and Steigen swarms are highlighted in Fig. 6. In addition, we show the hypocentre distribution in the Jektvik and Steigen areas located using the four velocity models developed in this study: 1-D, 3-D coarse, 3-D medium and 3-D fine models in Figs S9 and S10.

The 3-D seismic tomography results are presented as coast-normal cross-sections in Fig. 7. The coast parallel cross-sections are also presented in Fig. S11. The depth slice of V_P and V_P/V_S ratio for depths 4, 8 and 12 km are shown in Fig. 8 and for depths of 17, 32 and 40 km are presented in Fig. S12. Based on these results, we can estimate the position of the ‘tomography Moho’,

indicated by a sharp gradient from 7.0 to 8.0 km s⁻¹ (e.g. Husen *et al.* 2003). A number of tomography studies that used a similar approach to estimate the Moho depth adopted V_P contours between 7.25 and 7.4 km s⁻¹—see, for example studies of Diehl *et al.* (2009), Koulakov *et al.* (2015) and Leónios *et al.* (2021) which looked at Moho depths in the Alps, Himalaya and the Ecuadorian margin, respectively. Lange *et al.* (2018) used a higher V_P of 7.8 km s⁻¹ as a proxy for the Moho in the Central Sumatra subduction zone. Here, we chose the V_P 7.6 km s⁻¹ contour as an indicator of the continental Moho (Fig. 7) as this is close to the Moho depth derived from the receiver function studies for mainland Nordland from Ben-Mansour *et al.* (2018) and Michálek *et al.* (2018).

822 H.A. Shiddiqi et al.

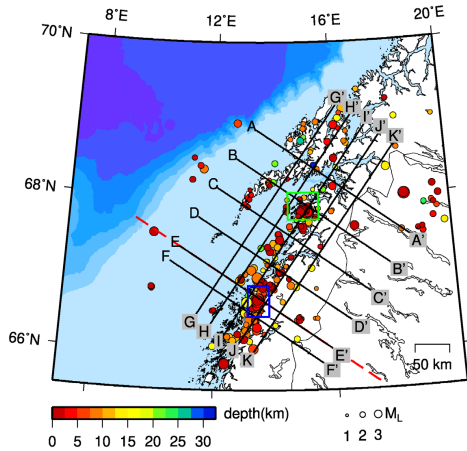


Figure 6. Distribution of final hypocentre locations. Large open circles mark the area of two earthquake swarms discussed in the text: Steigen swarm (green rectangle) and Jektvik cluster (blue rectangle). Positions of cross-section lines, shown in Figs 7 and S11, are depicted by black lines. Red dashed line is the location of extended E–E' section shown in Fig. 11. See Fig. 2 for the bathymetry scale.

We identified seven important features in our tomography results that are marked in Figs 7 and 8 with Roman numerals I–VII based on the order of their appearance in Section 7:

(i) A significant change of crustal thickness over a short distance (~ 25 km) or Moho step exists beneath the Vestfjorden basin (in Sections B–B' to F–F'). In the northern part of Lofoten and Vesterålen, the crust is relatively thick (> 35 km) and the transition towards the mainland (see Section A–A') is smoother. South of Lofoten (southern part of Lofoten islands and Lofoten ridge), the crust is thinner (around 27 km), and the Moho step is observed. The position of the Moho step comes closer to the coast as we move to the south. The crustal thickness in the mainland is greater than 40 km.

(ii) A thin layer of high V_p/V_S ratio anomaly (up to ≈ 1.84) exists at the upper crustal in the vicinity of the Steigen swarm within the Sagfjord shear zone (in Section B–B'). Below this anomaly, the V_p/V_S ratio is relatively low (down to ≈ 1.68).

(iii) A low V_p anomaly within the uppermost layer (Sections D–D' and E–E') extends from the mainland towards the Vestfjorden basin.

(iv) A low V_p/V_S ratio (down to ≈ 1.65) anomaly is observed at upper crustal depth (Sections E–E' and F–F') between 0 and 15 km depth. The low V_p/V_S ratio coincides with the Jektvik swarm.

(v) A high V_p/V_S ratio anomaly (up to ≈ 1.81) is observed around the Vestfjorden basin.

(vi) A high V_p/V_S ratio (up to ≈ 1.83) anomaly exists at upper-middle crustal depths further east in the model towards the area with high elevation (Sections E and F). The anomaly is observed between 5 and 15 km depth.

(vii) A high V_p/V_S ratio anomaly (up to ≈ 1.85) is observed at middle and lower crustal depths. The anomaly is most prominent in Sections C–C' and E–E'.

The interpretation of these features is presented in Section 7.

6.3 Focal mechanisms

We computed focal mechanisms for 41 events that have a minimum of six polarity observations. On average, each event has eight polarities. Based on our result, the focal mechanisms computed using the 3-D velocity model have smaller amplitude ratio misfits (average logarithmic misfits: 0.18) than the focal mechanism derived using 1-D velocity model (average logarithmic misfits: 0.43). We use solution range as an indicator of solution uncertainties. The 1-D velocity solution ranges are: strike 19° , dip 23° and rake 24° and the 3-D model solution ranges are reduced to: strike 10° , dip 7° and rake 16° . Fig. S13 demonstrates the improvement of focal mechanism solutions using the 3-D velocity model. This comparison also shows that the station positions on the focal sphere can vary significantly depending on the velocity model. Since we used the same hypocentre locations, the differences in take-off angles between 1-D and 3-D models are mainly caused by the variation of V_p , which can change the ray direction from downgoing to upgoing or the other way around.

Out of 41 events, we obtained reliable solutions for 21 events, that is 16 events of quality A and 5 events of quality B (Fig. 9). The remaining 20 events are categorized as quality C, and are not used in further interpretation. Most of the reliable solutions are normal and oblique-normal faulting mechanisms. The majority of events are part of the Jektvik swarm that have a near vertical P -axis and coast perpendicular T -axis (Fig. 9).

7 DISCUSSION

In following subsections, we discuss the interpretation of our velocity models and focal mechanism solutions, and their possible relation with the intraplate seismicity in Nordland.

7.1 Crustal thickness variation

From the 3-D V_p model, we estimated the crustal thickness, that here is defined as the thickness of crystalline crust plus overlying sediments. The differences between crustal structure of the southern and northern Lofoten-Vesterålen as well as the mainland area are already indicated by the P -wave station delays obtained from the 1-D velocity inversion, which reflect the deviation from the 1-D Moho depth of 40 km. The large negative delays in the southern Lofoten indicate the existence of a high velocity anomaly there, which possibly corresponds to a shallow Moho. The large positive delays in the mainland possibly correspond to thicker crust. Indeed, our 3-D V_p model shows variation from a thinner crust offshore towards a much thicker crust inland (Fig. 10). Along the Lofoten-Vesterålen islands (approximately SW–NE), the crustal thickness varies as well. The northern Lofoten-Vesterålen has crustal thickness around 35 km and further to the south the crust is thinner ~ 27 km.

In mainland Nordland, our Moho depth estimates range from 40 to 47 km. This result is comparable to crustal thickness models derived by receiver function studies (Ben-Mansour *et al.* 2018; Michálek *et al.* 2018). A slight Moho depth variation is found along the coast where the crust further south is thinner (~ 40 km, Section D–D' and E–E' in Fig. 7), and the crust beneath Steigen is thicker ~ 47 km (Section B–B' and C–C' in Fig. 7). Further to the north, the crustal thickness is ~ 42 km (profile A–A' in Fig. 7). This transition can be also seen in coast-parallel profile I–I' in Fig. S11.

Feature I in Fig. 7 shows an abrupt change in crustal thickness beneath the Vestfjorden basin, between southern Lofoten-Vesterålen and the mainland, which we refer to as a Moho step. With the

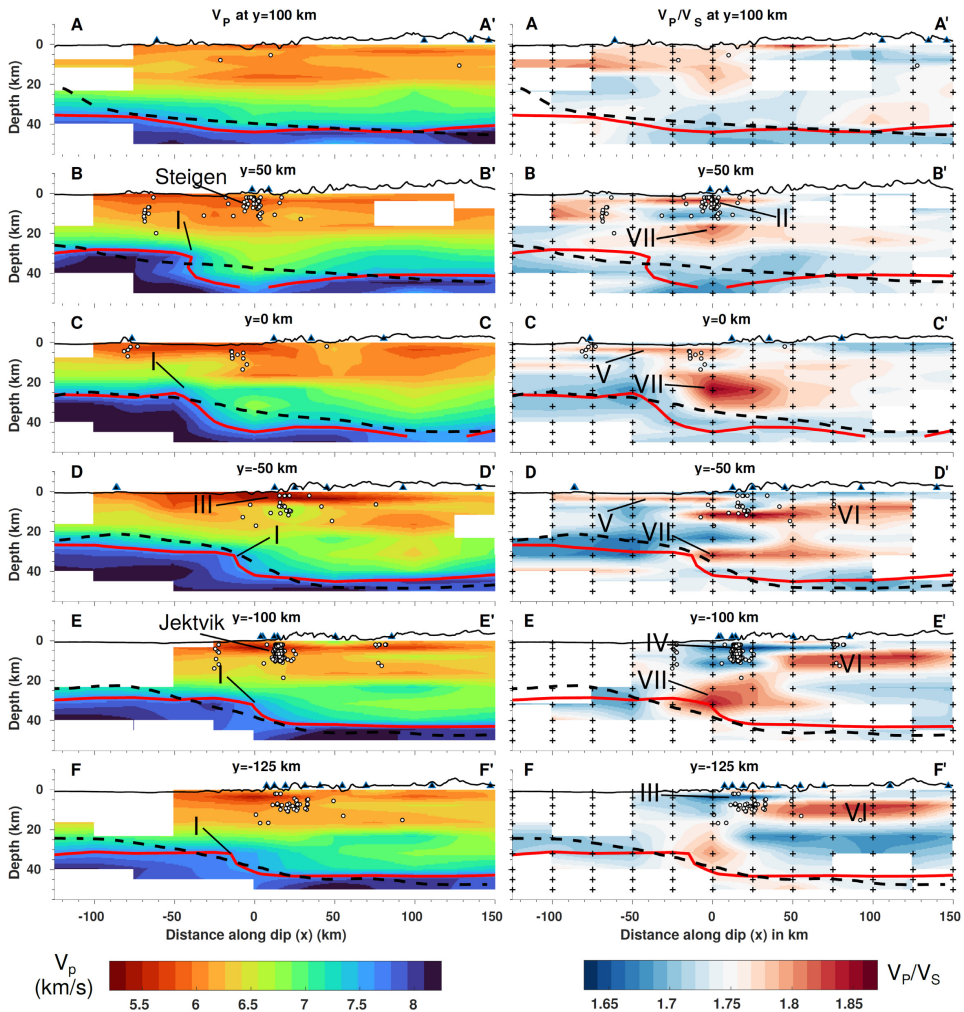


Figure 7. Coast normal cross-sections of V_p and V_p/V_s ratio across the resulting tomography model. Roman numeral labels are the features discussed in the text. Red lines are the contour of the ‘Moho velocity’ (V_p 7.6 km s^{-1}), and the dashed black lines is the Moho model compiled by Maystrenko *et al.* (2017). Hypocentres and stations are represented by white circles and black triangles, respectively. Surface topography (with $4\times$ vertical exaggeration) is plotted on the top of each cross-section. The inversion grids are plotted in V_p/V_s ratio sections. See Fig. S2 for the coordinate system of the model.

resolution test in Section 5.2, we showed that the velocity inversion can recover such sharp Moho change. The sharp details of this transition were not previously resolved and were not included in the compilation by Maystrenko *et al.* (2017) as it builds on lower resolution input than what is afforded by our new tomographic results.

The crustal thickness variation around the Lofoten-Vesterålen islands has been discussed in recent publications (e.g. Breivik *et al.* 2017, 2020; Maystrenko *et al.* 2020b). As mentioned in the background section, there is an ongoing debate as to whether the crust

is thin or not in southern Lofoten and in this section we show our results can contribute to this debate. The seismic profile 1-88 (see Fig. 1) from Mjelde *et al.* (1993) has previously been used as the main constraint on crustal thickness in the southern Lofoten, particularly beneath the Lofoten Ridge. The model from Mjelde *et al.* (1993) suggested that the crustal thickness here is as low as 20 km in a narrow area below the Lofoten Ridge. In an updated interpretation, Mjelde *et al.* (2013) suggested that the crust is thicker than in their earlier model ($\geq 25 \text{ km}$). Further to the south of profile 1-88, using the Blue Norma profile (BNR profile in Fig. 1) Avedik *et al.*

824 H.A. Shiddiqi et al.

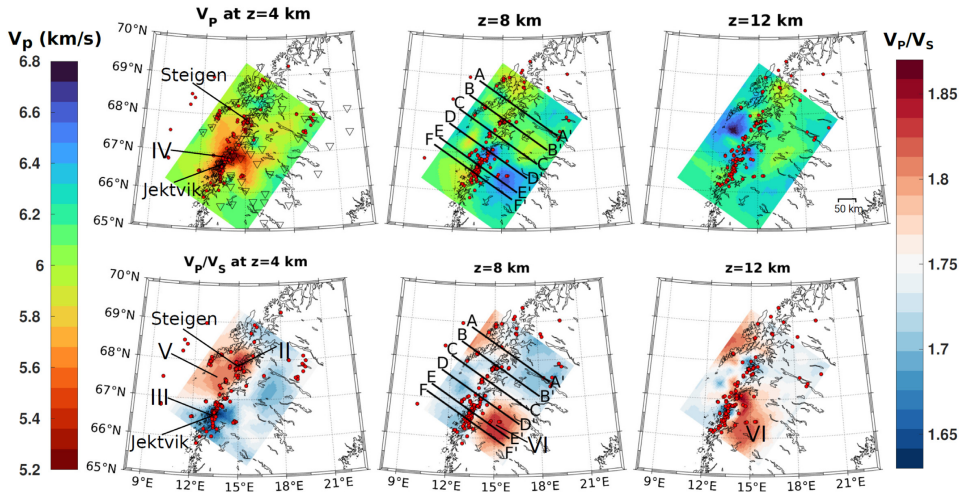


Figure 8. Horizontal depth slices of V_p and V_p/V_s ratio for the upper crustal depth. The colour scale for V_p is readjusted for a lower velocity range. Positions of the coast parallel cross-sections are shown at 8 km depth slices.

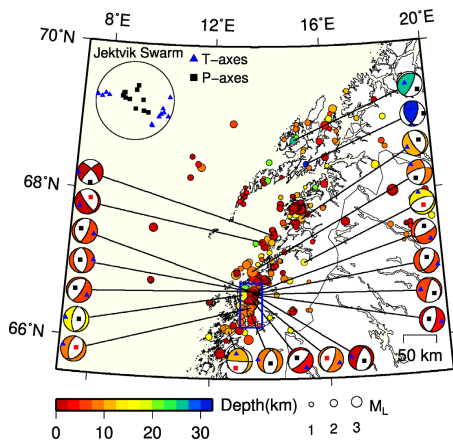


Figure 9. Distribution of the accepted focal mechanism solutions (Quality A and B). Small rectangles and triangles in the solutions represent the P - and T -axes, respectively. The quality A and B solutions are labelled with black and red triangles, respectively. The open blue rectangle is the location of Jektvik swarm. The P - and T -axes of solutions from Jektvik are shown in upper left circle.

(1984) also inferred that the region here has thin crust. In contrast, using profile 8-03 (Fig. 1), Breivik *et al.* (2020) proposed that the crust beneath southern Lofoten is thicker ($> \sim 30$ km).

Our larger crustal thickness estimates in the northern Lofoten-Vesterålen are similar to those of Breivik *et al.* (2017), and the

shallower Moho depth in the southern Lofoten-Vesterålen is comparable to that proposed by Mjelde *et al.* (2013). In Fig. 7, the profile A–A’ represents the northern Lofoten-Vesterålen area with a thicker crust, and profiles B–B’ until E–E’ represent the area with a thinner crust in the southern Lofoten-Vesterålen. We suggest that the transition occurs between profiles A–A’ and B–B’ (also see profile G–G’ in Fig. S11). Mjelde *et al.* (2013) proposed the existence of high velocity eclogitic layer in the lower crust of the Lofoten ridge. However, the proposed eclogite in the lower crust is not resolved in our model due to limited rays and our inversion grid spacing. Still we observe a thinner crust in the southern Lofoten-Vesterålen (~ 27 km), and conclude that the model of thinner crust in the southern Lofoten-Vesterålen is valid.

7.2 Crustal Structure and composition

The main upper crustal velocity anomalies are located in the vicinity of two distinct seismicity clusters: the Steigen swarm in the north, and the Jektvik swarm in the south. In the vicinity of the Steigen swarm, we observe relatively low V_p and high V_p/V_s ratio at shallow depths, and low V_p/V_s ratio at greater depths (anomaly II in Figs 7 and 8). Whereas in Jektvik, very low V_p (anomaly III) and low V_p/V_s ratio are observed (anomaly IV). The V_p around Jektvik swarm is significantly lower and extends over a larger area, while the low V_p around Steigen is more localized.

The low V_p in both regions can be an indication of fractured rocks and fluids (e.g. Unsworth & Rondenay 2013). The effect of fracture and fluid content can also play an important role in the variation of V_p/V_s ratios at shallower depth (e.g. Wang & Ji 2009; Kuo-Chen *et al.* 2012). However, the V_p/V_s ratio sign depends on the pore pressure, aspect ratio of the pore, fluid content, and the Poisson’s ratio of the host rocks (Takei 2002; Brantut & David 2018). While

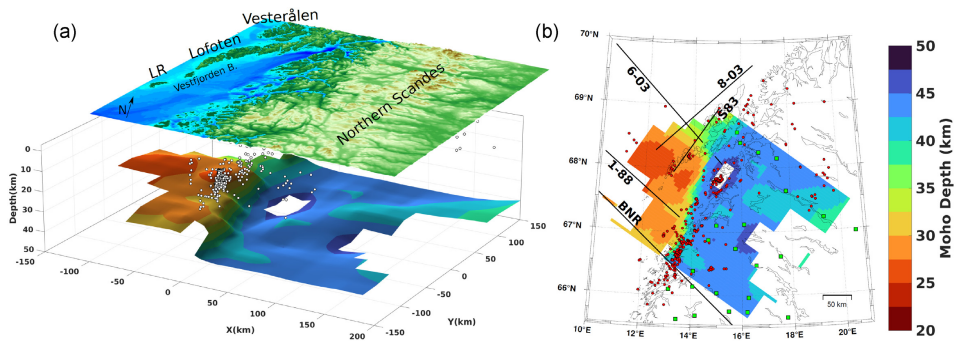


Figure 10. (a) 3-D block model of Moho surface extracted from the 3-D V_p model. Earthquake hypocenters are shown as white circles. The vertical axis has $2 \times$ exaggeration. (b) Map view of the Moho surface. Earthquake are shown as red circles. Black lines are the seismic lines discussed in the text. Small green squares are seismic stations used in receiver functions study in Ben-Mansour *et al.* (2018).

a small crack aspect ratio can increase the V_p/V_S ratio, large crack aspect ratio can decrease the V_p/V_S ratio (e.g. Shearer 1988; Takei 2002; Lin & Shearer 2009). Although it is difficult to pinpoint the exact rock units and physical parameters that govern the V_p/V_S ratio in Jektvik and Steigen, we speculate that fluids are present at the seismogenic depth in this region given the propensity for seismic swarms.

In case of ambiguity in the seismic velocity models, additional complementary constraints can be provided by electrical resistivity images. A recent magnetotelluric survey across Northern Norway and Sweden shows the presence of a large crustal conductive anomaly beneath Nordland (Cherevatova *et al.* 2015). They suggest the possibility of water infiltration through shear zones, for example Sagfjord shear zone. Some of the conductive anomalies are located near the high V_p/V_S ratio (Steigen region). From observations in active fault regions, low resistivity anomaly is often associated with the presence of fluid within the fault zones as observed in, for example San Andreas fault (Unsworth & Bedrosian 2004), and Kachchh rift (Kumar *et al.* 2017).

Along the Vestfjorden basin, we observe low V_p and high V_p/V_S ratio (~ 1.81) (anomaly V in Sections C–C' and D–D'). This basin is filled with Mesozoic sediments (Olesen *et al.* 2002), and several normal faults that formed during the rifting processes are identified from geophysical methods (Olesen *et al.* 2002; Tsikalas *et al.* 2005). The combination of sedimentary basin and fault zones in the Vestfjorden basin is likely to reduce the V_p , and increase the V_p/V_S ratio slightly.

The most prominent feature of the middle and lower crust is the high V_p/V_S ratio (up to ≈ 1.85) (anomalies VI and VII in Fig. 7). Anomaly VI is most prominent in Sections E–E' and F–F'. Anomaly VI can be possibly attributed to the rock composition rather than the existence of fluid, because it is accompanied by slightly elevated V_p . Anomaly VII, located near the Moho step, is a result of increasing V_p . Anomalies VI and VII possibly indicate mafic rock composition, which is also found in the lower crust offshore Lofoten by Avedik *et al.* (1984) and Breivik *et al.* (2017), and along the mid Norwegian margin (Mjelde *et al.* 2016). The high-velocity body found in the lower crust along the Norwegian margin can be interpreted as the Eocene magmatic intrusions or the Caledonian eclogites (Mjelde *et al.* 2016).

7.3 The causes of intraplate seismicity in the coastal area of Nordland

Earthquakes in Nordland predominantly occur offshore along the shelf edge and onshore in the coastal area (see Fig. 9). A small number of earthquakes are also observed along the Lofoten–Vesterålen islands. The earthquake mechanisms vary from thrust faulting along the shelf edge (somewhat poorly resolved) to normal faulting along the coast. Our focal mechanisms show normal and oblique-normal solutions for events along the mainland coastal area. We do not have reliable solution for the Steigen swarm due to limited number of stations during the 2008–2009 period. For Jetvik, we obtained 12 focal mechanisms which are normal or slightly oblique-normal. The plot of P - and T -axes in Fig. 9 indicates coast perpendicular extension, which matches previous observations (Hicks *et al.* 2000b; Janutyte *et al.* 2017b). Further to the east, outside of the study area, the stress regime tends to be compressive as implied by focal mechanism studies of earthquakes in Northern Sweden (e.g. Arvidsson 1996; Lindblom 2011).

The local stress along the coast of Nordland is the opposite of what is expected from the mid Atlantic ridge push. It has been suggested that the local stress effects in Nordland, for example GlA, sedimentary loading, topography and lateral variation within the lithosphere (e.g. Fejerskov & Lindholm 2000; Bungum *et al.* 2010; Keiding *et al.* 2015), are strong enough to overcome the regional stress. The assumption is that the state of stress in the crust leads to reactivation of pre-existing faults (Atakan *et al.* 1994; Bungum *et al.* 2010). Here we attempt to combine our new result with previous constraints to identify the primary stress mechanisms in the Nordland region (Fig. 11).

Mass redistribution and respective isostatic adjustment, either due to sediment redistribution or ice removal result in flexural stress in the region. The high lateral uplift gradient along the coast of Nordland shown by Keiding *et al.* (2015) is possibly related to the effects of the flexural stress. The deglaciation process caused rapid erosion with a high rate of removal, along the coast of Nordland and Lofoten (Riis 1996), and deposition of thick sedimentary layers offshore, in particular the Naust formation. This process is suggested as a cause of local subsidence and uplift along the coast, and a significant contributor to the local stress regime (e.g. Redfield & Osmundsen

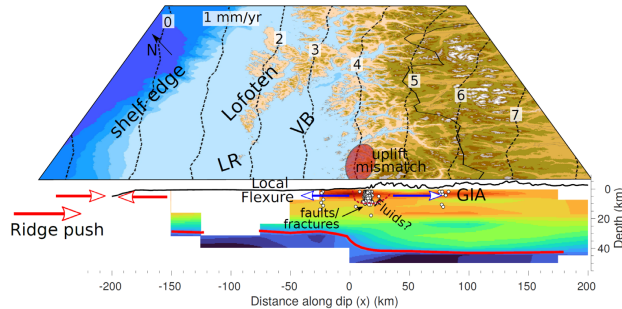


Figure 11. Sketch of the state of crustal stress in Nordland, overlain on the V_p model crossing the Jektvik area (extended E–E' section) (see Fig. 7 for the V_p colorscale). Red line is the Moho surface derived in this study. Red and blue arrows represent compressive and extensional regimes. White open circles are the earthquake hypocentres. The uplift rate contours from Vestøl *et al.* (2019) are shown as dashed black lines. Approximate area where the largest misfit between GNSS and the GIA uplift reported by Kierulf (2017) is shown as a red ellipse. See Fig. 2 for the bathymetry scale.

2014; Gradmann *et al.* 2018). However, the contribution of this sedimentation and GIA to the present day stress in the region is not well understood. Furthermore, Kierulf (2017) showed a discrepancy in the coast of Nordland between the uplift rate derived using GNSS observations and that derived using a best-fitting GIA model. Our 3-D velocity model can help to improve previous GIA and stress modelling efforts in Nordland.

Another possible contributor to an extensional stress regime is the gravitational potential energy (GPE) stress that arises from density differences within the lithosphere, for example crustal thickness difference, as well as topographical effect (Pascal & Cloetingh 2009). The seismicity in Nordland concentrates along the coast, which coincides with the location of the Moho step. We speculate that the 10–15 km difference of continental crust thickness affects the local stress via GPE. Pascal & Cloetingh (2009) modelled the GPE stress in southern Norway, which is mainly caused by lithospheric density variation, crustal thickness and topography. They suggested that thicker crust and higher topography in southern Norway have a significant contribution on the extension in the onshore region and compression in the coastal and offshore domains. The setting in Nordland is similar, which makes GPE a plausible factor that can influence the crustal stress. However, further modelling is needed to verify how significant their contribution is to the local crustal stress.

As discussed in the previous section, our results suggest the presence of water in the upper crust, near the locations of the Jektvik and Steigen swarms. Various observations have pointed to the importance of water in intraplate seismic swarm generation, for example in West Bohemia/Vogtland (Mousavi *et al.* 2015) and Kachchh rift (Kumar *et al.* 2017). There is no evidence for water migration from the deeper crust or mantle in this region. Alternatively, several studies have suggested that rainfall and surface water can trigger shallow seismicity (e.g. Hainzl *et al.* 2006; Bisrat *et al.* 2012; Craig *et al.* 2017), including in Nordland (Maystrenko *et al.* 2020a). However, in case of Nordland, this relation still needs to be verified with stress or hydrological modelling.

Whereas there may be explanations for the deviation from the regional compressive stress field, it is unclear how the system has changed with time and why the Nordland region remains critically stressed and thus near extensional failure. The effects of GIA may have resulted in an extensional setting after glaciation. The ridge push remains practically constant for the time frame considered

here and the tectonic processes that affected the crust and formed structures such as the Moho step, have not been active for several tens of millions of years. Yet, the Nordland region is seismically active in a manner that contrasts with what is expected from the regional stress field. It is possible that the erosion remains active and keeps the differential stresses high. The presence of fluids as suggested by our tomography model may play an important role in bringing the system to failure by reducing friction along the faults. In Norway, neither of these processes is unique to Nordland, but perhaps this combination can explain the high seismic activity of the area.

8 CONCLUSIONS

3-D V_p and V_p/V_s ratio models of the Nordland region were developed using seismic traveltimes tomography. These models then served as a basis to build a new seismicity catalogue and compute focal mechanisms. Our results provide important new insight into the crustal structure of the region and the causes of intraplate seismicity in Nordland.

The crustal thickness and seismic velocities inferred from our models were found to vary considerably across the study area. Below the Lofoten-Vesterålen islands, crustal thicknesses range from ~27 km in the south to ~35 km in the north. Between southern Lofoten and the mainland area, the crust thickens rather abruptly over a lateral distance of only ~25 km, forming a Moho step that runs parallel to the coast. The crust in the mainland part of Nordland is thicker, ranging from 40 to 47 km. The tomography images show low V_p and variable V_p/V_s ratio anomalies in the vicinity of the Steigen and Jektvik swarms, possibly indicating the existence of fractures and fluids in the upper crust.

To investigate the causes of seismicity, we considered our results in the context of local and regional stresses. In the coastal part of mainland Nordland, the stress regime exhibits coast-perpendicular extension, in contrast to the prevalent regional compressive stresses. We propose that the shallow crustal stress in Nordland is dominated by flexural stress due to sediment redistribution and GIA. The high seismicity area along the coast of Nordland coincides with the location of the Moho step. This is a possible indication that GPE can also contribute to the local stress here. Deformation localizes within pre-existing fault zones, which in some cases have been weakened by

fluids. This set of conditions leads to the occurrence of earthquakes and is favourable to the development of seismic swarms.

FUNDING

The study was supported by funding from the Research Council of Norway for the project 'IPSIN - Intraplate Seismicity in India and Norway: Distribution, properties and causes' (project 248815).

ACKNOWLEDGMENTS

We thank Richard England and Victoria Lane at SEIS-UK for providing us the seismic data for SCANLIPS3D (ZR) network. We acknowledge the operators of permanent and temporary seismic networks used in this study: NNSN (NS), NORSAR stations (NO), SNSN (UP), FNSN (HE), NEONOR2 (2G), ScanArray (1G), Scanlips2 (Y1) and Scanlips3D (ZR). The authors grateful for helpful discussions with Thomas Theunissen and Jhon Muñoz-Barrera of University of Bergen. We thank the editor Ian Bastow, an anonymous reviewer and Trine Dahl-Jensen for constructive comments on the manuscript.

DATA AVAILABILITY

Earthquake data catalogue from the Norwegian National Seismic Network (NNSN) (Ottmøller *et al.* 2018) with additional new phase picks processed in this study is available at NNSN webpage (<https://nnsn.geo.uib.no/nnsn/#/data/events/bulletins>). Seismic data from NNSN (network code: NS, Ottmøller *et al.* 2021), Norsar stations (NO, Schweitzer *et al.* 2021) and Neonor2 (2G, Michálek *et al.* 2018) are available at UiB-Norsar European Integrated Data Archive (EIDA) Node webpage (<https://nnsn.geo.uib.no/nnsn/#/data/waveforms/access>). Seismic data from SNSN (UP, Lund *et al.* 2021), FNSN (HE) (Veikkolainen *et al.* 2021) and ScanArray (1G, Thybo *et al.* 2021) networks are archived at the Observatories and Research Facilities for European Seismology (ORFEUS) EIDA (<http://www.orfeus-eu.org/data/eida/>, Strollo *et al.* 2021). Seismic data for Scanlips2 (Y1, https://www.fdsn.org/networks/detail/Y1_2007/) and Scanlips3D (ZR, England *et al.* 2016) network are archived at the Incorporated Research Institutions for Seismology (IRIS) Data Management Center (DMC, <http://ds.iris.edu/ds/nodes/dmc/>). Earthquake data were processed using Seisan earthquake analysis software (Havskov & Ottmøller 1999; Havskov *et al.* 2020) (<http://seisan.info/>). Figures in this paper were created using Generic Mapping Tools (Wessel *et al.* 2013), Matlab (<https://www.mathworks.com/products/matlab.html>), M_Map Matlab package (Pawlowicz 2020) (<https://www.eos.ubc.ca/~rich/map.html>) and Inkscape, a vector graphics editor (<https://inkscape.org/>). The hypocentre locations, focal mechanisms, velocity models and Moho surface depth generated in this study is available at Zenodo (<https://doi.org/10.5281/zenodo.5778841>).

REFERENCES

Altamimi, Z., Rebischung, P., Métivier, L. & Collilioux, X., 2016. ITRF2014: a new release of the International Terrestrial Reference Frame modeling nonlinear station motions, *J. geophys. Res.*, **121**(8), 6109–6131.

Arvidsson, R., 1996. Fennoscandian earthquakes: whole crustal rupturing related to postglacial rebound, *Science*, **274**(5288), 744–746.

Atakan, K., Lindholm, C.D. & Havskov, J., 1994. Earthquake swarm in Steigen, northern Norway: an unusual example of intraplate seismicity, *Terra Nova*, **6**(2), 180–194.

Crustal structure and seismicity in Nordland 827

Avedik, F., Berendsen, D., Fucke, H., Goldflam, S. & Hirschleber, H., 1984. Seismic investigations along the Scandinavian Blue Norma profile, *Ann. Geophys.*, **2**(5), 571–577.

Ben-Mansour, W., England, R.W., Fishwick, S. & Moorkamp, M., 2018. Crustal properties of the northern Scandinavian mountains and Fennoscandian shield from analysis of teleseismic receiver functions, *Geophys. J. Int.*, **214**(1), 386–401.

Bisrat, S., DeShon, H.R. & Rowe, C., 2012. Microseismic swarm activity in the New Madrid Seismic Zone, *Bull. seism. Soc. Am.*, **102**(3), 1167–1178.

Bleibinhaus, F., 2003. 3D Simultaneous Refraction and Reflection Seismic Travel Time Tomography and Application to Deep Seismic TRANSALP Wide-Angle Data, *PhD dissertation*, Ludwig-Maximilians-Universität, München, Germany.

Bleibinhaus, F. & Gebrande, H., 2006. Crustal structure of the Eastern Alps along the TRANSALP profile from wide-angle seismic tomography, *Tectonophysics*, **414**(1), 51–69.

Bleibinhaus, F. & Hilberg, S., 2012. Shape and structure of the Salzach Valley, Austria, from seismic traveltimes tomography and full waveform inversion, *Geophys. J. Int.*, **189**(3), 1701–1716.

Brantut, N. & David, E.C., 2018. Influence of fluids on VP/VS ratio: increase or decrease? *Geophys. J. Int.*, **216**(3), 2037–2043.

Brevik, A.J., Faleide, J.I., Mjelde, R., Flueh, E.R. & Murai, Y., 2017. A new tectono-magmatic model for the Lofoten/Vesterålen Margin at the outer limit of the Iceland Plume influence, *Tectonophysics*, **718**, 25–44.

Brevik, A.J., Faleide, J.I., Mjelde, R., Flueh, E.R. & Murai, Y., 2020. Crustal structure and erosion of the Lofoten/Vesterålen shelf, northern Norwegian margin, *Tectonophysics*, **776**, doi:10.1016/j.tecto.2020.228318.

Brønner, M., Gernigon, L. & Nasuti, A., 2013. Lofoten-Vestfjorden Aeromagnetic Survey 2011 – LOVAS-11 Acquisition, Processing and Interpretation report.

Bungum, H., Alsaker, A., Kvamme, L.B. & Hansen, R.A., 1991. Seismicity and seismotectonics of Norway and nearby continental shelf areas, *J. geophys. Res.*, **96**(B2), 2249–2265.

Bungum, H., Hokland, B.K., Husebye, E.S. & Ringdal, F., 1979. An exceptional intraplate earthquake sequence in Meløy, Northern Norway, *Nature*, **280**, 32–35.

Bungum, H. & Olesen, O., 2005. The 31st of August 1819 Luroy earthquake revisited, *Norveg. J. Geol.*, **(85)**, 245–252.

Bungum, H., Olesen, O., Pascal, C., Gibbons, S., Lindholm, C. & Vestøl, O., 2010. To what extent is the present seismicity of Norway driven by post-glacial rebound? *J. Geol. Soc.*, **167**(2), 373–384.

Bungum, H., Vaage, S. & Husebye, E.S., 1982. The Meløy earthquake sequence, northern Norway: source parameters and their scaling relations, *Bull. seism. Soc. Am.*, **72**(1), 197–206.

Cherevatova, M. *et al.*, 2015. Magnetotelluric array data analysis from north-west Fennoscandia, *Tectonophysics*, **653**, 1–19.

Corfu, F., Andersen, T.B. & Gasser, D., 2014. The Scandinavian Caledonides: main features, conceptual advances and critical questions, *Geol. Soc., Lond., Spec. Publ.*, **390**(1), 9–43.

Craig, T.J., Chanard, K. & Calais, E., 2017. Hydrologically-driven crustal stresses and seismicity in the New Madrid Seismic Zone, *Nat. Commun.*, **8**, doi:10.1038/s41467-017-0196-w.

Demuth, A., Ottmøller, L. & Keers, H., 2019. QLg wave tomography beneath Norway, *J. Seismol.*, **23**, 151–164.

Diehl, T., Husen, S., Kissling, E. & Deichmann, N., 2009. High-resolution 3-D P-wave model of the Alpine crust, *Geophys. J. Int.*, **179**(2), 1133–1147.

Ekström, G., Nettles, M. & Dziewionowski, A., 2012. The global CMT project 2004–2010: centroid-moment tensors for 13,017 earthquakes, *Phys. Earth planet. Inter.*, **200–201**, 1–9.

Eldholm, O. & Grue, K., 1994. North Atlantic volcanic margins: dimensions and production rates, *J. geophys. Res.*, **99**(B2), 2955–2968.

Ellsworth, W.L., 1978. Three-dimensional structure of the crust and mantle beneath the island of Hawaii, *PhD dissertation*, Dept. of Earth and Planetary Sciences, Massachusetts Institute of Technology, Cambridge, MA.

England, R.W., Ebbing, J. & Ben-Mansour, W., 2016. SCANLIPS3D: SCANDinavian Lithosphere P and S wave experiment

- 3D instrument loan report, NERC Geophysical Equipment Facility, <http://gef.nerc.ac.uk/reports.php>.
- Evans, D., McGiveron, S., McNeill, A., Harrison, Z., Østmo, S. & Wild, J., 2000. Plio-Pleistocene deposits on the mid-Norwegian margin and their implications for late Cenozoic uplift of the Norwegian mainland, *Global Planet. Change*, **24**(3), 233–237.
- Evans, J., Eberhart-Phillips, D. & Thurber, C., 1994. User's manual for SIMULP512 for imaging Vp and Vp/Vs: a derivative of the Thurber tomographic inversion SIMUL3 for local earthquakes and explosions, U.S. Geological Survey Open File Report 94–431.
- Faleide, J.I., Tsikalas, F., Breivik, A.J., Mjelde, R., Ritzmann, O., Øyvind, E., Wilson, J. & Eldholm, O., 2008. Structure and evolution of the continental margin off Norway and the Barents Sea, *Episodes*, **31**(1), 82–91.
- Fejerskov, M. & Lindholm, C., 2000. Crustal stress in and around Norway: an evaluation of stress-generating mechanisms, *Geol. Soc., Lond., Spec. Publ.*, **167**(1), 451–467.
- Fjeldskaar, W., Lindholm, C., Dehls, J.F. & Fjeldskaar, I., 2000. Postglacial uplift, neotectonics and seismicity in Fennoscandia, *Quater. Sci. Rev.*, **19**(14), 1413–1422.
- Fossen, H., 2010. Extensional tectonics in the North Atlantic Caledonides: a regional view, in *Continental Tectonics and Mountain Building: The Legacy of Peach and Horne*, Geological Society of London.
- Geological Survey of Norway, 2011. *Nasjonal berggrunnsdatabase*.
- Gradmann, S. & Ebbing, J., 2015. Large-scale gravity anomaly in northern Norway: tectonic implications of shallow or deep source depth and a possible conjugate in northeast Greenland, *Geophys. J. Int.*, **203**(3), 2070–2088.
- Gradmann, S., Haase, C. & Ebbing, J., 2017. Isostasy as a tool to validate interpretations of regional geophysical datasets – application to the mid-Norwegian continental margin, *Geol. Soc., Lond., Spec. Publ.*, **447**(1), 279–297.
- Gradmann, S., Olesen, O., Keiding, M. & Maystrenko, Y., 2018. The Regional 3D Stress Field of Nordland, Northern Norway - Insights from Numerical Modelling, chap. Neotectonics in Nordland - Implications for petroleum exploration (NEONOR2), Geological Survey of Norway, Trondheim.
- Hainzl, S., Kraft, T., Wassermann, J., Igel, H. & Schmedes, E., 2006. Evidence for rainfall-triggered earthquake activity, *Geophys. Res. Lett.*, **33**(19).
- Halpaap, F., Rondenay, S. & Ottemöller, L., 2018. Seismicity, deformation, and metamorphism in the Western Hellenic Subduction Zone: new constraints from tomography, *J. geophys. Res.*, **123**(4), 3000–3026.
- Halpaap, F., Rondenay, S., Perrin, A., Goes, S., Ottemöller, L., Austrheim, H., Shaw, R. & Eeken, T., 2019. Earthquakes track subduction fluids from slab source to mantle wedge sink, *Sci. Adv.*, **5**(4), doi:10.1126/sciadv.aav7369.
- Hardebeck, J.L. & Shearer, P.M., 2002. A new method for determining first-motion focal mechanisms, *Bull. seism. Soc. Am.*, **92**(6), 2264–2276.
- Havskov, J. & Bungum, H., 1987. Source parameters for earthquakes in the northern North Sea, *Norsk Geologisk Tidsskrift*, **67**, 51–58.
- Havskov, J. & Ottemöller, L., 1999. Seisan earthquake analysis software, *Seismol. Res. Lett.*, **70**(5), 532–534.
- Havskov, J. & Ottemöller, L., 2010. *Routine Data Processing in Earthquake Seismology: With Sample Data, Exercises and Software*, Springer.
- Havskov, J., Voss, P.H. & Ottemöller, L., 2020. Seismological observatory software: 30 Yr of SEISAN, *Seismol. Res. Lett.*, **91**(3), 1846–1852.
- Hicks, E.C., Bungum, H. & Lindholm, C.D., 2000a. Seismic activity, inferred crustal stresses and seismotectonics in the Rana region, Northern Norway, *Quater. Sci. Rev.*, **19**(14), 1423–1436.
- Hicks, E.C., Bungum, H. & Lindholm, C.D., 2000b. Stress inversion of earthquake focal mechanism solutions from onshore and offshore Norway, *Norsk Geologisk Tidsskrift*, **80**(4), 235–250.
- Horn, J.A. et al., 2017. Regional distribution of volcanism within the North Atlantic Igneous Province, *Geol. Soc., Lond., Spec. Publ.*, **447**(1), 105–125.
- Husen, S., Kissling, E. & Clinton, J., 2011. Local and regional minimum 1D models for earthquake location and data quality assessment in complex tectonic regions: application to Switzerland, *Swiss J. Geosci.*, **104**, 455–469.
- Husen, S., Kissling, E., Deichmann, N., Wiemer, S., Giardini, D. & Baer, M., 2003. Probabilistic earthquake location in complex three-dimensional velocity models: application to Switzerland, *J. geophys. Res.*, **108**(B2), doi:10.1029/2002JB001778.
- Janutyte, I., Lindholm, C. & Olesen, O., 2017a. Relation between seismicity and tectonic structures offshore and onshore Nordland, northern Norway, *Norveg. J. Geol.*, **97**(3), 211–225.
- Janutyte, I., Lindholm, C. & Olesen, O., 2017b. Earthquake source mechanisms in onshore and offshore Nordland, northern Norway, *Norveg. J. Geol.*, **97**(3), 227–239.
- Keiding, M., Kreemer, C., Lindholm, C., Gradmann, S., Olesen, O. & Kierulf, H., 2015. A comparison of strain rates and seismicity for Fennoscandia: depth dependency of deformation from glacial isostatic adjustment, *Geophys. J. Int.*, **202**(2), 1021–1028.
- Kierulf, H.P., 2017. Analysis strategies for combining continuous and episodic GNSS for studies of neo-tectonics in Northern-Norway, *J. Geodyn.*, **109**, 32–40.
- Kissling, E., 1995. *Velost user's guide*, Institute of Geophysics, ETH Zuerich, pp. 1–26.
- Kissling, E., Ellsworth, W.L., Eberhart-Phillips, D. & Kradolfer, U., 1994. Initial reference models in local earthquake tomography, *J. geophys. Res.*, **99**(B10), 19 635–19 646.
- Klein, F., 2002. User's Guide to HYPOINVERSE-2000, a Fortran program to solve for earthquake locations and magnitudes, U.S. Geological Survey Open File Report 02–171.
- Koulakov, I., 2009. Out-of-network events can be of great importance for improving rResults of local earthquake tomography, *Bull. seism. Soc. Am.*, **99**(4), 2556–2563.
- Koulakov, I., Maksotova, G., Mukhopadhyay, S., Raoof, J., Kayal, J.R., Jakovlev, A. & Vasilevsky, A., 2015. Variations of the crustal thickness in Nepal Himalayas based on tomographic inversion of regional earthquake data, *Solid Earth*, **6**(1), 207–216.
- Kumar, G.P., Mahesh, P., Nagar, M., Mahender, E., Kumar, V., Mohan, K. & Ravi Kumar, M., 2017. Role of deep crustal fluids in the genesis of intraplate earthquakes in the Kachchh region, northwestern India, *Geophys. Res. Lett.*, **44**(9), 4054–4063.
- Kuo-Chen, H., Wu, F.T., Jenkins, D.M., Mechie, J., Roecker, S.W., Wang, C.-Y. & Huang, B.-S., 2012. Seismic evidence for the - quartz transition beneath Taiwan from Vp/Vs tomography, *Geophys. Res. Lett.*, **39**(22), doi:10.1029/2012GL053649.
- Lange, D., Tilmann, F., Henstock, T., Rietbrock, A., Natawidjaja, D. & Kopp, H., 2018. Structure of the central Sumatran subduction zone revealed by local earthquake travel-time tomography using an amphibious network, *Solid Earth*, **9**(4), 1035–1049.
- Laske, G., Masters, G., Ma, Z. & Pasyanos, M., 2013. Update on CRUST1.0 - a 1-degree Global Model of Earth's Crust, in *EGU General Assembly Conference Abstracts*, Vol. **15**, pp. EGU2013–2658.
- Leónios, S. et al., 2021. 3D local earthquake tomography of the Ecuadorian margin in the source area of the 2016 Mw 7.8 Pedernales earthquake, *J. geophys. Res.*, **126**(3), e2020JB020701, doi:10.1029/2020JB020701.
- Lienert, B.R. & Havskov, J., 1995. A computer program for locating earthquakes both locally and globally, *Seismol. Res. Lett.*, **66**(5), 26–36.
- Lin, G. & Shearer, P.M., 2009. Evidence for water-filled cracks in earthquake source regions, *Geophys. Res. Lett.*, **36**(17), doi:10.1029/2009GL039098.
- Lindblom, E., 2011. Microearthquake study of end-glacial faults in Northern Sweden, *PhD dissertation*, Uppsala University.
- Lund, B., Schmidt, P., Hossein Shomali, Z. & Roth, M., 2021. The Modern Swedish National Seismic Network: two decades of intraplate microseismic observation, *Seismol. Res. Lett.*, **92**(3), 1747–1758.
- Mäntyniemi, P.B., Sørensen, M.B., Tatevossian, T.N., Tatevossian, R.E. & Lund, B., 2020. A reappraisal of the Luroy, Norway, earthquake of 31 August 1819, *Seismol. Res. Lett.*, **91**(5), doi:10.1785/0220190363.
- Mauerberger, A., Maupin, V., Sadeghshorkhani, H., Gudmundsson, O. & Tilmann, F., 2020. Scandinavian lithosphere structure derived from surface waves and ambient noise, in *EGU General Assembly Conference Abstracts*, pp. EGU2020–8366.

- Maystrenko, Y., Brønner, M., Olesen, O., Saloranta, T.M. & Slagstad, T., 2020a. Atmospheric precipitation and anomalous upper mantle in relation to intraplate seismicity in Norway, *Tectonics*, **39**(9), e2020TC006070, doi:10.1029/2020TC006070.
- Maystrenko, Y., Gernigon, L. & Olesen, O., 2020b. Comment on “Crustal structure and erosion of the Lofoten/Vesterålen shelf, northern Norwegian margin. *Tectonophysics* 776, 228318” by A.J. Breivik, J.I. Faleide, R. Mjelde, E.R. Flueh, Y. Murai, *Tectonophysics*, **793**, 228605, doi:10.1016/j.tecto.2020.228605.
- Maystrenko, Y., Olesen, O., Gernigon, L. & Gradmann, S., 2017. Deep structure of the Lofoten-Vesterålen segment of the Mid-Norwegian continental margin and adjacent areas derived from 3-D density modeling, *J. geophys. Res.*, **122**(2), 1402–1433.
- Michálek, J., Tjåland, N., Drottning, A., Stromme, M.L., Storheim, B.M., Rondenay, S. & Ottemöller, L., 2018. Report on seismic observations within the NEONOR2 project in the Nordland region, Norway (Aug. 2013–May 2016), chap. Neotectonics in Nordland - Implications for petroleum exploration (NEONOR2), Geological Survey of Norway, Trondheim.
- Midzi, V., Saunders, I., Brandt, M. B.C. & Molea, T., 2010. 1-D Velocity Model for Use by the SANSN in Earthquake Location, *Seismol. Res. Lett.*, **81**(3), 460–466.
- Mjelde, R. *et al.*, 1998. Crustal structure of the northern part of the Vøring Basin, mid-Norway margin, from wide-angle seismic and gravity data, *Tectonophysics*, **293**(3), 175–205.
- Mjelde, R., Goncharov, A. & Müller, R.D., 2013. The Moho: boundary above upper mantle peridotites or lower crustal eclogites? A global review and new interpretations for passive margins, *Tectonophysics*, **609**, 636–650.
- Mjelde, R., Kvarven, T., Faleide, J.I. & Thybo, H., 2016. Lower crustal high-velocity bodies along North Atlantic passive margins, and their link to Caledonian suture zone eclogites and Early Cenozoic magmatism, *Tectonophysics*, **670**, 16–29.
- Mjelde, R. & Sellevoll, M.A., 1993. Possible shallow crustal shear wave anisotropy off Lofoten, Norway, inferred from three-component ocean-bottom seismographs, *Geophys. J. Int.*, **115**(1), 159–167.
- Mjelde, R., Sellevoll, M.A., Shimamura, H., Iwasaki, T. & Kanazawa, T., 1993. Crustal structure beneath Lofoten, N. Norway, from vertical incidence and wide-angle seismic data, *Geophys. J. Int.*, **114**(1), 116–126.
- Mousavi, S., Bauer, K., Korn, M. & Hejrani, B., 2015. Seismic tomography reveals a mid-crustal intrusive body, fluid pathways and their relation to the earthquake swarms in West Bohemia/Vogtland, *Geophys. J. Int.*, **203**(2), 1113–1127.
- Muir-Wood, R., 1989. The Scandinavian earthquakes of 22 December 1759 and 31 August 1819, *Disasters*, **12**(3), 223–236.
- Newkirk, K., Shiddiqi, H.A., Jerkins, A.E., Keers, H. & Ottemöller, L., 2019. Implications of 3D Seismic Raytracing on Focal Mechanism Determination *Bull. Seism. Soc. Am.*, **109**(6).
- Olesen, O. *et al.*, 2010. Gravity anomaly map, Norway and adjacent areas; Scale 1:3 mill, Geological Survey of Norway.
- Olesen, O., Lundin, E., Nordgulen, O., Osmundsen, P., Skilbrei, J., Smethurst, M., Solli, A., Bugge, T. & Fichler, C., 2002. Bridging the gap between onshore and offshore geology in Nordland, northern Norway, *Norweg. J. Geol.*, **82**(4), 243–262.
- Ottmøller, L., Michálek, J., Christensen, J., Baadshaug, U., Halpaap, F., Natvik, y., Kvarnø, T. & Oye, V., 2021. UiB-NORSAR EIDA node: integration of seismological data in Norway, *Seismol. Res. Lett.*, **92**(3), 1491–1500.
- Ottmøller, L. & Midzi, V., 2003. The crustal structure of Norway from inversion of teleseismic receiver functions, *J. Seismol.*, **7**, 35–48.
- Ottmøller, L., Stromme, M.L. & Storheim, B.M., 2018. Seismic monitoring and data processing at the Norwegian National Seismic Network, in *Summary of the Bulletin of the International Seismological Centre 2015 January–June*, **51**(1), ed. Lieser, K., Harris, J. & Storchak, D., International Seismological Centre.
- Pascal, C. & Cloetingh, S.A., 2009. Gravitational potential stresses and stress field of passive continental margins: insights from the south-Norway shelf, *Earth planet. Sci. Lett.*, **277**(3), 464–473.
- Pawlowicz, R., 2020. M_Map: A mapping package for MATLAB (Computer software), <https://www.coas.ubc.ca/~rich/map.html>.
- Redfield, T.F. & Osmundsen, P.T., 2014. Some remarks on the earthquakes of Fennoscandia: a conceptual seismological model drawn from the perspective of hyperextension, *Norweg. J. Geol.*, **9**, 233–262.
- Rietbrock, A., 1996. Entwicklung eines Programmsystems zur konsistenten Auswertung großer seismologischer Datensätze mit Anwendung auf die Untersuchung der Absorptionsstruktur der Loma-Prieta-Region, Kalifornien, *PhD dissertation*, Ludwig-Maximilians-Universität, München, Germany.
- Riis, F., 1996. Quantification of Cenozoic vertical movements of Scandinavia by correlation of morphological surfaces with offshore data, *Global planet. Change*, **12**(1), 331–357.
- Rise, L., Ottesen, D., Berg, K. & Lundin, E., 2005. Large-scale development of the mid-Norwegian margin during the last 3 million years, *Mar. Petrol. Geol.*, **22**(1), 33–44.
- Schulte, S.M. & Mooney, W.D., 2005. An updated global earthquake catalogue for stable continental regions: reassessing the correlation with ancient rifts, *Geophys. J. Int.*, **161**(3), 707–721.
- Schweitzer, J., Köhler, A. & Christensen, J.M., 2021. Development of the NORSAR network over the last 50 Yr, *Seismol. Res. Lett.*, **92**(3), 1501–1511.
- Sellevoll, M., 1983. A study of the earth's crust in the island area of Lofoten-Vesterålen, Northern Norway, *Norsk Geologisk Tidsskrift*, **380**, 235–243.
- Shearer, P.M., 1988. Cracked media, Poisson's ratio and the structure of the upper oceanic crust, *Geophys. J. Int.*, **92**(2), 357–362.
- Shiddiqi, H.A., Tun, P.P. & Ottemöller, L., 2019. Minimum 1D velocity model and local magnitude scale for Myanmar, *Seismol. Res. Lett.*, **90**(5), 1923–1936.
- Snoke, J.A., 2003. FOCMEC: focal mechanism determinations, in *International Handbook of Earthquake and Engineering Seismology*, Chapter 85.12, pp. 1629–1630, eds Lee, W., Jennings, P., Kisslinger, C. & Kanamori, H., Academic Press.
- Steffen, H. & Kaufmann, G., 2005. Glacial isostatic adjustment of Scandinavia and northwestern Europe and the radial viscosity structure of the Earth's mantle, *Geophys. J. Int.*, **163**(2), 801–812.
- Strollo, A. *et al.*, 2021. EIDA: the European integrated data archive and service infrastructure within ORFEUS, *Seismol. Res. Lett.*, **92**(3), 1788–1795.
- Takei, Y., 2002. Effect of pore geometry on VP/VS: From equilibrium geometry to crack, *J. geophys. Res.*, **107**(B2), ECV6-1-ECV6-12.
- Takemura, S., Shiomi, K., Kimura, T. & Saito, T., 2016. Systematic difference between first-motion and waveform-inversion solutions for shallow offshore earthquakes due to a low-angle dipping slab, *Earth Planet Sp.*, **68**(149) 1–8.
- Thurber, C.H., 1983. Earthquake locations and three-dimensional crustal structure in the Coyote Lake Area, central California, *J. geophys. Res.*, **88**(B10), 8226–8236.
- Thurber, C.H. & Eberhart-Phillips, D., 1999. Local earthquake tomography with flexible gridding, *Comp. Geosci.*, **25**(7), 809–818.
- Thybo, H. *et al.*, 2021. ScanArray—a broadband seismological experiment in the Baltic Shield, *Seismol. Res. Lett.*, **92**(5), 2811–2823.
- Tozer, B., Sandwell, D.T., Smith, W.H.F., Olson, C., Beale, J.R. & Wessel, P., 2019. Global bathymetry and topography at 15 arc sec: SRTM15+, *Earth Space Sci.*, **6**(10), 1847–1864.
- Tsikalas, F., Eldholm, O. & Faleide, J.I., 2005. Crustal structure of the Lofoten–Vesterålen continental margin, off Norway, *Tectonophysics*, **404**(3), 151–174.
- Tsikalas, F., Faleide, J.I. & Eldholm, O., 2001. Lateral variations in tectono-magmatic style along the Lofoten–Vesterålen volcanic margin off Norway, *Mar. Petrol. Geol.*, **18**(7), 807–832.
- Unsworth, M. & Bedrosian, P., 2004. Electrical Resistivity structure at the SAFOD site from magnetotelluric exploration, *Geophys. Res. Lett.*, **31**, 12–5.
- Unsworth, M. & Rondenay, S., 2013. *Mapping the Distribution of Fluids in the Crust and Lithospheric Mantle Utilizing Geophysical Methods*, pp. 535–598, Springer Berlin Heidelberg.
- Veikkolainen, T. *et al.*, 2021. The Finnish National Seismic Network: toward fully automated analysis of low-magnitude seismic events, *Seismol. Res. Lett.*, **92**(3), 1581–1591.

830 H.A. Shiddiqi et al.

- Vestol, O., Ågren, J., Steffen, H., Kierulf, H. & Tarasov, L., 2019. NKG2016LU: a new land uplift model for Fennoscandia and the Baltic Region, *J. Geod.*, **93**, 1759–1779.
- Wang, Q. & Ji, S., 2009. Poisson's ratios of crystalline rocks as a function of hydrostatic confining pressure, *J. geophys. Res.*, **114**(B9), doi:10.1029/2008JB006167.
- Wessel, P., Smith, W.H.F., Scharroo, R., Luis, J. & Wobbe, F., 2013. Generic mapping tools: improved version released, *EOS, Trans. Am. Geophys. Un.*, **94**(45), 409–410.
- Wright, C., 2008. Station corrections for the Kaapvaal seismic network: Statistical properties and relation to lithospheric structure, *Phys. Earth planet. Inter.*, **167**(1), 39–52.
- Wu, P. & Hasegawa, H.S., 1996. Induced stresses and fault potential in eastern Canada due to a disc load: a preliminary analysis, *Geophys. J. Int.*, **125**(2), 415–430.

SUPPORTING INFORMATION

Supplementary data are available at [GJI](https://doi.org/10.1093/gji/ggk001) online.

Figure S1. Ray path distribution from NNSN data set (a) and ray path distribution from the final data set used in this study (b). Ray paths are shown as grey lines. Earthquake locations and stations are shown as circles coloured with depth and blue inverted triangles, respectively. Location of Kvannevaan mine is shown as the black stars.

Figure S2. Final ray path distribution (blue lines) and fine inversion grid nodes (black circles) in map view as well as along strike and dip sections. The central coordinate ($X = 0$ km, $Y = 0$ km) of the tomography model (shown as the green star) is 67.5°N , and 14.5°E , and the coordinate system is rotated 35° clockwise. Stations are shown as red inverted triangles.

Figure S3. Moho step test showing the synthetic model (left-hand panel) and the inversion result (right-hand panel). The synthetic model is created by combining two 1-D V_p models with a shallower Moho in the west and a deeper Moho in the east. This test was performed to demonstrate that our inversion can actually recover the Moho step feature in Nordland. The hypocentres are shown as white circles. The solid red lines are the ‘Moho velocity’ contour ($V_p = 7.6$ km s $^{-1}$).

Figure S4. Smooth Moho test showing the synthetic model (left-hand panel) and the inversion result (right-hand panel). The synthetic model is created by using two 1-D V_p with smooth transition. This test aimed to demonstrate that the Moho step is not an artefact created by the inversion set-up. The hypocentres are shown as white circles. The solid red lines are the ‘Moho velocity’ contour ($V_p = 7.6$ km s $^{-1}$).

Figure S5. Coast perpendicular cross-sections showing the ray path distribution (black dots) for observations used in the 3-D velocity inversion. Red lines are the contour of the ‘Moho velocity’ ($V_p = 7.6$ km s $^{-1}$). White circles represent the earthquake locations. Surface topography (with $4\times$ vertical exaggeration) are also plotted on the top of each sections.

Figure S6. Synthetic test to evaluate whether the Moho step (black lines) creates an artificial anomaly or not. The test includes (a) constant V_p/V_S ratio with higher random noise, (b) low V_p/V_S ratio in the lower crust of the offshore and (c) high V_p/V_S ratio in the upper crust of the mainland area. This test shows that our inversion set-up does not create artificial anomaly near the Moho step.

Figure S7. 1-D V_p and V_S models derived using six starting models, which used three Moho depths: 35, 40 and 45 km. The preferred 1-D model is the Crust1.0 based model with 40 km Moho depth.

Figure S8. P -wave station delays for six 1-D velocity models in Fig. S7. All delays are relative to the reference station.

Figure S9. Comparison of hypocentres in Steigen area determined using four velocity model (1-D, 3-D coarse, 3-D medium and 3-D fine models).

Figure S10. Comparison of hypocentres in Jektvik area determined using four velocity model (1-D, 3-D coarse, 3-D medium and 3-D fine models).

Figure S11. V_p and V_p/V_S ratio for coast parallel cross-sections. Red lines are the contour of the ‘Moho velocity’ ($V_p = 7.6$ km s $^{-1}$), and the dashed black lines is the Moho model compiled by Maystrenko *et al.* (2017). Hypocentre and stations are represented by white circles and black triangles, respectively. Surface topography (with $4\times$ vertical exaggeration) are plotted on the top of each cross-section. The inversion grids are plotted in V_p/V_S ratio sections.

Figure S12. Horizontal slices for V_p and V_p/V_S ratio in the middle and lower crustal depth. Earthquakes and stations are shown as red circles and open inverted triangles.

Figure S13. Comparison between focal mechanism solutions computed using 1-D velocity model (left-hand panel) and solutions computed using 3-D velocity model. Nodal lines represent all possible solutions that fit with the observations. Position of polarities and amplitude ratios are plotted within the lower hemisphere projection. Compression and dilatation polarities are shown as open circles and open triangles, respectively, and amplitude ratios are plotted as H symbols.

Please note: Oxford University Press is not responsible for the content or functionality of any supporting materials supplied by the authors. Any queries (other than missing material) should be directed to the corresponding author for the paper.

**Supporting Information for”Crustal structure and
intraplate seismicity in Nordland, Northern Norway:
Insight from Seismic Tomography”**

**Hasbi Ash Shiddiqi¹, Lars Ottemöller¹, Stéphane Rondenay¹, Felix Halpaap¹,
Sofie Gradmann²and Jan Michálek¹**

¹Department of Earth Science, University of Bergen, Bergen, Norway

²Geological Survey of Norway, Trondheim, Norway

Contents

1. Figure S1 - Figure S13

Corresponding author: Hasbi Ash Shiddiqi, hasbi.shiddiqi@uib.no

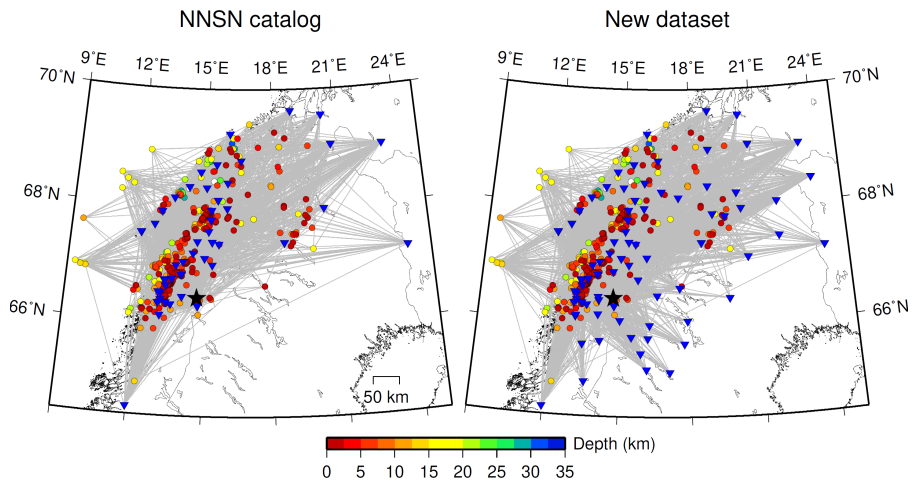


Figure S1. Ray-path distribution from NNSN dataset (a) and ray-path distribution from the final dataset used in this study (b). Ray-paths are shown as gray lines. Earthquake locations and stations are shown as circles colored with depth and blue inverted triangles, respectively. Location of Kvannevang mine is shown as the black stars.

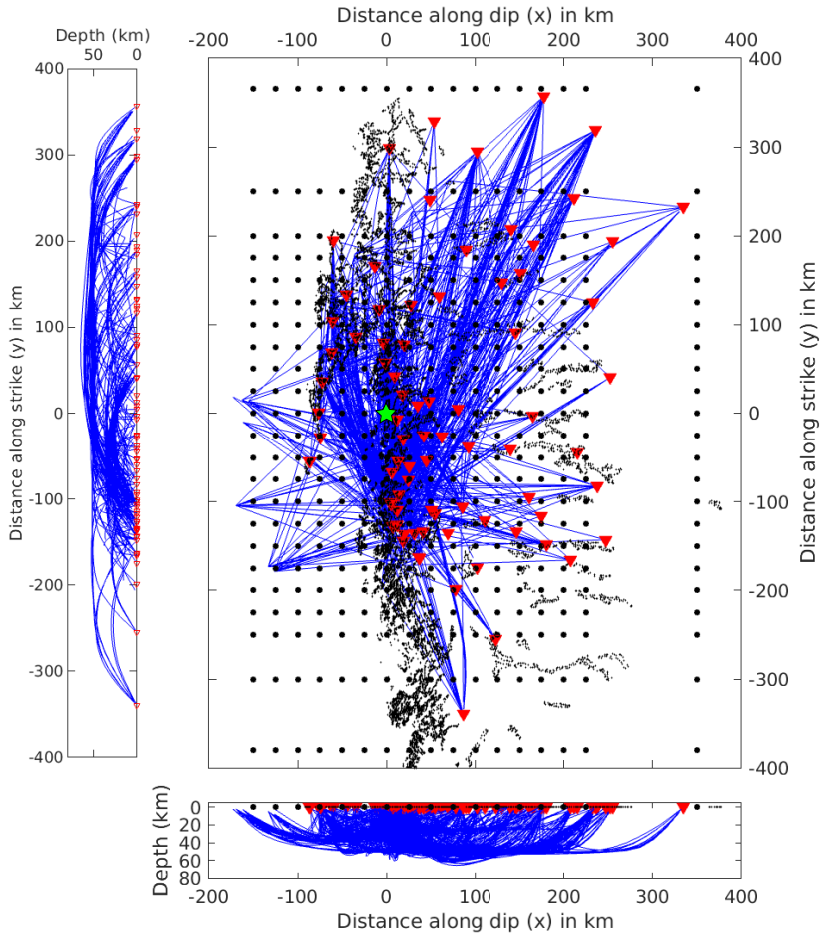


Figure S2. Final ray-path distribution (blue lines) and fine inversion grid nodes (black circles) in map view as well as along strike and dip sections. The central coordinate ($X=0$ km, $Y=0$ km) of the tomography model (shown as the green star) is 67.5° N, and 14.5° E, and the coordinate system is rotated 35° clockwise. Stations are shown as red inverted triangles.

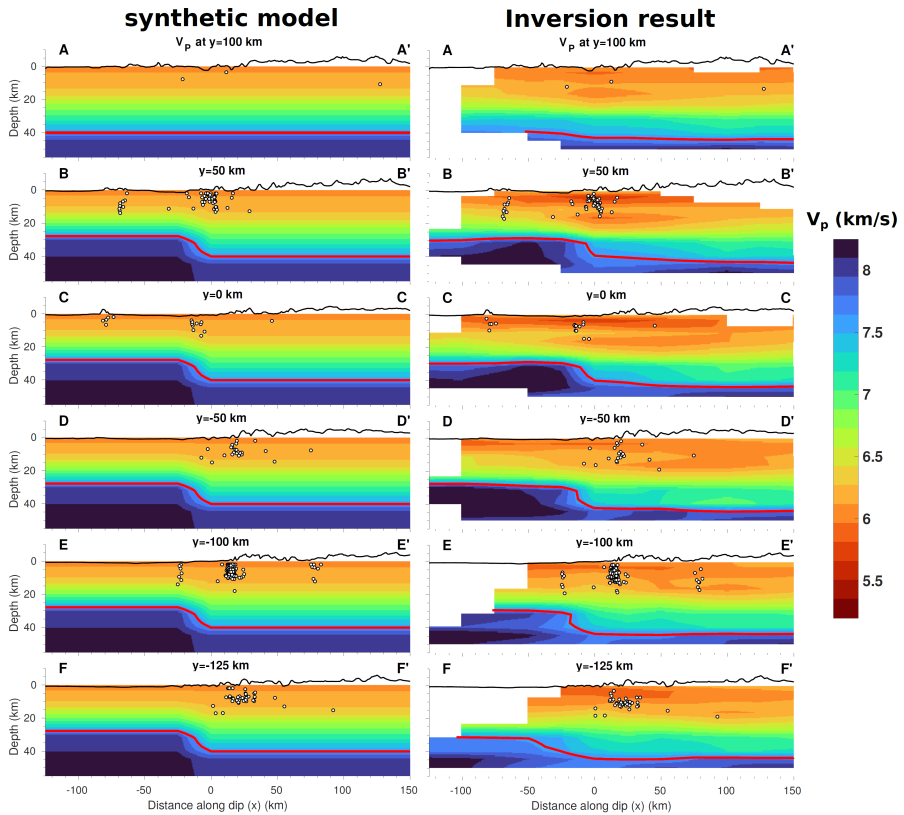


Figure S3. Moho step test showing the synthetic model (left) and the inversion result (right). The synthetic model is created by combining two 1-D V_P models with a shallower Moho in the west and a deeper Moho in the east. This test was performed to demonstrate that our inversion can actually recover the Moho step feature in Nordland. The hypocenters are shown as white circles. The solid red lines are the "Moho velocity" contour ($V_P = 7.6$ km/s).

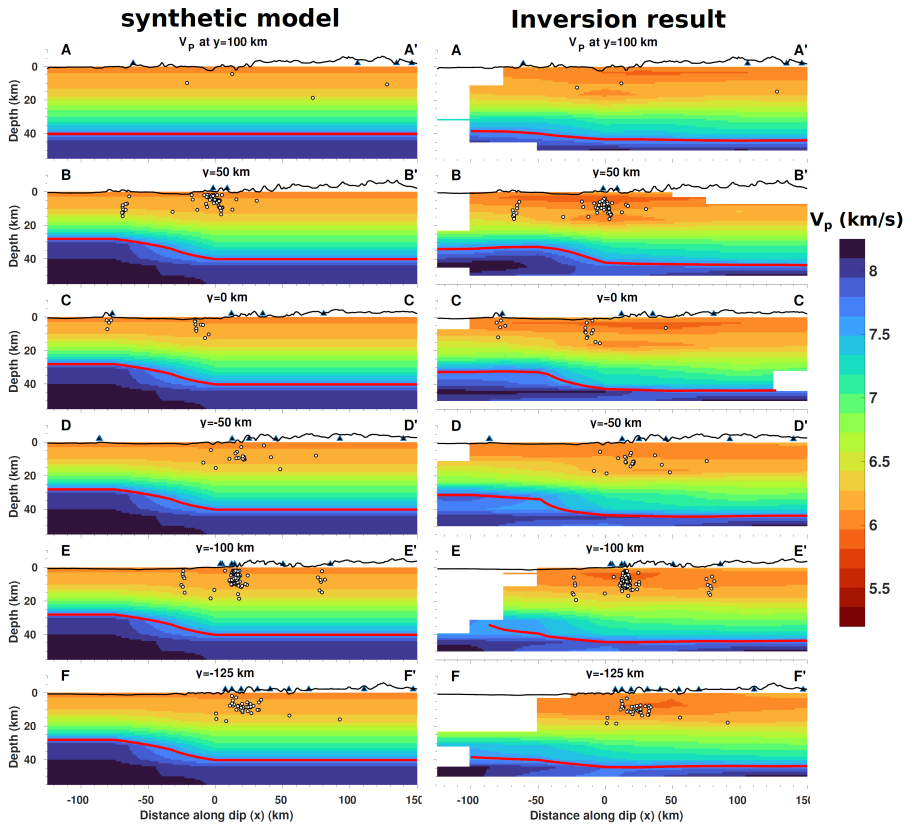


Figure S4. Smooth Moho test showing the synthetic model (left) and the inversion result (right). The synthetic model is created by using two 1-D V_P with smooth transition. This test aimed to demonstrate that the Moho step is not an artifact created by the inversion setup. The hypocenters are shown as white circles. The solid red lines are the "Moho velocity" contour ($V_P = 7.6$ km/s).

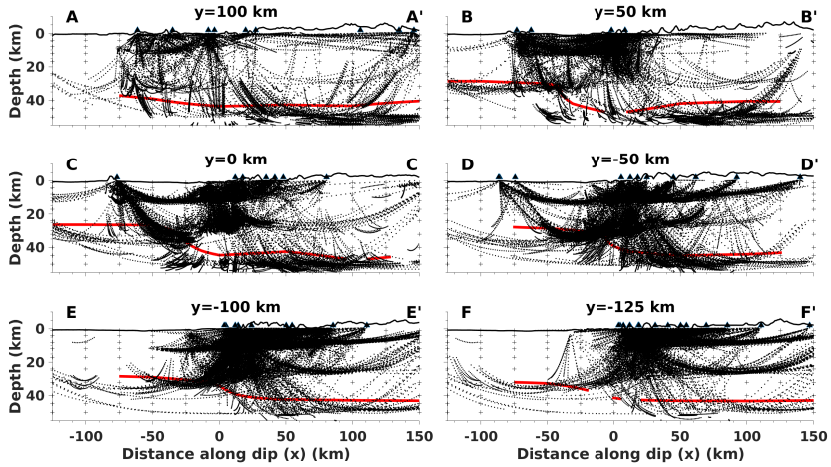


Figure S5. Coast perpendicular cross-sections showing the ray-path distribution (black dots) for observations used in the 3-D velocity inversion. Red lines are the contour of the "Moho velocity" ($V_P = 7.6$ km/s). White circles represent the earthquake locations. Surface topography (with 4x vertical exaggeration) are also plotted on the top of each sections.

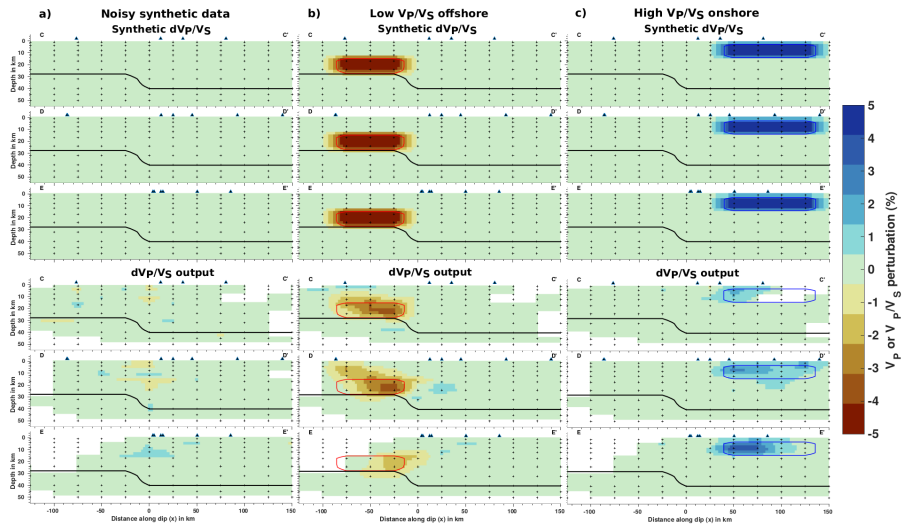


Figure S6. Synthetic test to evaluate whether the Moho step (black lines) creates an artificial anomaly or not. The test includes a) constant V_P/V_S ratio with higher random noise, b) low V_P/V_S ratio in the lower crust of the offshore, c) high V_P/V_S ratio in the upper crust of the mainland area. This test shows that our inversion setup does not create artificial anomaly near the Moho step.

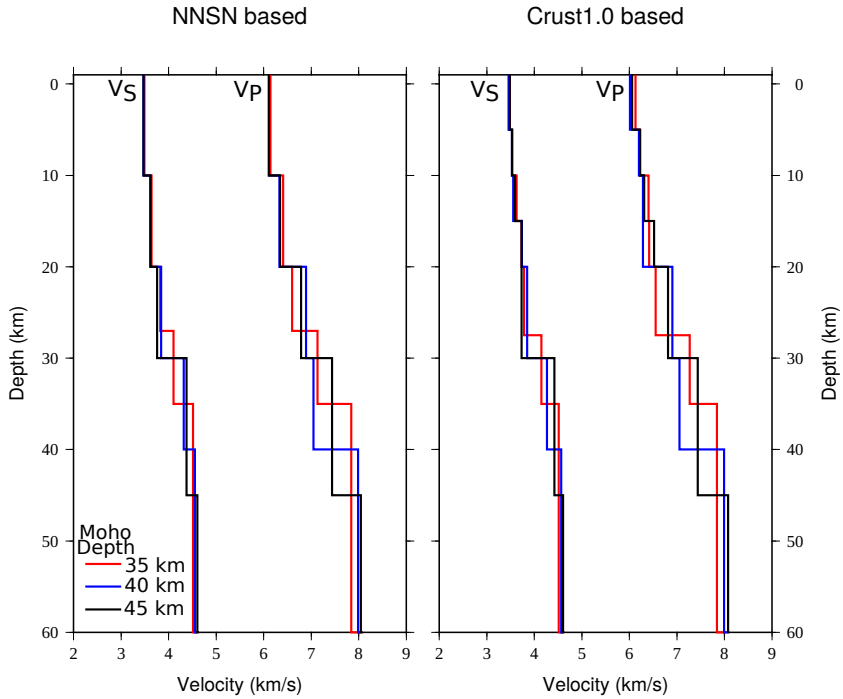


Figure S7. 1-D V_P and V_S models derived using six starting models, which used three Moho depths: 35, 40, and 45 km. The preferred 1-D model is the Crust1.0 based model with 40 km Moho depth.

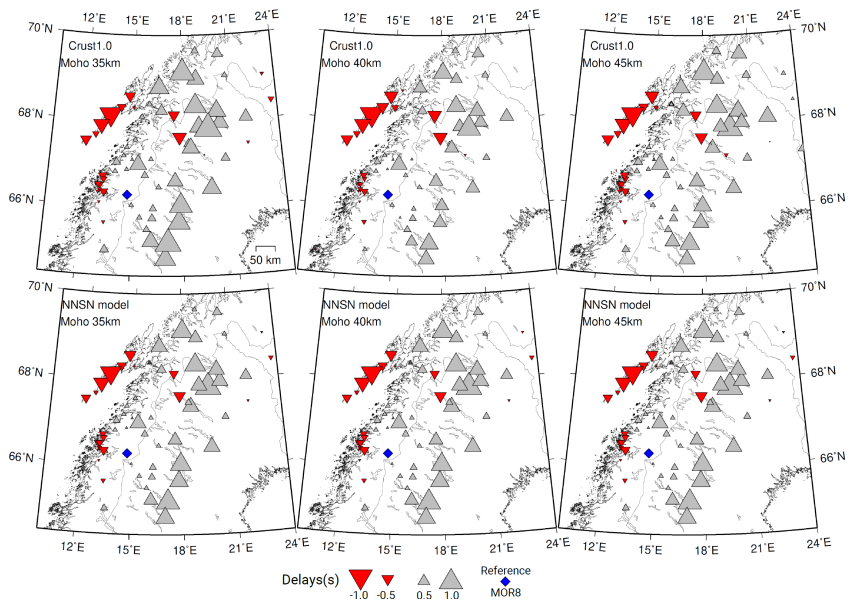


Figure S8. P-wave station delays for six 1-D velocity models in Fig. S7. All delays are relative to the reference station.

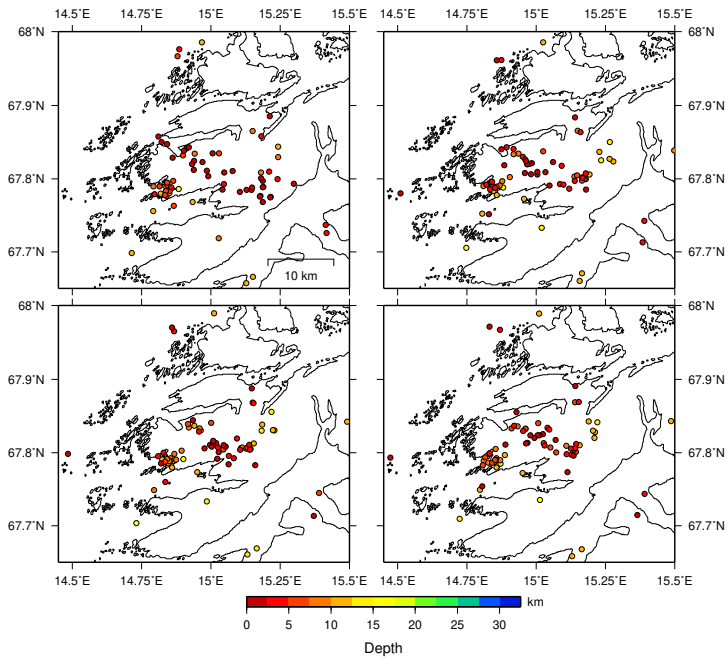


Figure S9. Comparison of hypocenters in Steigen area determined using four velocity model (1-D, 3-D coarse, 3-D medium, and 3-D fine models).

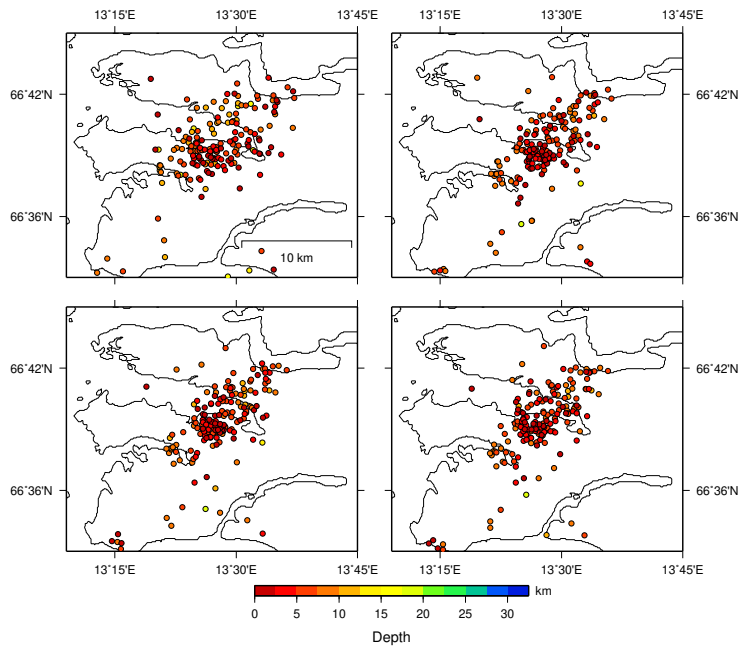


Figure S10. Comparison of hypocenters in Jektvik area determined using four velocity model (1-D, 3-D coarse, 3-D medium, and 3-D fine models).

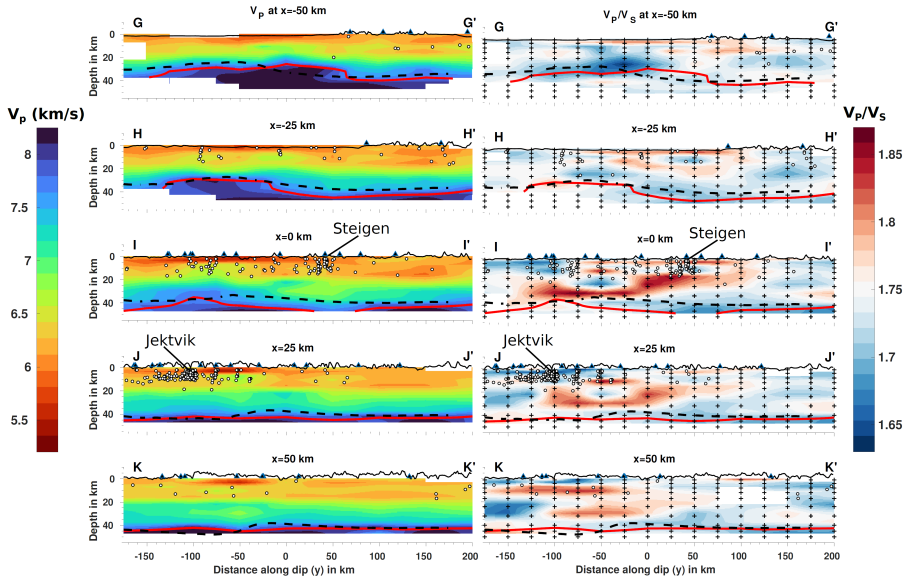


Figure S11. V_P and V_P/V_S ratio for coast parallel cross-sections. Red lines are the contour of the "Moho velocity" (V_P 7.6 km/s), and the dashed black lines is the Moho model compiled by Mayestrenko et al. (2017). Hypocenters and stations are represented by white circles and black triangles, respectively. Surface topography (with 4x vertical exaggeration) are plotted on the top of each cross-section. The inversion grids are plotted in V_P/V_S ratio sections.

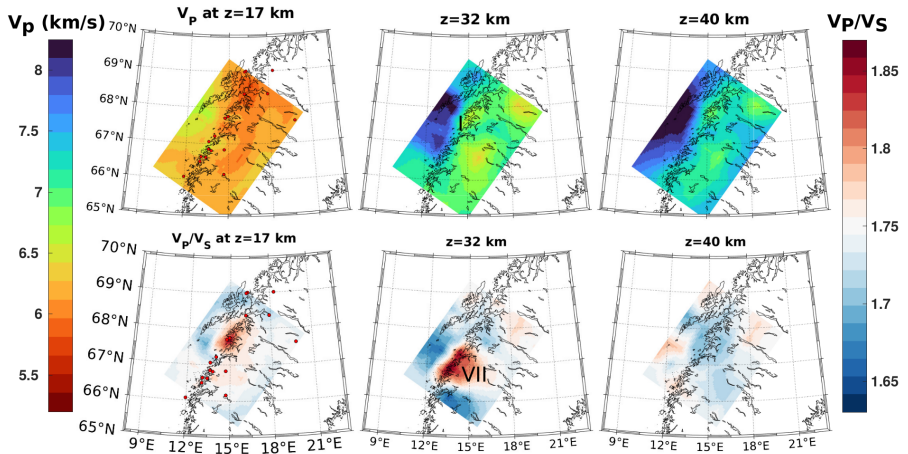


Figure S12. Horizontal slices for V_P and V_P/V_S ratio in the middle and lower crustal depth. Earthquakes and stations are shown as red circles and open inverted triangles.

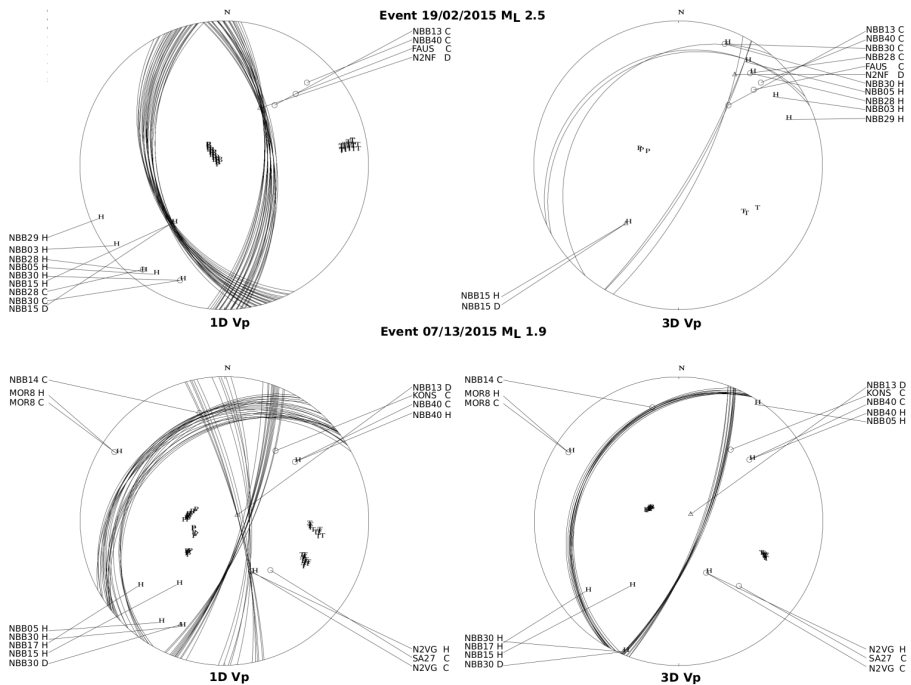


Figure S13. Comparison between focal mechanism solutions computed using 1-D velocity model (left) and solutions computed using 3-D velocity model. Nodal lines represent all possible solutions that fit with the observations. Position of polarities and amplitude ratios are plotted within the lower hemisphere projection. Compression and dilatation polarities are shown as open circles and open triangles, respectively, and amplitude ratios are plotted as H symbols.

3.2 Paper 2

Seismicity modulation due to hydrological loading in stable continental region: a case study from Jektvik swarm sequence in Northern Norway

H.A. Shiddiqi, L. Ottemöller, S. Rondenay, S. Custódio, V.K. Gahalaut, R.K. Yadav, F. Halpaap, and K. Gahalaut

submitted Geophysical Journal International

submitted to *Geophys. J. Int.*

Seismicity modulation due to hydrological loading in a stable continental region: a case study from the Jektvik swarm sequence in Northern Norway

Hasbi Ash Shiddiqi¹, Lars Ottemöller¹, Stéphane Rondenay¹, Susana Custódio², Vineet K. Gahalaut³, Rajeev K. Yadav³, Felix Halpaap¹, and Kalpna Gahalaut³

¹ *Department of Earth Science, University of Bergen, Bergen, Norway.*

² *Instituto Dom Luiz, Faculdade de Ciências, Universidade de Lisboa, Lisboa, Portugal.*

³ *CSIR-National Geophysical Research Institute, Hyderabad, India.*

Received ..; in original form ...

SUMMARY

Seismic swarms have been observed for more than 40 years along the coast of Nordland, Northern Norway. However, the detailed spatio-temporal evolution and mechanisms of these swarms have not yet been resolved due to the historically sparse seismic station coverage. An increased number of seismic stations now allows us to study a nearly decade-long swarm sequence in the Jektvik area during the 2013-2021 time window. Our analysis resolves four major groups of events, each consisting of several spatial clusters, that have distinct spatial and temporal patterns. Computed focal mechanism solutions are predominantly normal with NNE-SSW strike direction reflecting a near-vertical maximum principal stress and a NW-SE near-horizontal minimum principal stress, which are controlled by local NW-SE extension. We attribute the swarm sequence to fluid-saturated fracture zones that are reactivated due to this local extension. Over the time period, the activity tends to increase between February and May, which coincides with the late winter and beginning of spring time in Norway. We hypothesize that the seismicity is modulated seasonally by hydrological loading from snow accumulation.

2

This transient hydrological load results in elastic deformation that is observed at local GNSS stations. The loading is shown to promote failure in a critically stressed normal faulting system. Once a segment is activated, it can then also trigger neighboring segments via stress transfer. Our new results point to a close link between lithosphere and hydrosphere contributing to the occurrence of seismic swarm activity in northern Norway.

Key words: Seismicity and tectonics; Continental tectonics: extensional; Arctic region

1 INTRODUCTION

The coastal region of Nordland, northern Norway, experiences considerable earthquake swarm activity. The swarms are situated within one of the most seismically active regions in mainland Norway, where more than 200 earthquakes above M_L 0.5 are recorded annually, and which also hosted one of the largest documented earthquakes in Fennoscandia: the 1819 M 5.9 Lurøy earthquake (Muir-Wood, 1989; Bungum & Olesen, 2005; Mäntyniemi et al., 2020) (Fig. 1.a). Many spatio-temporal earthquake clusters have been reported here over the past few decades, including those of Meløy in 1978-1979 (Bungum et al., 1979, 1982), Steigen in 1992 (Atakan et al., 1994), Rana in 1998-1999 and 2005 (Hicks et al., 2000; Gibbons et al., 2007) and Jektvik in 2015-2016 (Michálek et al., 2018). Although some hypotheses to explain the regional seismicity in Nordland have been proposed, a detailed characterisation of these swarms has not been possible until now due to the sparsity of seismic stations. Addressing this shortcoming is important as swarms have the potential to help us better understand deformation in the region and the physical properties of the crust. These results can then be utilised to refine seismic hazard assessment in an intraplate region that experiences both swarms and large earthquakes.

The Nordland region has been shaped by a series of major geological episodes. The collision between Baltica and Laurentia resulted in the Caledonian orogeny with high mountains. It was followed by orogenic collapse in the Devonian and then rifting during the opening of the North Atlantic Ocean. Nordland is part of the Caledonian domain, which is dominated by nappe complexes as a result of the collision (Corfu et al., 2014). The area is mostly covered by the Upper and Uppermost Allochthons, which were thrust onto the Precambrian basement (Roberts, 1988; Corfu

et al., 2014)). Following the collapse of the Caledonides, extensional shear zones and detachment faults were formed (Fossen, 2010). Part of the Jektvik area, which is the focus in this study, consists of Precambrian granitoids dominated by granitic and tonalite gneiss (Fig. 1.b). The dominant strikes of extensional faults and shear zones in the area are NNE-SSW and WNW-ESE (Fig. 1.b). This is supported by detailed mapping of the Jektvik region, which identified a small shear zone and a set of fractures with dominant NNE-SSW and WNW-ESE directions (Rostad, H., 1990).

Earthquake fault plane solutions and observations of deformation indicate a rather complex stress regime in Nordland and the adjacent offshore areas. While the mechanisms of earthquake located along the shelf edge are mainly characterised by thrust faulting, those of earthquakes located along the coast are dominated by normal faulting (Michálek et al., 2018; Janutyte et al., 2017; Shiddiqi et al., 2022). The normal faulting events along the coast reflect a deviation from the compressive regional stress, which possibly arises due the additional interference from Glacial Isostatic Adjustment (GIA) and sediment redistribution (e.g., Bungum et al., 2010; Gradmann et al., 2018). Nordland is rising due to GIA, with an average uplift rate of around 4 mm/year in the coastal area (Kierulf et al., 2014). Furthermore, the differences between Global Navigation Satellite System (GNSS) observations and GIA models in Nordland are larger than in other parts of Scandinavia, which may indicate strong subsurface lateral heterogeneity or neotectonic processes (Kierulf et al., 2014; Kierulf, 2017).

Intraplate seismic swarms in various stable continental regions (SCR) worldwide can offer clues as to what causes swarms in Nordland. Swarms are often attributed to the reactivation of pre-existing faults under regional and local stress conditions (e.g., Talwani, 2017). Fluids can play an important role in facilitating seismic swarms by reducing the normal stresses via pore-pressure increase. In addition, hydrological load changes from water bodies, soil moisture and snow cause elastic deformation, which often is observable in GNSS data (e.g., Drouin et al., 2016; Springer et al., 2019). The load change can be significant enough to modulate stresses, pore-pressure and eventually seismic rupture, as suggested by Hainzl et al. (2006); Craig et al. (2017); Gahalaut et al. (2022). Possible links between hydrological processes and swarms have been inferred in various intraplate regions, notably Mt. Hochstaufen in Germany (Hainzl et al., 2006), New Madrid in

4

the USA (Bisrat et al., 2012), and Palghar in Western India (Sharma et al., 2020; Gahalaut et al., 2022). In order to investigate the possible role of hydrological processes in Nordland, we first need to characterize precisely the spatio-temporal evolution of seismicity - something that has not been possible until now.

In this study, we take advantage of improved station coverage to investigate the spatio-temporal distribution of the swarm sequence in Jektvik, which has been active for more than nine years. Our objective is to develop a high resolution earthquake catalog, supplemented with computations of focal mechanisms. We improve the existing earthquake catalog by adding previously undetected events using a deep-learning based algorithm. Then we relocate the earthquakes and identify clusters using differential times and waveform similarity. Using the high-quality seismicity and computed focal mechanisms solutions, we image the fault systems corresponding to the regions where the swarms occurred. We finally use these results to investigate the possible processes that can trigger the swarm sequence and the mechanisms that cause seismicity to migrate within and between fault segments.

2 IMPROVING THE EARTHQUAKE CATALOG

To date, swarm activity in Nordland has been characterized mainly using relatively sparse permanent stations, which usually results in catalogs with magnitude of completeness ≥ 1.0 . This is clearly insufficient to investigate the processes responsible for swarm activity. To address this shortcoming, we developed a high-quality earthquake catalog for Nordland by combining data from permanent stations with those from temporary stations deployed in the region over the past decade. Using this new expanded dataset, we first performed automatic event detection and phase picking to process events that have not been reported in the Norwegian National Seismic Network (NNSN) catalog (Ottemöller et al., 2018). Then we performed manual phase checking, hypocenter location and local magnitude determination using SEISAN software package (Havskov & Ottemöller, 1999; Havskov et al., 2020).

To establish a comprehensive dataset, we collected and integrated relevant catalogs and waveform data from temporary and permanent seismic stations. As a starting database, we used the

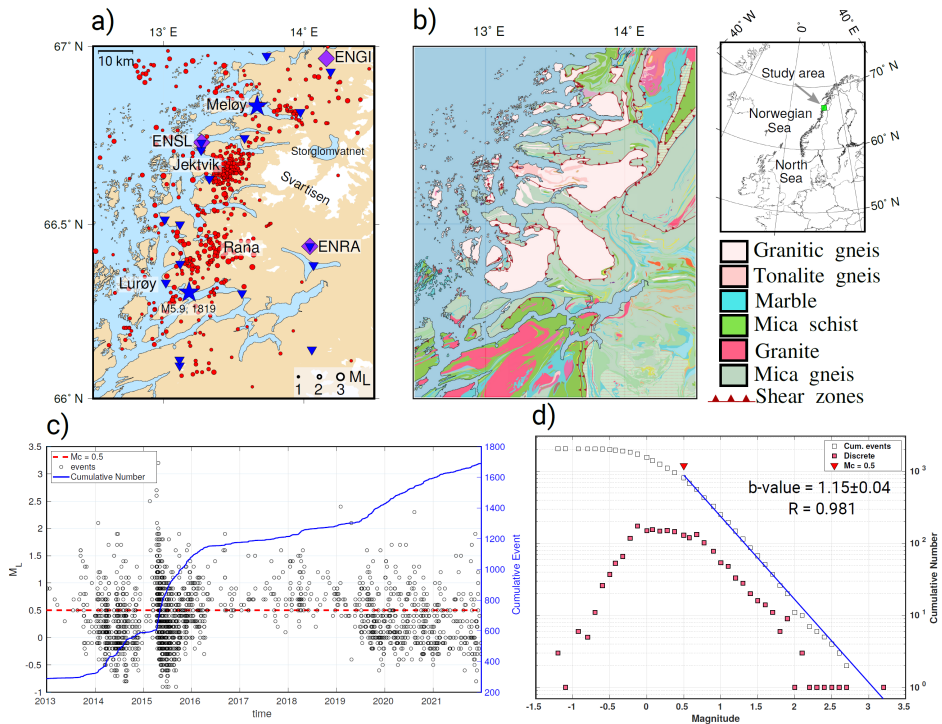


Figure 1. a) Seismicity maps ($M_L \geq 1.0$) in Jektvik and nearby regions. Epicenters are shown as red circles. Notable previous seismic events are marked as blue stars: the estimated location of the M 5.9 1819 Lurøy earthquake, and the center of the 1978-1979 Meløy swarms. Seismic and GNSS stations (ENSL, ENGI and ENRA) used in this study are depicted as blue inverted triangles and purple diamonds, respectively. Storglomvatnet: Storglomvatnet water reservoir. b) Bedrock geology map for the area from the National Bedrock Database from Geological Survey of Norway (2011). Inset map shows the location of the study area in a larger geographical context. c) Temporal variation of earthquakes with M_L and cumulative number of earthquakes. The magnitude of completeness ($M_c = 0.5$) is shown as dashed red line. d) Frequency magnitude distribution of the catalog. The b-value for the whole dataset is 1.15.

NNSN earthquake catalog in the 2013-2021 time window (with a cutoff year set at 2013 because station coverage was too sparse prior to that). The number of stations in the region has grown significantly since 2013 owing to the deployment of two temporary networks: Neonor2, 2013-2016 (Michálek et al., 2018) and Scanlips3D, 2013-2014 (England et al., 2016). Since 2018, the NNSN has added six permanent stations in Nordland within 150 km of Jektvik. These changes have re-

6

sulted in a variable station coverage over time that can be appraised by compiling the monthly number of stations operating within 150 km from the study area over the 2013-2021 period (see Fig. S1). The number of stations reached a maximum of 36 in 2014 and a minimum of 4 between June 2016 and October 2018, which resulted in a slightly decreased detection capability during this latter time window. It will be important to be aware of these fluctuations when we assess the magnitude of completeness of the whole catalog.

The integration of the various data sets allowed us to expand the existing catalogue (a product of routine processing by the NNSN) by adding smaller earthquakes. This was done by utilizing the Eqtransformer Python package (Mousavi et al., 2020) - a powerful deep-learning based tool employed for event detection and phase picking. The picker is trained using the STanford EArthquake Dataset (STEAD) (Mousavi et al., 2019), consisting of a global earthquake database that includes data from a few Norwegian earthquakes. Despite the fact that the picker was trained using mostly data from other regions, previous studies have shown that it can perform well under such conditions (e.g., Mousavi et al., 2020; Jiang et al., 2022; Münchmeyer et al., 2022). An example of event detection and phase picking for events with M_L 0.4 and M_L -0.8, recorded by the station closest to the Jektvik swarm (N2VG), is shown in Fig. S2. For each event detected and processed by Eqtransformer, we used SEISAN to perform a manual check of recordings from all available stations and to pick phase arrivals that may have been missed by the routine automated workflow. After verification, the newly detected events were merged with the NNSN catalog. We used events that were detected both by NNSN and Eqtransformer to evaluate the accuracy of the automatic picking results and estimate the picking errors for the whole catalog. Based on this comparison, we found that the mean difference between NNSN and Eqtransformer phase picks is 0.12 s for P-waves and 0.14 s for S-waves (Fig. S3) and conclude that manual and Eqtransformer processing are compatible. This is essential for further processing and interpretation of the combined catalog.

For the set of detected events we initially determined hypocenter locations by travel-time inversion using the Hypocenter program (Lienert & Havskov, 1995). The program requires a velocity model to compute travel-times - we used the minimum 1-D velocity model developed for the Nordland region by Shiddiqi et al. (2022). We estimated the location errors using a bootstrap re-

sampling analysis similar to that of Shiddiqi et al. (2019), in which the inversion procedure was repeated 100 times by adding random Gaussian noise with a standard error of 0.2 s to the arrival times and recomputing the hypocenter locations. Error estimates were then computed by taking the standard deviation of the 100 realizations in the horizontal (σ_H) and vertical directions (σ_V). In order to get reliable hypocenters without discarding large number of earthquakes, the events retained for further processing and interpretation are chosen based on a set of somewhat relaxed selection criteria: 1) a minimum of five picks with at least two S-picks, 2) azimuthal gap $\leq 225^\circ$, and 3) both σ_H and $\sigma_V \leq 5.0$ km. A total of 2063 events fit these criteria - including 1095 newly detected earthquakes. The histograms of σ_H and σ_V are shown in Fig. 2, and the mean of σ_H and σ_V are 1.14 km and 1.57 km, respectively.

We measured earthquake size for all detected earthquakes by computing local magnitudes, M_L , using the scale for Norway (Alsaker et al., 1991). This is achieved by measuring the maximum amplitudes of Sg waves on simulated Wood-Anderson traces of the vertical channels that are filtered between 2.0 - 18.0 Hz. We chose this frequency band because it yields considerably higher signal-to-noise ratio for small earthquakes compared to the standard frequency band of 1.25 - 18 Hz applied by the NNSN (see Havskov & Ottemöller (2010)). The amplitude measurements were performed automatically using the Automag program in SEISAN. To mitigate M_L overestimation at short-distance stations, we added a correction term for Northern Norway: $-0.74e^{0.09r}$, where r is distance in km (Luckett et al., 2018). With this correction, the M_L scale for Northern Norway becomes:

$$M_L = \log(amp) + 0.91\log(r) + 0.00087r - 0.74e^{0.09r} - 1.67 \quad (1)$$

where amp is the amplitude on the Wood-Anderson seismogram in nanometers. The magnitude-frequency distribution of the improved catalog gives an overall b-value of 1.15 and a magnitude of completeness (M_c) of M_L 0.5 (Fig. 1.d).

We computed focal mechanisms for events after May 2016 to complement previous studies that had computed fault plane solutions for earthquakes between August 2013 - May 2016 in the Jektvik area (Michálek et al., 2018; Shiddiqi et al., 2022). We used first motion polarities picked on unfiltered vertical traces, as well as amplitudes of direct Pg and Sg waves from distances ≤ 100

8

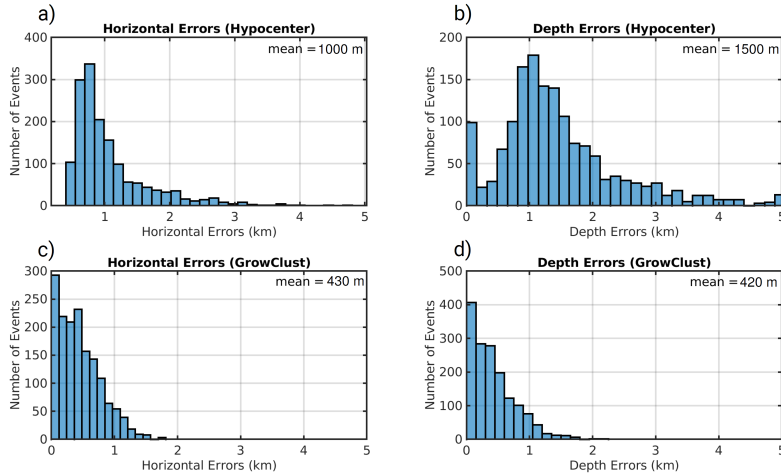


Figure 2. Comparison of initial and relative location errors estimated using a bootstrap resampling method. Histograms of σ_H and σ_V of initial locations shown in a) and b). Only earthquakes relocated by GrowClust program are presented here. Histograms of relative location σ_H and σ_V determined using GrowClust program are shown in c) and d).

km measured on the vertical and transverse traces, respectively. The Pg and Sg amplitudes were corrected for crustal attenuation and free surface. To correct for attenuation, we adopted the Q value for mainland Norway $Q_{Lg} = 529f^{0.42}$ (Demuth et al., 2019), and assumed that Q_P and Q_S have the same value. The focal mechanisms were estimated using the Focmec program (Snoke, 2003). Due to the relatively small number of stations, we set more relaxed acceptable solution criteria than Michálek et al. (2018); Shiddiqi et al. (2022). We did not allow for any polarity error, and the acceptable amplitude ratios were required to have a logarithmic misfit less than 0.2 (see the Focmec manual (Snoke, 2017)). Of the computed mechanisms, we retained those that satisfy the following criteria: 1) the input data include at least five polarities covering both compression and dilatation quadrants of the focal sphere, 2) more than half of the observations must yield acceptable amplitude ratios, and 3) all solutions obtained for one event have to be similar: P- and T-axes concentrate within $\sim \frac{1}{10}$ areas on the focal sphere.

3 HYPOCENTER RELOCATION AND CLUSTERING

To improve the locations of events and assess objectively their degree of clustering, we employed the GrowClust relocation program that combines earthquake relocation and hierarchical clustering (Trugman & Shearer, 2017). As input data, Growclust uses travel-time differences and waveform cross-correlation coefficients (CC) for event pairs recorded on single stations. We used the Obspy package (Beyreuther et al., 2010; Krischer et al., 2015; Megies et al., 2019) to carry out key pre-processing operations on the input waveforms, including instrument response removal and band-pass filtering between 3.0 to 9.0 Hz, and then the EQcorrscan package (Chamberlain et al., 2017) to compute the travel-time differences and waveform correlations. We computed correlations of event pairs with maximum separation of 10 km.

The Growclust algorithm employs a grid-search approach to minimize the L1 norm, which is least sensitive to outliers of travel-time residuals within a cluster. GrowClust uses a 1-D velocity model to compute the synthetic travel-times for direct arrivals (i.e., Pg and Sg), and does not take into account Moho refracted arrivals (i.e., Pn and Sn). Therefore, we selected observations from stations closer than the cross-over distance of 150 km in our case. Event clusters were identified using a hierarchical clustering algorithm in GrowClust, where events are paired based on a number of criteria: minimum CC cutoff (r_{min}), maximum root-mean-square of travel-time residuals (rms_{max}), and distance. We tested a number of r_{min} values to find the preferred value. The rms_{max} was set to a value of 0.2 second, which was found to be suitable in previous studies (Trugman & Shearer, 2017; Ross et al., 2020). Relaxing the rms_{max} value can increase the number of relocated events, but at the same time reduce the relative location quality. We allowed events to join a cluster if they are separated by no more than 8 km distance in the initial catalog, and 4 km distance in the relocated catalog. The relocation uncertainties (σ_H and σ_V) were estimated using bootstrap resampling method, which is integrated within the GrowClust algorithm. Furthermore, we evaluated clustering robustness by inspecting earthquake distribution and the hierarchical clustering trees (dendrogram), which show the links between events by means of CC and event clustering.

10

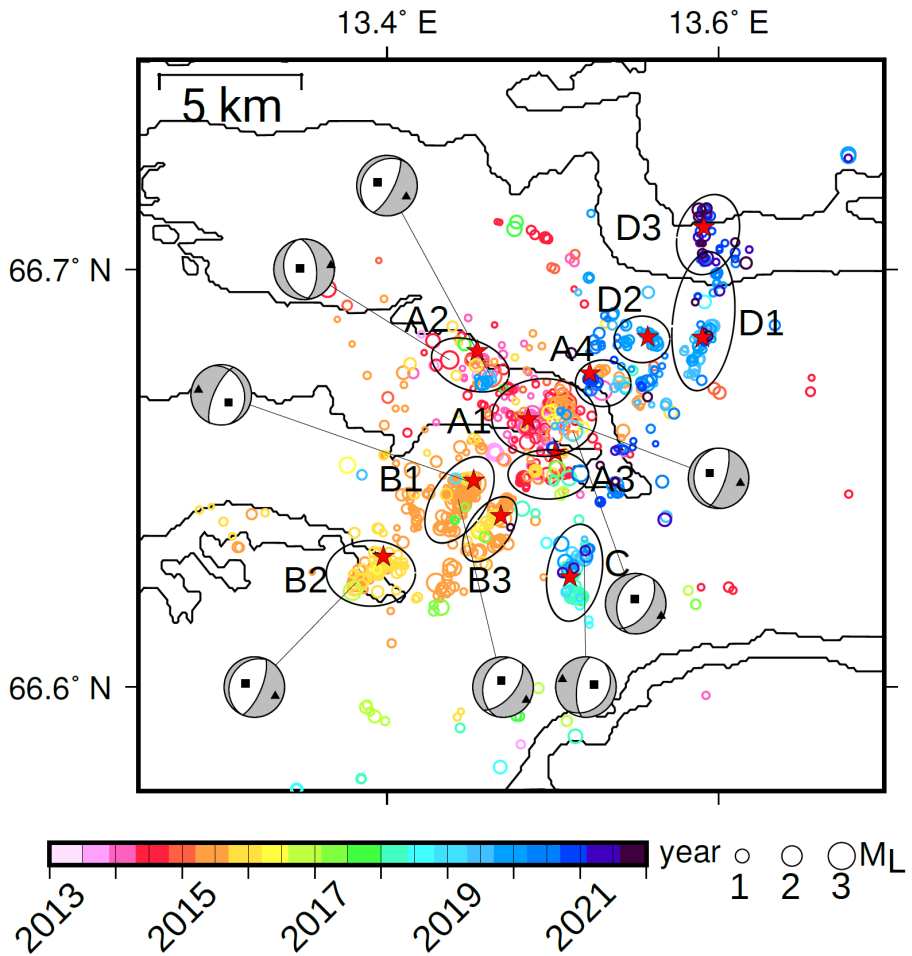


Figure 3. Relocated earthquakes ($M_L \geq 0$) and focal mechanism solutions in Jektvik for the period of 2013 to 2021. Epicenters are shown as open circle colored with time of occurrence. The major clusters that contain more than 25 events are marked with ellipses. The first event in each cluster is marked as red star. The P- and T-axes of the focal mechanisms are shown as black squares and triangles, respectively.

4 RESULTS

The analysis described in the previous sections yields an improved earthquake catalog that contains differential times, cross correlations, amplitudes and polarities. This provides us with more accurate relative locations, cluster identification, fault plane solutions and magnitude estimates.

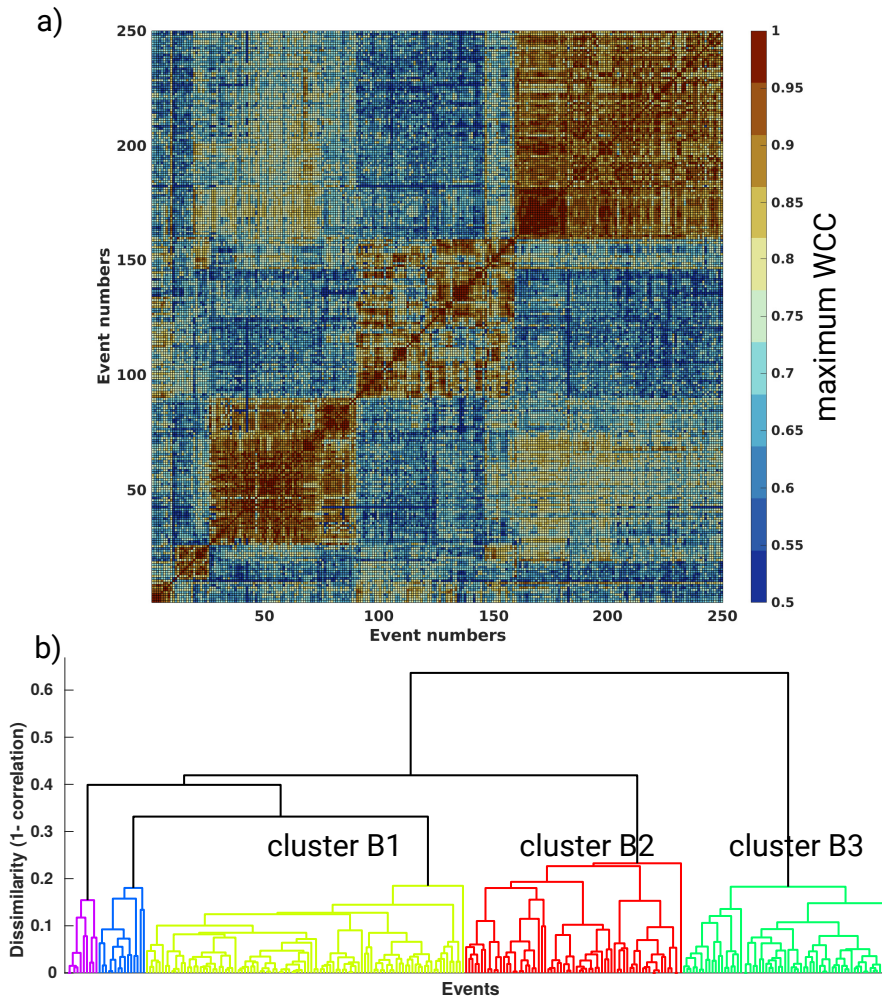


Figure 4. Waveform cross-correlation result and event links for events around group B. a) sorted CC matrix shows three major clusters, b) dendrogram plot, which shows links between events by means of CC, also indicate that there are three major clusters in Group B.

In total we relocated 1590 events. On average, each event location was determined by more than 200 differential times. The quality of the relative locations is best expressed via the reduction in location error compared to the initial hypocenters (Fig. 2). The average σ_H and σ_V of the relocated earthquakes are 430 and 420 meters, respectively, in comparison to 1000 and 1500 meters

12

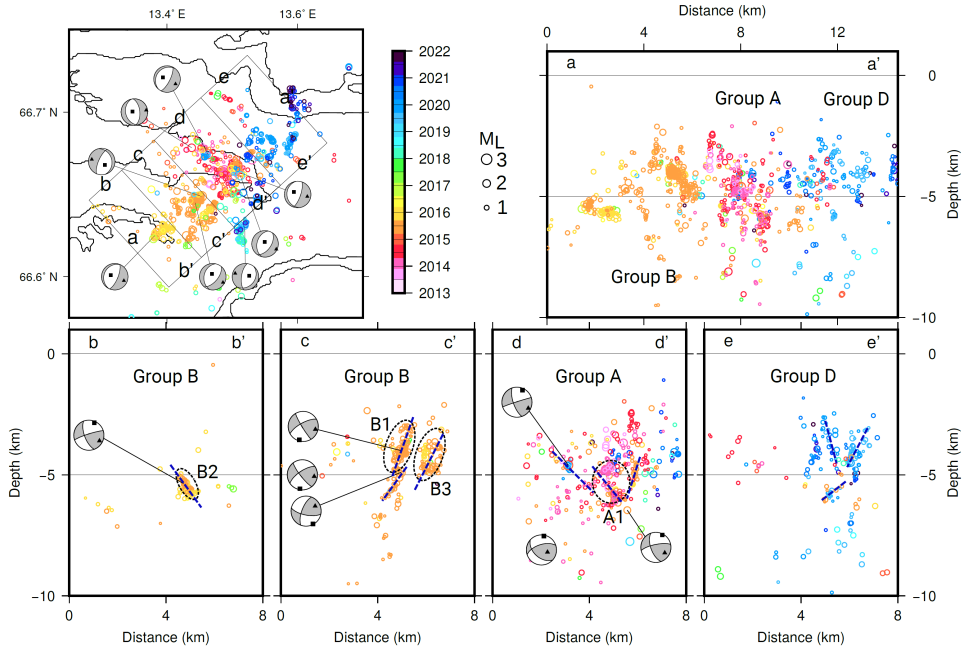


Figure 5. a) Map view of relocated seismicity, focal mechanisms and position of five profiles: strike parallel (a-a') and perpendicular (b-b' - b-b'). b-e) profiles showing the relocated seismicity and focal mechanisms. The relocated earthquakes ($M_L \geq 0$) are shown as open circles colored based on time of occurrence. Focal mechanisms are plotted in cross-section view, with The P- and T-axes shown as black squares and triangles, respectively. Interpreted structures based on seismicity are shown as blue dashed lines. Major clusters are marked with black dashed ellipses. Locations of the profiles are shown in Fig. 5

for their initial absolute locations. To ensure the reliability of our analysis, we only use events below the 95th percentile of the location errors, i.e., less than 1000 meters (for the complete catalog including unrelocated events, see the data availability section).

Our relocation results allow us to resolve the details of the sequence in time and space. Based on location and time we identified four main groups of earthquakes (A, B, C and D) (Fig. 3). Generally, the relocated earthquakes show a similar NE-SW trend. Each group consists of 1-4 individual clusters that each contain ≥ 25 events. We evaluated the event clustering using CC matrices and the links between events using dendrogram. As an example, Fig. 4 shows that group B consists of three individual clusters (B1, B2, and B3), which is consistent with the GrowClust

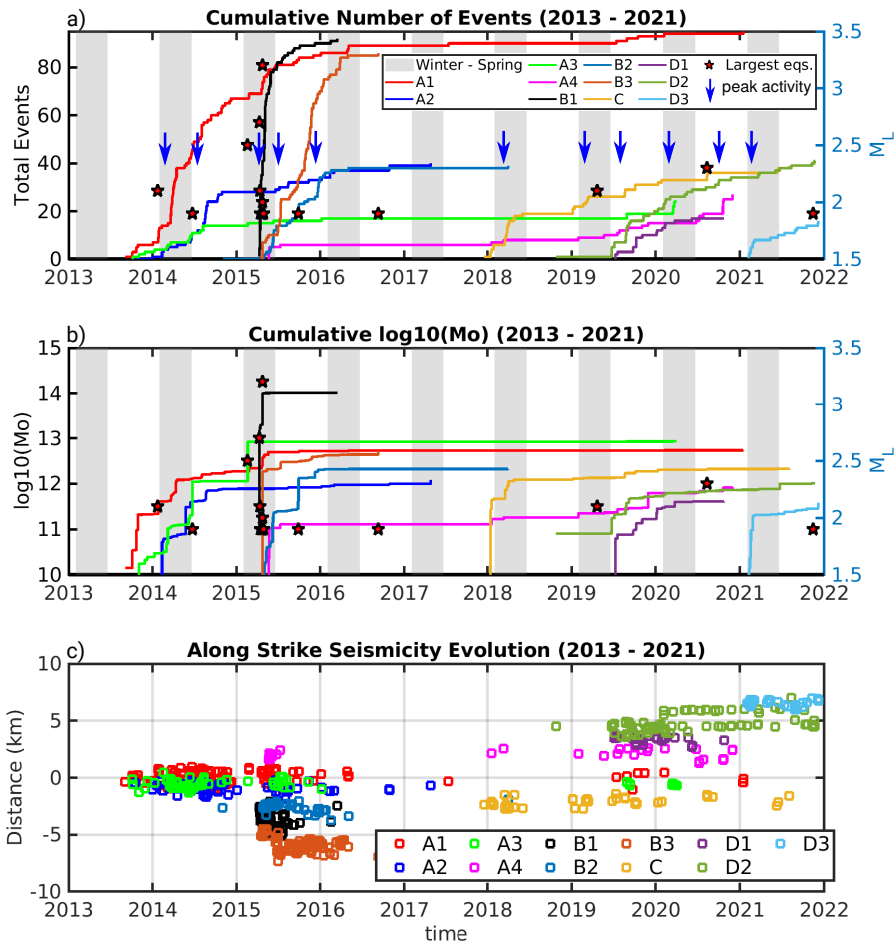


Figure 6. Evolution of the swarm sequences: a) Cumulative number of events for each cluster, shown as solid lines. Blue arrows depict the time when the activity began to increase. Red stars depict the 15 largest events. b) Cumulative $\log_{10}(\text{Mo})$ for each cluster. c) Along strike (NNE-SSW) seismicity migration. The earthquake locations relative to the center of cluster A1 are depicted as open circles colored based on their cluster. Only events with $M_L \geq M_c$ are shown here.

clustering result. Swarm activity in Jektvik started in 2013 with Group A, which has remained active throughout the period of investigation. Group A is seen as the center of the swarm and eventually developed into four distinct clusters. Sharp increases in activity for this group were seen in early 2014 and early 2015. Most of the seismicity in this group occurred beneath or nearby

14

Tjongsfjorden. From 2013 to early 2015, areas outside Group A were relatively quiet, but from April 2015, a new set of earthquakes (Group B) started to appear southwest of Group A. Cluster B1, where the largest event of the whole sequence (M_L 3.2) occurred, was confined in space and time, with most of the seismicity occurring over a two month period. Cluster B2 was located further to the southwest by more than 7 km from the center of Group A and became active a few days after B1. This cluster was also confined in space, but not so much in time, lasting for more than a year. Cluster B3, with an epicentral trend parallel to cluster B1, became active as well during this period, eventually ending in 2016. In 2019, a new patch of seismicity appeared to the southeast of the swarm center forming Group C, which remained active for 3.5 years. Other areas were not very active between 2016 and 2018, although smaller earthquakes would have been missed during this time due to the reduced number of stations. Since 2019, a significant change in the spatial distribution of earthquakes has occurred with the appearance of group D, which is located near the northeastern edge of group A from where it has expanded progressively in a north-northeast direction. By the end of 2021, the Group D hypocenters were located 6.8 km away from the center of Group A. The total extent of the swarm activity is ca. 14 km in SW-NE and ca. 6 km in NW-SE direction, giving a total area of ca. 84 km².

We attempted to compute the focal mechanisms of 20 events that occurred after mid-2016, and found two solutions that were deemed acceptable. After mid-2016, stations are fewer, which makes obtaining good solutions challenging. The two solutions from this study, together with those by Michálek et al. (2018) and Shiddiqi et al. (2022) are shown in Fig. 3. They show normal and oblique-normal faulting with strike along NE-SW direction, in agreement with the epicenter trend. The fault planes reveal two possible mechanisms: shallow NW dipping (20 ° - 40 °) and steep SE dipping (50 ° - 70 °) planes. The seismicity profiles in Fig. 5 indicate a number of steeply SE dipping planes in sections b-b' and d-d', which correspond to clusters B2 and A1. The NW shallow dipping mechanisms do not fit with the NW dipping seismicity lineaments, which tend to be steeper. This can be related to the mechanism uncertainty or fault complexity. Therefore, for this plane, we follow the seismicity trends and interpret them as steeply NW dipping planes, which correspond to clusters B1, B2, and A1 (Fig. 5). The stress orientation inferred from the

NE-SW striking parallel normal faults indicate near vertical maximum compression (σ_1) and near horizontal minimum compression (σ_3) in the WNW direction.

To gain better insight into the characteristics of the seismicity, we analyzed the temporal evolution of the cumulative number of events ($M_L \geq Mc$), the cumulative seismic moment (assuming $M_L = M_w$), and the spatio-temporal distribution of along-strike seismicity (Fig. 6). The 15 largest events are also shown in Fig. 6. The occurrence of the largest events, combined with a sequence of sharp increases in cumulative event number and seismic moment, indicate that activity prior to mid-2016 was higher than afterwards. In several clusters, there is a delay between the sharp increases in seismic moment and cumulative event number. The sharp increase in cumulative seismic moment tends to generally occur earlier, which indicates that the larger magnitude events occur relatively early within a swarm and are then followed by many smaller earthquakes. We identified 11 sharp increases in cumulative event number (Fig. 6), with eight of these occurring between February and May, which coincides with the northern hemisphere late winter and spring time (Fig. 6), hinting at a possible seasonality pattern in the seismic activity of the region.

In order to characterise physical properties, we compiled statistics for each cluster (see Table 1): duration, maximum M_L , total seismic moment and the M_w equivalent of all events. We also look at the size of the complete swarm sequence between 2013 and 2021. The total seismic moment for the whole catalog is 1.54 E+14 N.m , which is equivalent to M_w 3.4. We can alternatively estimate the seismic moment from the extent of the faults. The seismicity is distributed onto a number of fault segments, which in total encompass an 11 km NNE-SSW elongated line. If we look in detail at individual segments, for example group B, clusters B1, B2, and B3 cover areas of approximately 9, 5 and 5 km^2 , respectively. These correspond to M_w 5.1, 4.9 and 4.9 based on the scaling relationship for SCR earthquakes of Leonard (2010). However, the total moment releases for these clusters correspond to M_w of 3.27, 2.15 and 2.41, which means that only small parts of the fault segments failed.

16

Table 1. Maximum M_L , total seismic moment and the M_w equivalent of all events for each cluster.

Cluster ID	Duration	Largest ML	Total Mo (N.M)	M_w equivalent
A1	88 months	1.9	5.45E+12	2.4
A2	42 months	1.5	1.21E+12	2.0
A3	77 months	2.5	8.64E+12	2.6
A4	66 months	1.6	8.31E+11	1.9
B1	11 months	3.2	1.03E+14	3.3
B2	12 months	1.9	2.11E+12	2.2
B3	16 months	2.0	5.28E+12	2.4
C	42 months	1.6	2.15E+12	2.2
D1	14 months	1.2	4.05E+11	1.7
D2	36 months	1.5	1.02E+12	1.9
D3	9 months	1.2	3.83E+11	1.7

5 DISCUSSION

The spatio-temporal evolution of the Jektvik swarm sequence shows both distinct patterns in each group and possibly a physical connection between various groups. To better understand the characteristics and causes of the swarm, we address the following questions: 1) How does the sequence fit into the regional geological framework and crustal stress? 2) What triggers the seismicity and causes the seasonality? and 3) How do the clusters interact and influence each other?

The seismicity distribution and focal mechanisms highlight NNE-SSW trending fault zones that are dipping either NW or SE. This trend was previously reported in a geotechnical survey undertaken during the planning phase of a road tunnel (Straumdaltunnelen) (Rostad, H., 1990), where a NNE-SSW trending shear zone and a number of fractures with NNE-SSW and ESE-WNW strikes were identified in the area of our Group B. These orientations are also visible in high resolution Digital Terrain Model images (Figs. S4 and S5, from the Norwegian Mapping Authority (Kartverket)).

Most of the seismic activity is confined to Precambrian granitic and Tonalite gneiss units (Geological Survey of Norway, 2011), which have a high quartz content (e.g., Rutland & Sutherland,

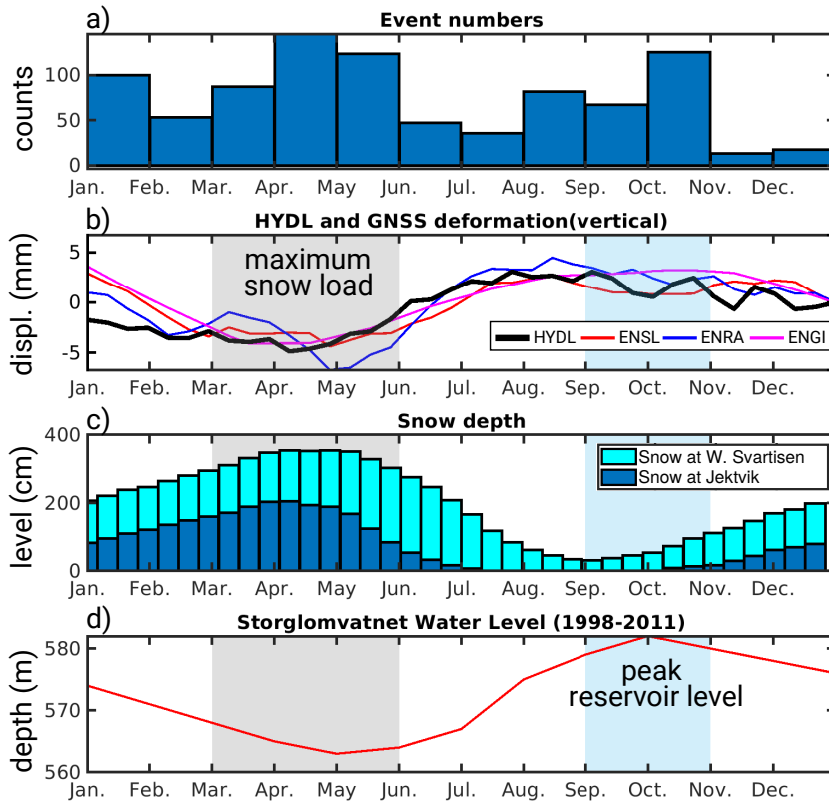


Figure 7. a) Normalized stack of monthly event numbers for the center of Jektvik (Group A). b) Weekly average of vertical displacement from HYDL hydrological loading model (2010-2021) and continuous GNSS (Mid-2019 to Mid-2022) from three stations close to Jektvik region. Linear trend in the GNSS data is removed. c) Weekly average of snow thickness at Jektvik and West Svartisen glacier obtained from SeNorge portal (<https://www.senorge.no/>). The data are averaged over 10-day intervals. d) Monthly average level of Storglomvatnet water reservoir for the period 1998-2011 obtained from Bønsnes et al. (2015). Time windows with maximum snow load and peak reservoir level are marked as gray and blue areas, respectively. Locations GNSS stations are shown in Fig. 1.a

1967; Castro, 2013). The upper crust of the area has low V_P , which has been linked to a fractured crust and to the presence of fluids (Shiddiqi et al., 2022). Water leakage into a road tunnel is observed several km east of cluster B3 (personal communication, Sølve Utstøl Pettersen, Nordland county), indicating fluid flow within the fracture zones. A shallow refraction seismic profile located

18

near the tunnel showed that V_P within the fractures dropped 30-40% relative to the surrounding rocks (GEOMAP, 1990). Both a fractured crust and a high quartz content indicate weaknesses in the continental crust where strain can localize and have been previously linked to intraplate seismicity (Lowry & Pérez-Gussinyé, 2011; Costain, 2017). In our case, the earthquakes within the swarms are relatively small compared to the size of the active fault segments, suggesting that they represent failure of relatively small fractures.

The underlying driver of the ongoing deformation and resulting earthquakes is given by the present day stress pattern. As previously shown by Shiddiqi et al. (2022), the stress pattern inferred from fault plane solutions in the area indicates NW-SE extension, where σ_1 is nearly vertical and σ_3 is subhorizontal in NW direction, which favors the reactivation of NNE-SSW structures. As suggested by previous studies (e.g., Bungum et al., 2010; Gradmann et al., 2018), this extension likely arises from a combination of GIA and sediment redistribution, which overcome the regional compressive stress.

From past studies, we have a reasonable understanding of why there are earthquake swarms in Nordland: failure occurs due to local stresses within fracture zones that are likely fluid saturated, with the fluids potentially bringing the faults closer to rupture. But our analysis of seismicity patterns shows that this process is not randomly distributed in space and time. Therefore, we explore the existence of external processes that may trigger and modulate the seismic activity within and between the different clusters. We expect the modulating process to be of natural origin and, therefore, likely to have a seasonal pattern. When looking at the seasonality of the seismicity, we notice a general increase of earthquake numbers in several years between March and May (Fig. 6), corresponding to the end of winter and spring time in Norway. A possible modulating candidate is the change in hydrological load, which has been linked to seismicity in other regions.

The response of the Earth's surface to changes in hydrological load can be observed with geodetic Global Navigation Satellite System (GNSS) data. To investigate the seasonality of the hydrological load, we plotted yearly averaged distributions of normalized earthquake numbers, vertical component GNSS measurements, Hydrological Loading Model (HYDL), snow depth and water reservoir level for the region (Fig. 7). We plotted these datasets in yearly average since

19

the GNSS data around Jektvik are only available from mid-2019. The selected GNSS stations are located within 50 km of the swarm activity (Fig. 1). After removal of the linear trend, the vertical component of GNSS data is rather constant between July and December, but shows a strong dip, indicating relative subsidence between January and June, which has a maximum amplitude of -10 to -16 mm between March and May. There is a second, but smaller dip between September and November. The GNSS stations have only been operational for less than three years, but we consider the signals reliable as a similar seasonal pattern (although with different amplitudes) is seen on GNSS stations in the broader region of northern Scandinavia (as shown in <http://geodesy.unr.edu/NGLStationPages/gpsnetmap/GPSNetMap.html>). HYDL is a crustal deformation model derived from global hydrological constraints (Dill & Dobslaw, 2013). For the Jektvik region, it shows the same seasonal pattern as the GNSS data with an estimated maximum ground vertical displacement of -8 mm. The small mismatch between the GNSS data and HYDL estimates is due to the low resolution of the hydrological load model. While the vertical displacement is affected by different processes (e.g., tides (Drouin et al., 2016), rainfall (Hsu et al., 2021)), our assumption is that the main signal of relative subsidence during March-May is caused by the regional snow load, while the secondary signal during September-November could be caused by the maximum filling of water reservoirs in the autumn (as seen for the Storglomvatnet reservoir shown in Fig. 7).

The seasonal peak in seismicity that we identify in Fig. 7.a coincides with the maximum hydrological load that we ascribe to snow accumulation in the winter. Hydrological loads can be significant enough to cause elastic ground deformation, alter tectonic stress and modulate seismicity, as shown for northeastern Japan by Heki (2003). To test the significance of the static load change from snow accumulation in the area, we follow (Deng et al., 2010; Büyükakpınar et al., 2021) and model 3-D Coulomb failure stress changes (ΔCFF). We computed the 3-D stress tensor due to surface loading on a half-space elastic media using Boussinesq-Cerruti solutions (see Deng et al., 2010). We used a simple snow thickness model that contains two peaks: 2 meters in Jektvik and 4 meters in the Svartisen glacier area (Fig. 8). Then we computed the changes in shear

20

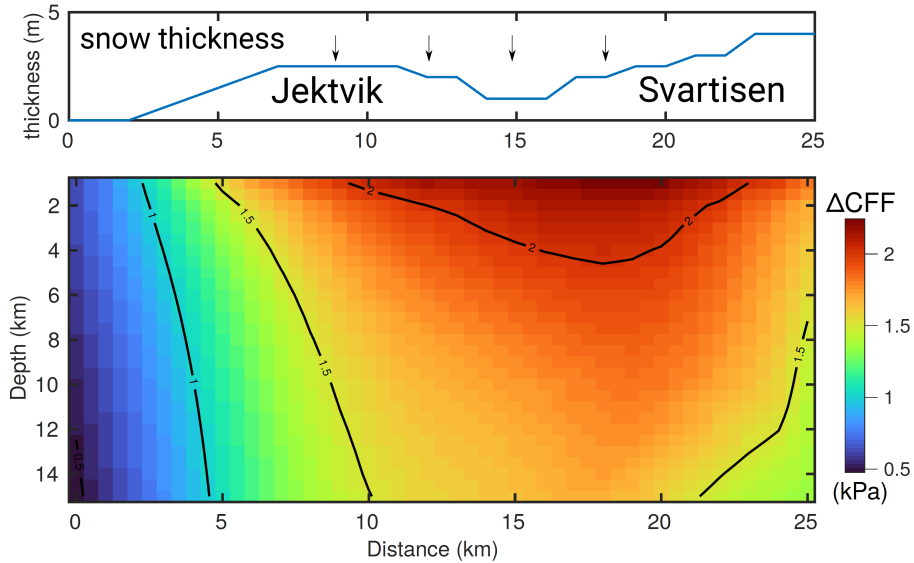


Figure 8. ΔCFF modeling result using a simple snow thickness model consists of two peaks in Jektvik and Svartisen. a) 2-D profile of the snow thickness used to calculate the ΔCFF due to snow load. b) ΔCFF resolved on normal faults beneath Jektvik and Svartisen. Black lines are contours of ΔCFF with 0.5 kPa interval.

($\Delta\tau$) and normal stresses ($\Delta\sigma_n$) for a 45° dip and -90° rake receiver fault due the load. Ignoring the pore-pressure change, ΔCFF is defined as

$$\Delta CFF = \Delta\tau + \mu\Delta\sigma_n \quad (2)$$

where μ is the friction coefficient that is assumed to be 0.6. From this modeling, we found that snow load increases the ΔCFF on normal faults (Fig. 8) in Jektvik by 1.5 to 1.8 kPa at depth of up to 8 km. We consider that these changes in hydrological loading are sufficient to trigger seismicity through stress and pore pressure changes (Deng et al., 2010; Büyükakpınar et al., 2021), even though they are quite small. Previous studies show that small ΔCFF variations (a few kPa) are able to modulate the seismicity (Christiansen et al., 2007; Pollitz et al., 2013; Craig et al., 2017).

The stress modulation affects a larger region, but it can only trigger fault system that are critically stressed and optimally oriented. In the case of Jektvik, such hydrological load is efficient

in triggering seismicity owing to the existence of an intricate network of steeply dipping normal faults at shallow depth. With a near vertical σ_1 direction, an increase in hydrological load enhances the tectonic stress most efficiently. While the hydrological load changes present a tenable trigger mechanism for seismicity in our case, additional work will be needed to model pore-pressure changes and to understand the relative contribution from different processes such as snow cover over the broader region versus higher snow accumulation on glaciers, the filling of reservoirs and changes in the ocean loading.

While the hydrological load change appears to be a likely seismicity modulating trigger mechanism, the spatio-temporal evolution of the Jektvik seismicity indicates further interaction and triggering within and between clusters, which can be explained by co-seismic ΔCFF . Clusters of small to moderate earthquakes can increase Coulomb stress on faults within or on neighboring segments and bring them closer to failure (Gahalaut et al., 2004; Hauksson et al., 2017). In addition to ΔCFF , co-seismic pore-pressure increase caused by earthquakes in one segment can reduce the normal stress, hence can increase the ΔCFF .

In order to understand the ΔCFF effect due to earthquakes in one cluster on to the seismogenic faults of other clusters, we performed simple but representative modeling using the Coulomb 3.3 software (Lin & Stein, 2004; Toda et al., 2005), ignoring the possibility of co-seismic pore-pressure change. We used a cumulative fault source in a cluster following the approach of Gahalaut et al. (2004, 2022). We modeled ΔCFF due to slip on the NNE-SSW oriented normal fault, simulating a typical earthquake cluster source of the Jektvik swarm. We used the maximum cumulative M_0 of $1.03\text{E}+14$, which is equivalent to M_w 3.3. Based on the scaling relation for SCR dip-slip earthquakes of Leonard (2010), we used a length of 400 m and downdip width of the source fault as 400 m, and assumed a normal slip of 2 cm. We resolved ΔCFF on faults with orientation similar to the source fault. As expected, the modeling result shows increasing ΔCFF at the tip of the source faults (King et al., 1994). This implies that ΔCFF will increase on normal fault segments which are sub-parallel and are almost aligned with the source fault (Fig. 9). This simple model can explain the fault interaction through stress transfer and triggering of seismic events in between clusters. For example, cumulative ΔCFF generated by events in cluster A1 can trigger seismicity

22

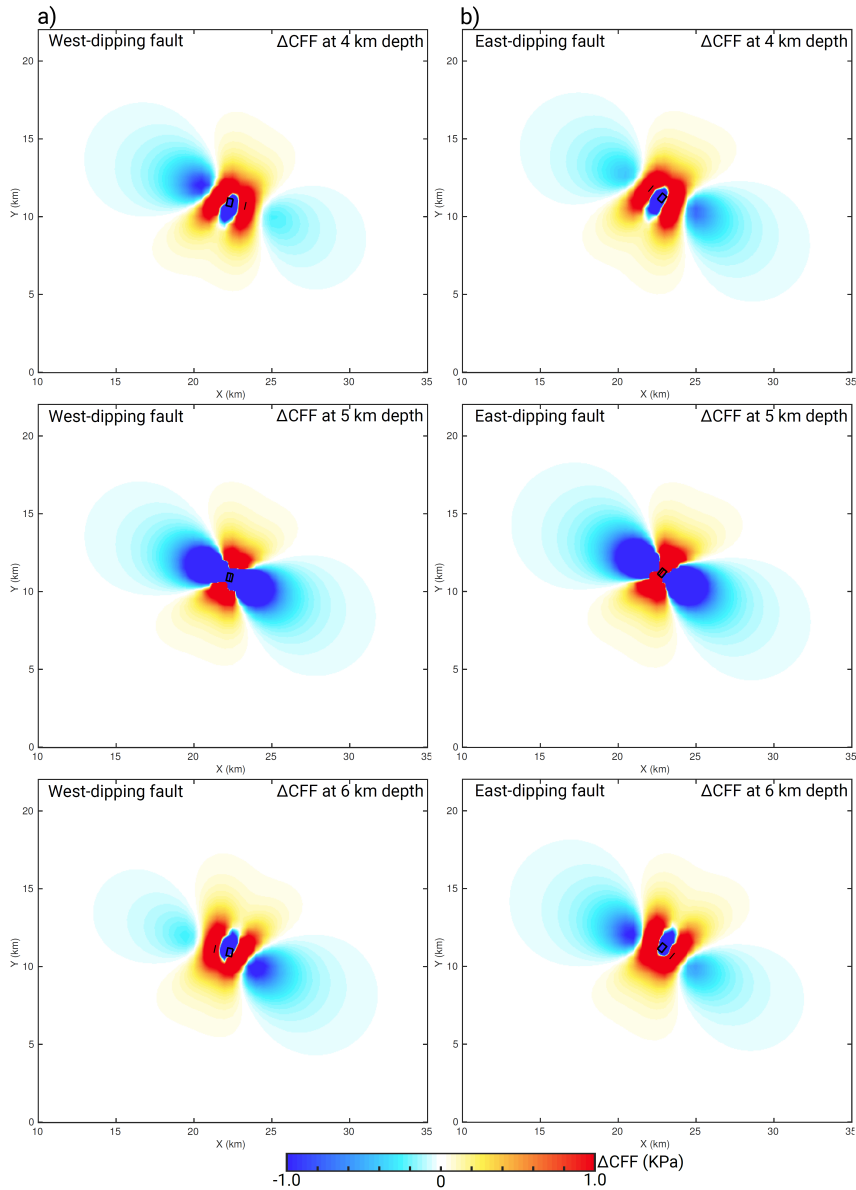


Figure 9. Coulomb stress change (ΔCFF) using a typical normal faulting earthquake in Jetkvik to show the possible inter-cluster triggering. The modeling was performed using using a normal event with M_w 3.3 with NNE-SSW strike. The ΔCFF are computed for west- and east-dipping planes with normal motion at 4, 5 and 6 km depth.

in clusters A4, B1, B3 and possibly later events in group D. Additionally, triggering of parallel segments will be effective if the receiver faults are shallower or deeper than the source faults. This condition can explain the triggering of clusters A2 and A3 due to cumulative ΔCFF from cluster A1.

In light of the ΔCFF modeling, we hypothesize that seasonal load changes are able to trigger and modulate the seismicity. Once a cluster becomes active, it can possibly trigger earthquakes in neighboring clusters. These processes help to promote seismic rupture where the fracture system is already in a critically stressed state in response to present day stresses. Therefore, small increase in ΔCFF can trigger the swarm activity. Pore-pressure changes due to load changes and co-seismic processes are likely to play a role and can further promote failure (Gahalaut et al., 2022). However, given that hydrological loading appears to be the dominant times-dependent process and considering location uncertainties, it is not possible to test the contribution of additional processes on this complex swarm sequence using widely used modelling schemes (e.g., Shapiro et al., 1997; Shapiro, 2015).

6 CONCLUSIONS

We present detailed spatio-temporal and seismogenesis characterisation of a seismic swarm sequence in Jektvik, northern Norway, using an enhanced earthquake catalog that spans a period of nine years. As expected for earthquake swarm activity, the affected area is large but the overall moment release is relatively small. In this case, the active area was ca. 84 km², but the maximum earthquake magnitude was only M_L 3.2. The hypocenters were relocated and clustered using differential time data and waveform cross-correlation. The swarms occurred within an intricate system of NNE-SSW striking fluid-saturated fracture zones, where the earthquakes themselves are seen as failure of smaller fractures that are aligned with the orientation of the zones. This is apparent from the NNE-SSW trending normal fault mechanisms, which are a result of local extensional stresses, and from the alignment of seismicity in the region. The seismicity trend matches the surface lineaments that are seen on high resolution terrain models. Based on precise locations and origin times, we combined earthquake clusters into four main groups. The relocated seismicity

24

shows distinct spatio-temporal patterns within and in between the groups. The seismic activity expanded progressively from the center, first toward SW and later toward east and NE. While the center of the sequence remained active during the entire observation period, the neighboring segments were mostly active only for a limited time.

Based on the coincidence of times of highest seismic activity and maximum hydrological load, we hypothesize that the hydrological load acts as a seasonal modulator. The seismic activity tends to increase between February and May, at the end of the northern hemisphere winter and beginning of spring. Vertical components of GNSS data show a maximum subsidence during this period, which correlates with the peak of snow load in the region. We show that the snow load increases the ΔCFF on the normal fault system and is possibly responsible for the seasonal modulation of seismicity. The response of each segment to this load is different, reflecting the ambient stress heterogeneity and fault characteristics. We further invoke the co-seismic ΔCFF as an additional process that promotes failure within and between fault segments.

ACKNOWLEDGMENTS

The study was supported by funding from the Research Council of Norway for the project “IPSIN - Intraplate Seismicity in India and Norway: Distribution, properties and causes”. The authors VKG, RKY and KG acknowledge the support from the IPSIN Project (MOES/India-Nor/PS-3(GH)/2015). The author S.C. acknowledges support from the Portuguese FCT – Fundação para a Ciência e a Tecnologia, I.P., within the scope of project PTDC/CTA-GEF/6674/2020. We thank Odleiv Olesen and Sofie Gradmann from the Geological Survey of Norway for discussion on geology of Nordland. We thank Sølve Utstøl Pettersen, Nordland Fylkeskommune, for providing geotechnical information and technical reports on Straumdaltunnelen (Straumdal tunnel) near the study area. We acknowledge the operators of permanent and temporary seismic networks used in this study: NNSN (NS; <https://doi.org/10.7914/SN/NS>), Neonor2 (2G), and Scanlips3D (ZR; https://doi.org/10.7914/SN/ZR_2013).

DATA AVAILABILITY

Earthquake data catalog from the Norwegian National Seismic Network (NNSN) is available at NNSN webpage (<https://nnsn.geo.uib.no/nnsn/#/data/events/bulletins>). Seismic data from NNSN (network code: NS) (Ottemöller et al., 2021) and Neonor2 (2G) (Michálek et al., 2018) are available at UiB-Norsar European Integrated Data Archive (EIDA) Node webpage (<https://nnsn.geo.uib.no/nnsn/#/data/waveforms/access>). Seismic data for Scanlips3D (ZR) (England et al., 2016) network are archived at the Incorporated Research Institutions for Seismology (IRIS) Data Management Center (DMC) (<http://ds.iris.edu/ds/nodes/dmc/>). Earthquake data were processed using EQtransformer package (<https://eqtransformer.readthedocs.io>), eqcorrscan package (<https://eqcorrscan.readthedocs.io>), Obspy package (<https://docs.obspy.org/>) and Seisan earthquake analysis software (<http://seisan.info/>). The Norwegian bedrock geology map (Geological Survey of Norway, 2011) is available at Geological Survey of Norway portal (https://geo.ngu.no/kart/berggrunn_mobil). Digital Terrain Model images are available at Norwegian mapping authority (Kartverket) portal (<https://hoydedata.no/LaserInnsyn/> and <https://www.geonorge.no/>). The HYDL model is available at <ftp://esmdata.gfz-potsdam.de/LOADING>. Snow depth data is available at SeNorge portal (<https://www.senorge.no/>). The processed GNSS data are available from Nevada Geodetic Laboratory webpage (<http://geodesy.unr.edu/magnet.php>). Figures in this article were created using Matlab (<https://www.mathworks.com/products/matlab.html>), Generic Mapping Tools (Wessel et al., 2013), QGIS software (QGIS Development Team, 2021) and Inkscape, a vector graphics editor (<https://inkscape.org/>). Earthquake catalog generated in this study is available at at Zenodo <https://doi.org/10.5281/zenodo.7101184>.

References

- Alsaker, A., Kvamme, L. B., Hansen, R. A., Dahle, A., & Bungum, H., 1991. The ML scale in Norway, *Bulletin of the Seismological Society of America*, **81**(2), 379–398.
- Atakan, K., Lindholm, C. D., & Havskov, J., 1994. Earthquake swarm in Steigen, northern Norway: an unusual example of intraplate seismicity, *Terra Nova*, **6**(2), 180–194.

26

- Beyreuther, M., Barsch, R., Krischer, L., Megies, T., Behr, Y., & Wassermann, J., 2010. ObsPy: A Python Toolbox for Seismology, *Seismological Research Letters*, **81**(3), 530–533.
- Bisrat, S., DeShon, H. R., & Rowe, C., 2012. Microseismic Swarm Activity in the New Madrid Seismic Zone, *Bulletin of the Seismological Society of America*, **102**(3), 1167–1178.
- Bønsnes, T. E., Elvehøy, H., Vatne, A., & Kvambekk, Å., 2015. Oppdragsrapport A: Storglomfjordutbyggingen Hydrologiske undersøkelser i 2014.
- Bungum, H. & Olesen, O., 2005. The 31st of August 1819 Lurøy earthquake revisited, *Norwegian Journal of Geology*, (85), 245–252.
- Bungum, H., Hokland, B. K., Husebye, E. S., & Ringdal, F., 1979. An exceptional intraplate earthquake sequence in Meløy, Northern Norway, *Nature*, (280), 32–35.
- Bungum, H., Vaage, S., & Husebye, E. S., 1982. The Meløy earthquake sequence, northern Norway: source parameters and their scaling relations, *Bulletin of the Seismological Society of America*, **72**(1), 197–206.
- Bungum, H., Olesen, O., Pascal, C., Gibbons, S., Lindholm, C., & Vestøl, O., 2010. To what extent is the present seismicity of Norway driven by post-glacial rebound?, *Journal of the Geological Society*, **167**(2), 373–384.
- Büyükkapınar, P., Cesca, S., Hainzl, S., Jamalreyhani, M., Heimann, S., & Dahm, T., 2021. Reservoir-Triggered Earthquakes Around the Atatürk Dam (Southeastern Turkey), *Frontiers in Earth Science*, **9**.
- Castro, A., 2013. Tonalite–granodiorite suites as cotectic systems: A review of experimental studies with applications to granitoid petrogenesis, *Earth-Science Reviews*, **124**, 68–95.
- Chamberlain, C. J., Hopp, C. J., Boese, C. M., Warren-Smith, E., Chambers, D., Chu, S. X., Michailos, K., & Townend, J., 2017. EQcorrscan: Repeating and Near-Repeating Earthquake Detection and Analysis in Python, *Seismological Research Letters*, **89**(1), 173–181.
- Christiansen, L. B., Hurwitz, S., & Ingebritsen, S. E., 2007. Annual modulation of seismicity along the san andreas fault near parkfield, ca, *Geophysical Research Letters*, **34**(4).
- Corfu, F., Andersen, T. B., & Gasser, D., 2014. The Scandinavian Caledonides: main features, conceptual advances and critical questions, *Geological Society, London, Special Publications*,

390(1), 9–43.

- Costain, J. K., 2017. Groundwater recharge as the trigger of naturally occurring intraplate earthquakes, *Geological Society, London, Special Publications*, **432**(1), 91–118.
- Craig, T. J., Chanard, K., & Calais, E., 2017. Hydrologically-driven crustal stresses and seismicity in the New Madrid Seismic Zone, *Nature Communications*, **8**(1), 2143.
- Demuth, A., Ottemöller, L., & Keers, H., 2019. QLg wave tomography beneath Norway, *Journal of Seismology*, **23**, 151–164.
- Deng, K., Zhou, S., Wang, R., Robinson, R., Zhao, C., & Cheng, W., 2010. Evidence that the 2008 Mw 7.9 Wenchuan earthquake could not have been induced by the Zipingpu reservoir, *Bulletin of the Seismological Society of America*, **100**(5B), 2805–2814.
- Dill, R. & Dobslaw, H., 2013. Numerical simulations of global-scale high-resolution hydrological crustal deformations, *Journal of Geophysical Research: Solid Earth*, **118**(9), 5008–5017.
- Drouin, V., Heki, K., Sigmundsson, F., Hreinsdóttir, S., & Ófeigsson, B. G., 2016. Constraints on seasonal load variations and regional rigidity from continuous GPS measurements in Iceland, 1997–2014, *Geophysical Journal International*, **205**(3), 1843–1858.
- England, R. W., Ebbing, J., & Ben-Mansour, W., 2016. SCANDinavian Lithosphere P and S wave experiment 3 D, Tech. rep.
- Fossen, H., 2010. Extensional tectonics in the North Atlantic caledonides: a regional view, in *Continental tectonics and mountain building: the legacy of Peach and Horne*, Geological Society of London.
- Gahalaut, K., Gahalaut, V., Bandari, N., Shekar, M., Tc, S., & Srinagesh, D., 2022. Long duration non-volcanic and non-tectonic palghar earthquake swarm in the stable continental region of india—role of seasonal rainfall and earthquake cascading, *Journal of Seismology*.
- Gahalaut, V. K., Kalpna, & Singh, S. K., 2004. Fault interaction and earthquake triggering in the koyna-warna region, india, *Geophysical Research Letters*, **31**(11).
- Geological Survey of Norway, 2011. Nasjonal berggrunnsdatabase.
- GEOMAP, 1990. RV. 17 Tunnel Reppen - Strømdal: Resfraksjonsseismiske Målinger 1990 (In Norwegian), Tech. rep.

28

- Gibbons, S. J., Bøttger Sørensen, M., Harris, D. B., & Ringdal, F., 2007. The detection and location of low magnitude earthquakes in northern Norway using multi-channel waveform correlation at regional distances, *Physics of the Earth and Planetary Interiors*, **160**(3), 285–309.
- Gradmann, S., Olesen, O., Keiding, M., & Maystrenko, Y., 2018. *The Regional 3d Stress Field of Nordland, Northern Norway - Insights from Numerical Modelling*, chap. Neotectonics in Nordland - Implications for petroleum exploration (NEONOR2), Geological Survey of Norway, Trondheim.
- Hainzl, S., Kraft, T., Wassermann, J., Igel, H., & Schmedes, E., 2006. Evidence for rainfall-triggered earthquake activity, *Geophysical Research Letters*, **33**(19).
- Hauksson, E., Meier, M.-A., Ross, Z. E., & Jones, L. M., 2017. Evolution of seismicity near the southernmost terminus of the San Andreas Fault: Implications of recent earthquake clusters for earthquake risk in southern California, *Geophysical Research Letters*, **44**(3), 1293–1301.
- Havskov, J. & Ottemoller, L., 1999. SeisAn Earthquake Analysis Software, *Seismological Research Letters*, **70**(5), 532–534.
- Havskov, J. & Ottemöller, L., 2010. *Routine Data Processing in Earthquake Seismology: With Sample Data, Exercises and Software*, Springer.
- Havskov, J., Voss, P. H., & Ottemöller, L., 2020. Seismological Observatory Software: 30 Yr of SEISAN, *Seismological Research Letters*, **91**(3), 1846–1852.
- Heki, K., 2003. Snow load and seasonal variation of earthquake occurrence in Japan, *Earth and Planetary Science Letters*, **207**(1), 159–164.
- Hicks, E. C., Bungum, H., & Lindholm, C. D., 2000. Seismic activity, inferred crustal stresses and seismotectonics in the Rana region, Northern Norway, *Quaternary Science Reviews*, **19**(14), 1423 – 1436.
- Hsu, Y.-J., Kao, H., Bürgmann, R., Lee, Y.-T., Huang, H.-H., Hsu, Y.-F., Wu, Y.-M., & Zhuang, J., 2021. Synchronized and asynchronous modulation of seismicity by hydrological loading: A case study in Taiwan, *Science Advances*, **7**(16), eabf7282.
- Janutyte, I., Lindholm, C., & Olesen, O., 2017. Earthquake source mechanisms in onshore and offshore Nordland, northern Norway, *Norwegian Journal of Geology*, **97**(3), 227–239.

- Jiang, C., Zhang, P., White, M. C. A., Pickle, R., & Miller, M. S., 2022. A Detailed Earthquake Catalog for Banda Arc–Australian Plate Collision Zone Using Machine-Learning Phase Picker and an Automated Workflow, *The Seismic Record*, **2**(1), 1–10.
- Kierulf, H. P., 2017. Analysis strategies for combining continuous and episodic GNSS for studies of neo-tectonics in Northern-Norway, *Journal of Geodynamics*, **109**, 32 – 40.
- Kierulf, H. P., Steffen, H., Simpson, M. J. R., Lidberg, M., Wu, P., & Wang, H., 2014. A GPS velocity field for Fennoscandia and a consistent comparison to glacial isostatic adjustment models, *Journal of Geophysical Research: Solid Earth*, **119**(8), 6613–6629.
- King, G. C. P., Stein, R. S., & Lin, J., 1994. Static stress changes and the triggering of earthquakes, *Bulletin of the Seismological Society of America*, **84**(3), 935–953.
- Krischer, L., Megies, T., Barsch, R., Beyreuther, M., Lecocq, T., Caudron, C., & Wassermann, J., 2015. ObsPy: A bridge for seismology into the scientific Python ecosystem, *Computational Science Discovery*, **8**, 014003.
- Leonard, M., 2010. Earthquake Fault Scaling: Self-Consistent Relating of Rupture Length, Width, Average Displacement, and Moment Release, *Bulletin of the Seismological Society of America*, **100**(5A), 1971–1988.
- Lienert, B. R. & Havskov, J., 1995. A computer program for locating earthquakes both locally and globally, *Seismological Research Letters*, **66**(5), 26–36.
- Lin, J. & Stein, R. S., 2004. Stress triggering in thrust and subduction earthquakes and stress interaction between the southern san andreas and nearby thrust and strike-slip faults, *Journal of Geophysical Research: Solid Earth*, **109**(B2).
- Lowry, A. R. & Pérez-Gussinyé, M., 2011. The role of crustal quartz in controlling Cordilleran deformation, *Nature*, **471**(7338), 353–357.
- Lockett, R., Ottemöller, L., Butcher, A., & Baptie, B., 2018. Extending local magnitude ML to short distances, *Geophysical Journal International*, **216**(2), 1145–1156.
- Mäntyniemi, P. B., Sørensen, M. B., Tateviossian, T. N., Tateviossian, R. E., & Lund, B., 2020. A reappraisal of the Lurøy, Norway, earthquake of 31 August 1819, *Seismological Research Letters*.

30

- Megies, T., Krischer, L., Chambers, D. J., Eulenfeld, T., Chamberlain, C. J., Lecocq, T., & Barsch, R., 2019. ObsPy - A Python Library for Seismology, in *AGU Fall Meeting Abstracts*, vol. 2019, pp. NS21A–12.
- Michálek, J., Tjåland, N., Drottning, A., Strømme, M. L., Storheim, B. M., Rondenay, S., & Ottemöller, L., 2018. *Report on seismic observations within the NEONOR2 project in the Nordland region, Norway (Aug. 2013 - May 2016)*, chap. Neotectonics in Nordland - Implications for petroleum exploration (NEONOR2), Geological Survey of Norway, Trondheim.
- Mousavi, S. M., Sheng, Y., Zhu, W., & Beroza, G. C., 2019. STanford EArthquake Dataset (STEAD): A Global Data Set of Seismic Signals for AI, *IEEE Access*, **7**, 179464–179476.
- Mousavi, S. M., Ellsworth, W., Weiqiang, Z., Chuang, L., & Beroza, G., 2020. Earthquake transformer—an attentive deep-learning model for simultaneous earthquake detection and phase picking, *Nature Communications*, **11**, 3952.
- Muir-Wood, R., 1989. The Scandinavian earthquakes of 22 December 1759 and 31 August 1819, *Disasters*, (412), 223–236.
- Münchmeyer, J., Woollam, J., Rietbrock, A., Tilmann, F., Lange, D., Bornstein, T., Diehl, T., Giunchi, C., Haslinger, F., Jozinović, D., Michelini, A., Saul, J., & Soto, H., 2022. Which picker fits my data? a quantitative evaluation of deep learning based seismic pickers, *Journal of Geophysical Research: Solid Earth*, **127**(1), e2021JB023499.
- Ottemöller, L., Strømme, M. L., & Storheim, B. M., 2018. *Seismic monitoring and data processing at the Norwegian National Seismic Network*, vol. 52, chap. Summary of the Bulletin of the International Seismological Centre 2015 January-June, pp. 27–40, International Seismological Centre, Thatcham, United Kingdom.
- Ottemöller, L., Michálek, J., Christensen, J., Baadshaug, U., Halpaap, F., Natvik, o., Kværna, T., & Oye, V., 2021. UiB-NORSAR EIDA Node: Integration of Seismological Data in Norway, *Seismological Research Letters*, **92**(3), 1491–1500.
- Pollitz, F. F., Wech, A., Kao, H., & Bürgmann, R., 2013. Annual modulation of non-volcanic tremor in northern cascadia, *Journal of Geophysical Research: Solid Earth*, **118**(5), 2445–2459.
- QGIS Development Team, 2021. *QGIS Geographic Information System*, QGIS Association.

- Roberts, D., 1988. The terrane concept and the Scandinavian Caledonides: a synthesis, *Norges Geologiske Undersøkelse Bulletin*, (413), 93–99.
- Ross, Z. E., Cochran, E. S., Trugman, D. T., & Smith, J. D., 2020. 3D fault architecture controls the dynamism of earthquake swarms, *Science*, **368**(6497), 1357–1361.
- Rostad, H., 1990. Strømdal Tunnel Sør: Ingeior Geologisk Rapport (In Norwegian), Tech. rep.
- Rutland, R. W. R. & Sutherland, D. S., 1967. The chemical Composition of Granitic Gneisses and Spragmitic Meta-Sediments in the Glomfjord Region, Northern Norway., *Norsk Geologisk Tidsskrift*, **47**(4), 359–374.
- Shapiro, S. A., 2015. *Fluid-Induced Seismicity*, Cambridge University Press.
- Shapiro, S. A., Huenges, E., & Borm, G., 1997. Estimating the crust permeability from fluid-injection-induced seismic emission at the KTB site, *Geophysical Journal International*, **131**(2), F15–F18.
- Sharma, V., Wadhawan, M., Rana, N., Sreejith, K., Agrawal, R., Kamra, C., Hosalikar, K., Narkhede, K. V., Suresh, G., & Gahalaut, V. K., 2020. A long duration non-volcanic earthquake sequence in the stable continental region of India: The Palghar swarm, *Tectonophysics*, **779**, 228376.
- Shiddiqi, H. A., Tun, P. P., & Ottemöller, L., 2019. Minimum 1D Velocity Model and Local Magnitude Scale for Myanmar, *Seismological Research Letters*, **90**(5), 1923–1936.
- Shiddiqi, H. A., Ottemöller, L., Rondenay, S., Halpaap, F., Gradmann, S., & Michálek, J., 2022. Crustal structure and intraplate seismicity in Nordland, Northern Norway: Insight from Seismic Tomography, *Geophysical Journal International*, **230**, 813–830.
- Snoke, J. A., 2003. FOCMEC: Focal mechanism determinations, *International Handbook of Earthquake and Engineering Seismology*, **85**, 1629–1630.
- Snoke, J. A., 2017. *FOCMEC: FOCal MEchanism Determinations Manual*.
- Springer, A., Karegar, M. A., Kusche, J., Keune, J., Kurtz, W., & Kollet, S., 2019. Evidence of daily hydrological loading in gps time series over europe, *Journal of Geodesy*, **93**(10), 2145–2153.
- Talwani, P., 2017. On the nature of intraplate earthquakes, *Journal of Seismology*, **21**(1), 47–68.

32

- Toda, S., Stein, R. S., Richards-Dinger, K., & Bozkurt, S. B., 2005. Forecasting the evolution of seismicity in southern california: Animations built on earthquake stress transfer, *Journal of Geophysical Research: Solid Earth*, **110**(B5).
- Trugman, D. T. & Shearer, P. M., 2017. Growclust: A hierarchical clustering algorithm for relative earthquake relocation, with application to the spanish springs and sheldon, nevada, earthquake sequences, *Seismological Research Letters*, **88**(2A), 379–391.
- Wessel, P., Smith, W. H. F., Scharroo, R., Luis, J., & Wobbe, F., 2013. Generic mapping tools: Improved version released, *Eos, Transactions American Geophysical Union*, **94**(45), 409–410.

submitted to *Geophys. J. Int.*

Supporting information for "Seismicity modulation due to hydrological loading in a stable continental region: a case study from the Jektvik swarm sequence in Northern Norway"

Hasbi Ash Shiddiqi¹, Lars Ottemöller¹, Stéphane Rondenay¹, Susana Custódio²,
Vineet K. Gahalaut³, Rajeev K. Yadav³, Felix Halpaap¹, and Kalpna Gahalaut³

¹ *Department of Earth Science, University of Bergen, Bergen, Norway.*

² *Instituto Dom Luiz, Faculdade de Ciências, Universidade de Lisboa, Lisboa, Portugal.*

³ *CSIR-National Geophysical Research Institute, Hyderabad, India.*

September 29, 2022

Contents

(i) Figure S1 - Figure S5

2

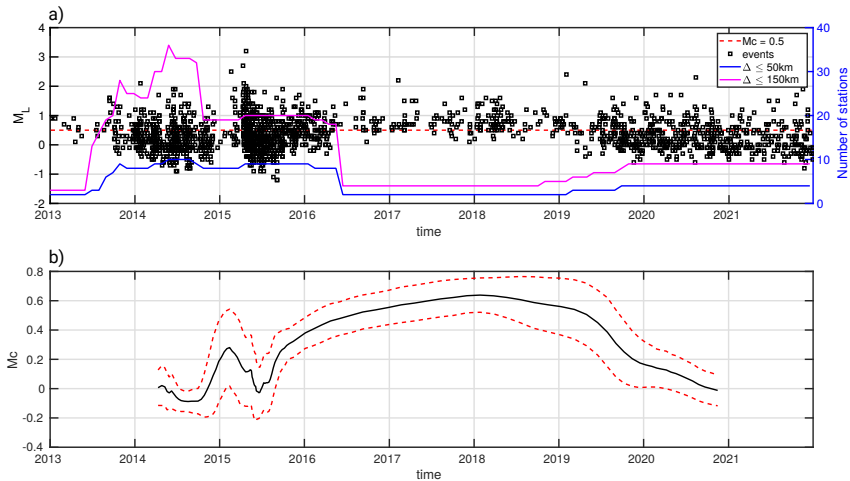


Figure S1. a) Time series plot of M_L and number of stations within 50 and 150 km radius from the center of Jektvik area. The period with the highest number of stations are between mid 2013 and mid 2016 during a number of temporary deployments. The number of stations dropped significantly between mid 2016 and late 2018, resulting in fewer small magnitude events. The number of station is increasing again since late 2018, which is shown by the reduction of detection threshold. b) Time evolution of Magnitude completeness (Mc) reflecting the changes in the station numbers. The Mc become the highest between mid 2016 to late 2019, when the station number is less. The Mc is computed using a sampling window of 400 earthquakes in the ZMAP matlab package (ref.). The solid black and dashed red lines represent the Mc and its error ranges, respectively.

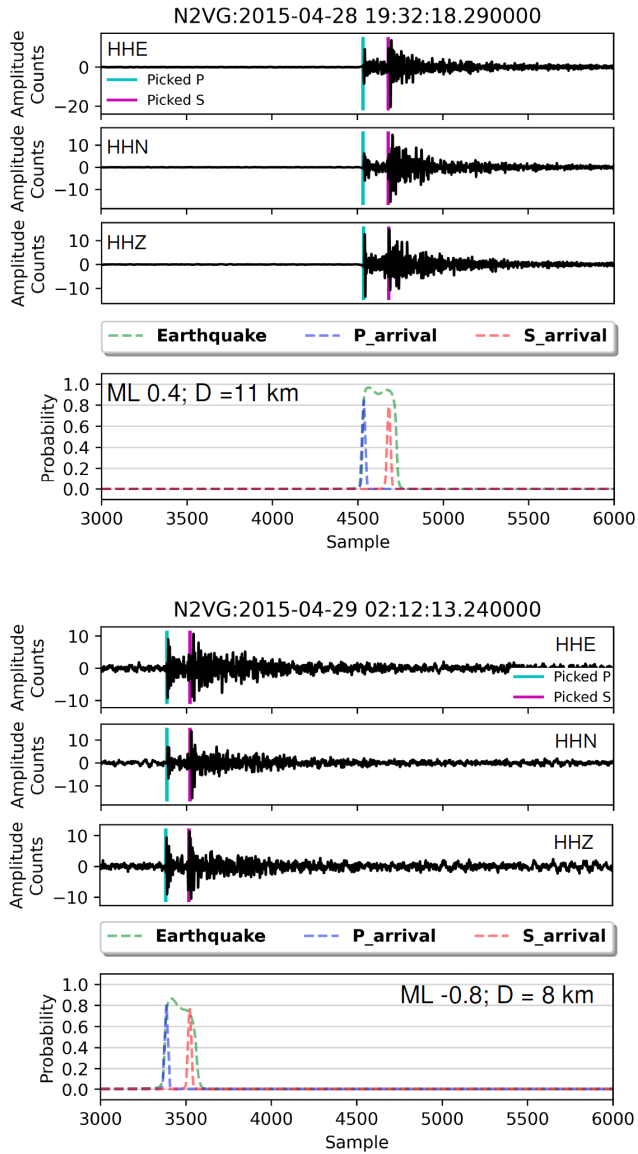


Figure S2. Eqtransformer event detection and picking examples for M_L 0.4 and M_L -0.8 events recorded on N2VG station. For each event, the first three panels are the traces in E-W, N-S and vertical components, and the fourth panel shows the probability associated with earthquake signal, P- and S-arrivals.

4

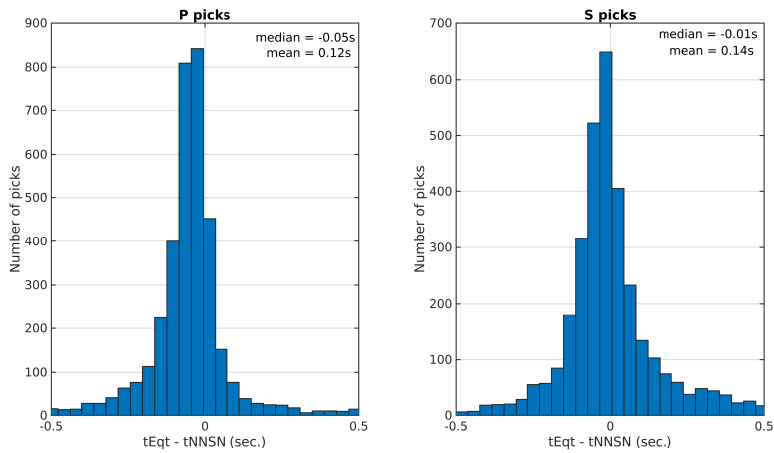


Figure S3. Difference between P- and S-picks from Eqtransformer and from the NNSN catalog. The mean of absolute difference for P-picks are 0.12 s and for S-picks are 0.14 s.

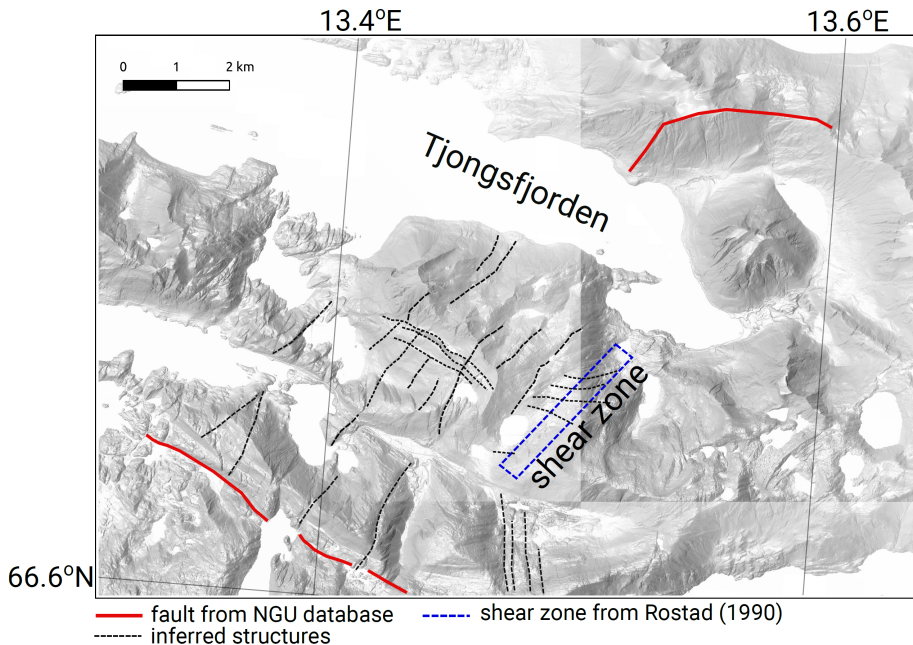


Figure S4. Digital terrain model (DTM) for Jektvik area derived. Interpreted structures are shown as dashed black. Approximate location of a shear zone reported by (Rostad, H., 1990) is shown as blue dashed box. Faults reported in the National bedrock database provided by the Geological Survey of Norway (NGU) (Geological Survey of Norway, 2011). The DTM image is provided by the Norwegian Mapping Authority via geonorge portal (<https://www.geonorge.no/>).

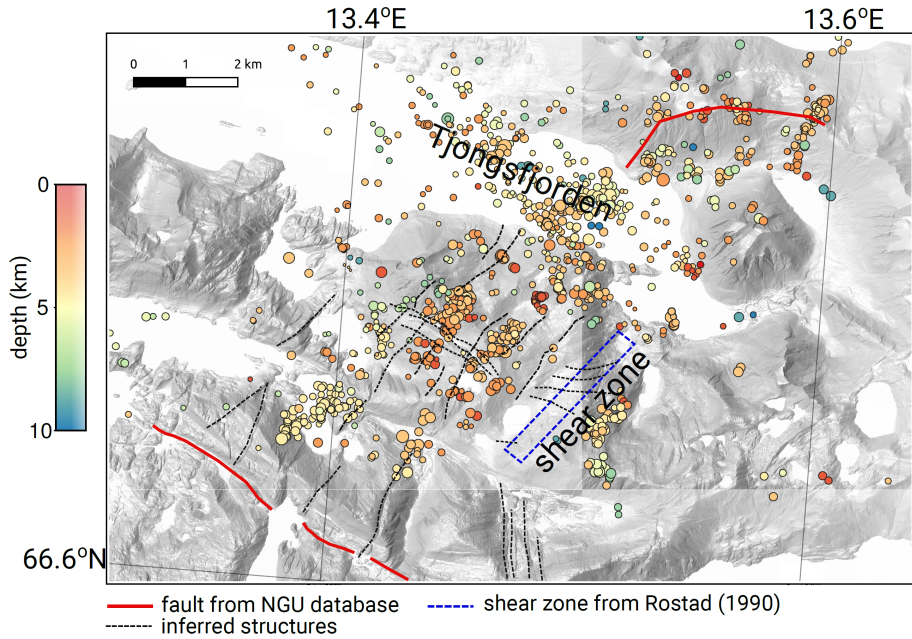


Figure S5. Digital terrain model (DTM) for Jektvik area derived, along with seismicity colored with depth and interpreted structures. The DTM image is provided by the Norwegian Mapping Authority via geonorge portal (<https://www.geonorge.no/>).

6

References

Geological Survey of Norway, 2011. Nasjonal berggrunnsdatabase.

Rostad, H., 1990. Strømdal Tunnel Sør: Ingeior Geologisk Rapport (In Norwegian).

Appendices

Appendix 1

Minimum 1D Velocity Model and Local Magnitude Scale for Myanmar

H.A. Shiddiqi, P.P. Tun, and L. Ottemöller

Seismological Research Letters, **Volume 90**, Issue 5, pp. 1923–1936 (2019).

The published article and supplementary data are available at:

<https://doi.org/10.1785/0220190065>

Accepted version of an article published in Seismological Research Letters (2019) 90 (5): 1923–1936. <https://doi.org/10.1785/0220190065>.

Minimum 1D Velocity Model and Local Magnitude Scale for Myanmar

Hasbi Ash Shiddiqi¹, Pa Pa Tun², Lars Ottemöller¹

¹Department of Earth Science, University of Bergen, Allègaten 41, N-5007 Bergen, Norway.

²Department of Meteorology and Hydrology, Office No. 5, Ministry of Transport and Communications, Zeya Htani Road, Nay Pyi Taw, Myanmar.

Abstract

Earthquake monitoring in Myanmar has improved in recent years because of an increased number of seismic stations. This provides a good quality dataset to derive a minimum 1D velocity model and local magnitude (M_L) scale for the Myanmar region, which will improve the earthquake location and magnitude estimates in this region. We combined and reprocessed earthquake catalogs from the Department of Meteorology and Hydrology of Myanmar (DMH) and the International Seismological Centre (ISC). Additional waveform data from various sources were processed as well. A total of 419 earthquakes were selected based on azimuthal gap, minimum number of stations and RMS travel-time residual. A set of initial seismic velocity models were derived from various seismic velocity models. These models were randomly perturbed and used as initial models in a coupled hypocenter and 1D seismic velocity inversion procedure. We compared the average mean travel-time residuals from the initial and inverted models. The best final model showed an improvement of location standard errors compared to the old model. Furthermore, the local magnitude scale inversion for the Myanmar region was performed using 194 earthquakes that have a minimum of two amplitude observations. The following M_L scale was obtained:

$$M_L = \log A (nm) + 1.485 * \log R (km) + 0.00118 * R(km) - 2.77 + S$$

This scale is valid for hypocentral distance up to 1000 km and magnitudes up to $M_L=6.2$.

Introduction

Myanmar falls into an active tectonic region situated between the Himalaya Mountain belt and Sumatra-Andaman subduction zone. The earthquakes in the country are monitored by the Myanmar National Seismic Network which is operated by Department of Meteorology and

Hydrology (DMH). The current earthquake location procedure is conducted using a preliminary 1D seismic velocity model.

It is still common to use 1D velocity models for routine earthquake location (e.g., Midzi et al. 2010; Husen et al. 2011), although it appears inappropriate in relatively complex tectonic region like Myanmar. There are several local 1D velocity models available in the surrounding region, e.g., Northeast India (Mukhopadhyay et al. 1997) and Bay of Bengal (Rao *et al.*, 2015). Several regional 3D seismic velocity models for the surrounding regions have also been developed (e.g., Li et al. 2008; Pesicek et al. 2008; Pesicek et al. 2010), however, these models have very few stations in Myanmar and are larger scale tomography models that have low resolution at depth shallower than 50 km for Myanmar region. There is, therefore, a need to derive a regional 1D seismic velocity model for Myanmar in order to improve the earthquake location accuracy.

Currently, DMH adopted the local magnitude (M_L) scale from Southern California (Hutton and Boore, 1987). The appropriate M_L scale for Myanmar will be useful to give a better estimate of the earthquake size and provide a better input for seismic hazard analysis.

In this study, we aim to develop a minimum 1D seismic velocity model for the Myanmar region by inverting a set of travel-time data for earthquakes in Myanmar and the surrounding regions. We selected different initial models from global velocity models and other studies from the Myanmar and the surrounding areas, and then we applied random perturbation to these initial models. A simultaneous inversion of 1D velocity and hypocenters was conducted using a set of initial models. Furthermore, we also aim to develop an M_L scale for the Myanmar region. The amplitude data from the vertical component of 15 stations were inverted to obtain the M_L distance correction term for Myanmar.

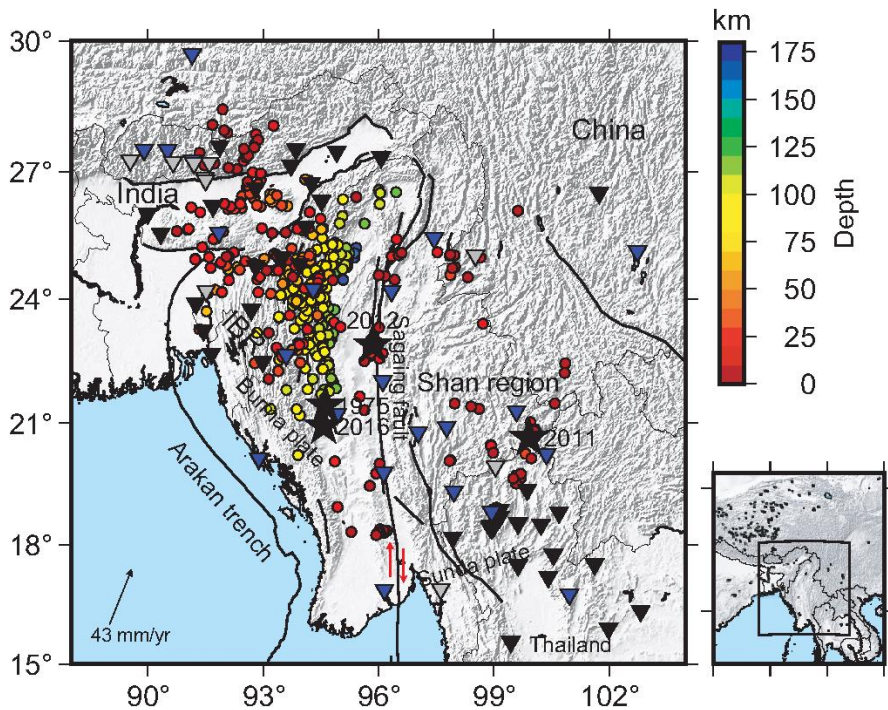


Figure 1. The distribution of earthquakes used in this study (circles colored according to the depths). Seismic stations (triangles) used in this study: 1. Seismic stations used in real-time seismic monitoring by Department of Meteorology and Hydrology of Myanmar (blue), 2. Other seismic stations that waveforms are available to this study (gray), 3. Seismic stations only with travel-time data only (black). Damaging earthquakes mentioned in the text are shown as black stars labelled with the year of occurrence. Active faults in Myanmar and the surrounding regions are depicted by black lines. The slip direction of Sagaing fault is shown by red arrows. Velocity vector is ITRF 2008 (Altamimi et al. 2012) velocity of Indian plate relative to Eurasian plate. The insert map is the area of study (black rectangle) in larger scale map.

Tectonic and Seismicity in Myanmar

The convergence between the Indian and Burma plates created the Indo-Burman range (IBR) in the western part of Myanmar. The subducted Indian plate beneath this region is shown by the intermediate-depth seismicity down to about 150 km depth (see Figure 1) and the slab is clearly imaged by several teleseismic and regional seismic travel-time tomography studies with high P-wave velocity anomaly (e.g., Li et al. 2008; Pesicek et al. 2008; Pesicek et al. 2010; Raouf et al. 2017). The large scale regional and teleseismic tomography studies from Li et al. (2008) and Pesicek et al. (2008) show that the subducting Indian slab penetrates down to the mantle transition zone and then deflects around this depth to the east beneath Myanmar. A smaller scale seismic tomography illuminates the slab discontinuity between 50 to 100 km depth beneath the northern IBR (Raouf *et al.*, 2017). Hurukawa et al. (2012) showed that the strike of the subducted Indian slab is changing from north-northeast direction in the North to south-southeast in the South and the slab dip becomes steeper around the depth of ~50 to ~80 km.

The Sagaing fault, a major dextral strike-slip fault situated in the central part of the country (Figure 1), is a result of the highly oblique motion of the Indian plate relative to the Burma plate where the movement on the Sagaing Fault is about 18 mm/year (Socquet *et al.*, 2006). The Sagaing fault represents the boundary between the Burma Plate and the Sunda Plate (e.g., Le Dain et al. 1984; Ni et al. 1989). Several other active strike-slip faults are present in the Shan region of eastern Myanmar as a result of the extrusion-rotation of the northern part of the Sunda block (Wang *et al.*, 2014). The principal tectonics in the Myanmar region, as well as earthquakes and stations used in this study, are shown in Figure 1.

Before the 20th century, there were several records of historical earthquakes in Myanmar, e.g., the 1762 Arakan earthquake (Cummins, 2007; Gupta and Gahalaut, 2009). A number of shallow earthquakes related to the strike-slip faults across the country have caused damage (see also Aung (2017) for complete list). Hurukawa and Maung (2011) analyzed six $M \geq 7.0$ earthquakes that occurred around the Sagaing fault for the period between 1930 and 1956.

In recent years, shallow earthquakes have caused significant damage, e.g., the 2011 $M_w=6.8$ Tarlay earthquake in eastern Myanmar and the 2012 $M_w=6.8$ Shwebo earthquake in central Myanmar (Tun *et al.*, 2014; Wang *et al.*, 2014) (See Figure 1 for the location of the earthquakes). Some intermediate depth earthquakes also caused damage, especially around the

IBR. Previous studies suggested that these earthquakes are a result of fault reactivation within the subducted slab (e.g., Kundu and Gahalaut 2012). In July 1975, an $M_w(\text{GCMT})=7.0$ intermediate-depth earthquake (GCMT centroid depth = 95.7 km) struck central Myanmar, and caused severe damage to the old town of Bagan. In August 2016, an intra-slab $M_w(\text{GCMT})=6.8$ (depth = 90 km) earthquake which also occurred at intermediate depth, occurred about 45 km south of the 1975 event (Shiddiqi *et al.*, 2018) (See Figure 1). This earthquake has also caused a minor damage in the old Bagan (Zaw *et al.*, 2017).

Seismic Monitoring in Myanmar

The earthquake monitoring in Myanmar dates back to 1963. The installation of the first analog seismographs was conducted in 1976 in Yangon and 1977 in Mandalay (Thiam *et al.*, 2017). The historic overview of seismic monitoring in Myanmar and the installation of five broadband stations by the U.S. Geological Survey and DMH were explained by Thiam *et al.* (2017). DMH is currently (January 2019) running 19 broadband seismic stations and 10 strong-motion stations that are collocated with some of the broadband stations. DMH is also using real-time data from broadband stations from the neighboring countries. For the real-time monitoring, DMH uses both the SeisComp3 (<http://www.seiscomp3.org/>; Weber *et al.* 2007) and Antelope software, while SEISAN (Havskov and Ottemoller, 1999; Ottemöller *et al.*, 2018) is used for interactive processing. SEISAN is configured to read continuous data from the SeisComp3 archive and to transfer event data into the database for further interactive processing.

Until 2013, DMH was mostly relying on the processing of analog seismograms. However, with the operation of digital stations there was a need to integrate data from different sources and to operate a common processing platform. To achieve this, DMH received technical and scientific support from the University of Bergen, Norway, under a project coordinated by the Asian Disaster Preparedness Center (ADPC) with funding from the Norwegian Ministry of Foreign Affairs. Between 2013 and 2017, various training activities were conducted in Myanmar and Norway including courses, workshops and research visits. The focus of the activities was hands-on training to solve practical problems within basic seismology, earthquake data processing, seismic hazard analysis, and instrumentation. SEISAN was adopted at DMH as the interactive processing tool to combine the various data sets and to store the processed data in a single event database.

Data

The DMH started to build an earthquake catalogue from 2014. The quality and completeness of this catalogue has been improving with the installation of new stations. We combined the DMH catalog with the Bulletin from the International Seismological Centre (ISC) for the region from January 2012 to April 2018. Furthermore, we re-picked the P- and S-wave arrivals with consistency from waveform data that are available from DMH, Incorporated Research Institutions for Seismology (IRIS), and the Observatories and Research Facilities for European Seismology (ORFEUS) European Integrated Data Archive (EIDA). We used data from permanent stations from the Myanmar National Seismic Network (MM), GEOFON Network (GE), Thai Seismic Monitoring Network (TM), National Seismic Network of India (IN), Bhutan Seismic Network (K5), China National Seismic Network, (CB), New China Digital Seismograph Network (IC), and Regional Integrated Multi-Hazard Early Warning System (RM). We also used the temporary networks, GANSSER broadband seismic experiment in Bhutan (XA) (Swiss Seismological Service (SED) at ETH Zurich, 2013) (six stations) and PIRE: Life on a tectonically active delta in Bangladesh (Z6) (one station). In total, this amounts to 76 stations in Myanmar and neighboring countries.

The data processing was conducted using the SEISAN software (Havskov and Ottemoller, 1999). The picked arrival times were combined with the reported arrival times from the ISC catalog. We also picked the maximum amplitude (in nanometers) of the S- or Lg waves of the simulated Wood-Anderson seismograms to obtain the local magnitudes of the earthquakes. We measured the zero-to-peak amplitude on the vertical components as that is the routine practice at DMH. To determine earthquake location and local magnitude, we used the HYPOCENTER program (Lienert *et al.*, 1986; Lienert and Havskov, 1995). Initially, we used the ak135 velocity model for continental structure (Kennett *et al.*, 1995) to perform the earthquake travel-time calculations. We removed the P- and S-arrival time data that have travel-time residuals greater than 2.0 seconds and 3.0 seconds, respectively, and then located the earthquakes again with cleaned the P- and S-arrival times.

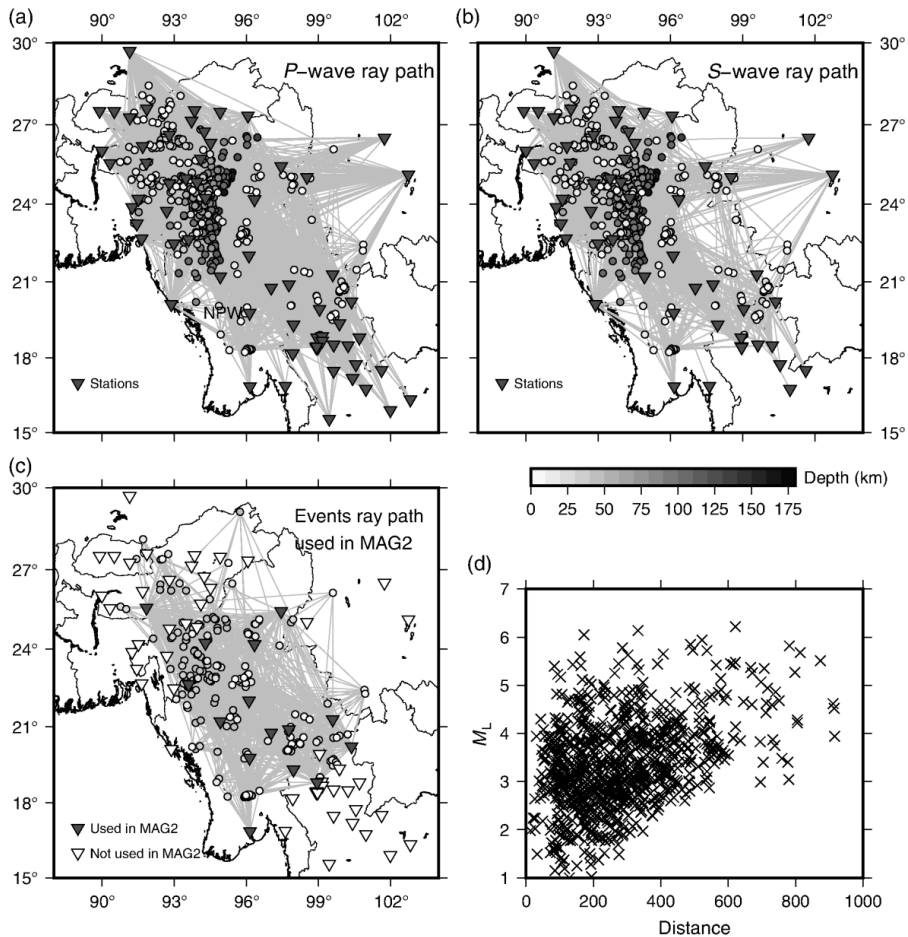


Figure 2. a. The P-waves ray-path coverage of 419 earthquakes (circles) used in 1D seismic velocity inversion, b. The S-waves ray-path coverage. c. The ray-path coverage of 194 earthquakes used in M_L scale inversion (MAG2). d. Data distribution with respect of the Southern California M_L scale (Hutton and Boore 1987) and distance.

To ensure the quality of earthquake location, we selected the earthquakes based on several criteria: 1) the earthquake is recorded by a minimum of eight stations, 2) the RMS travel-time residuals are less than 2.0 seconds, 3) the maximum azimuthal gap is 170° . We selected 419 earthquakes that passed the criteria for further analysis. In total, the dataset consisted of 5163 P-wave arrivals and 3583 S-wave arrivals. The ray-paths of the events mostly cover the entire

Myanmar except for the southwest region since it lacks both stations and earthquakes (Figure 2.a and 2.b).

1D velocity model

The minimum 1D seismic velocity was inverted for simultaneously with hypocenter locations and station corrections by using the VELEST program (Ellsworth, 1978; Kissling *et al.*, 1994). The seismic travel-time problem is a non-linear problem of seismic velocity model along the ray-path and the earthquake locations (Kissling *et al.*, 1994). The quality of the 1D velocity model solution depends on earthquake location quality. This problem is referred to as coupled hypocenter-velocity problem, where the 1D velocity model is solved simultaneously with hypocenter locations (Kissling *et al.*, 1994). The inversion is linearized to solve the problem in a least square sense. It is essential to assign an appropriate number of layers and their thicknesses since VELEST does not invert for these. Hence, the appropriate initial seismic velocity model and high quality P- and S-arrival time dataset are essential input.

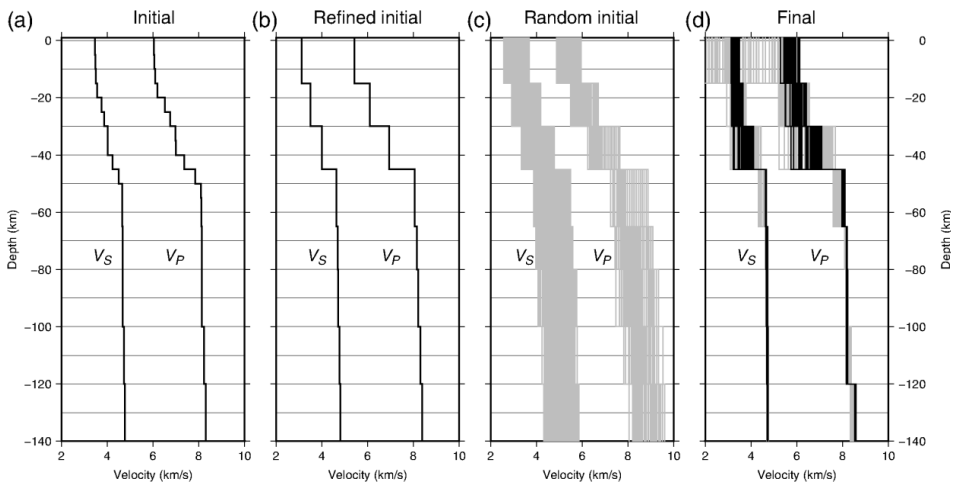


Figure 3. An example of the inversion step using the NEI model: a. The initial model with 5 km layer thicknesses in the crust and 10 km thickness in the mantle, b. The refined initial model which is obtained by inverting the initial model and combine the layers with similar velocities, c) the initial models for the random initial test, d. the result of random initial test where all inverted models are depicted by gray lines, and the accepted models are depicted by black lines.

No	Velocity Model	Source	Comments
1	ak135	ak135	Without Sedimentary layer
2	ak135sed	ak135	With Sedimentary layer
3	MC1.0	Crust1.0 and ak135	Without Sedimentary layer
4	MC1.0sed	Crust1.0 and ak135	With Sedimentary layer
5	NEI	1D model from Raouf et al. (2017) and ak135	Without Sedimentary layer
6	NEIsed	1D model from Raouf et al. (2017) and ak135	With Sedimentary layer
7	MH1	Myanmar Hybrid model v1 (Wang et al., 2018), Crust1.0 and ak135	Without Sedimentary layer
8	MH1sed	Myanmar Hybrid model v1 (Wang et al., 2018), Crust1.0 and ak135	With Sedimentary layer

Table 1. The list of initial 1D velocity models used in this study.

Initial velocity models

In the absence of a specific velocity model for earthquake location in Myanmar, we built starting models based on various global models: Crust 1.0 (Laske *et al.*, 2012) and the ak135 velocity model (Kennett *et al.*, 1995). We constructed an initial 1D velocity model Crust1.0 (referred to as MC1.0) by averaging the V_p and V_s for each layer and layer thicknesses for the study region. Below the Moho, velocities are not defined in Crust1.0 and we extracted values from ak135. The ak135 velocity model is also used as an initial model.

Wang et al. (2018) developed a 3D S-wave velocity model using a temporary network concentrated in the Central Myanmar and other temporary and permanent networks in the surrounding regions. They applied a joint inversion of receiver functions, surface wave dispersion measurements and H/V amplitude ratio of Rayleigh waves combined with velocities from Crust1.0 (referred to as Myanmar-Hybrid1 (MH1)) (Wang *et al.*, 2018). We calculated the average velocity for each layer of MH1 to create an initial 1D S-wave velocity model and combine it with 1D P-wave velocity model from Crust1.0. In addition, a 1D model from Northeast India from Raoof (et al. 2017) which was inverted using the VELEST program is also adopted (will be referred to as NEI Model). The NEI model was derived from local and regional data mostly from Northeast India and the surrounding regions including the Himalaya region, IBR region and northern Thailand. This model comprises a larger area than our study and there were only few arrival-time data from stations inside Myanmar. Mantle velocities from ak135 were combined with MH1 and NEI models. For each model, we constructed a model with a sedimentary layer (low velocity layer as the first layer) and a model without a sedimentary layer. The list of all initial velocity models used in this study is shown in Table 1 and the initial models are plotted in Figure S1.

Inverting for a 1D velocity model in a complex tectonic region like Myanmar is not an easy task, since there is huge variability in crustal thicknesses where the recent study from Wang et al. (2018) shows that the average crustal thickness around central Myanmar is around 30 km, and increases up to 35 km toward eastern Myanmar and IBR. In the northern part of Myanmar toward Tibet and Northeast India, the crustal thickness increases up to more than 50 km (Singh *et al.*, 2017). We obtained average crustal thickness of 37.5 km from MH1 model and 35 km from Crust1.0 model. However, Singh et al. (2017) showed the crustal thickness estimation from a receiver functions study in India and the surrounding region differs about up to 10 km compared to Crust1.0 model.

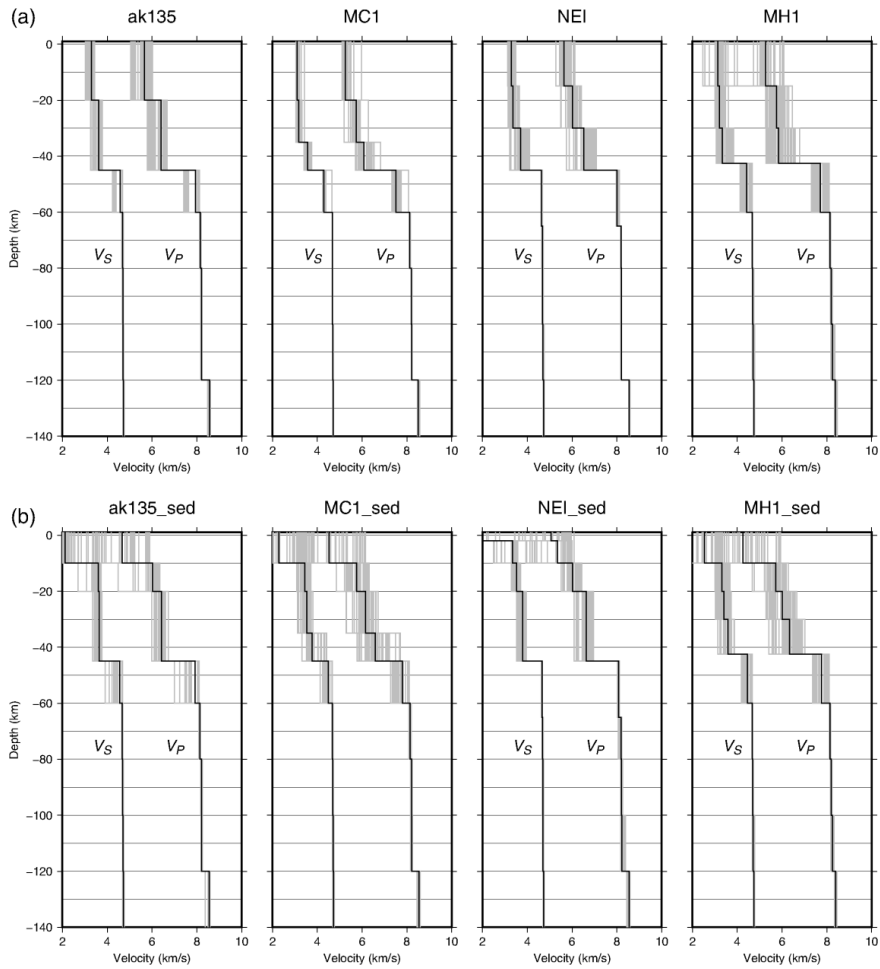


Figure 4. The accepted results from the random initial test. The final velocity models are depicted with black lines, and all the accepted results from random test are shown as gray lines. a. The result for models without sedimentary layers, b. The result for models with sedimentary layers.

Inversion for velocity model

Since the layer thicknesses are not inverted, first we tested the layer thicknesses by dividing the crust into 5 km layers and added two 5 km thick layers below the expected Moho to test the Moho depth as suggested by Kissling et al. (1995). The velocities for these layers are interpolated from the original models, and the velocities increase with depth. To improve earthquake location, in every first iteration the hypocenters were relocated, and in every second iteration the velocity model inversion is conducted simultaneously with hypocenter relocation. This process is repeated for 20 iterations. Finally, the layers with similar velocities are merged. Based on this analysis, we determined the average crustal thicknesses for Myanmar in MH1 and MH1_sed model at 42.5 km and for other models, the crustal thickness is 45 km. We tested sedimentary thickness of 2, 5, and 10 km for the models with the sedimentary layers.

We conducted a random initial model test to find our best velocity model. This was done by creating 500 perturbations for each model by randomly modifying each V_p and V_s in every layer within the range of $\pm 10\%$, and we keep the V_p/V_s ratio within the range of 1.6 to 1.9. Each initial model is then inverted using VELEST. We adopted damping parameters suggested by Kissling et al. (1994), i.e. origin time damping = 0.01, hypocenter damping = 0.01, depth damping = 0.01, velocity damping = 1.0, and station correction damping = 1.0. The maximum number of iteration was set to 20.

We only accepted the inverted models with the lowest 10% of travel-time RMS residuals for each set of initial models. The final velocity models are obtained by averaging the accepted models. The distribution of inversion results for each model will give an indication of the inversion robustness. The results for all models are shown in Figure 3. This test showed that the initial models with sedimentary layer produced a relatively high uncertainty especially in the crust.

Our next step was to refine the station corrections by using the final velocity models from the first step and set a higher damping value for the velocity model (Husen *et al.*, 2011). In this case, the velocity model will not change significantly while the inversion updates the station corrections and hypocenters. Following Husen et al. (2011), we set a damping of 10.0 for the velocity model. The NPW station, located in Nay Pyi Taw (Figure 8.a) was used as reference

station for station corrections, because it is located roughly in the center of the study area, and is operated during most of the period.

To assess the quality of the inversion result, we located the events with HYPOCENTER using the new velocity models along with the station corrections. Then, we compared the RMS travel-time residuals for each velocity model. The relocated events using models with sedimentary layers produced higher mean travel-time residual than the initial locations (Table 2). Based on the average weighted RMS travel-time residuals, the new 1D velocity model from ak135 and NEI gave the lowest values (Figure 4, Table 3). In the Discussion, we look at the estimation of the standard errors of hypocenter locations using these models. Furthermore, VELEST only uses the first arriving P- and S-waves, while in earthquake monitoring at DMH, the analysts also use other crustal phases to locate shallow earthquakes, e.g., Pn, Pg, Sn, and Sg. In the Discussion, we also show that when using these crustal phases for shallow earthquake location, the result using the new velocity model improves the earthquake locations.

No	Velocity Model	Initial mean residual (s)	Final mean residual (s)
1	ak135	1.286	1.085
2	ak135sed	1.272	1.519
3	MC1.0	1.269	1.244
4	MC1.0sed	1.246	1.386
5	NEI	1.255	1.084
6	NEIsed	1.289	1.647
7	MH1	1.307	1.200
8	MH1sed	1.3	1.278

Table 2. The comparison of initial and final models mean residuals.

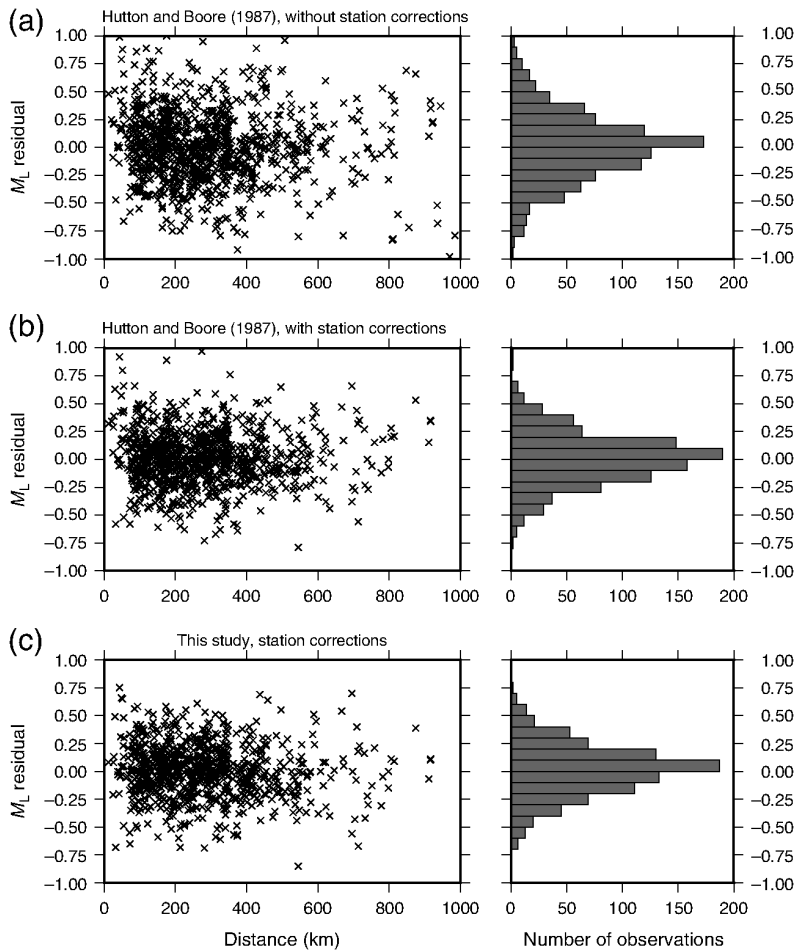


Figure 5. M_L residuals with respect of distances (left) and M_L residuals vs number of observations (right): for Southern California scale (Hutton and Boore 1987) without station corrections (a) and with station corrections (b), and M_L derived in this study with station corrections (c).

Local magnitude inversion

Currently, DMH is using the Southern California local magnitude scale (Hutton and Boore, 1987). This may be a reasonable starting point as both areas are tectonically active. The tectonic

settings are still quite different and it is important to test whether the Southern California scale may be appropriate, or if it is necessary to replace with a new scale derived for Myanmar that would provide better estimation of earthquake magnitude.

The local magnitude scale (M_L) was first introduced by Richter (1935) to estimate the size of earthquakes by measuring the maximum amplitude from the horizontal component seismogram recorded by the Wood-Anderson (WA) seismograph. This method is still widely used for local earthquake monitoring because of its simplicity and widespread use. Since this magnitude scale was introduced using the WA seismograph, today's digital seismogram is transformed into the equivalent of the WA recording with a period of 0.8 s and a damping factor of 0.8 (Havskov and Ottemöller, 2010; Ottemöller and Sargeant, 2013).

Richter (1935) introduced the M_L as

$$M_L = \log A - \log A_0 + S \quad (1)$$

in which A is the amplitude from the WA seismograph in mm, $-\log A_0$ is the epicentral distance dependent correction term, and S is the station correction. Bakun and Joyner (1984) later developed the M_L scale for Central California and introduced the correction term as

$$-\log A_0 = a \log \left(\frac{R}{100} \text{ km} \right) + b(R - 100 \text{ km}) + 3.0 \quad (2)$$

where a and b are the parameters that depend on geometrical spreading and attenuation, respectively. R is the hypocentral distance in kilometers. Hutton and Boore (1987) obtained the constants $a = 1.11$ and $b = 0.00189$ for Southern California.

Inserting equation (2) into (1), and converting the WA peak amplitude in mm into peak amplitude in nanometers with unit gain instead of 2080 for original WA instrument, M_L scale for Southern California is,

$$M_L = \log A \text{ (nm)} + 1.110 \log R \text{ (km)} + 0.00189R - 2.09 \quad (3)$$

where the constants a and b from Hutton & Boore (1987) are used (IASPEI, 2013). Since different tectonic and geological conditions yield different attenuation, it is important to use the appropriate correction terms to obtain the appropriate M_L . In order to obtain the M_L scale for Myanmar region, we use the following equation

$$M_L = \log A \text{ (nm)} + a \log(R) \text{ (km)} + bR + C + S \quad (4)$$

We invert for M_L , a, b, the base level C, and S using the singular value decomposition method. This inversion follows the method described in Ottemöller and Sargeant (2013) and is implemented in the MAG2 program in the SEISAN package (Havskov and Ottemöller, 1999; Ottemöller *et al.*, 2018).

Inversion and Result

We used the earthquake catalog from January 2014 to April 2018 with the updated locations obtained in this work and selected only the stations that are used by DMH for real-time earthquake monitoring. The events that are used for this inversion have a minimum of two amplitude readings. We only used earthquakes that were shallower than 50 km. The total number of earthquakes is 194 which are recorded by a total of 15 stations. The number of S- and Lg-waves maximum amplitudes is 891. The ray-path coverage of the events used for the M_L inversion is shown in Figure 2.c.

The distribution of data with respect to distance and the old M_L is shown in Figure 6. We used the amplitudes with hypocentral distance less than 1000 km, while most of the hypocentral distances are within 100 to 400 km. The magnitude range is from $M_L=1.0$ to $M_L=6.2$. The tectonic settings of the East and Central and the West region of Myanmar are different. Earthquakes in the East and Central regions occur in the crust, while in western Myanmar or the IBR region, earthquakes occur from shallow crustal depth down to intermediate depth. However, our objective at this stage is to obtain a single magnitude scale for the whole region.

We obtained the following M_L scale for Myanmar:

$$M_L = \log A + 1.485 * \log R + 0.00118 * R - 2.77 + S \quad (5)$$

Furthermore, we also conducted another inversion where a and b values are fixed to the Southern California scale, and only invert for the station corrections. We compared the residuals of M_L obtained by using the Southern California scale without and with the stations corrections, the new M_L for Myanmar with station corrections (Figure 6). Both the M_L scale for Southern California and Myanmar with station corrections have much lower residuals compared to the Southern California scale without stations corrections, which suggests that local site variations significantly affect the maximum amplitudes.

Discussions

Minimum velocity model and earthquake location tests

To improve earthquake location in Myanmar, we inverted for a 1D velocity model using a catalog based on DMH and ISC data. We tested the inversion using different initial velocity models. The results from initial models with sedimentary layer gave the highest residuals. This is probably due to the difference of sedimentary thickness in the Myanmar region. The random initial models test showed that the velocity models with sedimentary layer produced quite large uncertainties especially for the velocities in the crust (Figure 4). Therefore, we decided not to use the velocity model with a sedimentary layer and sedimentary thickness in Myanmar can be accommodated by using station corrections.

After testing different initial models, the ak135, and NEI models produce the best results. Since these two models produced similar residuals, we estimated the standard errors of these models using bootstrap resampling analysis for 276 events recorded by at least 10 stations. We did the bootstrap analysis by adding random Gaussian noise with a standard error of 1.0 second to the arrival times in the earthquake catalog and then located the earthquakes using the initial and new models, and at every run, 10% of the data are excluded from the inversion. This process was repeated 200 times. Then, we calculated the horizontal and vertical standard errors of each event for these models (Figure 7). The lowest horizontal and depth standard errors were produced by the locations obtained using the final model from NEI. Therefore, we chose the final model from NEI as the best model and will be referred to as Myanmar Minimum 1D Velocity model (MM_1D) (Figure 5).

The low standard errors for the hypocenters located using the MM_1D model can be attributed to unevenly distributed earthquakes and stations throughout the study region. The majority of the earthquakes are located around the IBR, and many of the stations are also located around IBR and Northeast India region. This condition may explain the tendency of the MM_1D model to produce the smallest hypocentral standard errors compared to other models. On the other hand, the MH1 model was mostly derived using temporary stations mainly distributed in Central Myanmar, where there are only few earthquakes in our dataset. Figure 3 shows that the velocity models below the Moho tend to converge into smaller velocity range which indicates smaller velocity uncertainties. The earthquakes with depth below the Moho (45 km) make up 53% of the data set and are located mostly beneath the IBR. We can assume that the P- and S-

waves travel through similar heterogeneities. As for the crustal part, the huge crustal thickness and velocity variations, and unevenly distributed crustal earthquakes can make velocities in the crustal layers difficult to resolve. Hence, our result produces higher uncertainty for the crustal models.

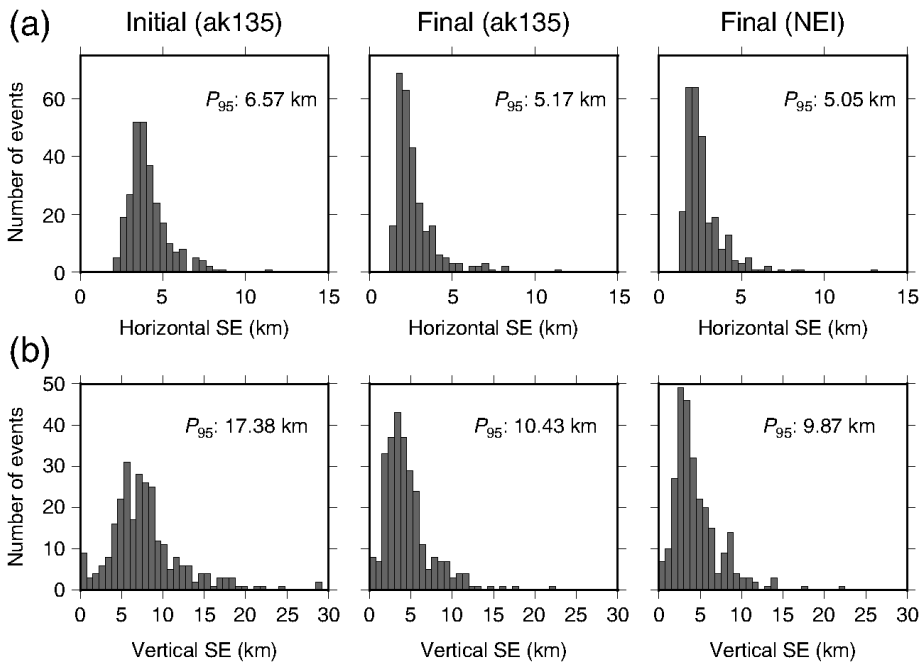


Figure 6. a. Histogram of horizontal location standard error for the initial and the final from ak135 and NEI velocity models. The 95th percentile (P_{95}) of each model is also shown on the upper right of the figures. b. Histogram of vertical location standard error for the initial and the final velocity models.

The station corrections for P-wave travel-times are shown in Figure 8.a and the station corrections for P-waves and S-waves are shown in Figure S2. The station corrections depict the difference between observed and calculated travel-times, where positive and negative values

correspond to late and early observed arrival times, respectively (e.g., Wright, 2008; Midzi *et al.*, 2010). Most of the stations in the center of the study area have relatively small residuals except MDY, which has a station correction of -0.98 seconds. MDY is located on hard-rock (Thiam *et al.*, 2017), which make this station tend to have faster observed travel-time. There are other stations that have relatively large station corrections (>1 second), however we do not have any information about station site condition. Stations around the IBR have positive station corrections which can be attributed to the local site conditions or lateral velocity anomaly beneath this region. Since most of the earthquakes recorded by these stations are from the subducted slab, the upgoing seismic waves probably encounter low velocity anomaly beneath the IBR. A seismic tomography by Raouf *et al.* (2017) showed the existence of a low V_p anomaly beneath the IBR region down to ~ 40 km, which was interpreted as sediment metamorphosis at greater depth. There are also several stations in the east which have quite large travel time corrections (> 1.5 seconds). We suspect, that there are due to some misidentified phases included from the ISC catalog. Most of the earthquakes that were recorded by these stations are shallow earthquakes at regional distances, and in some cases the first arriving Pn phases are not easily picked, and sometimes Pg phases are identified as the first arriving phases.

We conducted a test to see whether the new model can produce relatively good hypocenter locations of events which have more relaxed constraints (e.g., fewer number of stations and larger azimuthal gap). We also tested if the location solutions improve when additional regional phases are used (e.g., Pg and Sg) in addition to the first arriving P- and S-waves, especially for the small shallow earthquakes where there is no station within a radius of 100 km.

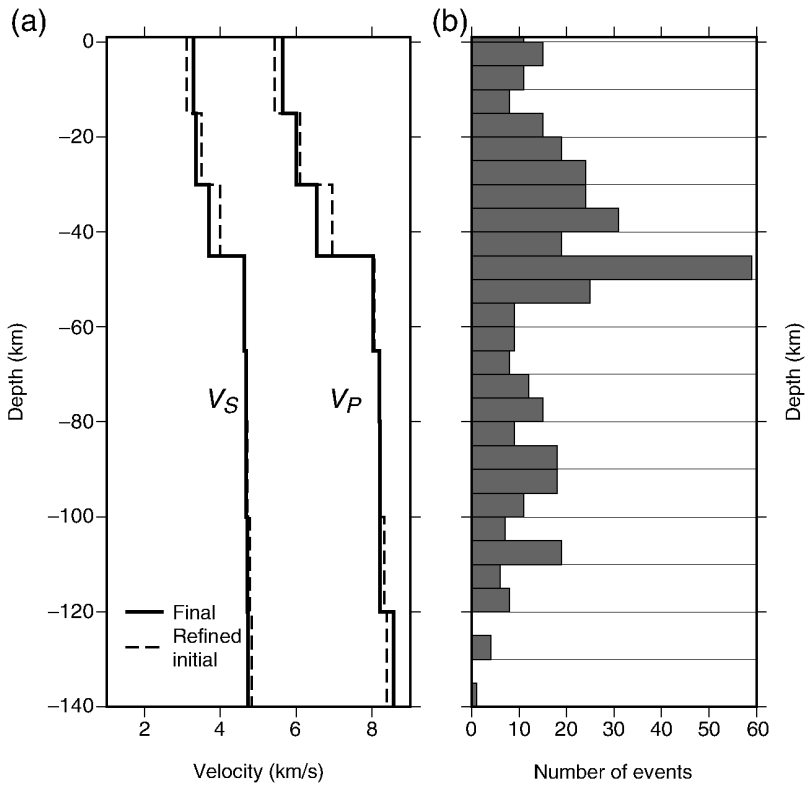


Figure 7. a. The plot of V_p and V_s versus depth of final model (MM_1D). b. The histogram that shows the depth distribution of the events used in the inversion.

For the first test, we compared the hypocenter solutions using the initial velocity model (ak135) and the final velocity model along with the station corrections. A total of 649 earthquakes were selected by using relaxed criteria, i.e., minimum number of stations: seven stations, maximum azimuthal gap: 200° , and RMS travel-time residuals ≤ 3.5 seconds. The hypocenter locations using the initial velocity model (ak135) and the MM_1D model will be referred to as old hypocenters and new hypocenters, respectively. To estimate the standard errors of the old and final hypocenters, we also did the bootstrap resampling test. The 95th percentile (P_{95}) of final horizontal standard errors is slightly reduced compared to the old locations where the P_{95} for final hypocenter is 5.11 km while it is 6.21 km for the old locations. The vertical standard errors for final locations are significantly reduced, where the P_{95} for final hypocenters is 13.73 km and

for the old hypocenters is 20.05 km. The cross-section plot of the old and final locations is shown in the supplementary material (Figure S3).

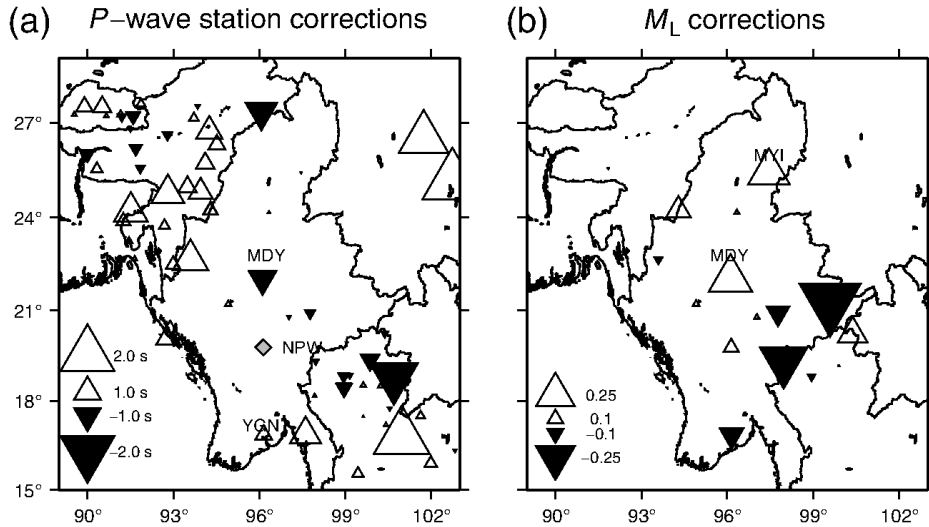


Figure 8. a. P-wave travel-time corrections obtained from VELEST. The reference station (NPW) is depicted with a gray diamond. b. M_L station corrections. The stations discussed in the text are labelled

In the second test, we compared the mainshock and aftershocks of the $M_w(\text{USGS})=6.0$ Phyu earthquake at 10 km depth that struck the southern region of Myanmar on 11 January 2018 . The mechanism of this event was oblique thrust. This earthquake occurred about 20 km from the Sagaing fault. DMH reported that the event was followed by more than 50 aftershocks at shallow depths. The closest stations are the NPW and YGN stations, both about 160 km from the epicenter (see Figure 8a). In order to reduce the depth uncertainty especially for the smaller events, we picked the crustal phases, e.g., Pg and Sg. We selected 28 earthquakes recorded by a minimum of five stations and with an azimuthal gap $< 210^\circ$. We then located the events using the HYPOCENTER program using two velocity models, i.e., the initial velocity model (ak135) and the MM_1D velocity model along with the station corrections (Figure 9).

Most of the initial locations have depth less than 10 km, where some of the depths are close to zero due to the layer boundary resulting in minimum RMS error. The initial epicenter distribution shows an east-west trend, however, there is no clear pattern in the cross-section view. On the other hand, the new locations show a pattern with the dip around 40° to 50° , which is quite consistent with the focal mechanism of the mainshock (Figure 9). The mainshock depth using the final model is 10.4 km. We also plotted horizontal location uncertainty by using error ellipses obtained from the inversion as well as the vertical uncertainty. Both of the horizontal and vertical uncertainties of the final locations are reduced significantly compared to the old location uncertainties (Figure 9).

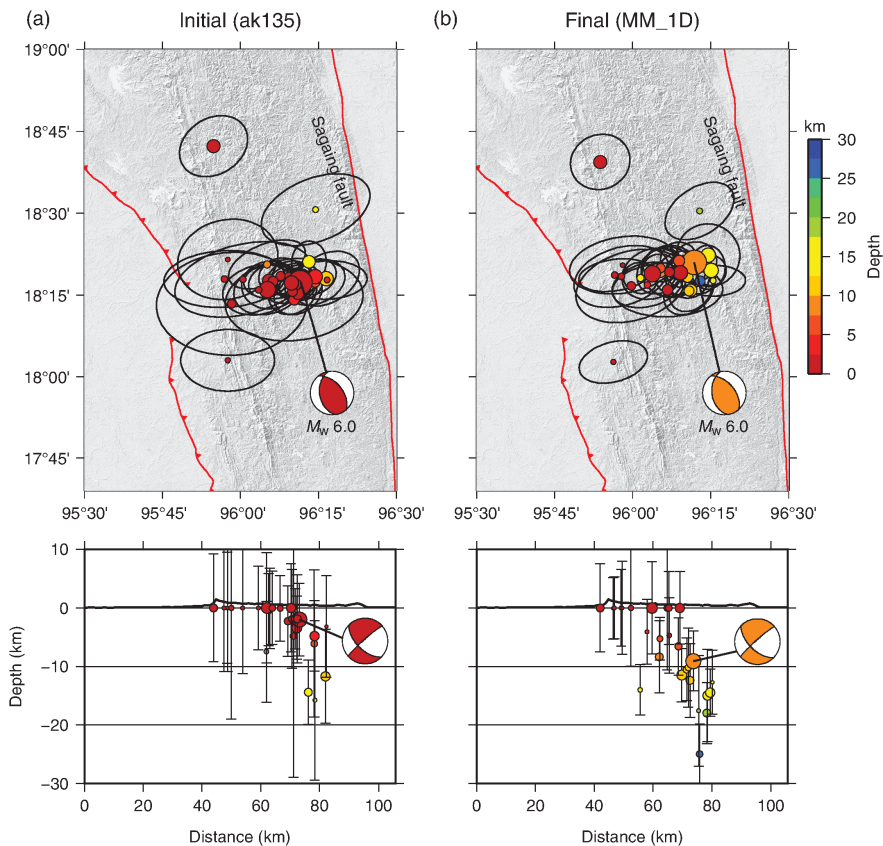


Figure 9. a. The hypocenters distribution (with epicentral error ellipses) of the 11 January 2018 Phyu earthquake and its aftershocks located using the initial model (ak135). The focal mechanism is the solution from Global CMT. The east-west cross-section view is shown at the bottom. The vertical bars are proportional with the depth error of the events. Thick black line is the topographic projection. b. the hypocenters distribution located using the final (MM_1D) velocity model.

Top layer depth (km)	Vp (km/s)	Vs (km/s)
above 0	5.58	3.31
15	6.10	3.32
25	6.62	3.83
45	8.07	4.65
65	8.19	4.66
80	8.19	4.70
120	8.53	4.72
165	8.70	4.83

Table 3. Final Velocity model.

M_L amplitude-distance curve for Myanmar and M_L -mb(ISC) comparison

The M_L scale for Myanmar is obtained using the new seismic network data in Myanmar and the surrounding regions. Based on the dataset, this scale is valid for M_L up to 6.2 and distance up to 1000 km. We compared the M_L distance correction term ($a * \log R + b * R + c$) obtained in this study with the correction terms for other regions, i.e. Southern California (Hutton and Boore, 1987), Central California (Bakun and Joyner, 1984), Eastern U.S. (Kim, 1998), and Norway (Alsaker *et al.*, 1991) (Figure 10). The M_L distance correction term for Myanmar for the distance up to about 100 km is smaller than the Southern California scale. However, this is based only on about 60 observations. For distances greater than 100 km up to 400 km, where we have the most observations, the correction is slightly higher than the Southern California

scale. As for the distances greater than 500 km the correction term become increasingly lower as the distance increases.

The residuals of M_L are significantly reduced if the new M_L scale is used together with station corrections (Figure 8.b). The sedimentary thickness is one of the factors that affects ground motion, even though we used the vertical components for amplitude reading, some variations are still expected. The amplitude used in the M_L scale introduced by Richter (1935) are measured on the horizontal components, however the common routine practice at DMH is to use the vertical components. Therefore, we decided to only measure the amplitudes on the vertical components. The Mandalay (MDY) and Myitkyina (MYI) stations have relatively large positive station corrections which suggests that the amplitudes on these stations are much lower than expected. As mentioned before, Thiam et al. (2017) reported that the MDY station is located on hard-rock and has low site amplification. As for the MYI station, we do not have any information about the site condition.

Even though the new M_L scale for Myanmar and the Southern California scale with station corrections produced similar residuals, the M_L values can be different. The a and b value are also different which reflects the different crustal conditions between Myanmar and Southern California. In most cases, the differences between these two magnitudes are mostly about ± 0.1 magnitude units (m.u.), but the differences can reach up -0.2 m.u. (Figure S4). Therefore we suggest the usage of the new M_L scale instead of the Southern California scale for Myanmar region.

Since the new M_L scale for Myanmar was derived for shallow earthquakes, we tested the M_L calculation for deeper earthquakes, which are mostly intra-slab earthquakes (deeper than 50 km). Despite having larger residuals than shallow earthquakes, the residuals for M_L of deeper events are still within an acceptable range (Figure S6). Therefore, we suggest that for routine location procedure in Myanmar, the new M_L scale can be used for deeper earthquakes.

The new M_L scale for Myanmar is compared with the teleseismic body-wave magnitude m_b reported in the ISC bulletin. 73 events in our dataset are reported in the reviewed ISC catalog for the period between January 2014 to August 2016. A linear orthogonal regression between M_L and m_b (ISC) for 73 common events is m_b (ISC) = $1.08 M_L - 0.18$ with scatter of 0.23 m.u. The regression indicates that the two magnitudes converge at magnitude 2.25, but m_b (ISC) is greater than M_L at large magnitudes (see Figure S6). The mean of M_L for 73 events is 4.25 ± 0.63 ,

whereas corresponding mean of m_b (ISC) is 4.43 ± 0.68 , and hence m_b is about 0.18 m.u. greater than M_L (Figure S5).

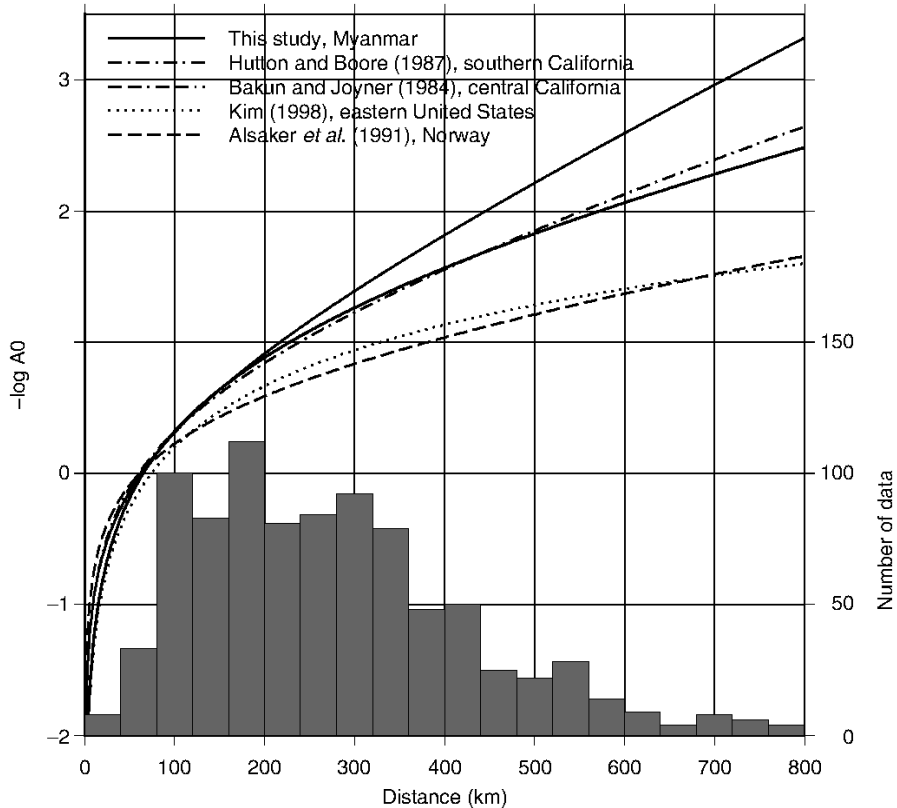


Figure 10. Comparison of M_L correction term for unit of displacement in nanometers from this study and other regions. Below the curves, histogram of number of data used at different hypocentral distances is also shown.

Conclusions

We have demonstrated that the new seismic velocity model and local magnitude scale along with the station corrections produced better locations and local magnitude estimates than what was obtained with current models. The MM_1D produces more accurate hypocenter solutions compared with other models tested in this study. When locating shallow earthquakes by using different crustal phases (P_n , P_g , S_g , and S_n), the use of the MM_1D model reduced the depth

uncertainties of shallow earthquakes. The new M_L scale in Myanmar together with the station corrections produces lower residuals than the Southern California scale.

Further improvement is possible in the future, since Myanmar is a complex tectonic region where strong lateral variation exist, specific 1D velocity models and probably specific M_L scale can be developed for the different regions in Myanmar. As the Myanmar Seismic Network and the earthquakes database grow, there will be a good enough dataset to derive such models in the future.

Data and Resources

The local catalog data used in this study were provided by the Department of Meteorology and Hydrology of Myanmar. Additional data were downloaded from The International Seismological Centre (<http://www.isc.ac.uk/>, last accessed July 2018). Waveform data were obtained from Department of Meteorology and Hydrology of Myanmar, Incorporated Research Institutions for Seismology (IRIS), and the Observatories and Research Facilities for European Seismology (ORFEUS) European Integrated Data Archive (EIDA). The Obspy python package (Beyreuther *et al.*, 2010) was used to obtained some of the waveform data. Some of the figures were created using the Generic Mapping Tools (www.soest.hawaii.edu/gmt, last accessed December 2017; Wessel *et al.* 2013). The topography data of ETOPO1 Global Relief model was used in Figure 1 and was obtained from <https://www.ngdc.noaa.gov/mgg/global/> (last accessed September 2018). The ITRF2008 (Altamimi *et al.*, 2012) velocity vector in Figure 1 was obtained from UNAVCO Plate Motion Calculator (<https://www.unavco.org/software/geodetic-utilities/plate-motion-calculator/plate-motion-calculator.html>, last accessed May 2019). The topography data of Shuttle Radar Topography Mission (SRTM) 1 Arc-Second Global model was used in Figure 9. The SRTM model is available from the U.S. Geological Survey and was downloaded via <https://earthexplorer.usgs.gov/> (last accessed, September 2018).

Acknowledgements

This research was conducted under “Seismic Monitoring, Myanmar II Project” which is funded by The Royal Norwegian Ministry of Foreign Affairs. The authors are grateful to Won-Young Kim for providing comments on the manuscript and to Felix Halpaap for the help on obtaining

and managing waveform and catalog data. We thank Editor-in-Chief Zhigang Peng for his suggestions and his effort in handling this article and two anonymous reviewers for their constructive comments. We also thank our project partners, Asian Disaster Preparedness Center (ADPC) and Department of Meteorology and Hydrology (DMH), Ministry of Transport and Communication, Myanmar for their support during this project.

References

- Alsaker, A., L. B. Kvamme, R. A. Hansen, A. Dahle, and H. Bungum (1991). The ML scale in Norway, *Bull. Seismol. Soc. Am.* **81**, no. 2, 379–398.
- Altamimi, Z., L. Métivier, and X. Collilieux (2012). ITRF2008 plate motion model, *J. Geophys. Res. Solid Earth* **117**, no. 7, 1–14, doi: 10.1029/2011JB008930.
- Aung, H. H. (2017). *Myanmar Earthquakes History*, Myanmar Engineering Society, Yangon.
- Bakun, W. H., and W. B. Joyner (1984). The ML scale in central California, *Bull. Seismol. Soc. Am.* **74**, no. 5, 1827–1843.
- Beyreuther, M., R. Barsch, L. Krischer, T. Megies, Y. Behr, and J. Wassermann (2010). ObsPy: A Python Toolbox for Seismology, *Seismol. Res. Lett.* **81**, no. 3, 530–533.
- Cummins, P. R. (2007). The potential for giant tsunamigenic earthquakes in the northern Bay of Bengal., *Nature* **449**, no. 9, 75–78, doi: 10.1038/nature06088.
- Le Dain, Y. A., P. Tapponnier, and P. Molnar (1984). Active faulting and tectonics of Burma and surrounding regions, *J. Geophys. Res.* **89**, no. B1, 453–472, doi: 10.1029/JB089iB01p00453.
- Ellsworth, W. L. (1978). Three-dimensional structure of the crust and mantle beneath the island of Hawaii., Ph.D. Thesis, Massachusetts Institute of Technology (<http://hdl.handle.net/1721.1/52834>, last accessed February 2019).
- Gupta, H., and V. Gahalaut (2009). Is the northern Bay of Bengal tsunamigenic?, *Bull. Seismol. Soc. Am.* **99**, no. 6, 3496–3501, doi: 10.1785/0120080379.
- Havskov, J., and L. Ottemoller (1999). SeisAn Earthquake Analysis Software, *Seismol. Res. Lett.* **70**, no. 5, 532–534.
- Havskov, J., and L. Ottemöller (2010). *Routine Data Processing in Earthquake Seismology*, Springer, New York.
- Hurukawa, N., and P. M. Maung (2011). Two seismic gaps on the Sagaing Fault, Myanmar, derived from relocation of historical earthquakes since 1918, *Geophys. Res. Lett.* **38**, no. 1, 1–5, doi: 10.1029/2010GL046099.
- Hurukawa, N., P. P. Tun, and B. Shibazaki (2012). Detailed geometry of the subducting Indian Plate beneath the Burma Plate and subcrustal seismicity in the Burma Plate derived from joint

- hypocenter relocation, *Earth, Planets Sp.* **64**, no. 4, 333–343, doi: 10.5047/eps.2011.10.011.
- Husen, S., E. Kissling, and J. F. Clinton (2011). Local and regional minimum 1D models for earthquake location and data quality assessment in complex tectonic regions: Application to Switzerland, *Swiss J. Geosci.* **104**, no. 3, 455–469, doi: 10.1007/s00015-011-0071-3.
- Hutton, L. K., and D. M. Boore (1987). The *M_L* Scale in Southern California, *Bull. Seismol. Soc. Am.* **77**, no. 6, 2074–2094.
- IASPEI (2013). Summary of Magnitude Working Group Recommendations on Standard Procedures for Determining Earthquake Magnitudes from Digital Data.
http://iaspei.org/_Resources/Persistent/3de00aeb67e3ff2e6e78472357cd2899c633edea/Summary_WG_recommendations_20130327.pdf (la.
- Kennett, B. L. N., E. R. Engdahl, and R. Buland (1995). Constraints on seismic velocities in the Earth from traveltimes, 108–124.
- Kim, W.-Y. (1998). The *M_L* scale in eastern North America, *Bull. Seismol. Soc. Am.* **88**, no. 4, 935–951.
- Kissling, E. (1995). *Program Velest user's guide - Short Introduction*, Institute of Geophysics, ETH Zurich.
- Kissling, E., W. L. L. Ellsworth, D. Eberhart-Phillips, and U. Kradolfer (1994). Initial reference models in local earthquake tomography, *J. Geophys. Res.* **99**, no. B10, 19635–19646.
- Kundu, B., and V. K. Gahalaut (2012). Earthquake occurrence processes in the Indo-Burmese wedge and Sagaing fault region, *Tectonophysics* **524–525**, 135–146, doi: 10.1016/j.tecto.2011.12.031.
- Laske, G., G. Masters, Z. Ma, and M. E. Pasyanos (2012). CRUST1.0: An Updated Global Model of Earth's Crust, in *Geophysical Research Abstracts EGU General Assembly*, 2012–3743.
- Li, C., R. D. van der Hilst, A. S. Meltzer, and E. R. Engdahl (2008). Subduction of the Indian lithosphere beneath the Tibetan Plateau and Burma, *Earth Planet. Sci. Lett.* **274**, no. 1–2, 157–168, doi: 10.1016/j.epsl.2008.07.016.
- Lienert, B. R., E. Berg, and L. N. Frazer (1986). Hypocenter: an Earthquake Location Method Using Centered, Scaled, and Adaptively Damped Least Squares, *Bull. Seismol. Soc. Am.* **76**, no. 3, 771–783.
- Lienert, B. R., and J. Havskov (1995). A Computer Program for Locating Earthquakes Both Locally and Globally, *Seismol. Res. Lett.* **66**, no. 5, 26–36, doi: 10.1785/gssrl.66.5.26.
- Midzi, V., I. Saunders, M. B. C. Brandt, and T. Molea (2010). 1-D Velocity Model for Use by the SANSN in Earthquake Location, *Seismol. Res. Lett.* **81**, no. 3, 460–466, doi: 10.1785/gssrl.81.3.460.
- Mukhopadhyay, S., R. Chander, and K. N. Khattri (1997). Crustal properties in the epicentral tract of the Great 1897 Assam Earthquake, northeastern India, *Tectonophysics* **283**, no. 1, 311–330, doi:

- [https://doi.org/10.1016/S0040-1951\(97\)00148-0](https://doi.org/10.1016/S0040-1951(97)00148-0).
- Ni, J. F., M. Guzman-Speziale, M. Bevis, W. E. Holt, T. C. Wallace, and W. R. Seager (1989). Accretionary tectonics of Burma and the three-dimensional geometry of the Burma subduction zone, *Geology* **17**, no. 1, 68–71, doi: 10.1130/0091-7613(1989)017<0068:ATOBAT>2.3.CO;2.
- Ottmöller, L., and S. Sargeant (2013). A local magnitude scale ML for the United Kingdom, *Bull. Seismol. Soc. Am.* **103**, no. 5, 2884–2893, doi: 10.1785/0120130085.
- Ottmöller, L., P. Voss, and J. Havskov (2018). SEISAN: Earthquake Analysis Software, Department of Earth Science, University of Bergen, Bergen.
- Pesicek, J. D., C. H. Thurber, S. Widiyantoro, E. R. Engdahl, and H. R. DeShon (2008). Complex slab subduction beneath northern Sumatra, *Geophys. Res. Lett.* **35**, no. 20, L20303, doi: 10.1029/2008GL035262.
- Pesicek, J. D., C. H. Thurber, S. Widiyantoro, H. Zhang, H. R. DeShon, and E. R. Engdahl (2010). Sharpening the tomographic image of the subducting slab below Sumatra, the Andaman Islands and Burma, *Geophys. J. Int.* **182**, no. 1, 433–453, doi: 10.1111/j.1365-246X.2010.04630.x.
- Rao, C. N., N. P. Rao, M. R. Kumar, S. Prasanna, and D. Srinagesh (2015). Structure and Tectonics of the Bay of Bengal through Waveform Modeling of the 21 May 2014 Earthquake of Magnitude 6.0, *Seismol. Res. Lett.* **86**, no. 2A, 378–384.
- Raouf, J., S. Mukhopadhyay, I. Koulakov, and J. R. Kayal (2017). 3-D seismic tomography of the lithosphere and its geodynamic implications beneath the northeast India region, *Tectonics* **36**, no. 5, 962–980, doi: 10.1002/2016TC004375.
- Richter, C. F. (1935). An instrumental earthquake magnitude scale, *Bull. Seismol. Soc. Am.* **25**, no. 1, 1–32.
- Shiddiqi, H. A., P. P. Tun, T. L. Kyaw, and L. Ottmöller (2018). Source Study of the 24 August 2016 Mw 6.8 Chauk, Myanmar, Earthquake, *Seismol. Res. Lett.* **89**, no. 5, 1773–1785, doi: 10.1785/0220170278.
- Singh, A., M. Ravi Kumar, D. D. Mohanty, C. Singh, R. Biswas, and D. Srinagesh (2017). Crustal Structure Beneath India and Tibet: New Constraints From Inversion of Receiver Functions, *J. Geophys. Res. Solid Earth* **122**, no. 10, 7839–7859, doi: 10.1002/2017JB013946.
- Socquet, A., C. Vigny, N. Chamot-Rooke, W. Simons, C. Rangin, and B. Ambrosius (2006). India and Sunda plates motion and deformation along their boundary in Myanmar determined by GPS, *J. Geophys. Res. Solid Earth* **111**, no. 5, 1–11, doi: 10.1029/2005JB003877.
- Swiss Seismological Service (SED) at ETH Zurich (2013). GANSSER broadband seismic experiment in Bhutan, ETH Zurich. Other/Seismic Network. (<https://doi.org/10.12686/sed/networks/xa>, last accessed February 2019).
- Thiam, H. N., Y. M. Min Htwe, T. L. Kyaw, P. P. Tun, Z. Min, S. H. Htwe, M. M. M. Aung, K. K.

- Lin, M. M. M. Aung, D. Cristofaro, *et al.* (2017). A Report on Upgraded Seismic Monitoring Stations in Myanmar: Station Performance and Site Response, *Seismol. Res. Lett.* **88**, no. 3, 1–9, doi: 10.1785/0220160168.
- Tun, S. T., Y. Wang, S. N. Khaing, M. Thant, N. Htay, Y. Myo Min Htwe, T. Myint, and K. Sieh (2014). Surface ruptures of the Mw 6.8 march 2011 tarlay earthquake, Eastern Myanmar, *Bull. Seismol. Soc. Am.* **104**, no. 6, 2915–2932, doi: 10.1785/0120130321.
- Wang, Y., K. Sieh, S. T. Tun, K.-Y. Lai, and T. Myint (2014). Active tectonic and earthquake Myanmar region, *J. Geophys. Res. Solid Earth* **119**, no. 4, 3767–3822, doi: 10.1002/2013JB010762. Received.
- Wang, X., S. Wei, Y. Wang, P. Maung Maung, J. Hubbard, P. Banerjee, H. Bor-Shouh, K. Moe Oo, T. Bodin, A. Foster, *et al.* (2018). A 3D Shear‐Wave Velocity Model for Myanmar Region, *J. Geophys. Res. Solid Earth*, 1–23, doi: 10.1029/2018JB016622.
- Weber, B., J. Becker, W. Hanka, A. Heinloo, M. Hoffmann, T. Kraft, D. Pahlke, J. Reinhardt, and H. Thoms (2007). SeisComP3 - automatic and interactive real time data processing, in *Geophysical Research Abstracts EGU General Assembly*, 09219.
- Wessel, P., W. H. F. Smith, R. Scharroo, J. Luis, and F. Wobbe (2013). Generic mapping tools: improved version released, *EOS Trans AGU* **94**, doi: 10.1002/2013eo450001.
- Wright, C. (2008). Station corrections for the Kaapvaal seismic network: Statistical properties and relation to lithospheric structure, *Phys. Earth Planet. Inter.* **167**, no. 1, 39–52, doi: <https://doi.org/10.1016/j.pepi.2008.02.003>.
- Zaw, S. H., T. Ornthammarath, and N. Poovarodom (2017). Seismic reconnaissance and observed damage after the Mw 6.8, 24 August 2016 Chauk (Central Myanmar) earthquake, *J. Earthq. Eng.* **2469**, no. August, 13632469.2017.1323050-13632469.2017.1323050, doi: 10.1080/13632469.2017.1323050.

Appendix 2

Implications of 3D Seismic Raytracing on Focal Mechanism Determination

K. Newrkla, H.A. Shiddiqi, A.E. Jerkins, H. Keers, and L. Ottemöller

Bulletin of the Seismological Society of America, **Volume 109**, Issue 6, pp. 2746–275
(2019)

The published article is available at:

<https://doi.org/10.1785/0120190184>

Accepted version of an article published in Bulletin of the Seismological Society of America (2019) Vol. 109 No. 6, Pages 2746–2754. <https://doi.org/10.1785/0120190184>

Implications of 3D seismic ray-tracing on focal mechanism determination

Katharina Newrkla¹, Hasbi Ash Shiddiqi¹, Annie Elisabeth Jerkins², Henk Keers¹, and Lars Ottemöller¹

¹Department of Earth Science, University of Bergen, Allègaten 41, N-5007 Bergen, Norway

²NORSAR, Gunnar Randers vei 15, PO Box 53, N-2007 Kjeller, Norway

Abstract

The purpose of this study is to investigate apparent first motion polarities mismatch at teleseismic distances in the determination of focal mechanism. We implement and compare four seismic ray tracing algorithms to compute ray paths and travel times in a 3D velocity model. The comparison is done for both 1D and 3D velocity models. We use the ray tracing algorithms to calculate the take-off angles from the hypocenter of the 24 August 2016 Chauk M_w 6.8 earthquake (depth 90 km) in Central Myanmar to the stations BFO, GRFO, KONO and ESK in Europe using a 3D velocity model of the upper mantle below Asia. The differences in the azimuthal angles calculated in the 1D and 3D velocity models are considerable and have a maximum value of 19.6°. Using the take-off angles for the 3D velocity model, we are able to resolve an apparent polarity mismatch where these stations move from the dilatational to the compressional quadrant. The polarities of synthetic waveforms change accordingly when we take the take-off angles corresponding to the 3D model into account. This method has the potential to improve the focal mechanism solutions, especially for historical earthquakes where limited waveform data are available.

Introduction

The moment tensor solutions of large earthquakes are often obtained through inversion of teleseismic body waves using waveform modeling through a 1D model (e.g. Kikuchi and Kanamori, 1991, 2003). Recently, we computed the moment tensor of the 24 August 2016 Chauk M_w 6.8 earthquake in Central Myanmar that occurred at intermediate depth within the subducting slab using such a 1D model (Shiddiqi et al., 2018) (Figure 1a). The inversion

results were robust, but we also found that at some stations, the observed waveform polarities did not match the solution. Our hypothesis is that deviations from the 1D model in the larger source region are responsible for this misfit.

The moment tensor and slip inversion for this earthquake conducted by Shiddiqi et al. (2018) showed that the event had a thrust mechanism (Figure 1b). Knowledge of the mechanism improves the understanding of the tectonic processes in the Indo-Burma subduction zone that forms a convergent boundary between the subducting Indian plate and the Burma microplate.

Several stations located near the vertical nodal plane (azimuths around $168^\circ \pm 15^\circ$, and $348^\circ \pm 15^\circ$) did not agree with the observed waveforms (Shiddiqi et al., 2018). The computed first motion polarities of these stations are the opposite of the observed traces. To obtain the final result, these stations were excluded from the inversion. As an example, we show observed and synthetic traces for station GRFO (epicentral distance 69.98°) in Figure 1c. The first motion polarity of the observed trace (up) does not agree with the synthetic trace (down). Based on the take-off angle estimate using a 1D velocity model, GRFO is in the dilatational quadrant (Figure 1b). However, its observed polarity is compressional.

Several seismic tomography studies have been conducted in the Indo-Burma region and the surrounding regions (Pesicek et al., 2008; Koulakov, 2011; Raoof et al., 2017). These studies show a clear high velocity anomaly down to the mantle transition zone. This anomaly is interpreted to be the subducted Indian slab.

Previous studies have shown that the use of 3D velocity models can improve the polarity matching and waveform modeling (e.g. Takemura et al., 2016; Frietsch et al., 2018). Perrot et al. (1996) conducted ray tracing and waveform modeling using a 2D crustal velocity model in addition to a 1D global velocity model to improve the depth phase modeling for moment tensor inversion.

In this study, we aim to resolve the apparently incorrect first motion polarities of the 2016 Chauk event. First we investigate different numerical integration methods for a 3D ray tracing algorithm. We compare the results of the Euler, symplectic Euler, midpoint and classical 4th-order Runge-Kutta methods in the 1D and 3D velocity models. Then, we use the best of these 3D ray tracing algorithms to compute the take-off angles and azimuths obtained from the 1D and 3D velocity models around the source to see if we can explain the observed misfit. The take-off angles obtained using 3D ray-tracing are also used to compute P-wave synthetic seismograms for comparison with the observations.

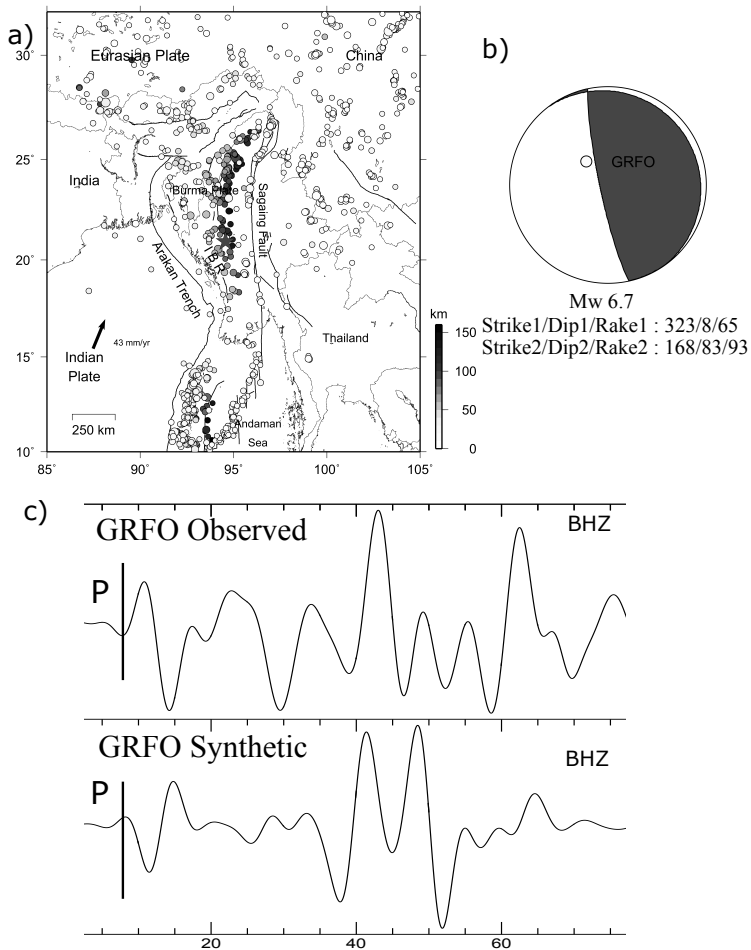


Figure 1: a) Tectonic map of Myanmar and the surrounding regions. Active faults are obtained from Wang et al. (2014) (black lines) and the epicenter of the 2016 M_w 6.8 Myanmar earthquake is depicted by the star. The seismicity catalog was taken from the International Seismological Centre-Engdahl, Hilst, and Buland (EHB) catalog (Engdahl et al., 1998; Weston et al., 2018). b) The focal mechanism solution for the 2016 M_w 6.8 earthquake from Shiddiqi et al. (2018), the polarity of GRFO station is depicted by the open circle. c) The observed (top) and synthetic (bottom) velocity waveforms of GRFO display the vertical component. The traces are bandpass filtered between 5 to 50 seconds. The instrument response on the observed trace is removed.

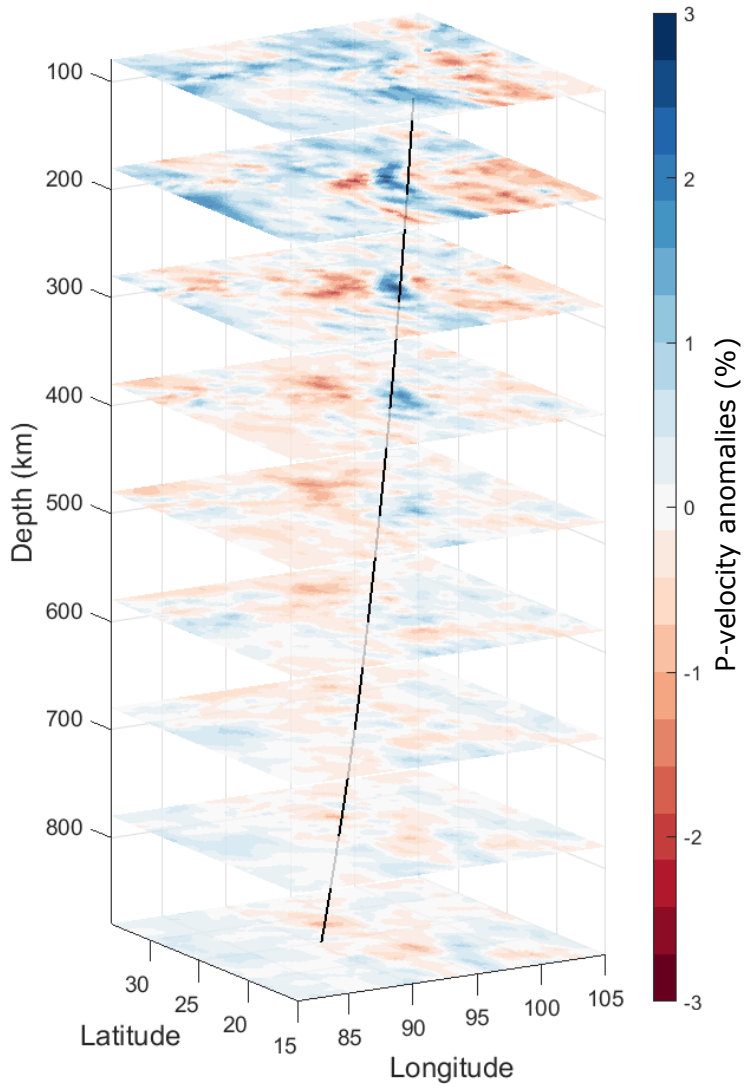


Figure 2: P-velocity anomalies in the upper mantle (Koulakov, 2011) with the ray path from the Myanmar epicenter to the GRFO station in Germany.

Ray tracing

Seismic ray tracing is an important tool to calculate the travel-times of seismic waves. Many previous studies have discussed global ray-tracing methods (e.g. Koketsu and Sekine, 1998; Bijwaard and Spakman, 1999; Zhao and Lei, 2004). To calculate the ray paths and travel times of seismic waves from the source to receivers on the surface of the Earth, we use a 3D ray tracing algorithm. One-point ray tracing was implemented using the following equations (Cerveny, 2001):

$$\begin{aligned} \frac{dr}{dt} &= c^2 T_r, & \frac{dT_r}{dt} &= -\frac{1}{c} \frac{\partial c}{\partial r} + \frac{c^2}{r^3} \left(T_\theta^2 + \frac{T_\varphi^2}{\sin^2 \theta} \right), \\ \frac{d\theta}{dt} &= \frac{c^2}{r^2} T_\theta, & \frac{dT_\theta}{dt} &= -\frac{1}{c} \frac{\partial c}{\partial \theta} + \frac{c^2 \cos \theta}{r^2 \sin^3 \theta} T_\varphi^2, \\ \frac{d\varphi}{dt} &= \frac{c^2}{r^2 \sin \theta} T_\varphi, & \frac{dT_\varphi}{dt} &= -\frac{1}{c} \frac{\partial c}{\partial \varphi}, \end{aligned} \quad (1)$$

where c is the 3D P-wave velocity, r is the radial distance, θ is the co-latitude and φ is the longitude. The slowness vectors \vec{p} are given by

$$p_r = T_r, \quad p_\theta = \frac{T_\theta}{r}, \quad p_\varphi = \frac{T_\varphi}{r \sin \theta}, \quad (2)$$

with

$$T_r = \frac{\partial t}{\partial r}, \quad T_\theta = \frac{\partial t}{\partial \theta}, \quad T_\varphi = \frac{\partial t}{\partial \varphi}. \quad (3)$$

and t is the travel time along the ray. The initial values of r , θ and φ are given by the coordinates at the source point and the initial values of T_r , T_θ and T_φ are given by

$$T_{r_0} = -\frac{\cos \alpha_0}{c_0}, \quad T_{\theta_0} = \frac{r_0}{c_0} \sin \alpha_0 \cos \psi_0, \quad T_{\varphi_0} = \frac{r_0}{c_0} \sin \theta_0 \sin \alpha_0 \sin \psi_0, \quad (4)$$

where α_0 is the angle between $\vec{p}(0)$ and the radial vector pointing towards the center of the Earth and ψ_0 is the angle between p_{θ_0} and the projection of $\vec{p}(0)$ onto the plane normal to the radial vector. Transmission across velocity discontinuities, such as the 410 km and 660 km discontinuities, are taken into account using Snell's law in vector form (Keers et al., 1997; Cristiano et al., 2016).

To create the 3D velocity model, the 3D P-wave velocity model beneath Asia (Koulakov, 2011) was combined with the ak135 reference model (Kennett et al., 1995). This 3D model has P-velocity anomalies between -3% and 3% (Figure 2). As the tomographic image is smoothed we expect that increasing the strength of the anomalies is reasonable. Therefore,

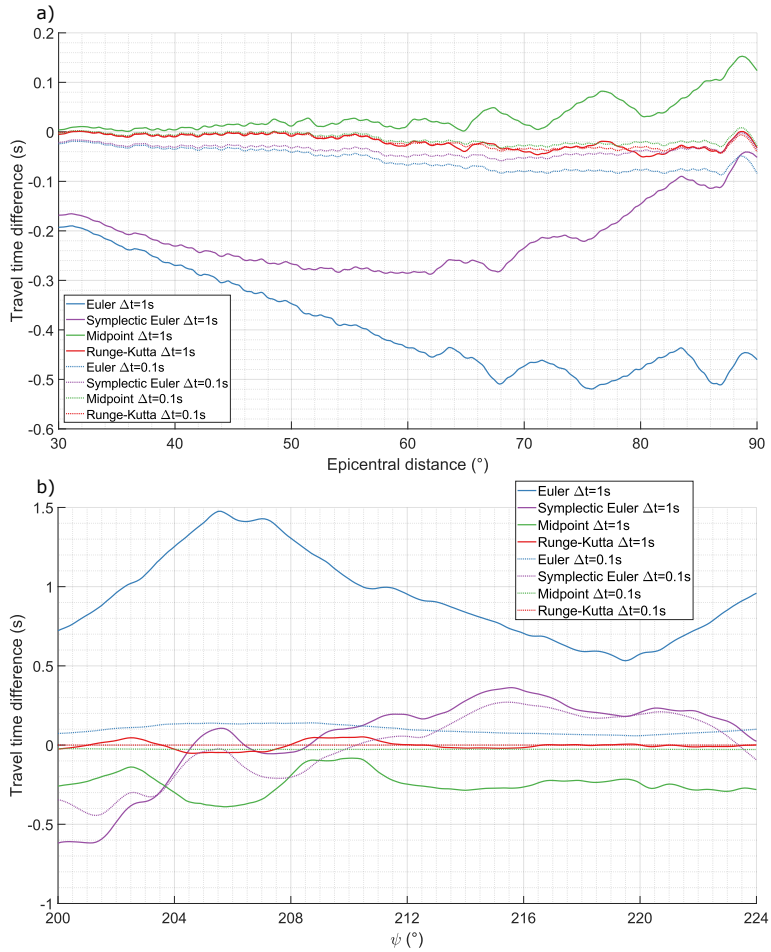


Figure 3: a) Travel time difference calculated using different numerical integration methods compared to the values from the 1D ak135 travel time table. b) Travel time difference between the Runge-Kutta ($\Delta t = 0.1s$) and other numerical integration methods for rays from the Myanmar earthquake epicenter towards Europe with $\alpha = 25^\circ$ and varying azimuthal take-off angle ψ using the 3D velocity model.

we also multiplied the P-velocity anomalies by factors of 2 and 3, to obtain 3D models with P-velocity anomalies in the intervals $[-6\%, 6\%]$ and $[-9\%, 9\%]$, respectively. For the region outside the 3D model, we used the 1D ak135 model. The boundaries between the ak135 model and the 3D model were smoothed using a Gaussian filter. For crustal correction near the receivers, the CRUST1.0 model (Laske et al., 2013) was used.

Numerical implementation

Even though 3D ray tracing is very useful, little attention has been paid in the geophysics literature to the accuracy of the various numerical ray-tracing schemes. Ray-tracing is often based on the Runge-Kutta method (e.g. Cerveny, 2001; Červený et al., 2007; Tian et al., 2007; Virieux and Farra, 1991; Virieux and Lambaré, 2007), but comparison to other methods appears to be limited. The ray tracing equations are solved using a numerical integration scheme with a constant timestep. The two-point ray tracing problem of determining the ray path to a specific receiver was solved by creating a Delaunay triangulation using the one-point ray tracing results for a range of take-off angles. The take-off angles to the receiver were then calculated using linear interpolation.

In order to evaluate the accuracy of different numerical integration methods in the calculation of ray paths and travel times, we implemented the Euler, symplectic Euler, midpoint and classical 4th-order Runge-Kutta methods (e.g. Hairer et al., 2003; Sauer, 2018) to solve the ray tracing equations as given in equation 1. For a system of first-order differential equations

$$\dot{\vec{u}} = \vec{f}(\vec{u}, \vec{v}), \quad \dot{\vec{v}} = \vec{g}(\vec{u}, \vec{v}), \quad (5)$$

where \vec{u} , \vec{v} , \vec{f} , and \vec{g} are 3D vectors. Euler's method is given by

$$u_{n+1} = u_n + f(u_n, v_n) \Delta t, \quad v_{n+1} = v_n + g(u_n, v_n) \Delta t, \quad (6)$$

where Δt is a constant timestep and this equation is for each one of the components of \vec{u} and \vec{v} . Modifying these equations to evaluate the function g at u_{n+1} instead of u_n results in the symplectic Euler method:

$$u_{n+1} = u_n + f(u_n, v_n) \Delta t, \quad v_{n+1} = v_n + g(u_{n+1}, v_n) \Delta t. \quad (7)$$

The midpoint method is a second-order method that modifies Euler's method by first evaluating the function f at the midpoint between u_n and u_{n+1} , and then using this midpoint

value to calculate u_{n+1} :

$$u_{n+\frac{1}{2}} = u_n + f(u_n, v_n) \frac{\Delta t}{2}, \quad u_{n+1} = u_n + f\left(u_{n+\frac{1}{2}}, v_{n+\frac{1}{2}}\right) \Delta t, \quad (8)$$

with equivalent equations for $v_{n+\frac{1}{2}}$ and v_{n+1} . The classical 4th-order Runge-Kutta method is given by

$$u_{n+1} = u_n + \frac{1}{6} (k_1 + 2k_2 + 2k_3 + k_4), \quad v_{n+1} = v_n + \frac{1}{6} (l_1 + 2l_2 + 2l_3 + l_4), \quad (9)$$

with

$$\begin{aligned} k_1 &= f(u_n, v_n) \Delta t, \\ k_2 &= f\left(u_n + \frac{k_1}{2}, v_n + \frac{l_1}{2}\right) \Delta t, \\ k_3 &= f\left(u_n + \frac{k_2}{2}, v_n + \frac{l_2}{2}\right) \Delta t, \\ k_4 &= f(u_n + k_3, v_n + l_3) \Delta t, \end{aligned} \quad (10)$$

and equivalent equations for l . Thus for one time step, Euler and symplectic Euler have the same computational cost and, moreover, are considerably cheaper than midpoint and RK. However, the errors in the midpoint and RK methods are smaller than that of symplectic Euler, which has a smaller error than Euler. There is therefore a trade-off between cost and accuracy, and it is of interest to know which method works best in global seismology.

In order to compare these methods, the travel times were calculated for a source depth of 90 km and compared to the values from the corresponding ak135 travel time table (Kennett, 2005). The Runge-Kutta method with a timestep of 1 s produces travel times with deviations of less than 0.06 s from the values given in the travel time table (Figure 3a). Decreasing the timestep from 1 s to 0.1 s and 0.01 s in the Runge-Kutta method does not significantly change the obtained travel times. The comparison of computational time for these numerical methods with different timesteps is shown in Table 1. For the other three methods, decreasing the timestep causes the results to converge to the results of the Runge-Kutta method. The symplectic Euler method produces smaller absolute travel time differences (compared to the ak135 travel time table) than the Euler method, especially for big timesteps and epicentral distances. Furthermore, the distance at the surface from the ray path calculated using the Runge-Kutta method is up to 81 km removed from the Euler ray path, but only up to 37 km away from the symplectic Euler ray path. This shows that using symplectic methods can improve the accuracy of the results without increasing the computation time.

The travel time differences between the numerical integration methods are greater in the 3D velocity model than in the 1D velocity model (Figure 3b). This is because different ray paths sample different velocity anomalies, resulting in increased travel time differences. Although the symplectic Euler method seems to produce better results than the Euler method in the 3D velocity model for a timestep of 1 s, this is not the case at smaller timesteps (0.1 s). Therefore, a higher order numerical integration method is necessary for ray tracing in a 3D velocity model.

For all further calculations, the 4th-order Runge-Kutta method with a timestep of 1 s was used. In addition to its accuracy, it is significantly faster than using a timestep of 0.1 s with the other lower-order methods.

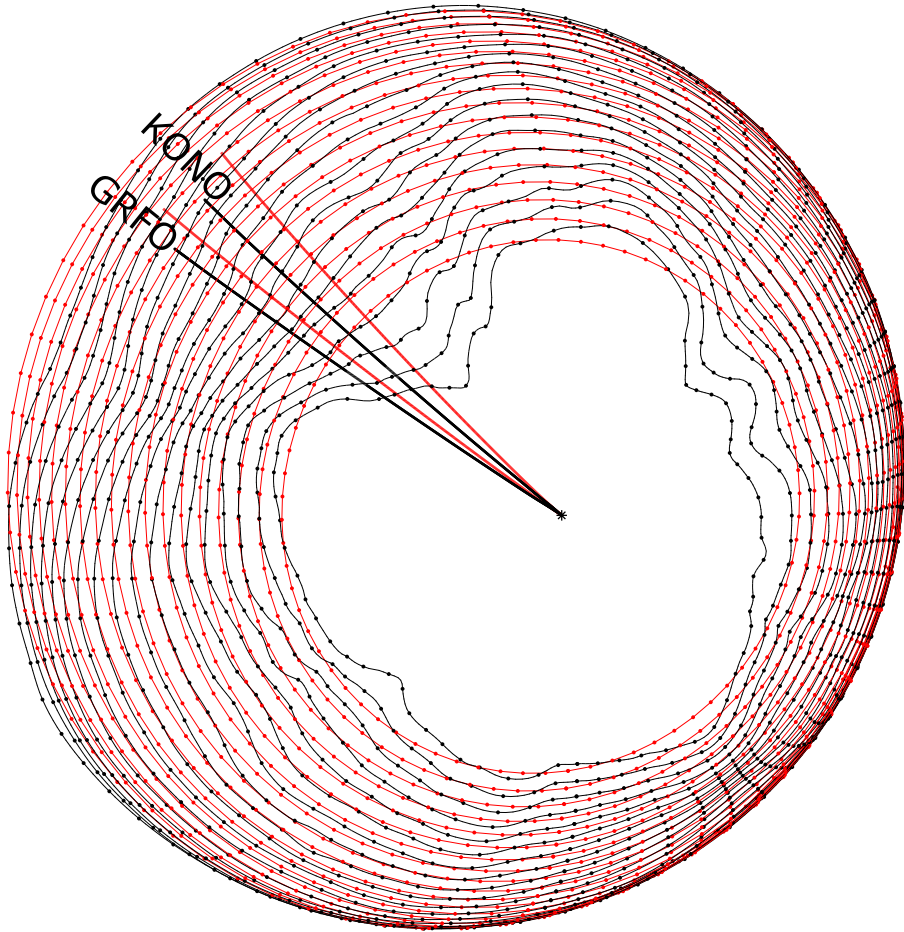


Figure 4: Arrival points of rays at the surface for take-off angles $\alpha = 22^\circ$ to 39° , calculated using the 1D velocity model (red dotted lines) and the 3D model with $\pm 3\%$ P-velocity anomalies (black dotted lines). The red lines represent ray paths from the epicenter toward stations in Europe (KONO and GRFO) in the 1D velocity model. The black lines are the ray paths calculated using the same take-off angles in the 3D velocity model.

Table 1: CPU time for various numerical methods used in 3D ray tracing for rays traveling from Myanmar to Europe

Stepsize (s)	Average ray tracing time (s) per ray in 3D velocity model			
	Runge-Kutta	Midpoint	Symplectic Euler	Euler
1	0.4	0.3	0.2	0.2
0.1	2.0	1.1	0.8	0.7
0.01	18.0	9.8	5.8	5.6

Results

Ray Tracing

The lateral heterogeneities in the 3D velocity model cause deviations in the ray paths, resulting in rays surfacing at large distances from the rays calculated in the 1D velocity model for the same take-off angles (Figure 4). Figure 4 shows that the differences between the 1D rays and 3D rays are large for the rays traveling from Myanmar to Europe, while the differences between all other directions are much smaller. For example, for take-off angles with values $\alpha = 25^\circ$ and $\psi = 225^\circ$, which correspond to a ray from Myanmar towards Europe, the difference in arrival points between the ray paths in the 1D and 3D velocity models is 1086 km. The difference between 1D and the selected regional 3D is more significant for rays to Europe, because the rays travel through the subducted slab represented by a high seismic velocity anomaly (Figure 2). This causes a relatively large distortion of the wavefronts that travels to Europe as can be seen in Figure 4.

Therefore, rays to specific seismic stations have different take-off angles in the 1D and 3D velocity models (Figure 5). The differences between the take-off angles α_0 and ψ_0 for rays to the same seismic station in the 1D and 3D velocity models are denoted by $\Delta\alpha$ and $\Delta\psi$. Increasing the strength of the anomalies increases $\Delta\psi$, as the steeper velocity gradients in θ and φ lead to a greater deviation in the ray path. At some points along the ray path in the 3D velocity model, the anomalies cause an increase compared to the 1D velocity gradient $\frac{\partial c}{\partial r}$, and at other points they cause a decrease in $\frac{\partial c}{\partial r}$. Therefore, the relationship between the strength of the P-velocity anomalies and $\Delta\alpha$ is not necessarily linear (Figure 5a and b). As for the depth changes, the relationship between $\Delta\alpha$, $\Delta\psi$ and depth changes are relatively linear. However, increasing depth does not change $\Delta\psi$ as much as increasing the P-wave velocity anomaly.

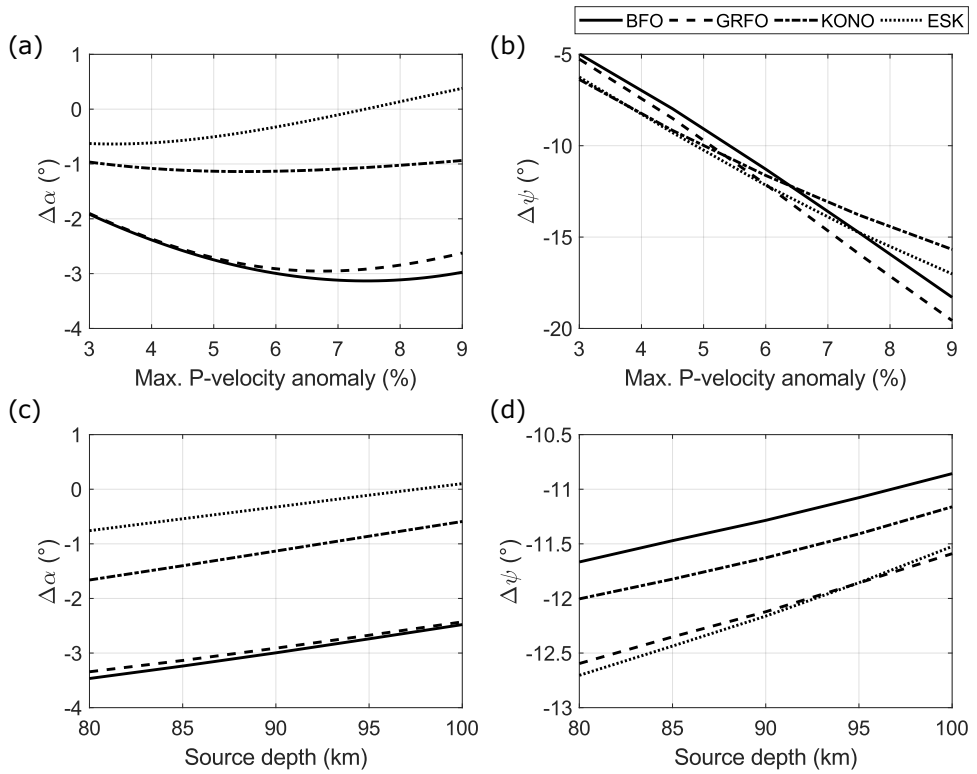


Figure 5: Difference in take-off angles $\Delta\alpha$ and $\Delta\psi$ between ray paths calculated using the 1D and 3D velocity models for rays to the stations BFO, GRFO, KONO and ESK, plotted (a and b) against the strength of the P-velocity anomalies at a source depth of 90 km and (c and d) against the source depth with $\pm 6\%$ P-velocity anomalies.

First Motion Polarities

We computed the take-off angles for four stations with an azimuth of $348^\circ \pm 15^\circ$, BFO (Black Forest Observatory, Schiltach, Germany), ESK (Eskdalemuir, Scotland, UK), GRFO (Grafenberg, Germany) and KONO (Kongsberg, Norway), to compare the position within the fault plane solution corresponding to take-off angles obtained from 1D and 3D velocity models (Figure 6). The take-off angles from the 3D velocity model were calculated using the model with a maximum P-wave velocity anomaly of 6% and 9%. The 3D ray-tracing improves the estimation of take-off angles, especially when we increase the magnitude of the 3D velocity anomalies. As shown in Figure 6, the first motion polarities move toward the compressional quadrant. This matches with the observed polarities when the 3D velocity model is used. Increasing the depth also moves the take-off angles near the compressional quadrant. However, the depth increase is not sufficient to make all of these stations have consistent polarities.

In addition, we also conducted forward waveform modeling, to see how the first motion polarities of the waveforms change when the 3D take-off angles are used. We computed waveforms for these four stations, i.e., BFO, ESK, GRFO and KONO (Figure 6). Green's functions were computed using the Computer Programs in Seismology package (Herrmann, 2013). The Green's functions were computed using the ak135 model (Kennett et al., 1995), and convolved with a triangular function with a base width of 15 seconds and with the seismic source mechanism from Shiddiqi et al. (2018). Since we only conducted ray-tracing for the direct P-wave, in this modeling we only focus on the direct P-wave group. The depth phases (e.g., pP, and sP), which usually are included in teleseismic waveform modeling, have different ray-paths and take-off angles.

Taking the 3D velocity anomaly near the source region into account, we computed the synthetics based on 3D take-off angles with a maximum P-wave velocity anomaly of 6% and 9%. We are able to match the observed waveforms with respect to polarity. This was not possible for waveforms computed using 1D take-off angles (Figure 6).

Discussion and Conclusion

This study was motivated by observation of inconsistent polarities for a few stations in north-western Europe for a global moment tensor inversion of an intermediate depth earthquake in Myanmar using a 1D model. These stations were close to a nodal plane, and a change of the focal mechanism could have been the solution. However, this would require a change

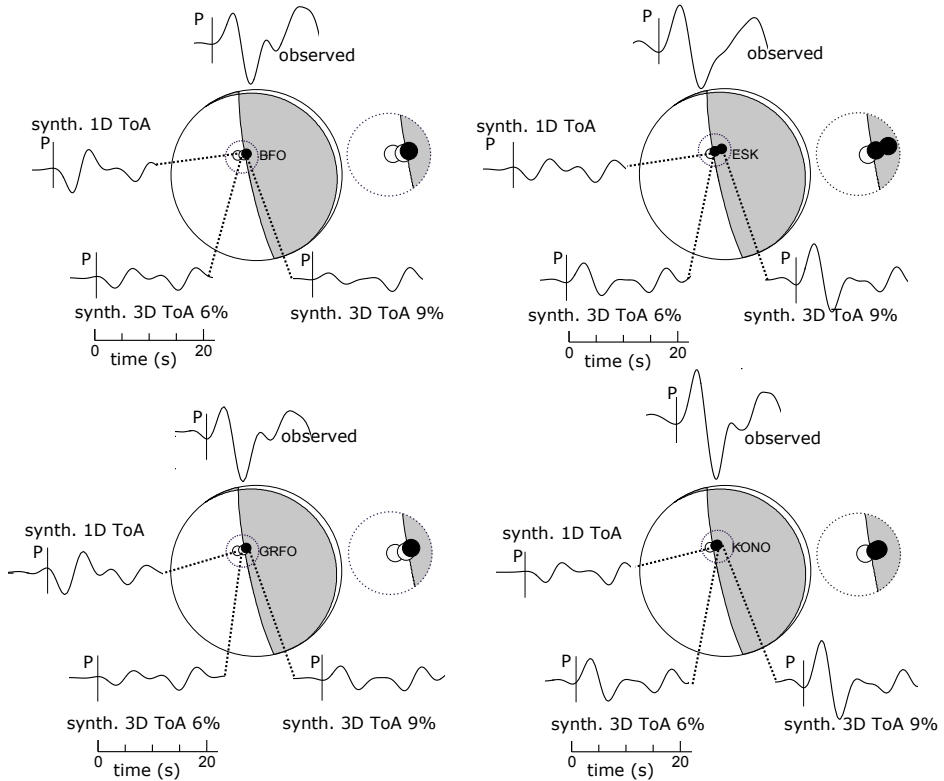


Figure 6: The changes of P-wave polarities on the focal mechanism solution for BFO, ESK, GRFO and KONO. The small circles correspond to the station positions on the stereographic projection (open circles: dilatation quadrant, black circles: compression quadrant). The areas around the circles are also magnified. The observed velocity traces are plotted at the top of each subfigure and followed by synthetics using 1D model, and synthetics using 1D model with take-off angles (ToA) obtained from ray-tracing in the 3D model with $\pm 6\%$, and $\pm 9\%$ anomaly. The traces are bandpass filtered between 0.02 Hz to 0.2 Hz.

in dip of the nodal planes by about 5° and the obtained resulting solution would have a worse misfit. Another possibility could have been to adjust the hypocentral depth, but the effect on the take-off angles was not significant enough for adjustments within the location uncertainties. Instead, we attempted to see if the observations in this particular case can be explained by the regional 3D structure in the source region.

This required the computation of take-off angles for a regional 3D model such as developed by Koulakov (2011) to see if the respective stations move from the dilational to the compressional quadrant. The ray tracing was developed as part of this study. We compared different numerical implementations of the ray equations and verified that the calculations have sufficient accuracy. The accuracy of the 3D ray tracing algorithm was tested by comparing the computed travel times to the 1D ak135 travel time tables (Kennett, 2005), and by comparing the four different methods for two different timesteps for the 3D model. Our preferred choice for the implementation was the 4th-order Runge-Kutta method as it produces accurate and fast results.

The strength of the anomalies in the 3D model (Koulakov, 2011) was $\pm 3\%$. Our tests showed that this was not sufficient for the stations to move across the nodal plane. We required regional velocity anomalies of $\pm 9\%$ for the ray-tracing results corresponding to our stations to be able to produce consistent take-off angles. The computed 3D take-off angles were also used to perform forward modelling based on a 1D model.

Our example of the Myanmar earthquake shows that 1D velocity models may not be sufficient for global moment tensor body wave inversion. One option is to omit the stations that cannot be explained with 1D velocity models as was done by Shiddiqi et al. (2018). However, with the advances in global 3D modelling (e.g. Frietsch et al., 2018) full 3D moment tensor inversion should become feasible. On the other hand, the study of the mechanism of historic earthquakes often requires the use of polarities only. The number of polarities in this case typically is limited and therefore it is important to compute accurate take-off angles based on 3D models rather than 1D model. It is possible to use recent earthquake moment tensor analysis to identify regions where this becomes important, and our approach can then be applied in such cases.

This study shows that apparent inconsistent polarities disappear when 3D ray tracing is used. The identification of stations with polarities that are not consistent with the source mechanisms using a 1D velocity model can further have a significant impact on the understanding of the global 3D structure.

Data and Resources

The 3D P-wave velocity model beneath Asia was downloaded from www.ivan-art.com/science/REGIONAL/ (last accessed: November 2018). Teleseismic data of Global Seismic Network (GSN) were provided by Incorporated Research Institutions for Seismology (IRIS).

Acknowledgments

Part of this work was done as part of KN's IAESTE internship at the University of Bergen. We thank Thomas Meier, Johannes Stampa, and Kai Olbert of the University of Kiel for discussions on global seismic ray-tracing. We thank Zeinab Jeddi for giving comments on the manuscript. We also thank two anonymous reviewers for their constructive comments.

References

- Bijwaard, H., Spakman, W., 11 1999. Fast kinematic ray tracing of first- and later-arriving global seismic phases. *Geophysical Journal International* **139** (2), 359–369.
URL <https://doi.org/10.1046/j.1365-246x.1999.00950.x>
- Cerveny, V., 2001. *Seismic Ray Theory*. Cambridge University Press, Cambridge.
- Cristiano, L., Meier, T., Krüger, F., Keers, H., Weidle, C., 2016. Teleseismic P-wave polarization analysis at the Gräfenberg array. *Geophys. J. Int.* **207** (3), 1456–1471.
- Engdahl, R. E., van der Hilst, R., Buland, R., 1998. Global teleseismic earthquake relocation with improved travel times and procedures for depth determination. *Bull. Seismol. Soc. Am.* **88** (3), 722–743.
- Frietsch, M., Ferreira, A., Vales, D., Carrilho, F., 07 2018. On the robustness of seismic moment tensor inversions for mid-ocean earthquakes: the Azores archipelago. *Geophysical Journal International* **215** (1), 564–584.
URL <https://doi.org/10.1093/gji/ggy294>
- Hairer, E., Lubich, C., Wanner, G., 2003. Geometric numerical integration illustrated by the Störmer–Verlet method. *Acta Numerica* **12**, 399–450.
- Herrmann, R. B., 2013. Computer Programs in Seismology: An Evolving Tool for Instruction and Research. *Seismol. Res. Lett.* **84** (6), 1081–1088.

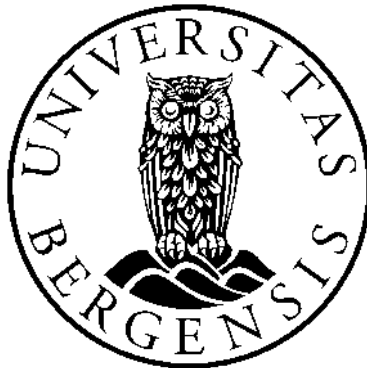
- Keers, H., Dahlen, F. A., Nolet, G., 1997. Chaotic ray behaviour in regional seismology. *Geophys. J. Int.* **131** (2), 361–380.
- Kennett, B. L. N., 2005. *Seismological Tables: ak135*. rses.anu.edu.au/seismology/AK135tables.pdf, [Online; accessed 28-03-2019].
- Kennett, B. L. N., Engdahl, E. R., Buland, R., 1995. Constraints on seismic velocities in the Earth from traveltimes. *Geophys. J. Int.* **122** (1), 108–124.
- Kikuchi, M., Kanamori, H., 1991. Inversion of Complex Body Waves-III. *Bull. Seismol. Soc. Am.* **81** (6), 2335–2350.
- Kikuchi, M., Kanamori, H., 2003. *Note on teleseismic body-wave inversion program*. www.eri.u-tokyo.ac.jp/ETAL/KIKUCHI/, [Online; accessed 28-03-2019].
- Koketsu, K., Sekine, S., 02 1998. Pseudo-bending method for three-dimensional seismic ray tracing in a spherical earth with discontinuities. *Geophysical Journal International* **132** (2), 339–346.
URL <https://doi.org/10.1046/j.1365-246x.1998.00427.x>
- Koulakov, I., 2011. High-frequency P and S velocity anomalies in the upper mantle beneath Asia from inversion of worldwide traveltime data. *J. Geophys. Res. B. Solid Earth* **116** (B4).
- Laske, G., Masters, G., Ma, Z., Pasyanos, M., Apr. 2013. *Update on CRUST1.0 - A 1-degree Global Model of Earth's Crust*. In: *EGU General Assembly Conference Abstracts*. Vol. 15. pp. EGU2013–2658.
- Perrot, J., Deschamps, A., Farra, V., Virieux, J., 05 1996. A 2-D velocity model of the Vrancea region in Romania: prediction of teleseismic waveforms. *Geophysical Journal International* **125** (2), 537–544.
URL <https://doi.org/10.1111/j.1365-246X.1996.tb00016.x>
- Pesicek, J. D., Thurber, C. H., Widiyantoro, S., Engdahl, E. R., DeShon, H. R., 2008. Complex slab subduction beneath northern Sumatra. *Geophys. Res. Lett.* **35** (20).
- Raooof, J., Mukhopadhyay, S., Koulakov, I., Kayal, J. R., 2017. 3-D seismic tomography of the lithosphere and its geodynamic implications beneath the northeast India region. *Tectonics* **36** (5), 962–980.
- Sauer, T., 2018. *Numerical analysis*, 3rd Edition. Pearson, Upper Saddle River, New Jersey.

- Shiddiqi, H. A., Tun, P. P., Kyaw, T. L., Ottemöller, L., 2018. Source Study of the 24 August 2016 M_w 6.8 Chauk, Myanmar, Earthquake. *Seismol. Res. Lett.* **89** (5), 1773–1785.
- Takemura, S., Shiomi, K., Kimura, T., Saito, T., 2016. Systematic difference between first-motion and waveform-inversion solutions for shallow offshore earthquakes due to a low-angle dipping slab. *Earth, Planets Sp.* **68** (1), 149.
- Tian, Y., Hung, S.-H., Nolet, G., Montelli, R., Dahlen, F., 2007. Dynamic ray tracing and travelttime corrections for global seismic tomography. *Journal of Computational Physics* **226** (1), 672 – 687.
- Virieux, J., Farra, V., 1991. Ray tracing in 3-D complex isotropic media: An analysis of the problem. *GEOPHYSICS* **56** (12), 2057–2069.
- Virieux, J., Lambaré, G., 2007. 1.04 - Theory and Observations – Body Waves: Ray Methods and Finite Frequency Effects. In: *Schubert, G. (Ed.), Treatise on Geophysics*. Elsevier, Amsterdam, pp. 127 – 155.
- Wang, Y., Sieh, K., Tun, S. T., Lai, K.-Y., Myint, T., 2014. Active tectonics and earthquake potential of the Myanmar region. *J. Geophys. Res. B. Solid Earth* **119** (4), 3767–3822.
- Weston, J., Engdahl, E. R., Harris, J., Di Giacomo, D., Storchak, D. A., 2018. ISC-EHB: reconstruction of a robust earthquake data set. *Geophys. J. Int.* **214** (1), 474–484.
- Zhao, D., Lei, J., 2004. Seismic ray path variations in a 3D global velocity model. *Physics of the Earth and Planetary Interiors* **141** (3), 153 – 166.
- Červený, V., Klimeš, L., Pšenčík, I., 2007. Seismic ray method: Recent developments. In: *Wu, R.-S., Maupin, V., Dmowska, R. (Eds.), Advances in Wave Propagation in Heterogeneous Earth*. Vol. 48 of *Advances in Geophysics*. Elsevier, pp. 1 – 126.

Errata for
Intraplate Earthquakes in Nordland, Northern
Norway

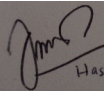
Insight from Seismic Tomography and Seismicity Analysis

Hasbi Ash Shiddiqi



Thesis for the degree philosophiae doctor (PhD)
at the University of Bergen

19.12.22


Hasbi Ash Shiddiqi

(date and sign. of candidate)

19.12.2022



(date and sign. of faculty)

Errata

Page 9: Missing word in Figure 1.2 caption: "red circles" - corrected to "red open circles"

Page 16: Removed brackets in equation 1.5: " $\log M_0 = 1.5(M_w + 9.105)$ " - corrected to " $\log M_0 = 1.5 M_w + 9.105$ "



Graphic design: Communication Division, UIB / Print: Skjipes Kommunikasjon AS



uib.no

ISBN: 9788230841488 (print)
9788230852590 (PDF)